Investigation into the Vortex Formation Threshold and Infrasound Generation in a Jet Engine Test Cell

Wei Hua, Ho
BEng (Hons)

A thesis presented for the degree of
Doctor of Philosophy
in
Mechanical Engineering
at the
University of Canterbury
2009

Dedicated to my late mum

Acknowledgements

在家靠父母，出外靠朋友

“When at home, depend on your parents; when away, depend on your friends”

---- A famous Chinese proverb

The last three years of my life have been filled with a myriad of experiences and trials. Some of them have been fun, interesting and enjoyable whilst others have been filled with pain and extreme anxieties. It was during these difficult times that I truly understand the meaning of the above proverb and appreciated the value of family, friends, colleagues and understanding supervisors. Without them, the road would have been a lot harder than it was.

This thesis is a culmination of years of hard work, dedication and sacrifice. The credit is certainly not all mine and many people have contributed to its successful submission. I will attempt my best to express my most heartfelt thanks and gratitude to all of them in these acknowledgements.

First and foremost, gratitude must be given to the Mechanical Engineering department at the University of Canterbury for providing me with a fees scholarship and also a conducive environment in which to conduct my research.

The person who has played the biggest part in my PhD would have to be my main supervisor Dr Mark Jermy. You have contributed immensely in the successful completion of this stage of my life. I was like a little boat facing an imminent storm in the ocean, your guidance, support and understanding acted like a lighthouse providing direction and confidence. I am especially grateful for the distant working relationship that we had I’m pretty sure not many supervisors would have been open to the idea let alone put in effort to ensure it worked out. Aside from being my supervisor, you are also a valued friend whom I am very honoured to have known and worked with.

I would also like to thank my girlfriend and faithful partner Yongrou for being so patient and caring especially the times when I am not by her side. Your love and support kept me going when the odds stacked higher and higher.

Special thanks to Richard Kruse and Joe Ziolkowski of CENCO Inc. for extending the scholarship to me. It took a great deal of load of my shoulders and allowed me to concentrate on the research rather than the need to worry about jobs and income. Technically you've also helped by providing data and experience. Although we did not have the opportunity to meet, I believe we had established a good working relationship.

Special mention must go to Sato Takanori, your presence in the office made going to work more enjoyable. You were a great de-stressing force. You were not just a source of entertainment but offered many valuable advice on my work and the PhD experience. Arigatou Gozaimasu!

To Jordan Gilmore, your help in FLUENT especially during the initial stages was invaluable. It made the steep learning curve a lot easier to scale. Without your help, I would not have been able to start generating results as early as I did. Thank you.

To Dr Mathieu Sellier, Dr John Pearse and Dr Steve Moore, although we only worked together on very limited occasions, I have benefited immensely from the help and advice you provided from time to time.

To all my good friends at the university, Naomi Zens, Vilailuck Siriwongrungson, Karl Buchanan, Hadley Cave, Mohamed Sohel, Muaviyath Mohamed, Lydia Yu, Callum Spence and the beautiful Angel Bright (congratulations on your engagement), Lim Chin Wai, thanks for being there and making the journey less arduous. Special thanks goes to Montira Watcharasukarn, Nicolas Buchmann and Samuel Gyamfi, I will miss our meals and drinks sessions.

I also would like to thank my landlords Mike and Robyn Robinson, from Urban Rooms, for being such an excellent landlord and providing me with a comfortable home in this city away from home.

Finally to my dad, thanks for being supportive of my studies and patiently awaiting the end of my income-less time.

Abstract

This thesis details an in investigation of two problems arising during the testing of a jet engine in a test cell, namely the formation and ingestion of vortices and the generation and propagation of infrasound. Investigation involved the use of computational fluid dynamic as well as analytical tools.

The author extended the work of previous researchers by investigating the effect when a suction inlet in surrounded by four walls, (as it is in a test cell). A previously suspected but not documented small region of unsteady vortex was discovered to lie between the steady vortex and no vortex regions. The preferential attachment of the vortex, when formed, to a particular surface was investigated and a low velocity region near that surface has been proven as a possible cause. A cell bypass ratio > 90% was found to be necessary to avoid the formation of vortices in typical situations.

Parametric studies (conducted cetaris paribus) on four different geometries and flow parameters were also conducted to determine how they affected the vortex formation threshold. Boundary layer thickness on the vortex attachment surface, upstream vorticity, size of suction inlet was found to have a direct relationship with probability of vortex formation whereas Reynolds number of flow was found to have an inverse relationship.

Three hypotheses regarding the generation and propagation of infrasound in test cells were analysed. The first hypothesis states that the fluctuating of flow within the test cell led to a periodic fluctuation of pressure. The second hypothesis predicts a change in flow conditions can leads to a change in the acoustic reflection characteristics of the blast basket perforates. The final hypothesis proposes that changing engine location and size of augmenter, can lead to a reduction in the slip velocity between the engine exhaust jet and the cell bypass flow thus reducing the engine jet noise.

The first hypothesis has been disproved using CFD techniques, although the results are as yet inconclusive. The second and third hypotheses have been proven to be potentially feasible techniques to be employed in the future. The changes proposed in the final hypothesis are shown to reduce the engine jet noise by up to 5 dB.

List of Publications

Journal Papers Published

M Jermy and W. H. Ho, "Location of the vortex formation threshold at suction inlets near ground planes by computational fluid dynamics simulation", Proceedings of the I Mech E Part G Journal of Aerospace Engineering Volume 222 Number 3, pp 393 – 402, 2008.

Ho Wei Hua, Mark Jermy and Henry Dumbleton, "Formation of Sink Vortices in a Jet Engine Test Cell", IAENG (International Association of Engineers) Engineering Letters Volume 16 Issue 3, pp 406 – 411, 2008.

Book Chapters

HO Wei Hua and MARK Jermy, "Formation and Ingestion of Vortices into Jet Engines during Operation", IAENG (International Association of Engineers) Transactions on Engineering Technologies Volume I: Special Edition of the International MultiConference of Engineers and Computer Scientists 2008, pp 132 – 143, 2009.

Refereed Conference Proceedings

Ho Wei Hua and Mark Jermy, "Validated CFD simulations of vortex formation in jet engine test cells" Proceedings for the 16th Australasian Fluid Mechanics Conference, pp 1102 – 1107, 2007.

W. H. Ho, H. Dumbleton and M. C. Jermy, "Effect of upstream velocity gradient on the formation of sink vortices in a jet engine test cell", Proceedings for the International MultiConference of Engineers and Computer Scientists, pp 1767 – 1772, 2008.

Awards

Certificate of Merit (Student) for the 2008 IAENG International Conference on Industrial Engineering.

Table of Contents

List of Figures

List of Tables

List of Symbols

Numbers in the right column denote equations where the symbols were used

A	area		13, 20
A	cross-sectional area of neck	m^2	10
c	speed of sound	m/s	8, 9, 10, 11, 12, 16, 17, 18, 19
CBR	cell bypass ratio		5
d	diameter	m	6, 7, 12, 13, 14, 15, 17, 19, 20
D_i	suction inlet diameter	m	4
f	body forces	N	1
f	frequency	Hz	6, 7, 8, 9, 10, 11, 12, 15, 25
h	height	m	11
K	constant of proportionality		17, 19
L	length of neck	m	10
L	length	m	6, 7, 8, 9, 14
l, m, n	resonance mode in x, y, z direction		8, 9
$\dot{m}$	mass flow rate	kg/s	5, 20
P	power	W	19, 20
P	pressure	Pa	1
Pe	Peclet number		3
r	distance from acoustic source	m	22, 23
r	distance from wall	m	24
r	radius		13
Ro	rossby number		4
R_c	room constant	m^2	22
S	surface area	m^2	24
SPL	sound pressure level	dB	22, 23, 24
SWL	sound power level	dB	22, 23
T	tensor of fluctuating Reynolds stresses		18
T	thickness	m	14, 15
t	time	s	18
TL	transmission loss	dB	24
V	velocity	m/s	1, 13, 18, 19
V_i	suction inlet velocity	m/s	4
Vol	volume of cavity	m^3	10
W	velocity gradient	/s	4, 21
x	axial location		18
Z	acoustic impedance	rayl	13, 16
z	specific acoustic impedance	Ns/m^3	14, 15
ρ	density	kg/m^3	1, 2, 13, 17, 18, 19, 20
Γ	stress tensor		1, 2
α	angle of incidence		16
Q_θ	directivity factor		22

τ_{av}	average transmission coefficient		24
ϕ	cell (CFD mesh) face value		2, 3
ϕ	porosity		14, 15
μ	dynamic viscosity	Pa.s	2, 13
λ	wavelength	m	14
Δ	difference		17

1 Introduction

This is the introductory chapter of this thesis where the industrial and academic impetus for the research is laid out together with the scope of the investigations.

The layout of this thesis is presented at the end of this chapter.

1.1 Impetus for Research

This research can be broadly divided into two distinct sections, one dealing with the generation and ingestion of vortices into the engine core and the other with the generation and propagation of infrasound during the operation of an engine test in the test cell.

The safe operation of a jet engine test facility is critical to the aviation industry in terms of both passenger and jet safety and costs to the airline. After the overhaul or repair of a jet engine, it will be tested in a jet engine test cell to ensure performance parameters are met according to specifications.

Some of the tests conducted in the test cell involve the stable operation of the engine. Parameters measured to determine the stability of operation include pressures, temperatures, rotor rpm, specific fuel consumption (SFC) and air flow rate etc.

Grounding of an aircraft is the worst cost related problem to the airline as it means loss income in terms of passenger fares and extra cost of parking the aircraft. However regular checks and overhaul are mandated by the relevant authorities (Civil Aviation Authority - CAA, Federal Aviation Authority – FAA etc.) to ensure safety in flight. These checks and overhaul represent aircraft downtime and airlines always try to keep these to the minimum whilst still adhering to the relevant standards. Hence, any mishaps or accidents that happen during the overhauling or testing stages mean unnecessary additional downtime, with a significant cost attached.

The list of possible mishaps or accidents is too long to be mentioned in detailed here. This research attempts to investigate perhaps the most serious possibility, the

generation and ingestion of vortices into the engine core during operation. This is a potentially calamitous event with the worse possible outcome being the stalling of the compressor leading to extensive damage to the compressor blades and thus requiring a major overhauling exercise. Such an event, as one would imagine, is highly undesirable to the airline.

This problem of generation and ingestion of vortices has been known and researched in the past but they are mostly limited to models with a suction inlet (representing the engine inlet) over a single solid boundary (representing the ground) and are experimental in nature. These models provide good information for vortex generation and ingestion when the engine is mounted on the aircraft and either performing a ground engine check or just prior to take-off on the runway. What is lacking however is the investigation of what happens when the engine is surrounded by four walls, as it would be when the engine is being tested in the test cell.

Another problem that can occur during the operation engine tests in test cell is the generation and propagation of low frequency noise. The effects of these low frequency noises can be broadly split into structural vibration leading to structural damage and physio-psychological effects that affect a proportion of the population.

Traditionally engine test facilities are built far away from urban settlements primarily because of the noise pollution (both at infrasonic and audible frequencies) related to them. However, with the increase in human population and size of cities, the distance between such test facility and urban settlements has decreased. This leads to the increase in people affected by the sound emitted. As a consequence of the increase in people affected and hence complaints, there is a trend of tightening infrasound emission standards from the various aviation authorities.

Test cell manufacturers have encountered an over-emission of low frequency noise in some of the test cells they have built. Although these have all been “solved” by numerous modifications done to the test cell, it was not done in a systematic manner leading to little improvement in the understanding of the problem. Adding to the confusion, some of the modifications seemed to “work” in some cells but does nothing in other cells.

The work described in the second part of this thesis (chapters 10 to 14) is an attempt to isolate the principal causes of infrasound and to develop tools to predict the effectiveness of the most promising and new mitigation strategies.

1.2 Scope of Research

The methodology of this research will be heavily based on calculations using the commercial computational fluid dynamics (CFD) package Fluent (ANSYS Inc.) Calculation results will be validated with experimental results from various sources including previous investigation work of various investigators and measurement data from a test cell manufacturer.

1.2.1 Vortex Problem

The scope of the vortex investigation is limited to the calculations on simplified engine-over-runway and engine-in-testcell models. The models have all the important generic features of each scenario whilst leaving out any specific details that characterises any particular engine or test cell. The decision to adopt only a simplified generic model was made early in the investigation so as to exclude any engine or cell specific parameters, such as details of the intake, the engine thrust stand, cone rail and amenities mounted on the walls (lights, sprinklers etc.), that may affect the generation and ingestion of vortices. These engine or cell specific parameters, although important to the understanding of the problem, may obscure the effects of parameters that are present in all scenarios.

The engine is simulated with a simple suction inlet at the end of a tube of negligible thickness and the structures surrounding the engine are simulated with flat no-slip walls. Although the engine inlet is termed as such, the boundary condition used in the CFD simulations used for this research is an outlet from the flow domain. Pictorial illustrations of the engine-over-runway and engine-in-testcell models are given in Figure 1 and Figure 2.

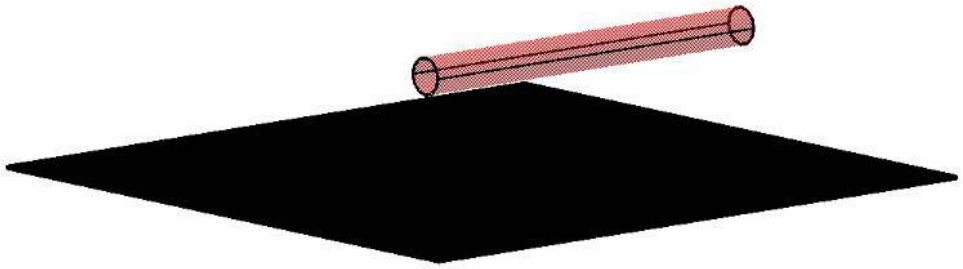

Figure 1: Engine-Over-Runway Model

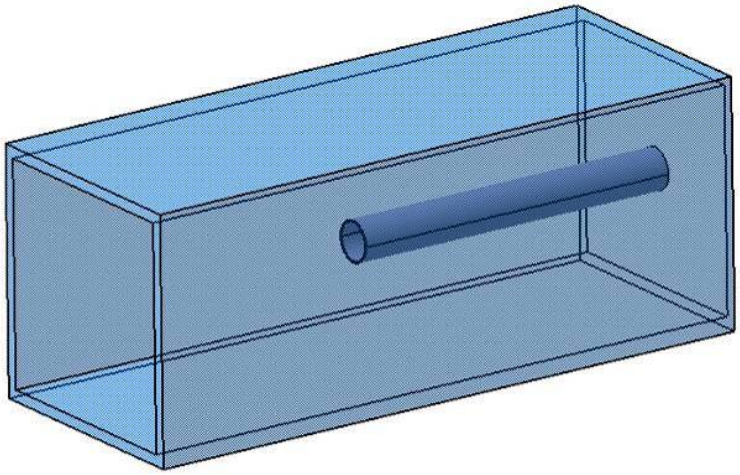

Figure 2: Engine-In-Testcell Model

Another limitation of scope for the vortex investigation is the type of vortex under investigation. The type of vortex concerned is the type that concentrates vertically aligned ambient vorticity. This condition limits the vortex formed to single-cored vortices forming at inlets in a headwind. Vortices and vortex mechanisms, which does not require non-zero ambient vorticity thus forming two or more counter-rotating vortex cores such as those described by de Siervi et al. [1] were not considered. Please refer to chapter 4.1 for more details

It is desired to conduct and obtain parametric relationships between flow and geometric parameters and the formation of these vortices.

1.2.2 Infrasound Problem

The scope of the infrasound problem is limited to calculations and simulations based on CFD models of a test cell which when initially built emitted unacceptable levels of infrasound while testing high thrust engines. Due to non-disclosure agreements with the relevant parties, the actual identity of the cell has to be obscured. For identification, the term 'the modelled cell' will be used. The model was constructed using CAD software and engineering drawings provided by the cell builder and no onsite measurements were conducted. It is expected that the model will differ from the actual cell structures but these differences should not be significant to the investigation. A graphical representation of the cell and the features that are modelled is shown in Figure 3.

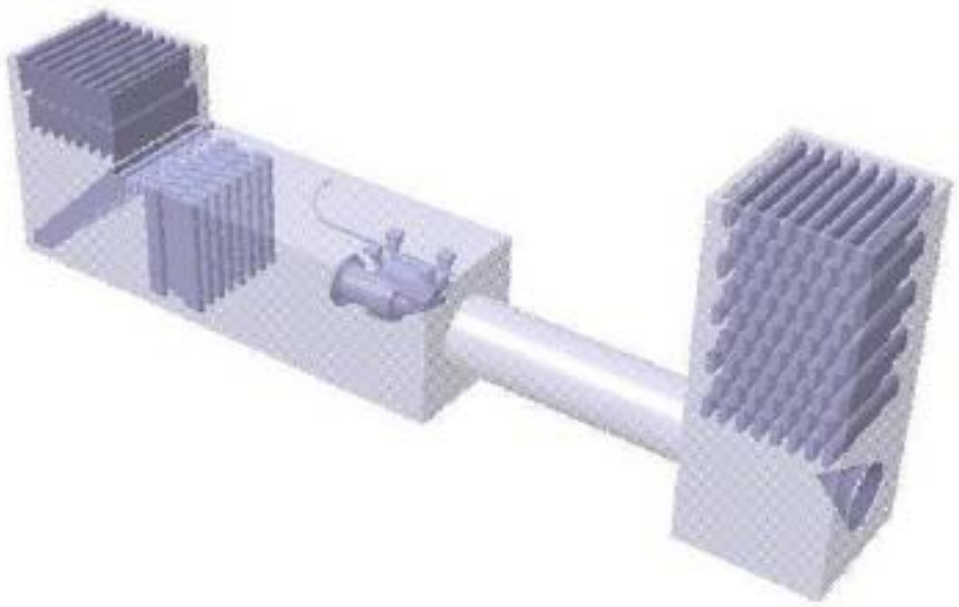

Figure 3: The Modelled Cell CAD Model

The commercial CFD package Fluent will be used to conduct any flow related calculations. All acoustic calculations will be conducted using analytical methods and no Boundary Element Method (BEM) or similar numerical based acoustic calculations were carried out.

The approach of the investigation is primarily fluid dynamic in nature. It also means that the most detailed and rigorous calculations are performed by CFD. Limited acoustic simulations or calculations were performed and any relationships that the

flow phenomenon has on the acoustics is either calculated through analytical or empirical formulae or by qualitative reasoning.

1.3 Layout of Thesis

This research can be broadly divided into two distinct sections, one dealing with the generation and ingestion of vortices into the engine core and the other dealing with the generation and propagation of infrasound during the operation of an engine test in the test cell. Hence, every "common" chapter in this thesis will contain descriptions of each separately. Each chapter will contain a summarised section providing a brief outline of the information that can be found in the chapter.

The "overview" chapter first introduces to the reader a brief history of the jet engine and test cells. This will be followed by one section each of the principles of the operation of test cells and the problems associated with running a test cell. Some of the "solutions" that have been implemented to deal with the two problems investigated in this research will be presented as the closure of the chapter.

After the "overview" chapter, the thesis will present details of the research investigation, first for the vortex problem then followed by the infrasound problem. Each of them will have the same general layout of first describing the methodology before presenting the results gathered in this research. The results will be presented in several chapters with each chapter highlighting the results due to the change in a particular parameter. Each of these "results" chapters can be read as a standalone chapter with suitable introduction, discussion and conclusions in addition to the result data.

The thesis is concluded with a summary chapter highlighting the achievements and new information gathered as a result of this research followed by recommendations for future work in the areas.

2 Overview

In this chapter, the general overview of the topics relating to the research is presented for readers that are new to the area and are not familiar with the basic ideas and concepts. It also contains some industrial rules of thumb, which may or may not be backed by rigorous investigation, relating to the research.

An introduction to the history of the jet engine and the jet engine test facility before the problems relating to their operation is presented. At the end of this chapter, some of the industrially familiar solutions to the problems will be discussed.

2.1 A Brief History of the Jet Engine

A jet engine is a reaction engine, which discharges a very fast moving jet of fluid. In the process, high thrust is generated, according to Newton's Laws of Motion. This common definition of jet engines includes many types such as turbojets, turbofans, rockets, ramjets, pulsejets and pump-jets. Most jet engines are internal combustion in nature but there are some non-combusting forms as well such as ion thrusters, hall thrusters and chemical jet engines.

Despite the increase in non-combustion engines, internal combustion engines remain the most common form of jet engine, even for space travelling vehicles. Some space travelling vehicles carry their own oxidiser and are termed "non air breathing" engines as opposed to the traditional "air breathing" ones. An internal combustion jet engine typically consists of a compressor or compression stage, combustion chamber, turbine (used to drive the compressor) and an exhaust nozzle that discharges the fluid at high velocities to create the necessary thrust. The fluid goes through a Brayton cycle, or Joule cycle, of compression, combustion and exhaust. These jet engines are the primary means of propulsion for aircraft on long haul flights. Earlier jet engines used turbojet engines but have since been replaced by high-bypass turbofan engines, which provide much better fuel efficiency.

The first appearance of a jet engine like device happened in ancient Greece (around 1st century AD) and is credited to Hero of Alexandra. Hero's device consists of an axially rotating sphere with two exhaust nozzles. The sphere was filled with water and heated until steam was produced and exited at high velocity through the two nozzles causing the device to spin and generated mechanical energy. This device is called an Aeolipile. This device was thought of as little more than a diversion during Hero's lifetime.

Although Hero's aeolipile utilises the basic principles of jet propulsion it took another 1200 years before recognisable propulsion devices appeared. In the 13th century, the Chinese used their previously gained knowledge of gunpowder and invented propulsive rockets. The Chinese used them initially for pleasure and then as weapons. From their beginnings in the Far East, the use of rockets spread westwards initially through the Mongols under Genghis Khan and subsequently by the Arabs.

The Indians developed a kind of pre-industrialisation rocket that was a pre-cursor to the European ones. In "A History of Greek Fire and Gunpowder", Partington [2] describes the Indian rockets as:

The Indian war rockets were formidable weapons before such rockets were used in Europe. They had bam-boo rods, a rocket-body lashed to the rod, and iron points. They were directed at the target and fired by lighting the fuse, but the trajectory was rather erratic. The use of mines and counter-mines with explosive charges of gunpowder is mentioned for the times of Akbar and Jahāngir.

An interesting piece of trivia is the mentioning of "rocket's red glare" in the United States of America national anthem, "The Star Spangled Banner". In this instance, it is the British Congreve rocket that is being referenced.

It took about another 500 years before the appearance of the next important development in propulsive jet technology. Between the 1781 and 1931, there was extensive work on understanding the thermodynamic aspects of propulsion and ways to increase their efficiency. The list below shows some of the important advancements timeline during this period. During this period, the use of propulsive jet to power human carrying flight vehicles was briefly investigated.

- 1791: John Barber receives British patent for “A method for rising inflammable air for the purposes of producing motion and facilitating metallurgical operations” A turbine was described in the patent.
- 1884: Charles Algernon Parsons patents the steam turbine. In the patent application he notes that the turbine could be driven "in reverse" to act as a compressor. He suggests using a compressor to feed air into a furnace, and a turbine to extract power to run the compressor. Although intended for factory use, he is clearly describing the gas turbine.
- 1903: Ægidius Elling builds a gas turbine using a centrifugal compressor that runs under its own power. This is perhaps the first modern example of a gas turbine.
- 1908: Hans Holzwarth starts work on extensive research on an "explosive cycle" gas turbine, based on the Otto cycle. This design burns fuel at a constant volume and is somewhat more efficient. By 1927, when the work ended, he has reached about 13% thermal efficiency.
- 1908: René Lorin patents a design for the ramjet engine.
- 1909: Marconnt proposes a modification of Lorin's design using a resonant compression chamber, creating the pulsejet.
- 1910: Henri Coandă builds and flies the world's first jet powered aircraft, the Coanda-1910. It uses an engine-powered compressor mounted in a short duct. Efficiency is low and he abandons the concept, although his studies of combustions resulted in the discovery of the Coanda effect. Although this is the first design to be powered by a jet of air, it does not get its power from a gas turbine and is thus not a "jet engine" in the current meaning of the term.
- 1917: Sanford Moss starts work on turbochargers at General Electric, which goes on to be the world leader in this technology.
- 1917: J.S. Harris patents a "Motor Jet" design, similar to Henri Coandă's.
- 1921: Maxime Guillaume patents the axial-flow turbine engine. It uses multiple stages in both the compressor and turbine, combined with a single very large combustion chamber. Although slightly different in form, the design is significantly similar to future jet engines in operation.

- 1929: Frank Whittle's thesis on future aircraft design is published. In it he talks about the needs for high-speed flight and the use of motorjets as the only reasonable solution to the problem of propeller efficiency.
- 1930: Schmidt patents a pulsejet engine in Germany.
- 1931: Secondo Campini patents his motorjet engine, referring to it as a thermojet.

The first attempts at flight using propulsive power occurred between 1933 and 1938. Prominent individuals that made significant contributions included Secondo Campini, Hans von Ohain, Sir Frank Whittle and Ernst Heinkel. In 1939, the Heinkel He 178 V1, powered by the HeS 3B flies making it the first aircraft to be propelled purely by jet power. After the Heinkel He 178 V1, jet powered aircraft started appearing with models such as the Gloster E.28/39 being developed and flying successfully. Huge interest and work also went into developing better and more efficient engines.

The world of aviation saw the first fighter jet in the form of the Messerschmitt Me 262, flying for the first time in April 1941. This German designed and produced aircraft served as a multi-role fighter/bomber/reconnaissance/interceptor warplane for the Luftwaffe during the Second World War.

On the commercial side of aviation, the pioneer was the de Haviland Comet. It was developed and manufactured by British aviation manufacturer de Haviland and was the first commercial jet airliner to reach production. Its first flight was in 1949 but was eventually withdrawn from production in 1964 due to recurring structural problems.

The first commercial jet airliner from the United States is the Boeing 707 in 1958. Since then the Boeing 700 series has been the forefront of the commercial jetliner business. Perhaps the most famous and recognisable of the series is the 747. It is a wide body commercial airliner and is often referred as the “Jumbo Jet” or “Megatop”. The Boeing 747 first flew commercially in the 1970 and is still active (with the latest variant being the 747-400). It held the passenger capacity record for 37 years before being displaced as the largest operational passenger aircraft by the Airbus A380 during its maiden flight from Singapore to Sydney Australia with Singapore Airlines

on October 2007. The A380 is also the second largest freight aircraft being exceeded only by the Russian monster Antonov AN-225. However, there is only one operational AN-225 with another being reconditioned.

Whilst Airbus A380 together with the Boeing 777 are the latest offerings in current subsonic commercial jet travel, the Boeing 787 dreamliner is being touted as its future. It will the first major airliner to use composite materials for most of its structures and will be more fuel efficient than previous airliners.

Jet powered aircraft entered the supersonic age with the appearance of the Bell X-1. This USAF aircraft achieved the first supersonic controlled level flight during flight tests in October 1947. This historic flight was piloted by Air Force Captain Charles "Chuck" Yeager.

Commercial supersonic jet travel began with the Russian made Tupolev TU-144 and ended with the iconic Concorde. Concorde commenced service in 1976 and continued for another 27 years. Concorde flew regular transatlantic flights from London Heathrow (British Airways) and Paris Charles de Gaulle (Air France) to New York JFK and Washington Dulles, flying these routes at record speeds, in less than half the time of other airliners. With only 20 aircraft ultimately built, the costly development phase represented a substantial economic loss to its developers Aérospatiale and British Aircraft Corporation. Additionally, Air France and British Airways were subsidised by their governments to buy the aircraft. Although the Concorde has only crashed once (25 July 2000), it ceased operations on 24 October 2003 due to world economic slowdown and other factors. The last "retirement" flight occurred on 26 November 2003.

With the development of jet engines aircraft both in the military and commercial sectors, test facilities became an integral part of the aviation industry.

2.2 The Jet Engine Test Cell (JETC)

Once the jet engine is developed sufficiently for commercial or military flight, the development of test facilities and procedures was a natural progression. Test

procedures are necessary to determine consistent performance, verify repairs and insuring the proper functioning of all the sub-systems prior to re-installation on the aircraft. Since the operation of the jet engine would be in the air mounted to the wing of an aircraft, an outdoor "free-air" environment therefore would represent the ideal condition for thrust measurement. In an outdoor no-wind condition, the engine draws only the air required for the thermodynamic cycles plus fan bypass flow and is operating at its "true" operating condition. However testing the engine outdoors is strongly dependent on the weather and wind conditions, something that is uncontrollable and to a strict extent unpredictable. It could also result in objectionable noise pollution. Hence the use of an indoor facility is desired despite the significantly different operating conditions.

The JETC is essentially an all-weather enclosed structure with an engine mounting mechanism intended to provide conditions for stable, repeatable and accurate post maintenance or modification engine performance testing. Other than providing the right conditions for the engine under test, the JETC should also minimise noise exposure of operating personnel and those in the vicinity. One of the critical problems that JETCs have which forms the impetus of part of the work for this thesis is the amount of noise (both infrasonic and in the audible frequencies) emitted from the cell. Due to the rapid urbanisation of population in most parts of the world, the relative distances between test cells and their nearest residential or commercial region have been reduced. This puts additional pressure on the test cell operators, manufacturers and relevant authorities to tighten the noise emission guidelines.

JETCs have a few major features and are usually either U or L shaped with the U shape ones being more common. A JETC has an intake and exhaust stack with the horizontal main test chamber and the augmenter in between. A U-shaped cell would have both the intake and exhaust stack vertical whereas the L shaped ones would have the intake horizontal and simplified. Figure 4 and Figure 5 shows an example of both cells with the main and other essential features labelled (extracted from the "Facility Planning Manual for PW4000 Engine Family" [3]). The L-shaped cell showed is more sophisticated than most. The modern JETC is usually constructed of reinforced concrete and are air-cooled.

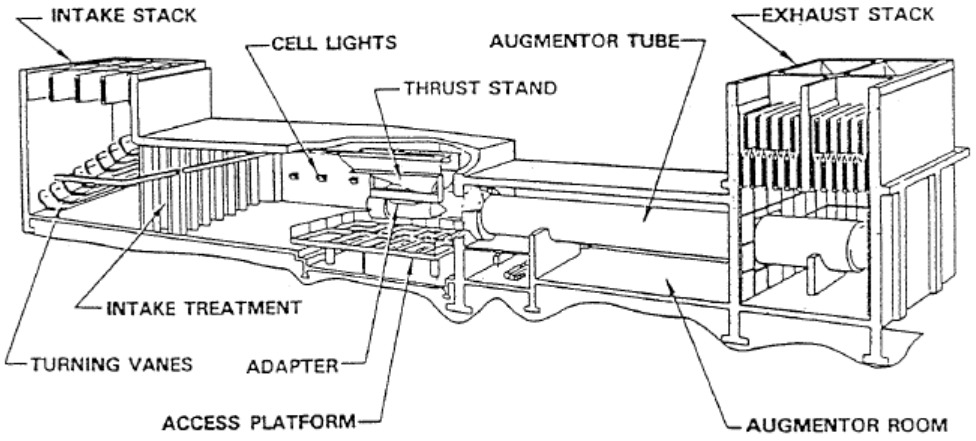

Figure 4: A U-Shaped JETC [3]

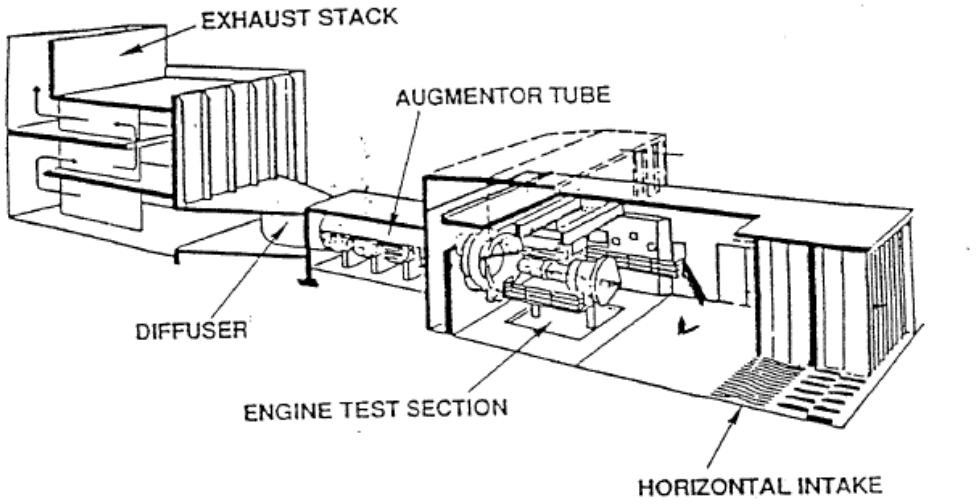

Figure 5: An L-Shaped JETC [3]

The L-shaped cell is simple in design and cheaper to construct. The horizontal inlet generally provides good flow distribution and reduced cell depression when wind is entering the inlet. This type of cell is sensitive to wind conditions and loses efficiency and repeatability when the wind changes direction and requires a relative large unobstructed area upstream of the cell. Consequently land costs may be very high.

The U-shaped cell on the other hand is more complicated in design and costly to build but provides a more uniform inlet air velocity and is less sensitive to wind disturbances.

Concrete was first used to construct JETCs in the mid 1950s. Before the 1980s, most of them were water-cooled. The water reduced the energy of the jet and decreased the associated jet noise. It also made the exhaust gases compatible with cell materials [4]. Water-cooled cells had several problems including the fallout from the exhaust and plume, which contains unburned fuel, particulate matter, NO_x and hydrocarbons from incomplete combustion. Besides being a nuisance, violation of visible emissions regulations was sometimes a problem as well.

Air-cooled JETC were first developed in Europe with the first U.S. air-cooled test cells being the hush houses built by the U.S. Navy.

2.2.1 Jet Engine Test Cell Correlations

As mentioned above, there are appreciable differences between the operations of the engine in the JETC as opposed to in an outdoor environment without wind. However due to the reliability and repeatability requirements, enclosed JETC represent the most practical and suitable environment for sea level testing. As a result of these differences, correlations need to be developed so that performance in the JETC can be correctly compared to their performance outside of the cell. Details of these correlations and procedures will not be discussed here; this section only seeks to provide the reader with a broad outline so that he/she can develop a basic appreciation of the process. The information provided below is taken from the U.S. Federal Aviation Administration Advisory Circular on Correlation, Operation, Design and Modification of Turbofan/Jet Engine Test Cells [5].

Normally, test cell correlation or re-correlation should be performed under the following circumstances:

1. Construction of a new cell
2. A new engine model or derivative model (usually of higher thrust) is introduced
3. Significant repairs or structural modifications have been made to the existing cell
4. Significant repairs or modifications are made to the engine test hardware

5. Significant modifications have been made to existing data acquisition or data reduction systems

The first stage of a correlation procedure is usually performed at an engine OEM pre-determined baseline test facility. This baseline facility would have been previously correlated or referenced to an open-air test site. An open-air test site or cell is basically a clearing with nothing except the engine mount. Pictures of the Poluevo open-air test cell in Russia are provided below:

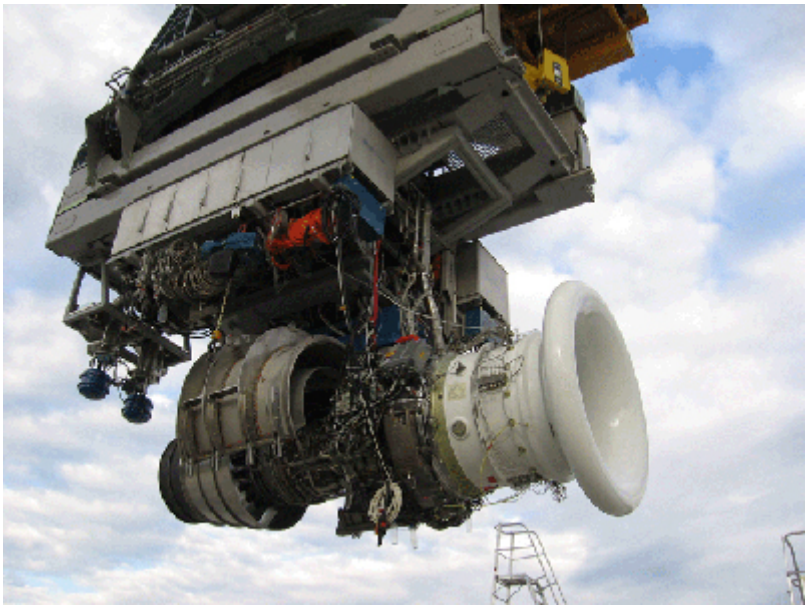

*taken from http://www.snecma.com/IMG/jpg/IMG_2380INTERNET.jpg

*taken from http://www.snecma.com/IMG/jpg/IMG_2383INTERNET.jpg

*taken from http://www.powerjet.aero/fichiers/Image/poluevo.gif

When access to an open-air test site is not available, an alternative accepted practice is to determine the correlations at another F.A.A. approved facility. This alternative facility is called a reference facility.

Instrument and thrust calibration is carried out during the correlation procedure. The following factors may influence the correlations:

1. Test cell configuration
2. Engine position (one of the factors investigated and detailed later in the thesis)
3. Ambient conditions
4. Fuel properties
5. Cell airflow

Some of the performance parameters that are collected and analysed during the correlation process include but are not limited to the following:

1. Engine thrust
2. Fuel consumption
3. Rotor performance
4. Engine pressure and temperatures
5. Cell flow
6. Ambient humidity
7. Barometric pressure

More details on the correlation procedures can be found in U.S. Federal Aviation Administration Advisory Circular on Correlation, Operation, Design and Modification of Turbofan/Jet Engine Test Cells [5] or equivalent articles.

2.3 Problems Associated with the Running of a Jet Engine Test Cell

Aircraft jet engines (including turbofan and turbojet) operating in a test facility can encounter many problems directly related to the characteristics of the cell and its environment. These problems can be minor such as unsteady thrust and engine performance. These problems are considered minor because they do not cause permanent and significant damage to the test cell, test equipment or the engine itself. However, these leads to uncertainty in engine performance and often cause unnecessary test rejections and a subsequent costly rebuilt of the cell, which is very likely to be accompanied by re-correlations.

These minor performance related problems are generally caused by temperature and pressure distortions arising from aerodynamic characteristics peculiar to the flow field of the test cell [6]. Specifically the problems are related to cell inlet design, exhaust systems and the cell bypass ratio. The cell bypass ratio (CBR) is the ratio of the flow passing around the engine versus the flow into the engine and is a common term in jet engine test cell industry.

Some other minor problems include the structural degradation that accompanies the use of the cells and are usually termed the "wear and tear" problems. These are more apparent in parts of the cell which are close the high velocity exhaust jet. One particular problem is the falling apart of the Koppers harp, a device used sometimes to prevent infrasound from being generated, during engine runs.

In addition to these minor problems, there a number of major problems which have potentially more catastrophic implications. Two of which are investigated in detail in this thesis; vortices forming from one of the walls and being ingested into the engine potentially causing engine surges, and the generation of infrasound.

2.3.1 Vortex Formation and Ingestion

When the inlet of a gas turbine engine or pump (basically any device that creates a relative negative pressure thus inducing mass flow into the inlet) is actuated near a surface, a vortex is sometimes observed to form. This vortex has one end anchored to

the solid surface and the other stretching into the inlet. The observation of these vortices can be done quite clearly on days of high humidity due to the condensation within the vortex core. The structure of the vortex is similar to the ones seen in a draining bath or basin where the streamlines spiral into the suction inlet with a radius of gyration that decreases as the inlet is approached. In that case, the solid surface is replaced by the free surface of the water.

The jet engine is an “excellent” example of such a suction device unfortunately and vortices are routinely seen to form and ingested into the core. These can happen when the engine is mounted on the aircraft just before take-off or during ground engine runs or in the test cell during testing. It could potentially also happen in open-air test facilities. When the engine is operated in open-air environment, the vortex would be anchored to the ground (the only solid surface in proximity to the inlet) but in the cell, it could be anchored to any of the four walls.

De Siervi et al [1] showed that there are potentially two fundamentally different mechanisms associated with the formation of this vortex. The first mechanism has been recognised to be the concentration or amplification of vertically aligned vorticity present in the ambient environment caused by the suction inlet. The second mechanism does not require ambient vorticity and can occur even when the upstream flow is irrotational. In such a situation, the inlet vortex will be accompanied by a trailing vortex of roughly equal magnitude but opposite in sign. The generation of the trailing vortex is due to the conservation of vorticity or circulation in the flow. The important feature of the trailing vortex that needs special attention is that the vorticity is opposite in sign to the main vortex. This is important because in some of the results presented in later sections what seems like a trailing vortex is also seen in the test cell simulations. However, this “trailing vortex” has the same vorticity sign and is likely due to the vertical velocity gradient inevitably imposed as part of the simulation constraints. An irrotational onset flow can also lead to the generation of vortices when the flow approaches at an angle to the engine.

These vortices, when formed, may be strong enough to lift items [7,8,9] from the ground leading to potentially catastrophic damage to the engine. Such damage is usually termed Foreign Object Damage (F.O.D.). Colehour and Farquhar estimates in

the 1970s that more than 50% of engines removed from the aircraft have suffered some form of F.O.D. [10]. This number may be somewhat lower now due to extensive efforts to keep the runways and taxiways clean of foreign objects.

Several devices were developed to suppress or blow-away the vortices. Ultimately the solution adopted by most flights is to keep the runway clear of loose objects and to schedule the throttle appropriately.

Even if no F.O.D. is imminent, the formation and ingestion of such vortices can also be potentially catastrophic as they can distort inlet airflow causing engine surges [11]. This is especially important to prevent when the engine is undergoing post overhaul tests.

Studies (details will be presented in Chapter 4) have shown that whether or not a vortex forms depends on the thrust (or mass flow rate) of the engine, the diameter of the engine inlet, the distance from the solid surface, and the ambient vorticity which in turn depends on the local flow field. For example, vortices may form on takeoff if there is a sufficiently strong component of crosswind on the runway.

Hence, an improved understanding of the parameters influencing the formation of such vortices has both academic as well as economic value.

2.3.2 Infrasound

Human hearing covers a certain frequency range and is traditionally termed the audible frequency range. This is usually quoted as ranging from 20 to 20 000 Hz. Infrasound is defined as sound that is lower than 20 Hz in frequency although some definitions go up to 60 Hz. Due to the decreased sensitivity of hearing as frequency decreases, perceivable sound in the infrasonic region has to be higher in amplitude than that in the audible range. There have been reports of certain people with unusually high sensitivity to low frequency noise [12,13] but these remain very rare.

Infrasound is usually “felt” by certain parts of the body. These feelings are enhanced especially when the infrasonic source occurs at the natural frequencies of certain body parts thus causing large vibrations. Moller and Pedersen [14] suggests that infrasound

can also be detected by hearing tones at higher harmonics of the infrasonic source tone.

Infrasound can sometimes be generated from naturally occurring phenomenon such as avalanches, earthquakes, aurora, lightning, waterfalls and surf [15]. The first observation of natural occurring infrasound was after the famous volcanic eruption of Indonesian volcano Krakatoa in 1883. In the aftermath of the eruption, concussive acoustic waves encircled the earth numerous times and were recorded by barometers all around the world.

Infrasound research pioneer French research scientist Vladimir Gavreau's [16] interest in the area started in the 60s when he and fellow lab assistants experience shaking equipment and pain in the eardrums during experiments. However, the microphones picked up no audible sound signal. One of his first experiments involved an infrasonic whistle.

In addition to the naturally sources, infrasound can also be man-made through processes such as sonic booms from supersonic aircraft, wind turbines, chemical and nuclear explosions and subwoofer loudspeakers [17].

Certain animals such as alligators and whales have been known to use infrasound to communicate over great distances. In particular, whales have been known to communicate using infrasound at distances of hundreds of miles. It has also been suggested that infrasound generated from turbulent flow over mountain ranges have been used by migrating birds for navigation. This use of naturally generated infrasound in the animal kingdom has been suggested to affect behavioural patterns in animals and act as a sort of early warning system. For example, animals were reported to flee from the 2004 Indian Ocean earthquake and tsunami long before it actually hit the shores of Asia [18]. It is not known if infrasound is really the warning signal as some have suggested electromagnetic waves instead [19].

Human beings are generally accepted as being less sensitive to sound in the infrasonic range than animals. Without the use of specialised electronic equipment, humans detect the presence of infrasound through vibrations of object and buildings and other

"strange" feelings, which are related to resonant vibrations of bodily organs. One of the "strange" feelings often quoted are feelings of awe, supernatural phenomenon, headaches and nausea. Sound at frequencies as high as 200 Hz are also known to produce similar feelings [14] although usually only sound from 20 to 200 Hz is called low frequency.

Vic Tandy [s20] suggested infrasound might be a cause of ostensible haunting using first person experience. In the paper, Tandy showed that a 19 Hz standing air wave may create sensory phenomena under certain conditions. These sensory phenomena could be mistaken for the presence of a ghost. Tandy described feelings of discomfort, breaking into cold sweat and experienced a feeling of depression. In additional to these feelings of discomfort, Tandy claimed to detect the apparent presence of a grey apparition on the periphery of his vision which he attributed to the coincidence of the frequency of the infrasonic source (a ventilation fan) and the resonant frequencies of the eyeball.

Tandy [21] went on to investigate and subsequently suggests a link between the presence of infrasound and the perception of apparitions in the 14th Century cellar beneath the Tourist Information Centre in Coventry, UK.

In addition to effects on sensory perception, low frequency noise also has certain physical effects on humans. Danielsson et al. [22] found that exposure to low frequency noise led to an increased in diastolic blood pressure and a decrease in the systolic blood pressure in comparison to a short period control exposure. Landstroem et al. [23] exposed ten normal and ten deaf subjects to 6 Hz sound for 20 minutes and observed changes in their EEG patterns (which he interpreted as diminished wakefulness), similar alterations of systolic and diastolic blood pressure and changes to heart rate in the normal subjects but these were absent in the deaf subjects. It is not known if these are linked to the altered sensory perception, which involves some kind of haunting apparition or are they independent effects.

One of the important man-made sources of infrasound is caused by accelerated flow in jet engine test cells. It is not well-understood phenomenon why infrasound should be generated during certain operations. Due to the rapid urbanisation of most parts of

the world, the relative distances between a test cell and the nearest area of high population density is reduced. This leads to increased awareness, through the complaints of affected personnel, of the effects of infrasound. It also led to the tightening of infrasound emission standards around the world.

The next chapter will provide some introduction into this phenomenon and description of the analysis and solutions that have been investigated and implemented in the past.

2.3.2.1 Infrasound in Jet Engine Test Cells

Test cell facilities are designed with special air intakes and exhaust, which presents a controlled environment for the testing of the engine. Other than presenting a controlled environment, the other important function of a test cell is to reduce the noise emission to the environment during engine tests. Some other functions of test cells include the reduction of heat and vibration of the engine from affecting the surrounding environment.

Although the presence of a test cell reduces the noise and other factors from the engine, it is still rather noisy. An inadequately designed cell can be a very noisy building even at far field. Far field noise can exceed 90 dBA in military cells [24,25,26].

The emitted noise from an engine, the primary source of noise in a test cell, is largely broadband in nature [27]. Despite this, the noise signature of the test cell may exhibit peaks at certain frequency. This is due to a combination of factors including attenuation, eddy shedding tones and resonances. Howe [28] identifies two fundamentally different types of resonant oscillations within the test cell. They are the classical acoustic resonances whose frequencies and mode shapes are unrelated to the unsteady flow in the cell but depend on the geometries of the cell, and sound produced by periodic components of the flow which can arise independently of the acoustic resonances. Although the second type is typically moderate in amplitude, they become important when their frequencies match with the classical acoustic resonance frequencies.

Attenuation by structures is more effective at high frequencies than at low frequencies. As a result, the measured noise is usually more pronounced in the low frequency region. For the same reason, low frequency noise management is arguably more difficult than at higher frequencies. Attenuation is usually not considered a viable option for very low frequency management in many industries.

Sometimes, it is possible for low frequencies to be experienced at certain locations around the test cells even though there are no low frequency sources. One such example is a test cell in Georgia where the low frequencies experienced were attributed to the "beating" of two non-infrasonic noise sources.

Evidence suggesting the beating phenomenon were the measurement of high and low pressures at distinct distances away from the cell. In the beating of two noise sources, the resultant noise has a frequency that is the absolute difference between the two source frequencies.

Flow induced low frequency noise is the most commonly suspected source of infrasound. The term "suspected" is used here because the methods employed to deal with this source of infrasound have not been successful in many situations and thus the problems they target may or may not be real sources. The current body of evidence does not allow the determination of whether flow induced noise is a necessary or sufficient cause of infrasound. However, the low success rate of methods employed to deal these flow situations warrants investigation on the matter.

Generally, the methods employed to deal with flow induced infrasound involves the additional placement of an object in the path of the air flow either in the augmenter tube or at the tail-end of the exhaust stack. Objects in the augmenter tube are placed at suitable locations and work by breaking up jet flow and coherent turbulent structures formed inside the augmenter tube into smaller structures generating higher frequency noise which is easier to attenuate to acceptable levels.

More details on these "solutions" will be provided in the next section.

2.4 Summary of "Solutions" Implemented

Vortex formation and ingestion together with low frequency noise generation and propagation are common problems when operating test cells. They are not new problems but have been around since the onset of engine tests in test cells, however their occurrence has become more frequent in recent times suggesting that perhaps it is related to the size of the engine.

This section highlights some of the more prominent "solutions" that have been discovered and implemented to solve both problems. The presence of these "solutions" does not negate the importance of the research detailed in this thesis because these "solutions" have been found to be applicable only to a limited category of engine-cell combination.

2.4.1 Vortex Ingestions

The formation and generation of vortices during the operation of a jet engine is not a new phenomenon and has been investigated quite extensively in the past by Nakayama and Jones [29], Glenny [30] and Ridder and Samuelsson [31]. However the models used in these and other investigations resemble an engine over a runway scenario rather than engine in a test cell scenario and no technical solutions were developed. The problem of generation and ingestion of vortices while the plane is on the runway was ultimately solved by keeping the runway clear of debris prior to operation of an engine and appropriate scheduling of throttle. Some other preventive measures include the use of a series of small air jets mounted on the wings and fuselage of the aircraft to blow away any debris from the inlet [32] and mounting the air jets beneath the lower lip of the inlet directed at the stagnation point (one of the important features of these vortices) [33, 7].

The formation and ingestion of vortices whilst the engine is in operation inside a test cell is perhaps more difficult to solve. Throttle scheduling cannot be used as a preventive measure in the test cell because it would disrupt the engine testing procedures hence other measures will have to be taken. Throttle scheduling works on the runway prior to take-off because the plane is moving and Vo becomes larger than the blow-away velocity by the time the throttle is fully opened. This does not work in

the cell as CBR is limited by the walls and may in some cases never exceed the blow-away velocity.

Clark et al. filed a US patent for the use of a 40 to 50 degree ramp positioned at the location where the vortex attaches to the cell ceiling as a means of preventing the formation of a vortex [34]. The ramp reduces the flow area by 30 to 50% and increases the cell bypass flow velocity hence preventing the formation of the vortex. One of the conditions necessary for a vortex to form is the velocity between the inlet and solid plane to be below a certain threshold, this threshold is sometimes termed the blow-away velocity. Hence increasing the cell bypass flow velocity would have a similar effect.

2.4.2 Infrasound Generation

Generation of infrasound in test cells during operation is a longstanding problem and although many solutions have been suggested and implemented, understanding of the problem has remained at a rather primitive level primarily because none of the "solutions" found have been universal in their results i.e. they have been very successful in certain cells but ineffective in others.

There are two feasible general explanations for such an observation. Firstly, the successful cases are in a large part due to good fortune where the "problems" that was supposedly targeted successfully were not solved at all and the resulting reduction in infrasound was due to an inadvertent solution of the "real problems" by changes implemented for other purposes. The second explanation is that there is more than one major source of infrasound and the occurrence of each source is independent of the others. Hence, a universal solution could never be reached unless it addressed all the problems together. This solution possibly may not be cost effective because it will also contains elements to deal with "problems" that are not all present in any individual cell. No significant effort has been put in to prove or disprove either explanation.

Some of the solutions that have been implemented successfully in at least one test cell and their proposed "problems" are highlighted in the following subsections below.

Limited quantitative data will be given as they are meant to introduce the “solutions” and provide the reader with a qualitative appreciation of them. More numerical details can be found in Chapter 10.2.

2.4.2.1 Core Busters

As mentioned in the previous section, incorporating core busters in the augmenter tube of the test cell is one of the most common methods to reduce infrasound. They work by breaking up jet flow and coherent turbulent structures in the augmenter. The high frequencies of flow noise are generated near the jet nozzle in the mixing zone while the lower frequencies, on the other hand, are generated at distances 5-20 nozzle diameters downstream [35]. This is where the core busters should be placed to maximise its efficiency.

Core-busters are installed on the RAF hush houses located in Markham, England [37], on the hush house used to test the engines of the supersonic Concorde and on many other jet engine facilities, but data detailing their effectiveness is not common. Kodres performed an experiment modelling the Concorde style sponson and found that they were moderately effective achieving a far field reduction of 2 dB [24].

Another type of core-buster that is sometimes employed to deal infrasound is the Koppers Harp. It is a structure consisting of concentric rings of different sizes with the largest ring being placed furthest upstream and the smallest rings downstream; see chapter 10.2 for more details. However the structural complexity of the structure introduces many problems with structural strength being the most serious of them. The high speed exhaust flow places severe stresses on the Harp, thereby leading to a high vibration level and increased mechanical failure rate.

2.4.2.2 Sawtooth Structures

Sawtooth structures mounted on the top of the exhaust stack perpendicular to the flow are sometimes used as a method to reduce noise emission from a test cell. The uneven edge of the structure spawns random sound waves, which tend to cancel rather than

reinforce [38]. This mechanism does not target low frequency noise preferentially but should be equally effective across the entire spectrum.

2.4.2.3 Height of Exhaust Stack

Increasing the height of the exhaust stack is a straightforward but expensive method of decreasing test cell noise emission. Several phenomena are suggested to aid in the reduction of test cell noise emission due to the increase in exhaust stack height. These included increasing the distance between the noise source and the exit, increase attenuation by wind at higher altitude and increasing ground effects.

Aero Systems Engineering Ltd filed a United States patent (5837890) which supposedly reduced infrasound from a test cell by installation of a structure near the open-end of the exhaust stack. It works by "artificially" increasing the height of the exhaust stack. However this patent was not renewed, thereby calling into question its effectiveness.

2.4.2.4 Exhaust Stack Screens

Dickman et al. [35] investigated and found that placing porous screens at the base of the exhaust stack has promising effects towards reducing infrasound emission in test cells.

2.4.2.5 Solutions from other Applications

Helmholtz resonators and anti-noise have been used to reduce noise emission in various other industries. These adaptive passive and active noise control procedures are attractive because they are generally quite effective at low frequencies and also have the advantage of being able to block noise selectively.

The use of a self-tuning Helmholtz resonator was investigated by de Bedout [39]. He experimented with a closed loop 'tuning' algorithm to adjust the Helmholtz cavity to achieve noise reduction in a duct system.

Active noise control using anti-noise have been around since Lueg [40] was first granted a patent in 1936 describing methods to cancel sinusoidal tones in ducts by inverting the polarity of a loudspeaker. By the 1950s, systems to cancel noise in helicopter and airplane cockpits were patented by Fogel [41, 42, 43]. Now anti-noise earphones and headphone are starting to appear on the market and are particularly attractive to music listeners. Modern active noise control is achieved with a computer which analyses the 'problem' noise and generates a reverse waveform signal. The reverse waveform signal generated cancels the 'problem' noise by destructive interference.

However, the use of these technologies on a scale as large as a JETC is unprecedented and probably impractical in current times. Considering the rapid advancement of electronics and computers, it is perhaps possible that the future of noise control in all industries (including the JETC industry) is in active noise control techniques.

3 Methodology

As the main investigative tool used in the research culminating in this thesis is computational fluid dynamics in nature, it is appropriate to provide a chapter on the basic concepts and terminologies used in CFD calculations.

It is not a textbook on CFD and should not be treated as such but it provides a concise description as a first read for a novice in CFD.

Fluent is the CFD package of choice for these investigation and chapter 3.2 introduces the solver parameters as used in Fluent alongside their technical description.

3.1 Computational Fluid Dynamics

Computational fluid dynamics or CFD as it is commonly known is a branch of fluid mechanics that utilises numerical methods and algorithms to solve the governing equations of fluid flow to predict the flow fields.

Fluid mechanics is a branch of physics, which deals with the properties of liquids and gases and how they interact or behave in the presence of forces. It can be divided into fluid statics and dynamics. Graves Jr. [44], credited Newton with the first mathematical formulation of the basic laws of fluid motion. Notable intellects that followed Newton include D'Alembert, Euler and Lagrange for ideal fluids and Prandtl, Blasius and Von Karman for inviscid and viscous flow. The fundamental principles in fluid dynamics are that energy, momentum and mass are conserved. These principles can be represented in many ways but the most common way in fluid dynamics is to represent them in partial differential form, which is their most general and basic form. The fundamental basis of almost all CFD problems is the Navier-Stokes equations, which define any single-phase fluid flow and are given below in the partial differential form:

$$\rho\left(\frac{\partial V}{\partial t} + V \cdot \nabla V\right) = -\nabla p + \nabla \cdot \Gamma + f \qquad \textbf{(1)}$$

Although the Navier-Stokes equations apply to a large collection of problems relating to academic and industrial interest, they are not universal in their application. The Navier-Stokes equations are only applicable to problems where the fluid properties are continuum and not otherwise such as in rarefied atmospheric conditions.

Due to the mathematical complexity of solving these partial differential equations (PDE), numerical solutions are often required. Numerical methods are an iterative way of guessing a solution and checking if it fits the solution at certain points known as boundary conditions.

The use of numerical analysis to solve mathematically complex problems of the time has been around for thousands of years. One of the earliest examples is the Babylonian approximation of the square root of 2.

Anderson [45] describes this as an art of replacing the governing PDEs with algebraic equations and solving them in space and/or time to obtain the final description of the complete flow field. The end-product of CFD is a collection of numbers rather than a complete analytical solution or description and its quantitative applicability is very much dependent on the individual situation. This is usually adequate especially in engineering analyses where a quantitative description of the problem is the desired output. This is certainly the case for the Navier-Stokes equations, whose stress depends linearly on velocity gradients, and for most boundary conditions do not currently posses a closed form analytical solution.

Solutions gathered from numerical methods are not exact answers but very close approximation that fall within reasonable error margins. When these error margins are so small that it is beyond current human engineering techniques to design and manufacture, the approximations may be treated as “exact” solutions. In this respect, CFD solutions can often be treated as “exact” solutions although it is usually accompanied by experimental validations such as wind tunnel tests and flight tests.

The equipment, that has accompanied and is essential to the practical growth of CFD as an engineering tool is the computer. CFD solutions are repetitive tasks involving

manipulation of millions of numbers and are generally accepted as humanly impossible, at least at speeds that are required for engineering analyses.

Since Kopal [46] compiled massive tables of supersonic flow over sharp cones by solving the governing differential equations numerically using a primitive computer at the M.I.T., CFD has grown from strength to strength. The current importance of CFD in engineering predictions can be viewed as a "third dimension" in fluid dynamics complementing experimentations and theoretical predictions [45].

The most accurate and direct form of CFD is the use of a direct numerical simulation (DNS) where the Navier-Stokes equations are solved numerically without employing the use of any turbulence models. The entire range of spatial and temporal scales of the turbulence is resolved in the computational mesh, from the smallest dissipative Kolmogorov microscales up to the length scales of the bounding walls. However due to the large memory requirement, complete DNS of commonly encountered industrial applications would exceed the capacity of even the most powerful supercomputers today. Hence, turbulence models have been developed and are in use whilst waiting for adequate computing hardware to be available. More description on turbulence models will be available in the later sections of this chapter.

Each CFD simulation is inherently different from others and complete automation of the process is not possible currently but there is a simple basic procedure that defines them. The entire process can be broadly broken down into the pre-processing, solving or simulation and post-processing stages.

The pre-processing stage is commonly termed the mesh generation stage and is often the most important. However other than generating the mesh, a number of other things are also performed in this stage. First, the geometry of the problem is defined and generated in a virtual environment. Although this can be done in some commercial "meshing" software, CAD software is usually tool of choice for most. Following this, the fluid volume is "meshed" by dividing the volume into discrete cells. Some new CFD software claims to be able to bypass the mesh generation stage for the user. However such software merely hides the mesh generation from the user and creates the mesh using an intelligent algorithm. Such software packages are currently still not

very common. An example of such a software package is “Converge” from Convergent Science Inc. Finally, the boundary conditions are defined. These are conditions implemented into the flow field at specific locations where the fluid properties are known. Usually these are at the extreme boundaries of the flow field. At these boundaries, fluid properties such as velocity, pressure, etc. are forced to take a certain value. The properties for the rest of the flow field are then calculated from these boundary values.

Next is the solving stage. In the initial phases of the solving stage user input is required to perform tasks such as setting up of the solver, solution initialisation, choice of discretisation schemes and solver schemes, linearisation schemes and the setting up of monitoring parameters and under-relaxation factors. However once the solving has commenced, little input is needed from the user except for periodic checks to ensure that the solution is progressing satisfactorily to avoid problems of divergence. In many instances, other equations are solved together with the Navier-Stokes equations. Most common of these are the energy equations for heat transfer or compressibility but can include those describing mass transfer, chemical reactions, heat transfer and even multi-phase flows. Advance codes have also been developed to simulation scenarios where the fluids are non-newtonian or are chemically reactive such as in combustion. These additional equations are usually formulated as conservation laws of different properties.

Lastly, the solution gathered is analysed and displayed using suitable post-processing software or techniques.

3.2 Important CFD Considerations

As mentioned above, CFD does not produce a closed form analytical solution but rather a numerical description of the problem. Unlike the use of an analytical equation where the only concern is the applicability of the assumptions used to generate the equations, CFD calculations have many other considerations, which can render results invalid. The common term used against the use of CFD by experimental fluid dynamists is “Garbage In, Garbage Out”. Aside from the appropriate use of boundary conditions and parameter values, there are a number of important considerations for a

researcher to consider when employing the use of CFD as a tool. These are listed below and described in detail in the proceeding sub-sections:

1. Creating an appropriate mesh.
2. Using the right turbulence models.
3. Selecting the appropriate discretisation scheme, solver parameters, under-relaxation factors etc. Only the discretisation scheme selection will be detailed below.
4. Selecting the appropriate pressure-velocity coupling.

As with the justification of the use of turbulence models as opposed to a DNS, computational expense or stability often forces the employment of less accurate schemes.

In terms of mesh sizing, it is highly dependent on the problem being solved. Obviously the mesh must be fine enough such that the desired flow phenomenon spans across at least enough cells for it to be picked up in the solution. One common guide to mesh density is the dimensionless wall distance, otherwise termed y^+ and is defined by $y^+ = \frac{u_* y}{\upsilon}$ where u_* is the relative velocity at the wall and y is the distance to the wall. y^+ is commonly used in determining appropriate mesh sizes in the boundary layer close to a wall.

3.2.1 Turbulence Models

The most accurate and direct form of CFD is the use of a direct numerical simulation (DNS) where the Navier-Stokes equations are solved numerically. The entire range of spatial and temporal scales of the turbulence is resolved in the computational mesh, from the smallest dissipative Kolmogorov microscales to those associated with high kinetic energy. However due to the large memory requirement, complete DNS of commonly encountered industrial applications would exceed the capacity of even the most powerful supercomputers today. Turbulence modelling tries to resolve this by avoiding the use of the full time dependent Navier-Stokes equations and using simpler

mathematical models to predict the effects of turbulence. These equations are termed as turbulence models.

Joseph Boussinesq was perhaps the first practitioner of turbulence modelling using the concept of eddy viscosity [47]. Ludwig Prandtl then advanced this with the idea that eddy viscosity vary with distance from a wall in a wall-bounded flow problem leading to the concept of mixing length leading to the introduction of mixing length and boundary layer.

Currently the turbulence models employed by most commercial CFD software are either Reynolds Averaged Navier-Stokes (RANS) or the Large Eddy Simulations (LES). RANS equations represent transport equations for the mean flow quantities with all the scales of the turbulence being modelled. This approach greatly reduces the computational resources requirement. The main benefits for using RANS are realised in steady state problems, although in some transient problems it is also suitable when the time step is determined by the global unsteadiness rather than by turbulence. The RANS models available in the commercial CFD package Fluent are:

1. The Spalart-Allmaras (SA) Model
2. The Standard, Renormalisation Group (RNG) and Realisable k-ε models
3. The Standard and Shear-Stress Transport (SST) k-ω models
4. The v^2-f model
5. The Reynolds Stress Model (RSM)

Each of the models has its advantages and disadvantages based on computational requirements and accuracy of solution as well as applicability based on situations. The following sections, in italics, are taken from the Fluent user guide [48] and provides a quick and concise description of the computational effort and solution behaviour of the various RANS model.

*In terms of computation, the Spalart-Allmaras model is the least expensive turbulence model of the options provided in **FLUENT**, since only one turbulence transport equation is solved.*

The standard k- ϵmodel clearly requires more computational effort than the Spalart-Allmaras model since an additional transport equation is solved. The realizable k- ϵ model requires only slightly more computational effort than the standard k- ϵmodel. However, due to the extra terms and functions in the governing equations and a greater degree of non-linearity, computations with the RNG k- ϵmodel tend to take 10-15% more CPU time than with the standard k- ϵmodel. Like the k- ϵmodels, the k- ω models are also two-equation models, and thus require about the same computational effort.

Compared with the k- $\epsilon$and k- ωmodels, the RSM requires additional memory and CPU time due to the increased number of the transport equations for Reynolds stresses. However, efficient programming in ***FLUENT*** *has reduced the CPU time per iteration significantly. On average, the RSM in* ***FLUENT*** *requires 50-60% more CPU time per iteration compared to the k- $\epsilon$and k- ωmodels. Furthermore, 15-20% more memory is needed.*

Aside from the time per iteration, the choice of turbulence model can affect the ability of ***FLUENT*** *to obtain a converged solution. For example, the standard k- ϵmodel is known to be slightly over-diffusive in certain situations, while the RNG k- ϵmodel is designed such that the turbulent viscosity is reduced in response to high rates of strain. Since diffusion has a stabilizing effect on the numerics, the RNG model is more likely to be susceptible to instability in steady-state solutions. However, this should not necessarily be seen as a disadvantage of the RNG model, since these characteristics make it more responsive to important physical instabilities such as time-dependent turbulent vortex shedding.*

Similarly, the RSM may take more iterations to converge than the k- $\epsilon$and k- ω models due to the strong coupling between the Reynolds stresses and the mean flow.

Fluent has two models in which eddies are explicitly resolved rather than modelled, the Detached Eddy Simulation (DES) and Large Eddy Simulation (LES) models. The LES model is pretty much self-explanatory in its name, where eddies larger than the mesh cells are simulated explicitly in an unsteady simulation and the smaller eddies are treated with a RANs turbulence model, whilst the DES is a modified version of

the SA model. The DES combines an unsteady SA model with a filtered version to create two separate regions inside the flow domain. The domain close to the wall is treated with the SA model whilst the rest of the flow is treated with the LES model. It provides a compromise between the accuracy desired of a LES model with a reduction of the computational requirements by using the SA model close to the wall, where viscous effects are more significant.

3.2.2 Mesh

In order to analyse the fluid dynamic PDEs, the flow domains are split into smaller sub-domains, otherwise known as cells (made up of a few different geometric shapes), where the governing equations are solved. Care is taken to ensure that proper continuity exists across the interfaces between domains so that the discrete solutions can be concatenated together to present a complete picture of the flow in the entire domain. The entire collection of cells forms the mesh or grid.

Generally three different categories of mesh are available, namely structured, unstructured and hybrid meshes. In terms of the development of automated meshing codes or software, structured meshes were the first to be made available followed by unstructured mesh and finally hybrid meshes.

Structured and unstructured meshes have their own pros and cons and the hybrid meshes attempts to collate the pros and discard the cons of either.

Structured meshes require less computational resources to generate as well as solve and their algorithm is more efficient.

Unstructured mesh has looser constraint on connectivity and cell locations allowing the meshing of geometries that would otherwise not be feasible using structured meshes.

For all three categories of mesh, alignment of the mesh in the direction of the flow increases the solution accuracies especially in high speed flow scenarios.

As with most other parameters in a numerical solution, the "best" mesh is often not known before any solution is carried out. Although rules of thumb and prior calculation can aid in the process, mesh convergence exercises is often still required. A mesh convergence exercise is usually carried out on the first simulation and refined before the "best" mesh is adopted for the remainder of the simulations. The mesh convergence exercise consists of refining the mesh density (either in entire domain or in certain areas) until the perceived accuracy of the solution converges to an acceptable error margin.

3.2.3 Discretisation Schemes

All engineering numerical simulations require the discretisation of the solution space via the generation of the mesh. There are a few discretisation methods currently employed and some are more prevalent in and are preferred by different applications. The following section discusses these briefly before delving into the details of the discretisation schemes that are available in Fluent.

The commonly available commercial discretisation methods include the "classical" or standard finite volume method (FVM), the finite element method (FEM), the finite difference method (FDM) and the boundary element method (BEM). The main difference is the smallest building block that is present within the solution space. This affects the way in which the solutions are derived but should be viewed as a consequence rather than the cause. The smallest building blocks for each of the methods are represented in the Table 1 below.

Table 1: Basic building blocks of different discretisation methods

Finite Volume Method	Volume surrounding node(s)
Boundary Element Method	Boundaries of the domain
Finite Element Method	Element connecting two or more nodes
Finite Difference Method	The node itself

After the solution space is broken down into the appropriate building blocks, the solution is preceded by a number of discretisation schemes. Discretisation schemes

are rules of calculating the gradient or derivative of a property from discrete values at known points (very often they are the neighbouring points) in space, time or other ordinates.

Fluent employs the FVM discretisation method and has the following discretisation schemes available:

- First Order Upwind Scheme
- Second Order Upwind Scheme
- Power Law Scheme
- QUICK Scheme
- Third Order MUSCL Scheme
- Central Differencing Scheme (can be first or second order)
- Bounded Central Differencing Scheme
- Low Diffusion Second Order Scheme
- Modified HRIC Scheme

Some of these schemes are only applicable for different turbulence models (or viscous models as they are called in Fluent) for example; the Central Differencing Scheme is only available for momentum equations when using LES. Since the only the RANS models were considered and eventually used in the investigations detailed in proceeding chapters, only the first five schemes were available for use and only these will be described in the proceeding sections. As Fluent is the only CFD software used in this research, the following sections describing the various discretisation schemes were paraphrased from the user manuals. In the investigations for this thesis, only the first and second order upwind schemes were considered for use.

3.2.3.1 First Order Upwind Scheme

In this scheme, cell (volume) centre values are assumed to be the cell average values that are representative of the associated variable throughout the cell. The upwind term

in the name implies that the value of the variable on a cell boundary is taken to be the centre, or representative value for the cell that is upwind of the boundary.

3.2.3.2 Second Order Upwind Scheme

This scheme is a higher order scheme and provides second order accuracy by utilising a multidimensional linear reconstruction approach to compute the cell face quantities.

Details on the exact reconstruction algorithm are available from the Fluent user guide.

3.2.3.3 The Power Law Scheme

The power law scheme calculates the cell face quantities by interpolating using the following one-dimensional convection-diffusion equation.

$$\frac{\partial}{\partial x}(\rho\mu\phi) = \frac{\partial}{\partial x}\Gamma\frac{\partial\phi}{\partial x} \tag{2}$$

Integrating the above equation yields the following solution describing the relationship between ϕ and x

$$\frac{\phi(x)-\phi_{x=0}}{\phi_{x=L}-\phi_{x=0}} = \frac{e^{\left(Pe\frac{x}{L}\right)}-1}{e^{(Pe)}-1} \tag{3}$$

One of the implications of the above relationship is that when the flow is dominated by convection, the interpolation is equivalent to the first order upwind scheme.

3.2.3.4 QUICK Scheme

The QUICK scheme is designed to compute a higher-order value of the cell face quantities for quadrilateral and hexahedral meshes where unique upstream and downstream faces and cells can be identified. It is based on a weighted average of second order upwind and central interpolation of the variable.

This scheme is described to be more accurate on structured grids aligned in the flow direction and is equivalent to the second order upwind discretisation scheme for unstructured or hybrid grids.

3.2.3.5 Third Order MUSCL

This scheme was conceived from the original MUSCL (Monotone Upstream-Centred Schemes for Conservation Laws) by blending the central differencing scheme and the second order upwind scheme using a weighted average.

Although the use of scheme potentially improves the spatial accuracy for all type of meshes by reducing numerical diffusion, it does not contain a flux limiter. Thus undershoot or overshoot can occur when there are discontinuities in the flow-field.

3.2.4 Pressure-Velocity Coupling

In CFD calculations, pressure does not appear explicitly in the discretised continuity equation for incompressible flow since density is not directly related to pressure. A pressure-velocity coupling procedure or algorithm is used to enable the pressure field is solved whilst ensuring that the velocity field satisfies mass conservation.

Fluent provides five pressure-velocity coupling schemes or algorithms to the user:

- SIMPLE
- SIMPLEC
- PISO
- Fractional Step Method (FSM)
- Implicit Body Force Treatment

SIMPLE and SIMPLEC are generally recommended for steady state calculations while PISO is recommended for highly skewed transient calculations.

The last two schemes are very limited in their application within Fluent and will not be discussed extensively.

The FSM is available only when the Non-Iterative Time Advancement (NITA) scheme is used. With this scheme, the use of FSM may be slightly less computationally expensive compared to the PISO scheme but could be less stable in certain scenarios.

The "Implicit Body Force Treatment" is introduced for multiphase flows with large body forces such as gravity or surface tension. In such flows, the body force and pressure gradient in the momentum equation are almost in equilibrium with little contribution from the convective and viscous terms. As the investigations do not involve multiphase flows, this scheme will not be discussed. Similar to the description on discretisation schemes, the following sections on the various pressure-velocity coupling is a paraphrase from the Fluent manual for the same reason.

3.2.4.1 SIMPLE Pressure-Velocity Coupling Algorithm

The SIMPLE algorithm is one of the most widely used approaches for overcoming the problem mentioned above. It is an acronym for Semi-Implicit Method for Pressure Lined Equation developed at the Imperial College in London in the 1970s [49].

It first obtains an approximation of the velocity field by solving the momentum equation and the pressure gradient is then calculated using the pressure distribution from the previous iteration or initial guess. After this, a pressure equation is formulated and solved to obtain the new pressure distribution. Finally the velocities are corrected resulting in a new set of conservative fluxes.

3.2.4.2 SIMPLEC Pressure-Velocity Coupling Algorithm

The SIMPLEC algorithm is similar to the SIMPLE algorithm with 'C' being the acronym for 'Consistent'. The only difference lies in the expression used for the face flux correction. Details can be found in the Fluent user guide [48].

The SIMPLEC algorithm has been shown to obtain converged solutions more quickly for uncomplicated problems such as one with simple laminar flow. For more complicated flows, the convergence rates are comparable to the SIMPLE algorithm.

For meshes with a certain amount of skewness, Fluent provides “skewness correction” with the SIMPLEC algorithm to reduce the convergence difficulties.

3.2.4.3 PISO Pressure-Velocity Coupling Algorithm

PISO stands for “Pressure-Implicit with Splitting of Operators”. It is part of the SIMPLE family of algorithm. It improves the efficiency of the SIMPLE and SIMPLEC algorithms by performing two additional corrections; the neighbour and skewness corrections [49].

These two corrections can be performed in a segregated or coupled manner. The main beneficiaries of coupling the corrections are meshes with a high degree of skewness.

4 Take-off Scenario

The take-off scenario or the engine-over-runway scenario, as it is sometimes called in this thesis, approximates what happens when an engine is mounted to the wing pylon on an aircraft just before take-off or whilst performing an engine test run. This scenario has been investigated by previous authors. However, the only significant parametric study has been on the effect of increasing ambient vorticity by Glenny [30].

This chapter first introduces the modelling methodologies and its validation against previous experimental results before embarking on further parametric studies.

The parameters investigated are velocity gradient, size of suction inlet, flow Reynolds number and ground boundary layer thickness. The results are presented in the last section of this paragraph together with the discussions.

4.1 Introduction and Literature Study

Vortices can develop in the intakes of aero engines during high power operation near solid surfaces. This may occur during takeoff or during test in a ground facility (a test cell). The structure of the vortex is similar to the vortex seen in draining basin or bath. The streamlines spiral into the suction inlet with a radius of gyration that decreases as the inlet is approached. One end of the vortex is anchored to the nearby solid surface.

Whether or not a vortex forms depends on the thrust (or mass flow rate) of the engine, the diameter of the engine inlet, the distance from the solid surface, and the ambient vorticity which in turn depends on the local flow field. For example, vortices may form on takeoff if there is a sufficiently strong component of wind perpendicular to the runway.

Karlsson and Fuchs [50] modelled unsteady vortex behaviour in an LES simulation of an inlet over a ground plane. Secareanu et al. [51] validated these numerical results to particle image velocimetry (PIV) and laser doppler anemometry (LDA) measurements and obtained data on the ingestion of particles by a vortex-inlet system. These studies

did not attempt to predict the vortex formation threshold. Other CFD studies have modelled test cell airflow, such as Gullia et al. [52] and Kodres and Murphy [4], extracting information on thrust correction factors or airflow rates.

To date no numerical method for the prediction of vortex formation threshold has been described in the literature prior to papers published as part of the work leading to this thesis. The object of this study is to determine whether the threshold of vortex formation can be predicted numerically, and to use the numerical simulations to investigate the influence of suction inlet geometry and the ground boundary layer on this threshold, and to validate the method against available experimental data.

On the runway, the threshold of vortex formation depends on the thrust of the engine, height of the engine above the ground, size of the engine intake diameter, upstream inlet velocity and gradient, and the ground boundary layer thickness.

As mentioned earlier in Chapter 1.2, this research is only concerned with vortex formation mechanisms that concentrate ambient vorticity leading to single cored vortices forming in inlets in a headwind. It does not consider vortex mechanisms that do not require nonzero ambient vorticity and which lead to two or more counter rotating vortex cores such as those described by de Siervi et al [1]. Besides a nonzero ambient vorticity (sometimes quantified by the Rossby number $\frac{V_i}{WD_i}$, where Vi is the engine inlet velocity, Di the internal diameter of the inlet and W is the ambient velocity gradient or shear [53]), these single cored vortices require the distance from inlet to free surface to be lower than a certain threshold, and the velocity of the air between the inlet and the solid surface to be lower than the blow-away velocity. The blow-away velocity is the velocity which when exceeded would prevent vortices from forming. The distance threshold and blow-away velocity are interdependent and are neatly combined in the plots used by several authors (Nakayama and Jones [29], Liu et al. and [54] Shin et al. [55], of H/Di versus Vi/Vo where,

Vi = Suction inlet velocity

Vo = Upstream ambient velocity

H = Height of suction inlet centreline above the ground

Di = Suction inlet diameter

Data from these references is reproduced in Figure 6 which summarises data from several independent published studies with different engine geometries, upstream conditions and vortex detection methods. The results from the different studies exhibit some scatter but show a consistent trend of increasing Vi/Vo with increasing H/Di.

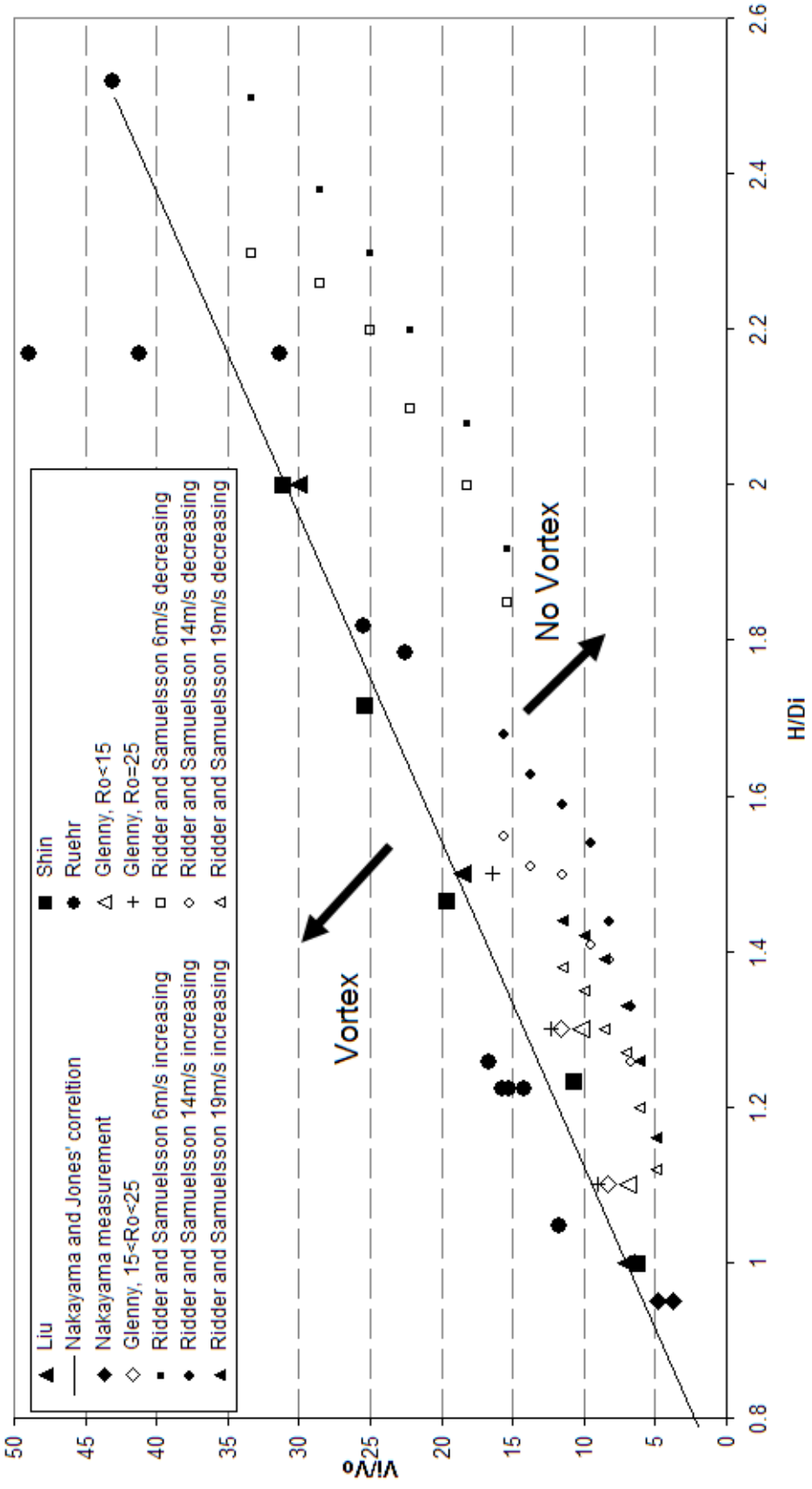

Figure 6: Threshold found by collating previous experimental data

On this plot, a straight line can be drawn marking, what seems to be, the boundary between a vortex forming regime and a non vortex forming regime. Vortices are formed at low H/Di and high Vi/Vo (the principal parameters are shown on the sketch in Figure 7). It should be noted that there is not yet any theoretical justification for the threshold being straight but it has been chosen because it fits the data as well as other type of lines.

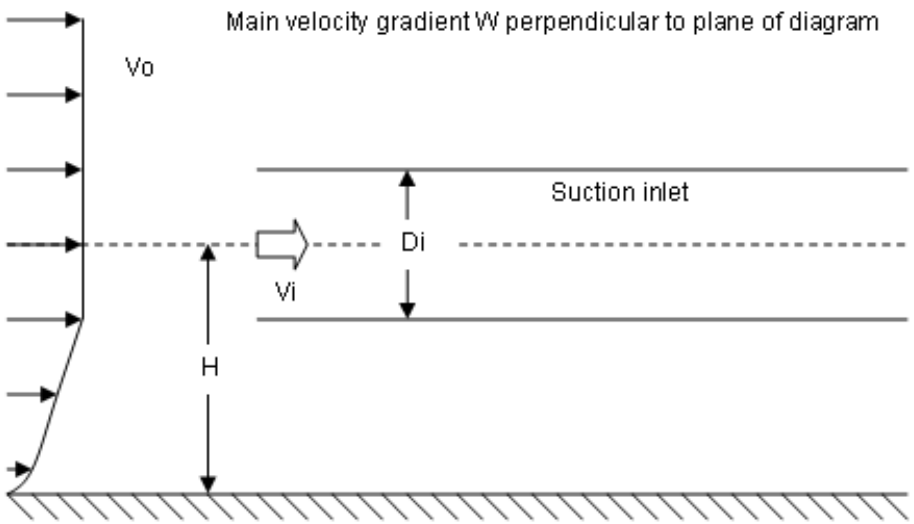

Figure 7: Principal parameters of vortex simulations

Experimental data from wind tunnel studies (Nakayama and Jones [29], Liu et al. [54], Shin et al. [55], Glenny [30], Motycka et al. [56], Ruehr [57] and Ridder and Samuelsson [31]) can be plotted in this way with agreement, although there is some variation from study to study (see Table 2 below for parameters of these experiments) in the location of the boundary of the vortex forming regime. This variation is due in part to the weak nature of the vortices produced near the boundary being hard to detect and the different detection techniques. It is also due to the variation in bellmouth geometry, scale and flow conditions from study to study. However, note should be given to the results from Ridder and Samuelsson [31], which has the lowest Reynolds number in all the experiments. Their results lie to the bottom right of the others suggesting Reynolds number to be an important parameter.

Table 2: Experimental conditions from previous investigations

	V_i/V_o	H/D_i	Ro	Re_i	Re_o	D_i/m	D/m	Yaw angle	Mach number	V_o/ms^{-1}	V_i/ms^{-1}	Shear generation
Glenny (1970)	5-18	0.9-1.8	8-25	460,000-2,100,000	25,000-360,000	0.152-0.305	N/A	0 and 55°	>0.14	2.5-18	46-107	Mesh
Motycka et al. (1973)	N/A	1-2	8-440	N/A	N/A	0.203	N/A	135°	N/A	N/A		Screens
Ruehr (1975)	12-50	1-2.5	N/A	N/A	N/A	N/A	N/A	60°	N/A	N/A		N/A
Liu et al. (1985)	6-35	1-2	Low	Up to 1,300,000 plus trip wires	Up to 219,000	0.15	0.2	90°	Up to 0.4	Up to 22	Up to 135	Inlet yawed relative to wind tunnel
Shin et al. (1986)	6-35	1-2	Low	Up to 1,300,000 plus trip wires	Up to 219,000	0.15	0.2	90°	Up to 0.4	Up to 22	Up to 135	Inlet yawed relative to wind tunnel
Nakayama and Jones (1996)	3.8-4.8	0.95	∞	N/A	N/A	N/A	N/A	0°	0.1-0.2	33-66		Inlet yawed relative to wind tunnel
Ridder and Samuelsson (1992)	5-35	1-2.5	Low	260,000-340,000	8000-26,000	0.020-0.039	0.023-0.043	0° and 45°	0.58-0.80 In inlet	6-20	200-260	Triangular obstacles

Kline [58] stated three conditions for the formation of a vortex: nonzero ambient vorticity, a stagnation point on the solid surface, and an updraught from just above the stagnation point to the inlet. These are necessary but not sufficient conditions. The H/Di and Vi/Vo conditions must be met. These conditions essentially define a blow-away velocity above which the vortex cannot persist. When Vo is greater than the blow-away velocity, the vortex will be stretched downstream and dissipated. Conversely if Vi is too low, the capture stream-line tube will not intersect with the ground plane resulting in the absence of a stagnation point. The same explanations can be deduced intuitively for H and Di.

In the absence of ambient vorticity, a stagnation point can exist without an associated vortex [58]. There is a threshold of ambient vorticity below which no vortex may be formed, and a further threshold below which the vortex may be formed but may be too weak to be detected.

Vortices observed during experiments and in test cells are unsteady in nature with the core seen to precess. However the hypothesis of Glenny [30] that this unsteady nature of the vortices is due to some unsteadiness in the surrounding fluid is taken as the explanation. He observes that the vortices were disturbed by the presence of slight disturbances due to the simple and common act of opening and closing of doors near the experimental apparatus. It is unlikely that absolutely steady conditions occur in experiments and test cells.

4.2 Investigation Methodology

The investigations carried out on the vortex formation and ingestion phenomenon were performed using the commercial CFD software package Fluent from ANSYS Inc. Throughout the investigation periods; new and updated versions of Fluent were made available and were used. The investigation used Fluent 6.2.16 as well as Fluent 6.3.26. The models were meshed using the commercial meshing tool Gambit. Similar to the Fluent case, more than one version of Gambit (2.1.22, 2.2.30 and 2.3.16) were used.

Although most of the simulations and all the results published and presented in this thesis were carried out using 3D simulations, a small number of 2D simulations were carried out at the initial stages of each parameter investigation. These are not included in this thesis. Mesh convergence tests were carried out at critical stages of the investigations to ensure that the solution is mesh convergent. Details of the mesh convergence exercise will be presented in the later sections

The simulations were carried out using the incompressible flow solver. The incompressible flow solver was selected because of the reduced complexity and ease of solution convergence. A test was conducted to determine that the incompressible flow solver was appropriate for the task. Details of this compressible vs. incompressible solver test will be presented in the later sections.

The turbulence model used for the simulations is the SST-Kω model. The SST-Kω model was selected because of it combined the best features of the K-ε scheme in free flows and the standard K-ω scheme in near wall flows, yet avoiding the computational expense of the Reynolds Stress Models (RSM). Details of a test showing that the SST-Kω model was adequate for the investigations will be presented in the later sections.

The simulations used the first order discretisation scheme for computational resource saving reasons. Details of the test showing the difference in results between the two schemes will be presented in the later sections.

During the simulation, the vortex threshold was determined by gradually increasing or decreasing the average upstream velocity until the appearance or disappearance of a vortex. Each average upstream velocity was solved until convergence by observing the residuals as well as the mass flow rates through the boundaries. Any possible hysteresis effects were avoided by initialising the flow before the start of each simulation.

4.2.1 Size of Ambient Environment

As the engine-over-runway scenario is an external flow scenario, a boundary to the simulated ambient environment volume needs to be established. If this ambient

boundary is too small it may not be enough to simulate far field effects accurately, if it is too large, there will be unnecessary waste of computational resources.

Some three dimensional external flow scenarios use a sphere as the ambient environment, especially common for flow around an airfoil, but after deliberation and advice from various parties (including with the local Fluent representative), a cuboid ambient environment was chosen. A test was conducted to establish the smallest necessary ambient environment for the simulation. During the course of this test, ambient environment larger then optimal have no negative effects on the simulation except waste of computational resources. During the test, the length of each dimension was increased until further enlargement had no effect on the vortex formation threshold or location and characteristics of vortex. The optimal size of ambient environment is found to be as follows:

a. Upstream, 5 x suction inlet diameter
b. Downstream, 10 x suction inlet diameter
c. Sides, ≈8 x suction inlet diameter
d. Ceiling, ≈7 x suction inlet diameter

The suction inlet diameter was chosen as the primary parameter because the vortex characteristics are expected to be influenced by it.

4.2.2 Geometry, Mesh and Boundary Conditions

A simple suction inlet tube over a ground plane model was used to simulate the engine-over-runway scenario. A picture of the model is shown in Figure 8 below. This model is similar in features to that used in previous investigations by Glenny [30]. Glenny's model is shown in Figure 9.

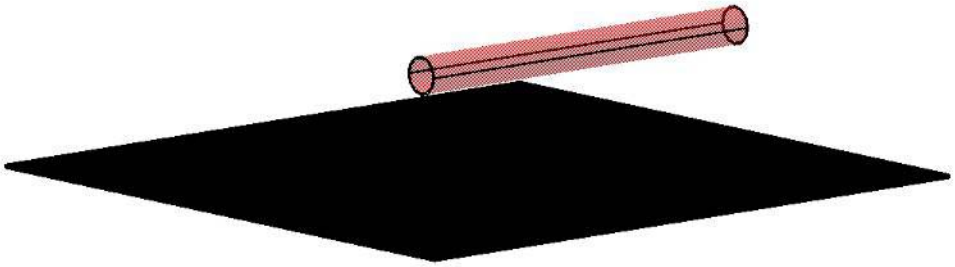

Figure 8: Engine-Over-Runway Model

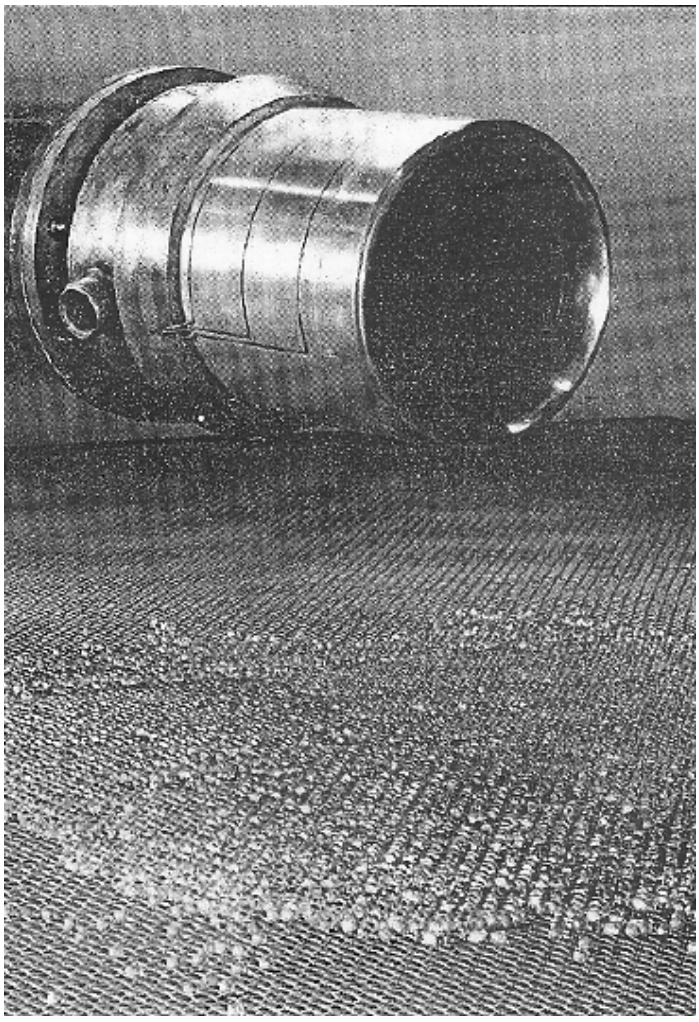

Figure 9: Glenny's Model

Upstream of the suction inlet tube was simulated using a velocity inlet boundary condition with a defined average velocity and a velocity gradient (W) defined by a

UDF whilst the surrounding ambient space was enclosed using a pressure inlet boundary. An example of the script used to define the velocity inlet at the upstream plane is provided in Appendix C. Downstream of the suction tube and the tube inlet was simulated using pressure outlet boundaries. Plane no-slip walls were used for the floor.

As mentioned previously, the model was meshed using Gambit across different versions. A typical mesh of the model is shown in Figure 10. This mesh has about 100 000 cells. The green section has a tighter mesh as this is where the vortex was expected to form. In all the simulations, a Y+ value of less than 300 was maintained in accordance to suggestions found in the Fluent manual for the turbulence model used.

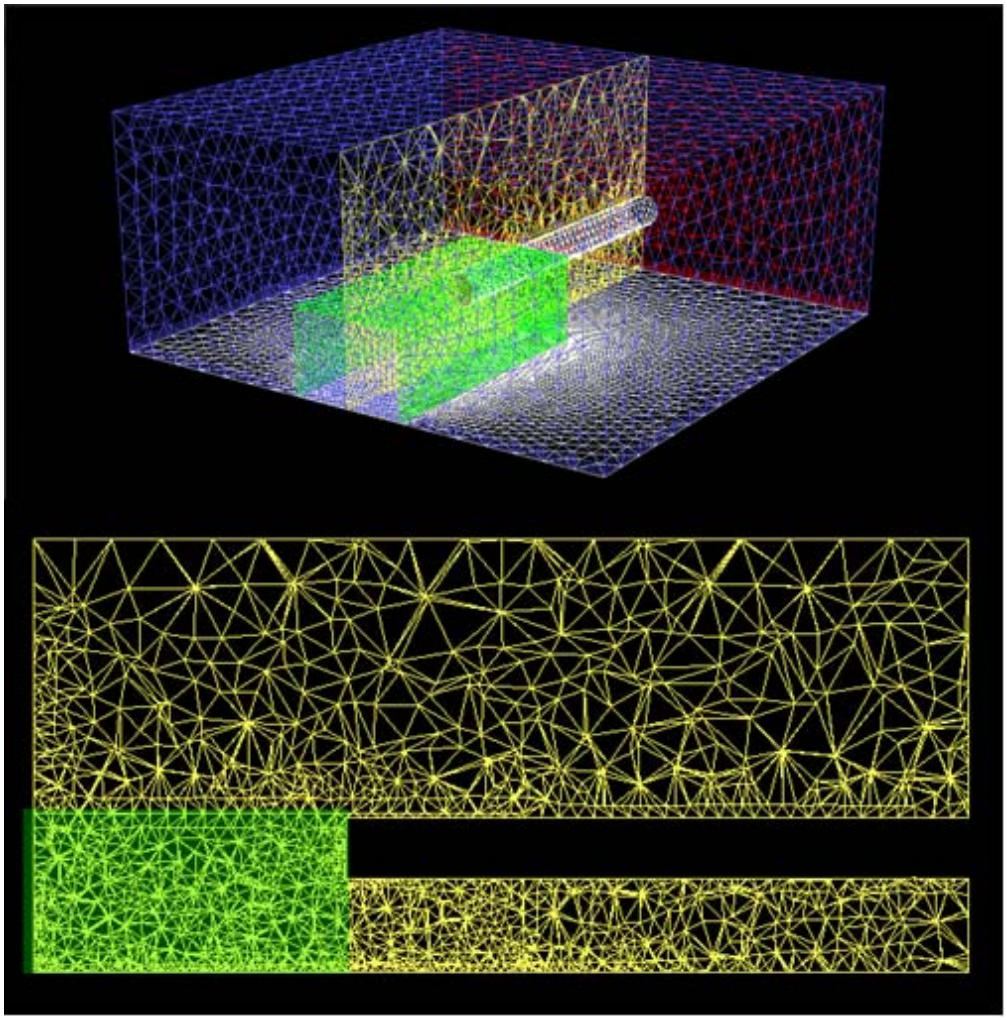

Figure 10: A typical mesh for the engine-over-runway model

In order to prevent inaccurate calculations due to mesh related issues, a mesh convergence test was conducted to determine the most appropriate mesh and is detailed below.

Three different meshes of around 300 000, 1 000 000 and 2 500 000 cells of the same geometry and boundary conditions were solved and the results analysed. Figure 11 shows the contour maps of the static pressure on the ground plane and one velocity vector field while Figure 12 shows a plot of the static pressure along a line that lies in the middle of the ground plane from upstream to downstream. The flow conditions shown are near the threshold and produce a clear stagnation point but weak vertical circulation. The suction inlet is at x = 0. The turbulence model used in these calculations was the SST-kω model.

The results show that although the numerical values of the pressure in the vortex core are affected by mesh density principally due to the spatial resolution at which the strong pressure gradient is sampled, the position of the vortex does vary not at all.

In addition, a test to determine if mesh density affects vortex formation threshold is also conducted. Three different mesh sizes of around 100 000, 200 000 and 500 000 cells of the same geometry and boundary conditions were solved and the results analysed. For H/Di = 2.0, the vortex formation threshold for these cases occurred at Vi/Vo between 37.8 and 38.5 for the 100 000 cells mesh, between 38.2 and 38.7 for the 200 000 cell mesh and between 38.0 and 38.6 for the 500 000 cells mesh. The results from this test shows that the vortex formation threshold is not affected significantly (less than 5%) by the increase in mesh density.

Together with the previous test, it can be deduced that if a particular mesh is sufficient to observe the vortex forming then increasing the mesh density will only affect the numerical values of the pressure and presumably get a more accurate description of the pressure profile within the vortex core. Vortex formation threshold is not affected significantly and location of vortex is not significantly affected at all. In these simulations, the detailed pressure characteristics of the vortex core are of secondary importance as compared to the threshold and vortex location. Hence investing

computational expanses to obtain a more accurate pressure profile is not deemed to be necessary.

Eventually a mesh of between 100 000 and 200 000 cells was used in the investigations. The difference in mesh density is a result of the geometrical differences between the different suction inlet heights.

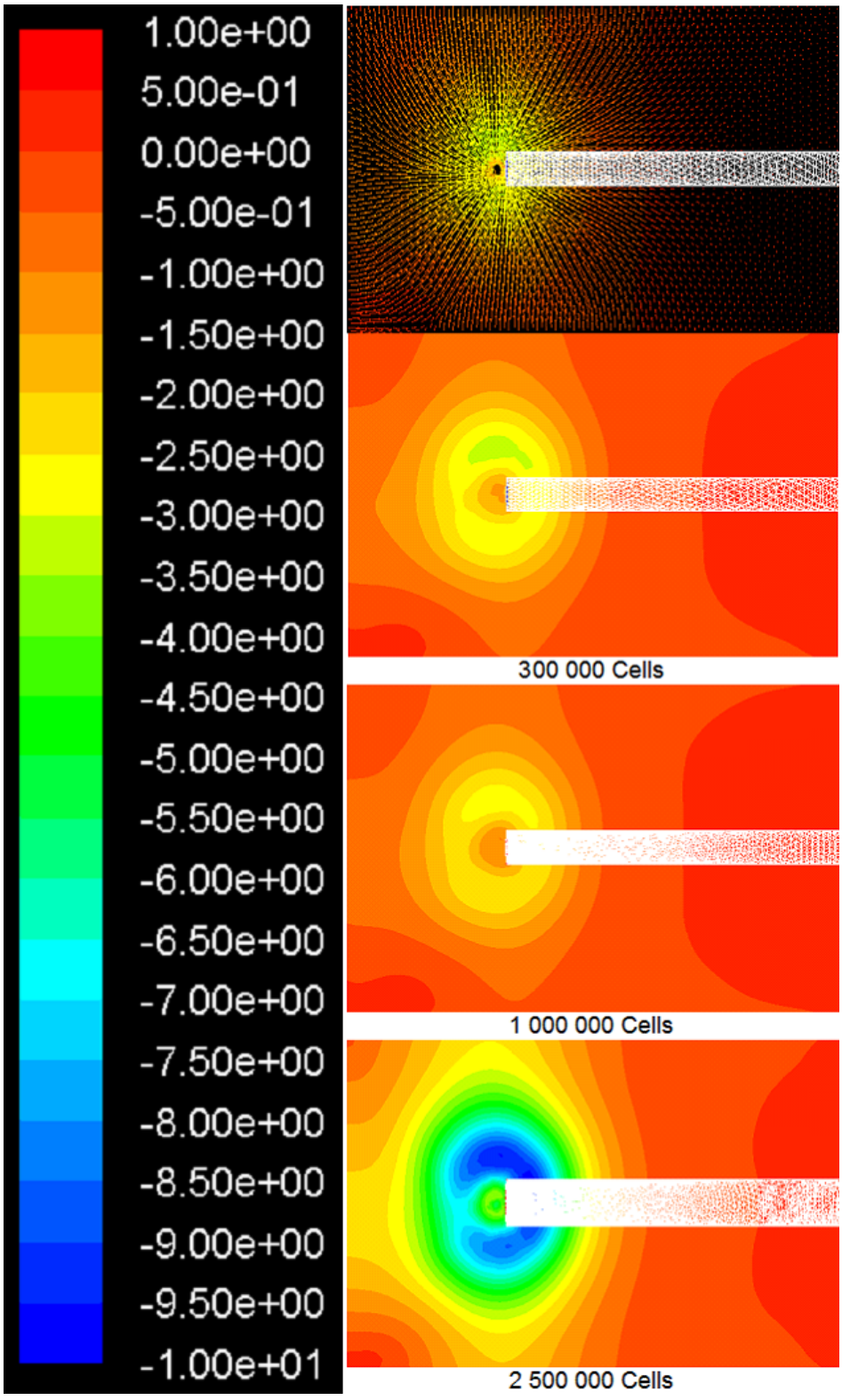

Figure 11: Static pressure and velocity on the ground plane as a function of grid refinement (H/Di = 2.0, H = 3.5m, W = 0.05/s, Vi/Vo ≈ 325)

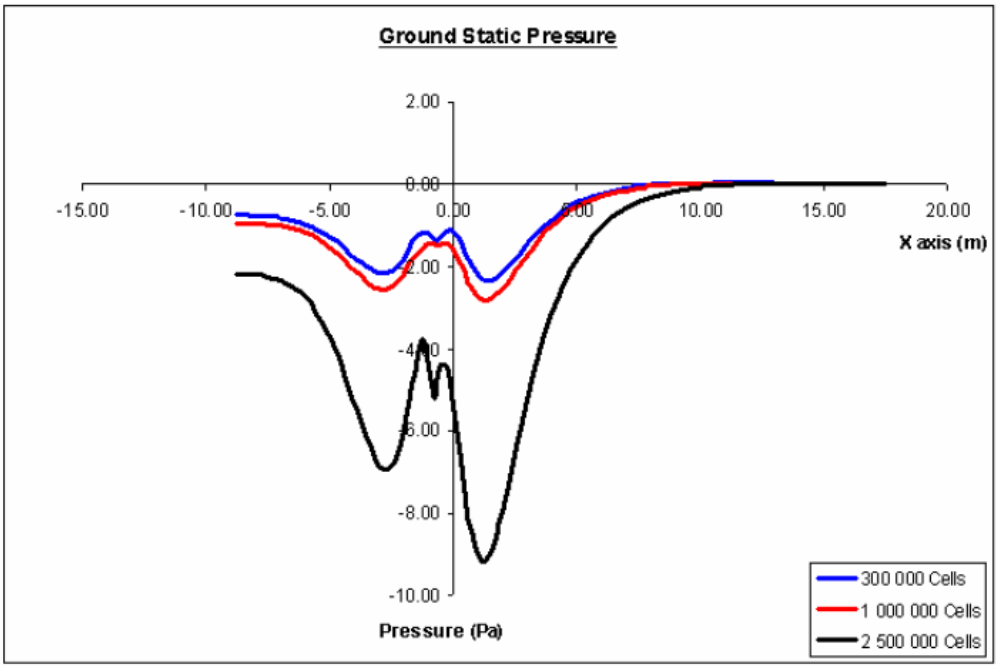

Figure 12: Ground static pressure plot of a line running through Z = 0 showing the results of mesh refining exercise (H/Di = 2.0, H = 3.5 m, W = 0.05/s, Vi/Vo ≈ 325)

4.2.3 Turbulence Models

The SST-kω and Reynolds Stress Model (RSM) were considered and solved on mesh size of approximately 150 000 cells with the same geometry and boundary conditions. The two equation models were not considered because the SST-kω model has a proven performance record in separated flows. Since desired results are steady state vortex formation, DES and LES were never considered as potential turbulence models. Figure 13 and Figure 14 show plots equivalent those in the previous section, on the two turbulence models. The suction inlet is at x = 0 in Figure 14. The result of this test shows that again only the numerical value of pressures and not the location of vortex were affected by the turbulence models. Unless otherwise stated default parameters from Fluent (k = 1 and ω = 1) were used for the turbulence models in all the simulations.

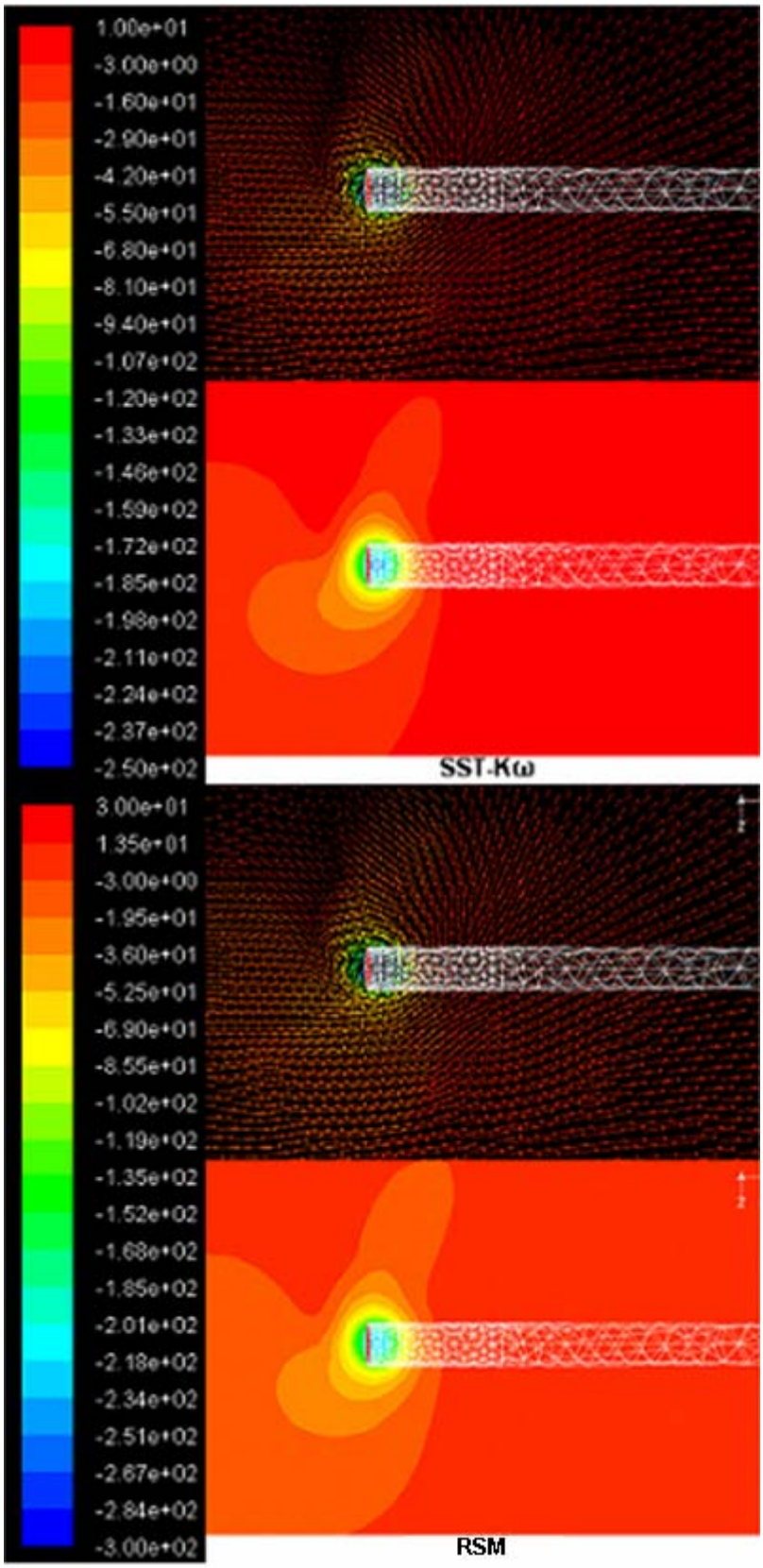

Figure 13: Static pressure and velocity on the ground plane as a function of turbulence model (H/Di = 2.0, H = 3.5 m, W = 0.4/s, Vi/Vo ≈ 38.0)

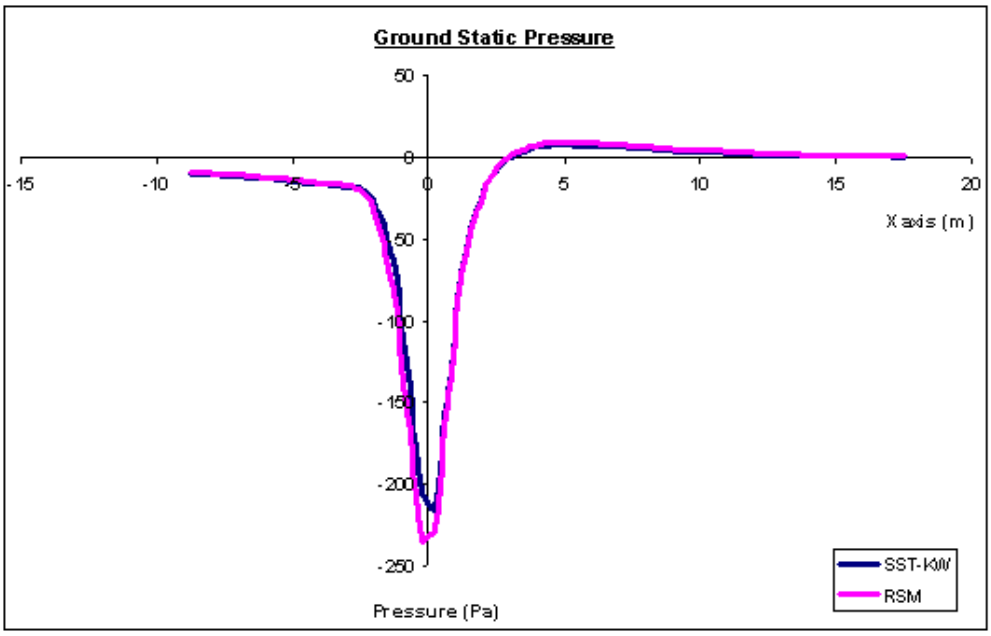

Figure 14: Ground static pressure plot of a line running through Z = 0 showing the results of k–ω SST and RNS turbulence models (H/Di = 2.0, H = 3.5 m, W = 0.05/s, Vi/Vo ≈ 38.0)

The SST-kω and RSM were considered and solved on mesh size around 150 000 (the same grid size as one of the cases used to generate the H/Di against Vi/Vo plots) with the same geometry and boundary conditions. For H/Di = 2.0, the vortex formation threshold for k–ω SST and RSM models occur at Vi/Vo between 37.8 and 38.5 (k–ω SST) and between 38.3 and 38.8 (RSM). The results from this test shows that the vortex formation threshold is not affected significantly (i.e. less than 5 per cent) by the use of the less computationally expensive SST-kω model.

4.2.4 Discretisation Scheme

First and second order discretisation schemes were considered and solved on two separate cases with mesh sizes around 150 000 with the same geometry and boundary conditions. Figure 15, Figure 16, show plots equivalent to Figure 13 and Figure 14, respectively, on the two discretisation schemes. In Figure 16 and Figure 18, the suction inlet is at position x = 0. The result of this test shows that only the numerical value of pressures and not the location of vortex were affected by the discretisation scheme. Hence a first order discretisation scheme was deemed to be sufficient. Figure 17 and Figure 18 shows the results from the second case. They were shown using a

more zoomed in picture to observe the potentially broadening of the vortex core as a result of the more dissipative nature of the first order discretisation scheme.

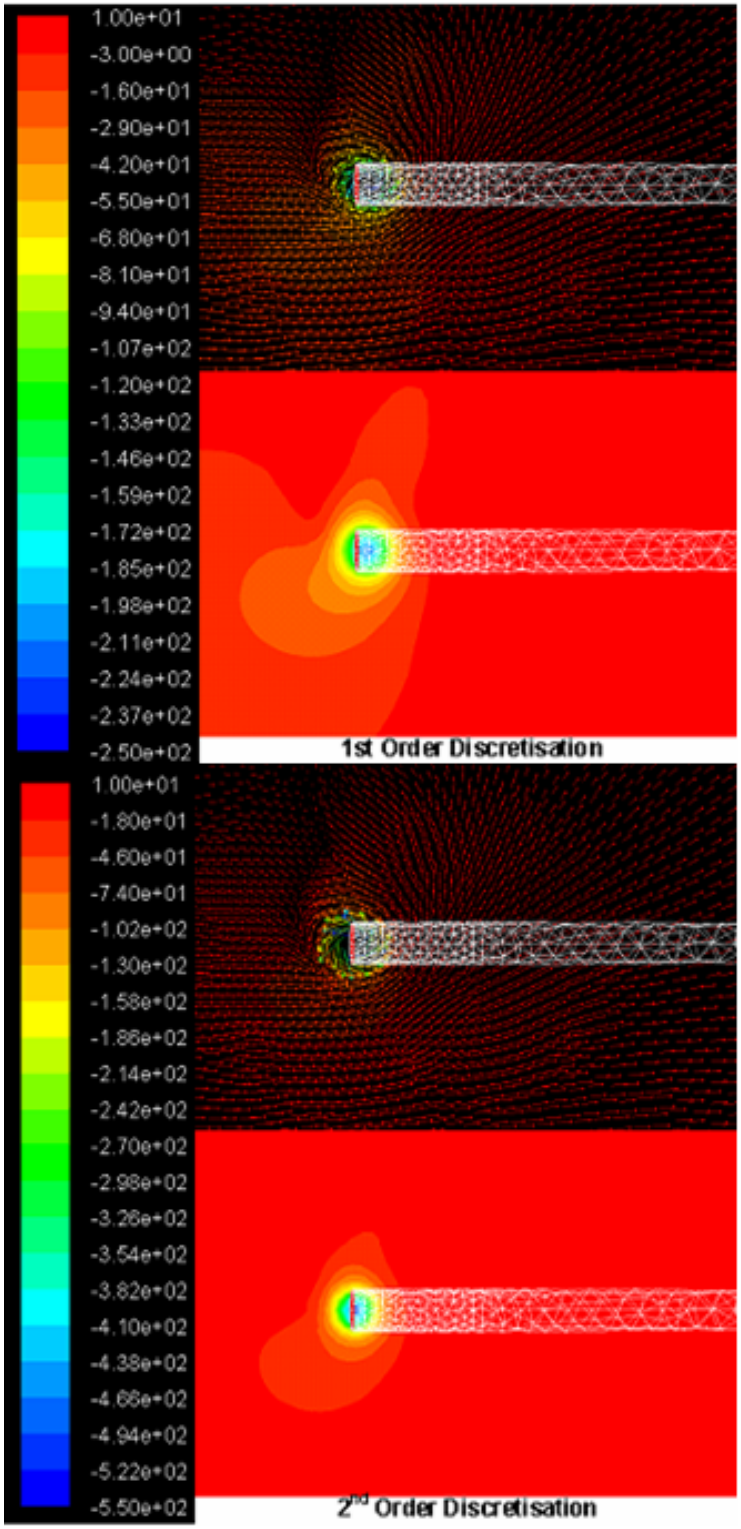

Figure 15: Static pressure and velocity on the ground plane as a function of discretisation scheme order (H/Di = 2.0, H = 3.5 m, W = 0.4/s, Vi/Vo ≈ 38.5)

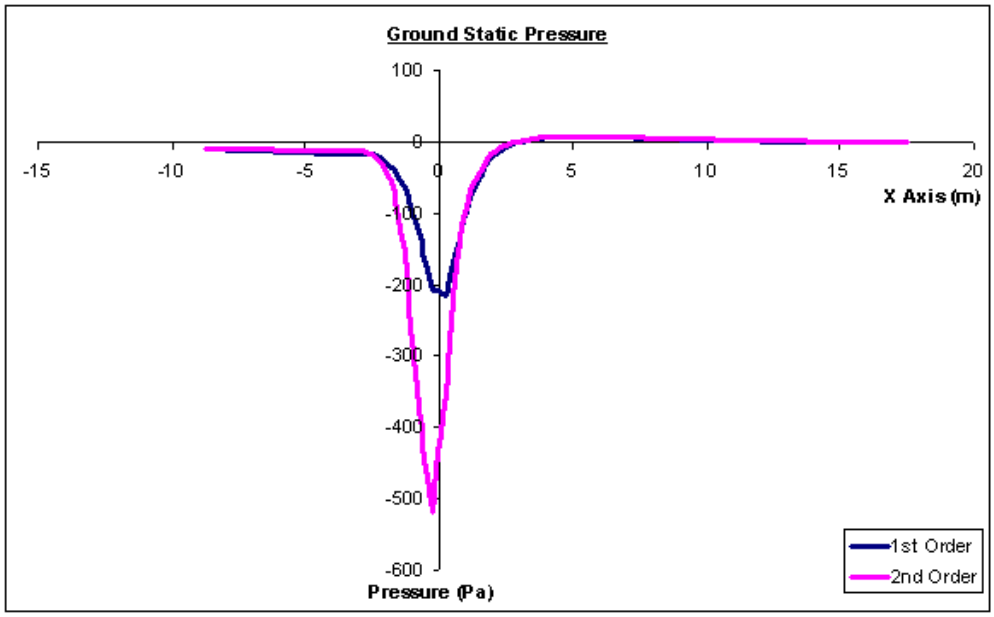

Figure 16: Ground static pressure plot of a line running through Z = 0 showing the results of first order and second order discretisation schemes (H/Di = 2.0, H = 3.5 m, W = 0.4/s, Vi/Vo ≈ 38.5)

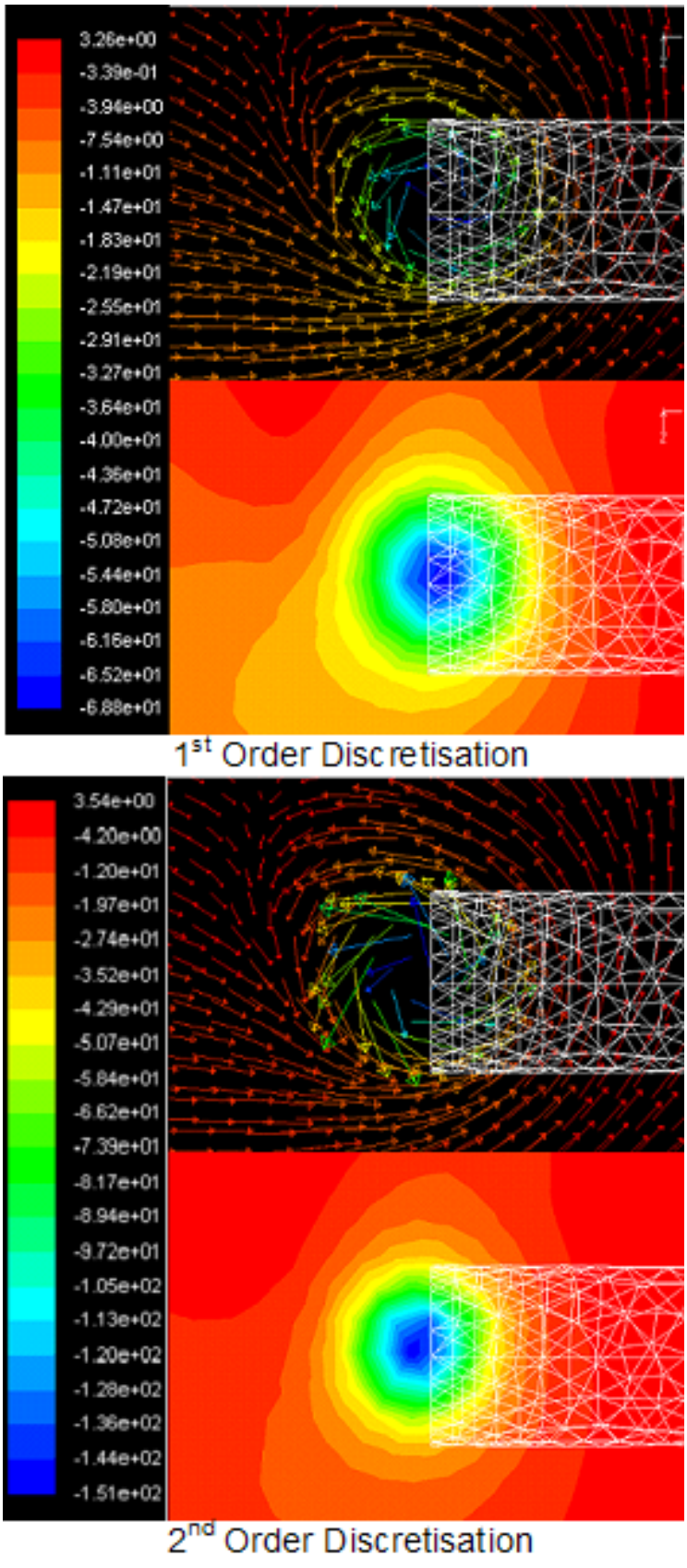

Figure 17: Static pressure and velocity on the ground plane as a function of discretisation scheme order (H/Di = 2.0, H = 2.0 m, W = 0.2 /s, Vi/Vo ≈ 38.5)

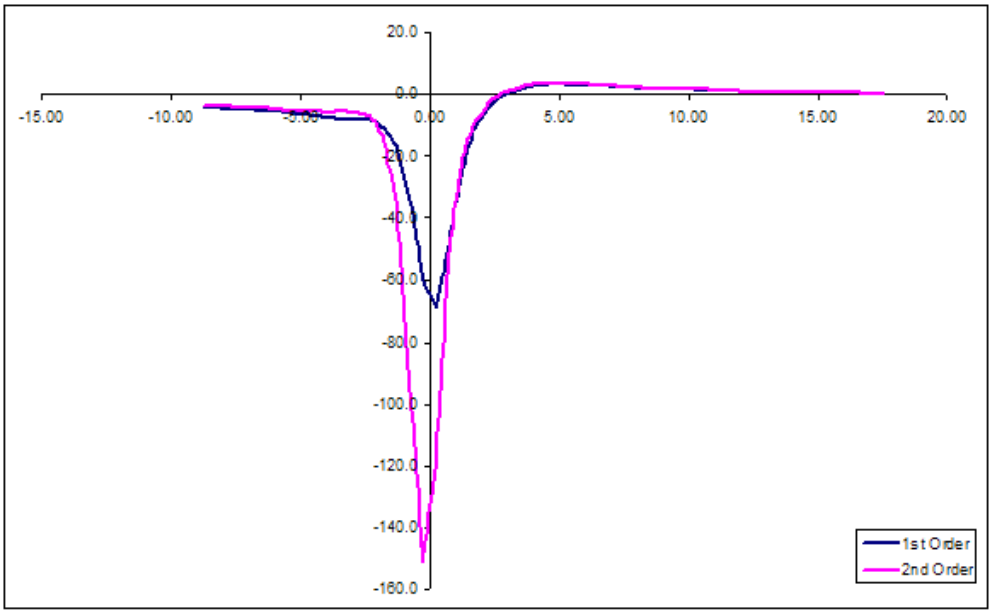

Figure 18: Ground static pressure plot of a line running through Z = 0 showing the results of first order and second order discretisation schemes (H/Di = 2.0, H = 2.0 m, W = 0.2 /s, Vi/Vo ≈ 38.5)

In a vortex, strong shear levels lead to high turbulence levels and high eddy viscosity. Thus, the natural dissipation is high. It is not easy to quantify the numerical dissipation but it is expected that the more dissipative nature of the 1st order discretisation scheme to have less impact on the flow solution in a strongly dissipative flow like the vortex, than in a weakly dissipative flow. The 1st order scheme may impact the accuracy of calculation of less dissipative features e.g. boundary layers in regions of slow flow so may impact the accuracy of the determined vortex threshold with boundary layers. Hence, a threshold test was conducted for both discretisation schemes and the results presented below.

First and second order discretisation schemes were considered and solved on mesh size around 150 000 (the same grid size as one of the cases used to generate the H/Di against Vi/Vo graphs) with the same geometry and boundary conditions. For H/Di= 2.0, the vortex formation thresholds for the first and second order discretisation schemes occur at Vi/Vo between 37.8 and 38.5 (first order) and between 37.7 and 38.4 (second order).The results from this test shows that the vortex formation threshold is not affected significantly (i.e. less than 5 per cent) by the discretisation scheme.

In conclusion, the first order scheme is more dissipative in nature compared to the second order schemes as the cell face values are assumed to be the same as the cell centre values. As a result, a broadening of the vortex core can be expected and is observed to be present, though very slightly and insignificant, in the velocity and contour plots shown in Figure 17. It is not so apparent in the static pressure plots. However, the computational savings gathered from the use of the first order discretisation scheme outweighed its loss in accuracy at the time of conducting the simulations.

4.3 Parameters Investigated

The runway scenario was investigated as a means of validating the CFD methodology by comparing the results to previous investigation notably that of Glenny [30]. Hence the first parameter that was investigated is upstream velocity gradient. Glenny used the dimensionless Rossby number (Ro) to represent velocity gradient. Glenny's results are reproduced below in Table 3.

$$Ro = \frac{V_i}{WD_i} \tag{4}$$

Table 3: Points on the threshold line from Glenny's reported data [30] at different Rossby numbers

Vi/Vo	H/Di	Ro
6.84	1.1	8.0
8.33	1.1	18.0
9.09	1.1	25.0
10.4	1.3	12.0
11.6	1.3	17.0
12.2	1.3	25.0
13.2	1.5	25.0

Glenny's data suggests that for a fixed geometry (H/Di), a decrease in Rossby number (increasing velocity gradient) increases Vi/Vo value of the vortex formation threshold implying an increase in the range of conditions at which vortices form.

The second parameter investigated is the effect of changes to the engine inlet diameter. As H/Di is an important parameter, and should be kept constant during the investigation, this parameter change can also be interpreted as the effects of scaling the entire model. As engine sizes increase, this parameter gives an indication of how much larger a new test cell should be. Previous experimental results indicate that Reynolds number has an effect on the vortex formation threshold (see discussion on previous experimental data shown in Table 2 and Figure 6). In the investigation of the size of the engine inlet diameter, care was taken to alter the upstream velocity so as to keep Reynolds number constant.

The third parameter is the effect of Reynolds number. It is suggested using evidences extracted from the previous experimental data (see Table 2 and Figure 6) that Reynolds number has an inverse relationship with threshold position. Reynolds number effects have implications on the operation of the test cell but more importantly on future experimental procedures because Reynolds number is a common dimensionless number used for dynamic scaling a flow where the viscous forces dominate and a full-scaled model test is not possible. Higher Reynolds number indicates higher rate of turbulent mixing thus inhibiting the formation of the vortex. Additionally, lower Reynolds number indicates that the separation of flow pathlines from the floor into the engine inlet is more likely to take place thus making it easier for the vortex to form.

Ridder and Samuelsson's experiments occurred at lower Reynolds number and their threshold occurs at a lower Vi/Vo. As this is merely a collection of previous results, the change in Reynolds number is not done cetaris paribus[1]. However it provides confidence for the existence of such a relationship and that the relationship is a direct one.

It is interesting to note that Ridder and Samuelsson's experiments had a higher throat Mach number between 0.5 and 0.8, clearly in the region where compressible effects

---

[1] *Cetaris Paribus* is a common latin term used particularly in economic theories for "keeping all other parameters constant".

are deemed to be important in classical analysis. It is not certain if this is also applicable in this instance or the effect of it. However an in-house experiment conducted at the university by Arnault Maheut, which was not published, had a Reynolds number that is much lower than the other studies but had a much lower throat Mach number than Ridder and Samuelsson's experiments (Arnault's experiment had throat Mach numbers of around 0.01, clearly in the region where compressible effects are not significant). This lends more confidence that the effect of Reynolds number is perhaps more dominant that any compressible effects that may be present.

Figure 19 and Table 4 below reproduces the same graph and table as Figure 6 and Table 2 respectively but with the inclusion of the results from the in-house experiment by Arnault.

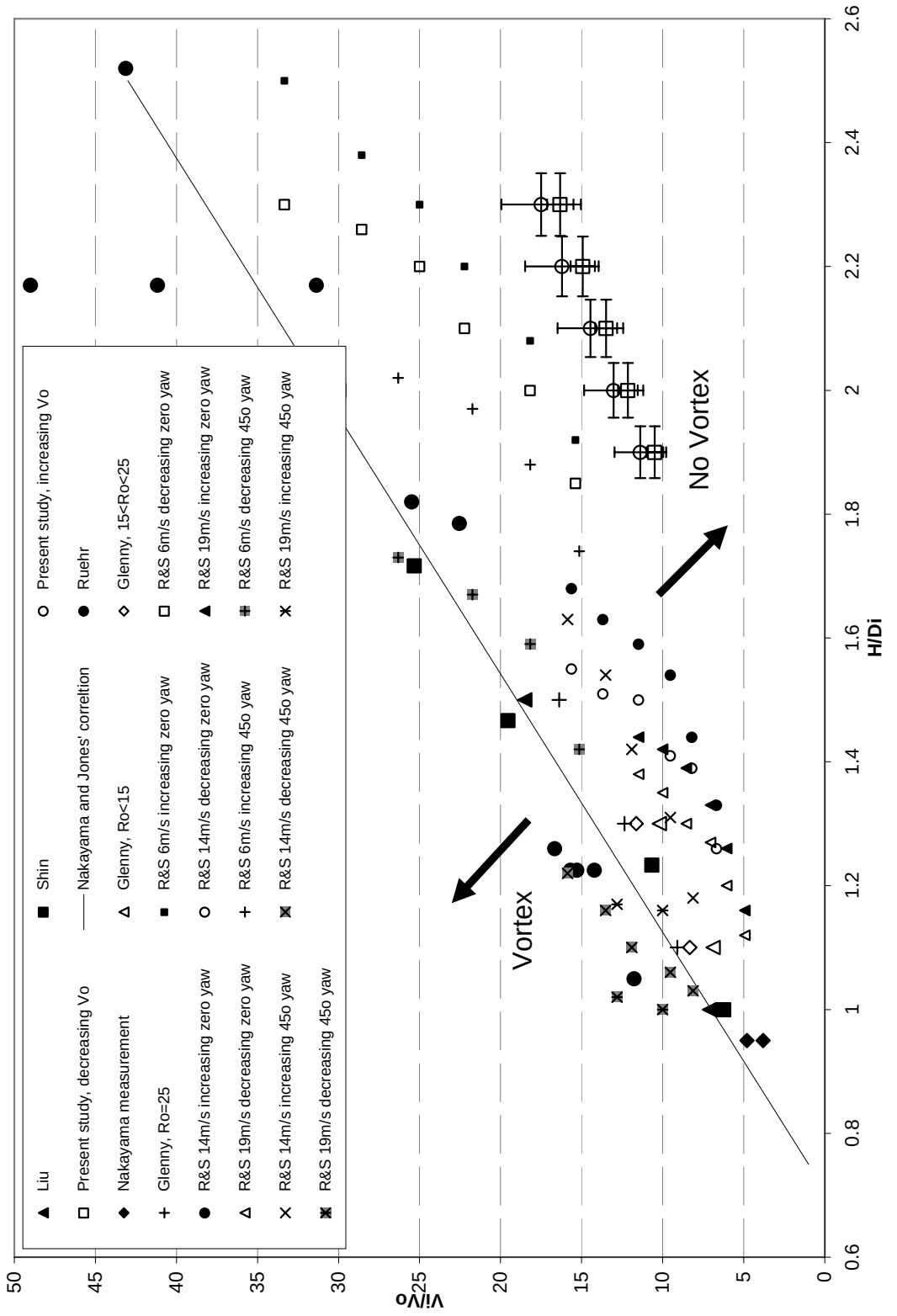

Figure 19: Experimental data showing the boundary between the vortex forming and non-vortex forming flow regimes including in-house results

Table 4: Investigation conditions from previous experiments including in-house experiment by Arnault

	V_f/V_0	H/D_i	Re_i	Re_0	D_i/m	D/m	Yaw angle	Mach number	V_0/ms^{-1}	V_f/ms^{-1}	Shear generation
Glenny (1970)	5-18	0.9-1.8	460,000-2,100,000	25,000-360,000	0.152-0.305	N/A	0 and 55°	>0.14	2.5-18	46-107	Mesh
Motycka et al. (1973)	N/A	1-2	N/A	N/A	0.203	N/A	135°	N/A	N/A		Screens
Ruehr (1975)	12-50	1-2.5	N/A	N/A	N/A	N/A	60°	N/A	N/A		N/A
Liu et al. (1985)	6-35	1-2	Up to 1,300,000 plus tip wires	Up to 219,000	0.15	0.2	90°	Up to 0.4	Up to 22	Up to 135	Inlet yawed relative to wind tunnel
Shin et al. (1986)	6-35	1-2	Up to 1,300,000 plus tip wires	Up to 219,000	0.15	0.2	90°	Up to 0.4	Up to 22	Up to 135	Inlet yawed relative to wind tunnel
Nakayama and Jones (1990)	3.8-4.8	0.95	N/A	N/A	N/A	N/A	0°	0.1-0.2	23-56		Inlet yawed relative to wind tunnel
Ridder and Samuelsson (1992)	5-35	1-2.5	260,000-340,000	8000-26,000	0.020-0.039	0.023-0.040	0° and 45°	0.58-0.80 In inlet	6-20	200-260	Triangular obstacles
Arnault Maheut*	10-18	1.9-2.3	17,000-52,000	1,700-2,900	0.014	0.03	0°	0.01	1.80-3.11	18-56	None

*The study by Arnault Maheut is an in-house experiment conducted before the commencement of investigations presented in this thesis. Although there was no direct form of shear generation leading theoretically to a zero velocity gradient and Re_0, it is likely that some form of velocity gradient was accidentally and perhaps inevitably introduced during the conduct of the experiment.

The final parameter investigated is the effect of the presence and height of a boundary layer forming on the ground. Many natural and man-made parameters can affect the height of the boundary layer forming upstream of the engine and an understanding of

this parameter will be extremely helpful. A pronounced power law boundary layer was defined in the UDF at the ground edge of the upstream plane to simulate the boundary layer. Two different boundary layer thicknesses (defined as the height at which the velocity reached 99 per cent of the free-stream velocity), of 2 and 5m were simulated. See Appendix C for an example of the source code for the UDF.

Vortices, when formed and observed, in cells and scaled experiments always seemed to be unsteady in nature. Glenny [30] hypothesized that this unsteady nature is due to some unsteadiness in the surrounding conditions. In practice, it extremely difficult to keep surrounding conditions absolutely steady but it is relatively simple in CFD calculations.

The in-house experiment conducted by Arnault showed that the direction of the vortex changed in an unsteady manner. The simulations were conducted in a wind-tunnel with no pre-designed velocity gradient. This increases the confidence that in experiments, keeping the surrounding conditions steady is extremely difficult and perhaps bordering on the impossible. See Appendix D for details of the experiment.

In addition to the four parameters discussed above, the steady nature of the vortex and the minimum velocity gradient necessary for a vortex to form were also investigated.

4.4 Result and Conclusions

This chapter presents the results of the investigation on the vortex formation threshold for the engine-over-runway scenario. The results will be presented in plots of Vi/Vo against H/Di.

The threshold is represented with a linear line of best fit created using Microsoft Office's Excel trendline function. This function generates a best fit line using the least squared regression.

The results shown represent the effects of changing individual parameters cetaris paribus unless described otherwise. In the current context, all perceivable parameters are kept within a certain bandwidth when it was not feasible to keep it absolutely

constant. An example of this was the very slight differences in Reynolds number in calculations when it was not the parameter of investigation.

A typical velocity field on the ground is shown in Figure 20 with the vortex clearly seen. This plot shows the velocity field in the first layer of cells above the ground plane. The cells are typically 0.1m thick. This was also used as the means of identifying the occurrence of the vortex. A vortex was deemed have formed if a clear rotation was observed on the vector plots.

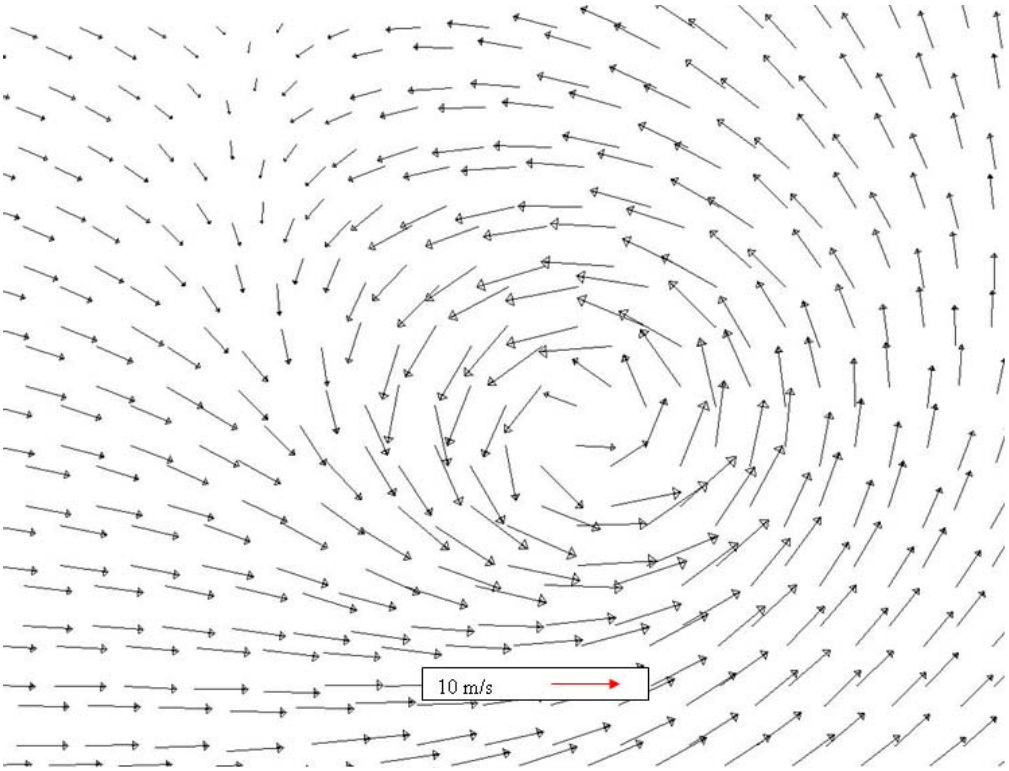

Figure 20: Typical velocity vector plot on the ground showing the presence of a vortex

Figure 21 shows the results of the effect of upstream velocity gradient on vortex formation threshold. The dashed line, as mentioned above, is a line of best fit to the experimental data with high Reynolds number (25 000–360 000 based on the outer diameter of the inlet and the free-stream velocity).

This high Reynolds number data comprises all the data shown earlier in the chapter with the exception of that of Ridder and Samuelsson [31], which lie at lower Vi/Vo possibly because their tests were carried out at significantly lower Reynolds numbers

(8000–26 000). The symbols in Figure 21 are the thresholds found by numerical simulation. Data for four different upstream velocity gradients (i.e. velocity shear at entrance plane) are presented.

This result agrees qualitatively with previous experimental data. The gradient of the thresholds shows very good agreement with the best fit line.

During the search for the threshold, Vstart was changed in steps of 0.1 m/s and this represents an uncertainty in Vi/Vo of not more than 5%.

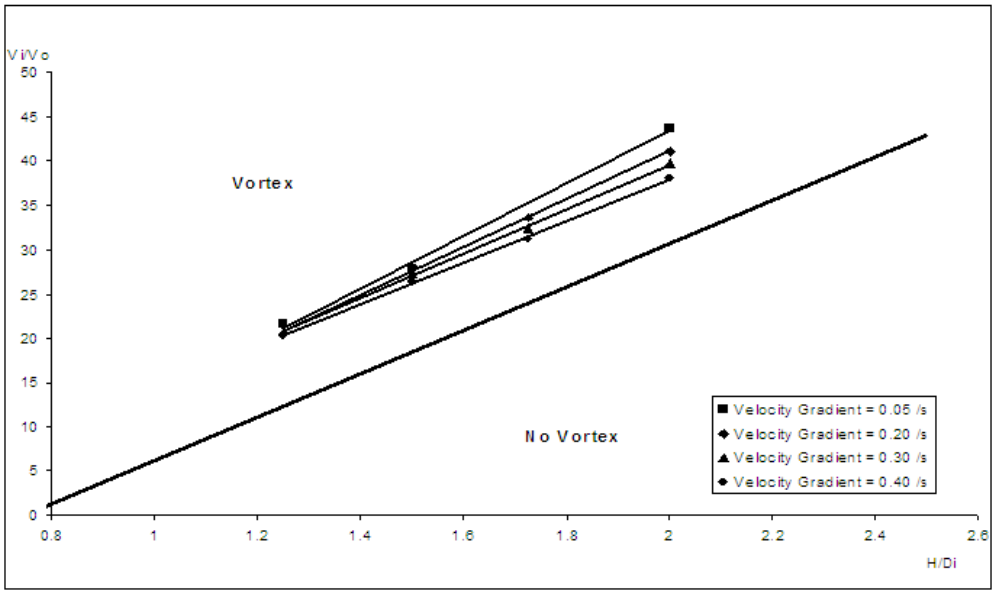

Figure 21: H/Di versus Vi/Vo plot showing the effects of upstream velocity gradient

Velocity gradient defines the degree of ambient vorticity and thus a higher value predictably resulted in more conditions favouring the formation of vortices.

The second parameter that was investigated was the effect of an increase in the engine diameter. It was found that the increase in the engine diameter caused the threshold to move to a lower Vi/Vo implying an increase in the probability of a vortex being formed as shown in Figure 22 below. In the same figure, the effect of Reynolds number is also shown. Increasing the Reynolds number is akin to increasing the upstream average velocity and thus convecting the vorticity downstream and dissipating it by increased diffusion. Increasing the Reynolds number moves the

threshold to a higher Vi/Vo and decreases the possible conditions for the vortex to form and hence the probability of vortex formation. Increased Reynolds number also increases the turbulence within the flow and smoothens out any concentration of vorticity thus making it harder for the vortex to form.

The large and small diameters are 1.75 and 0.75 m respectively and the high and low Reynolds numbers are on the scale of 1 x 10^7 and 1 x 10^6 respectively. The Reynolds numbers were calculated using the suction inlet diameter.

It is of particular interest to note that even when Reynolds number were the same, an increase in the suction inlet diameter has an effect on the vortex threshold. It would seem that the laws of dynamic scaling do not apply in this instance. It is also interesting to note that Glenny [30] suspected similar phenomenon. In his paper, he suggests that for a fixed H/Di and a fixed upstream flow, a larger diameter would increase the probability of a vortex forming, i.e. shift the threshold to a lower Vi/Vo as observed in these results. He attributed the phenomenon to a larger absolute velocity difference across width of the suction inlet. This could well be the case seen in these simulations. A possible explanation for this could lie with the inappropriate use of the distance between the suction tube longitudinal axis and the floor. Perhaps the distance between the lower lip of the tube and the floor is more appropriate.

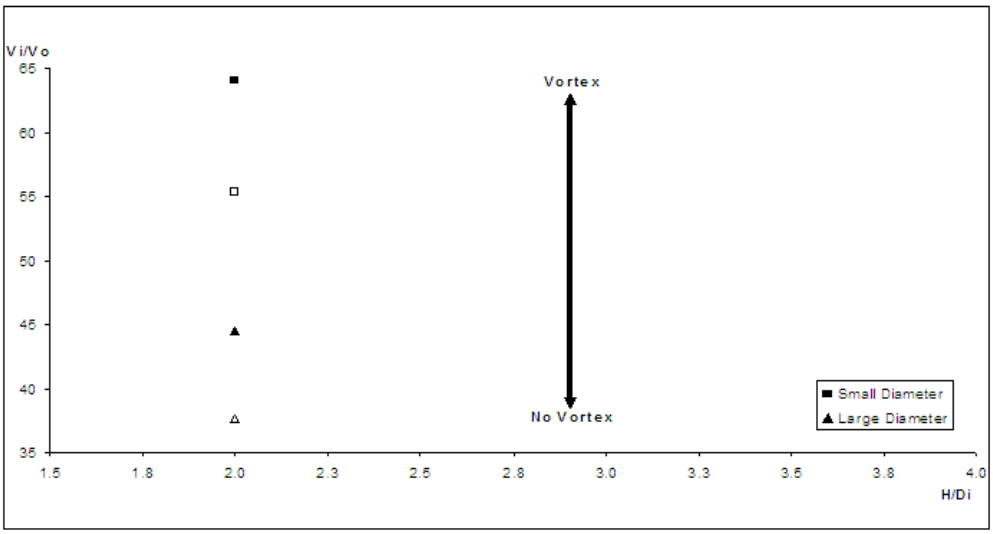

Figure 22: Effects of Reynolds Number and Suction Inlet Diameter on Vortex Formation

Finally it was found that the presence and height of boundary layer does in fact have an effect on the vortex formation threshold. Figure 23 shows the results of this investigation. The results show that as the boundary layer thickens, it becomes easier for a vortex to form. This is probably due to the use of the ambient velocity to calculate Vi/Vo. In the presence of a pronounced boundary layer on the ground, the velocity close to the ground would be lower than the ambient velocity (typically measured some distance off the ground) resulting in the lowering of the threshold. However this does not indicate that the use of ambient velocity to calculate Vi/Vo is inappropriate.

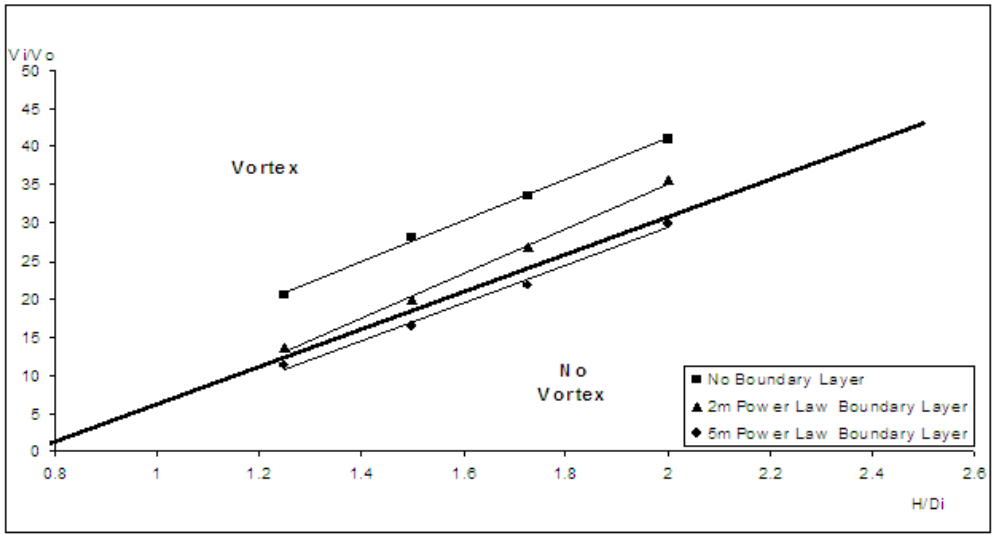

Figure 23: H/Di versus Vi/Vo plot showing the effects of a ground boundary layer (thick black line is the best fit line for previous experimental data)

The simulations do not show a clear vortex if the velocity gradient is less than 0.001/s (Rossby number of the order of 10^5). This is the minimum shear required to trigger a single vortex. At lesser shear values, two very small, counter-rotating vortices, not always of the same size, are observed. This is in agreement with the description of the alternate vortex formation mechanism, which does not require the presence of ambient vorticity by De Siervi [1]

Lastly, the steady or unsteady nature of the vortices is investigated and the results are shown in Figure 24 below. The results shown are for a time-converged unsteady calculation.

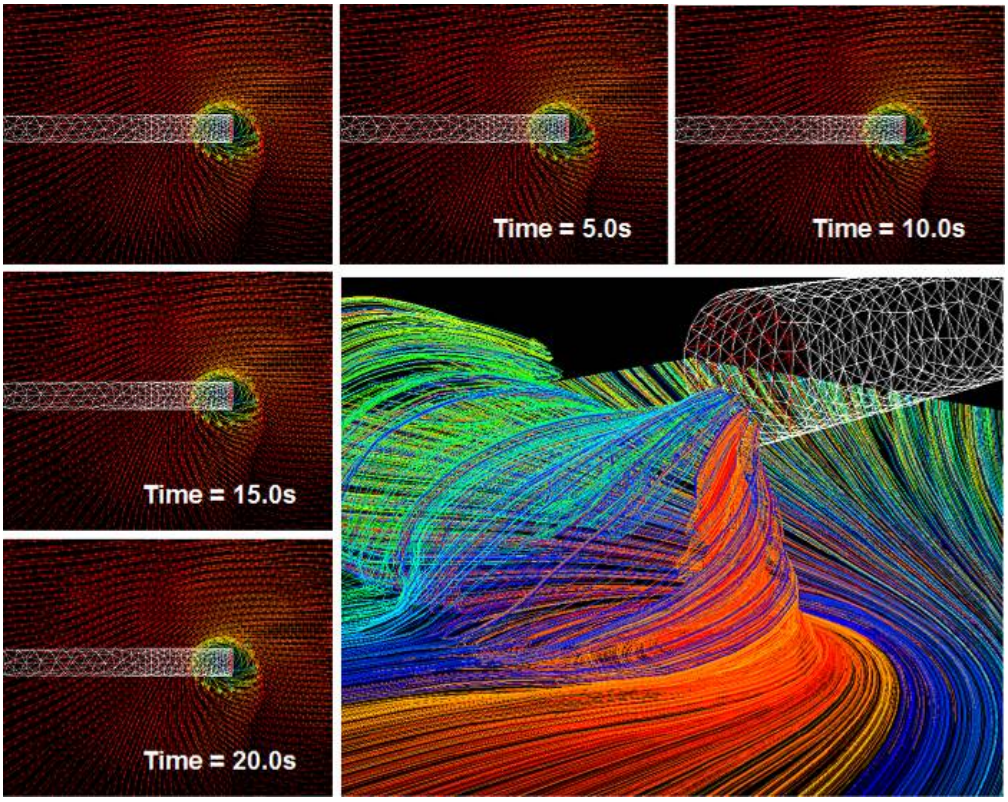

Figure 24: Velocity vector plot on the ground showing the steady nature of the vortex. The vectors are those in the first layer of cells above the ground, which are 0.1m thick (H/Di = 2.0, W = 0.4/s, Vi/Vo ≈ 38.0). The colours in the path-line plot indicate the point of origin

The unsteady simulations were solved with a velocity gradient of 0.4/s, H/Di= 2.0, and time-step = 0.5s. The vortex formation threshold at these conditions occurs between Vi/Vo = 37.8 and 38.5. The results show that the vortex is steady in nature with no movement of the vortex core, nor does the vortex disappear and reappear.

4.4.1 Explanation for the Disparity of Results

The results obtained from CFD simulations of this investigation (Figure 21), shows a higher threshold compared to the best-fit line of previous experimental data. There are a few potential reasons to account for this.

First, the velocity gradients used in the previous experiments are difficult to determine quantitatively. With the exception of Ridder and Samuelsson [31], all experiments generated vorticity by means of a yaw angle for the source of flow (fan or wind tunnel) and the suction inlet. Although it may be possible to calculate a theoretical velocity

gradient, the instantaneous velocity gradient may be difficult to maintain throughout the experiment. Glenny [30] noted that surrounding conditions had a high impact on the vortex, and it can be assumed that these surrounding conditions may have altered the instantaneous velocity gradients but were not detected. A velocity gradient calculation was performed using data from Glenny [30] and it showed a velocity gradient of at least 3 to 6 times higher than the one used for the simulations (See Appendix A for details). In the calculation, a correction to the velocity gradient reported by Glenny was performed essentially taking only the component in line with the longitudinal axis of the engine. It's been suggested [59] that crossflow velocity gradient may also contribute to the generation of vortices thus making the corrections unnecessary.

An additional couple of simulations were run using 1.2 /s as velocity gradient (a more reasonable estimate of the velocity gradient in Glenny's [30] experiment) and showed better agreement with the best-fit line and falls within the experimental scatter. This is shown in Figure 25 below. The 'x' denotes the new simulation results and the red lines being the simulation results presented earlier. The legend is omitted to prevent cluttering of the graph but it is an exact reproduction of Figure 21 for the simulation results and Figure 6 for the experimental results). If the correction to the velocity gradient (Appendix A) is not made, better agreement can be expected between the simulation and experimental data.

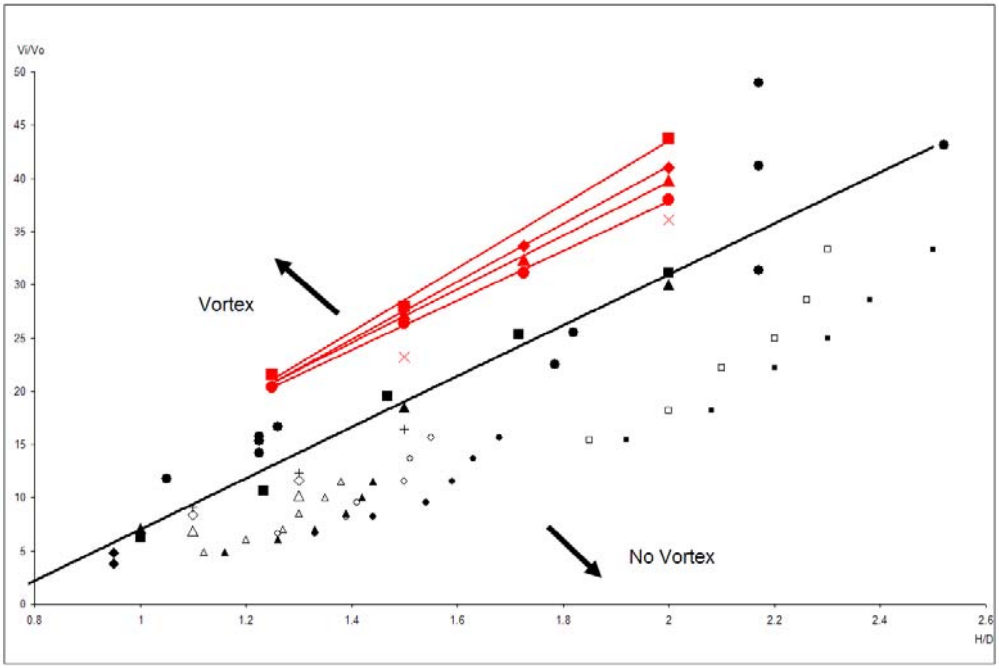

Figure 25: Data showing higher velocity gradient calculations (the points in red are simulation results)

Second, Nakayama and Jones [29] suggested that the threshold should be higher than that seen in the previous experiments. Their proposed threshold (dotted line) is reproduced together with the simulation results in Figure 26.

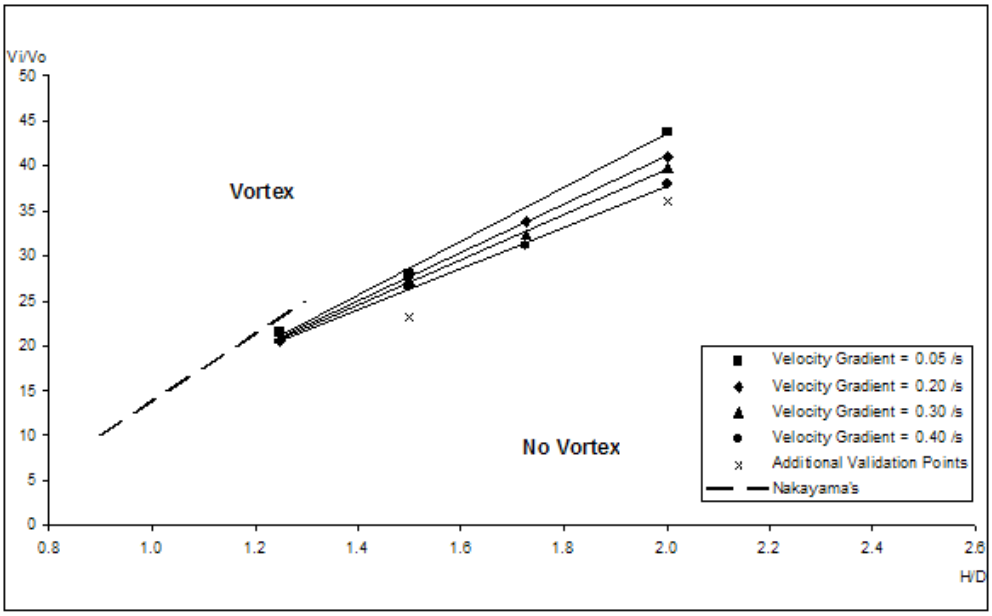

Figure 26: Simulation results compared to the higher threshold proposed by Nakayama and Jones [29]

Although their findings are not conclusive in terms of the results gathered (only two points), their proposed threshold is close to the simulated results.

Thirdly, the detection methods used in the experiments used pressure measurements or something similar to determine the threshold (Glenny [30] used the lifting of glass beads) used. The simulations used the appearance of a vortex in the velocity vectors near the floor to determine the threshold. A small region exists slightly below this threshold where pathlines from the floor flows away from the ground (hence has the similar pressure profile consisting of a local low pressure point) but no vortex was visible from the velocity vectors. Figure 27 and Figure 28 shows the velocity vector plots on the ground and a horizontal plane cutting through the centre of the suction inlet of this condition respectively. If the same detection method was used, the threshold could be shifted downwards to some extent.

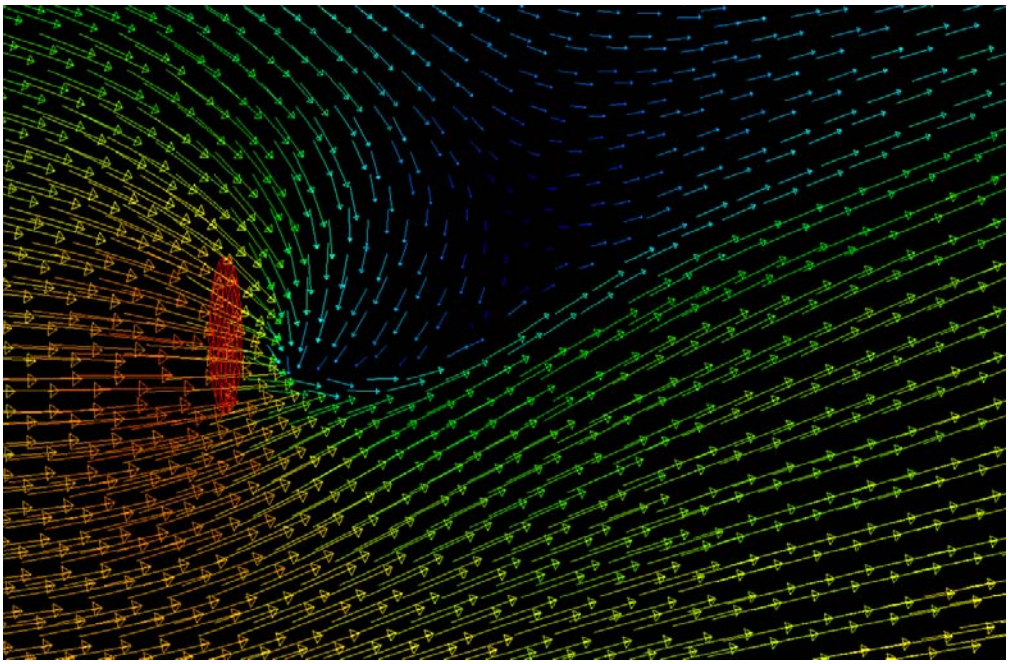

Figure 27: Ground velocity vectors when no vortex is detected

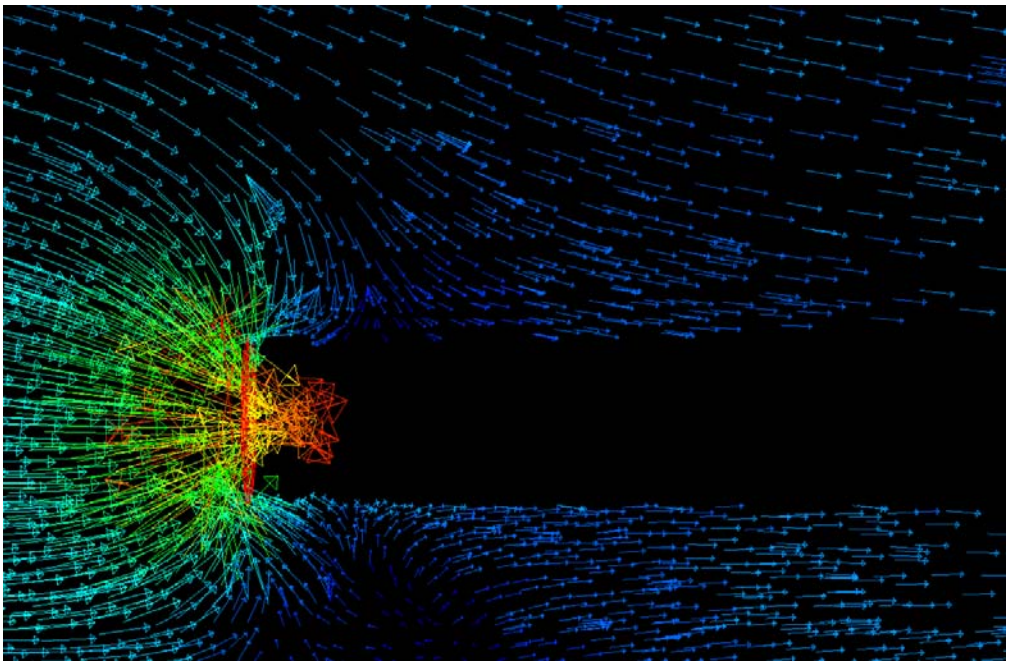

Figure 28: Velocity vectors showing stagnation point when no vortex is detected

It should be noted that the gradient of the threshold between the CFD simulations and the previous experimental data are very similar.

Finally, certain amount of numerical dissipation must be present even in the most well constructed mesh and discretisation scheme. This could lead to the destruction of incipient vortices that are near to the threshold.

5 Vortex Ingestion in a Test Cell

This chapter presents results from vortex forming investigations similar to those in chapter 1 but in a test cell environment.

The first two sections detail the methodologies that apply to results presented in this and the preceding three chapters.

Interesting results concerning the flow regimes and flow phenomenon as a result of the constraining nature of a test cell as compared to the open environment of the runway are discussed in the last two sections of this chapter.

5.1 Introduction and Literature Study

Similar to the engine-over-runway scenario, a vortex can form when an engine is operating in the test cell. As the engine is almost always positioned right in the middle of the cell, there are two horizontal and two vertical solid surfaces equidistant from the engine core, as opposed to one in the engine-over-runway scenario. In a U-shaped test cell, the vortex is usually attached to the ceiling of the cell.

Whether or not a vortex forms depends on the mass flow rate (although it is more commonly associated with the thrust) of the engine, the diameter of the engine inlet, the distance from the walls, and the cell inlet vorticity. A vortex will form in the test cell if there is sufficient distortion in the cell inlet velocity profile and if the velocity between the engine and the walls are below the blow-away velocity.

To date no investigation into the parameters affecting the threshold of vortex formation in an enclosed environment such as a test cell has been performed. Hence, the investigation presented in this thesis extends the knowledge of vortex formation.

In a test cell, there is a flow of excess air beyond that required by the engine, driven by entrainment by the exhaust plume. This flow passes between the engine and the internal walls of the cell. It is quantified by the cell bypass ratio (CBR):

$$\mathrm{CBR} = 100\%\left(\frac{\dot{m}_{\mathrm{cell}} - \dot{m}_{\mathrm{engine}}}{\dot{m}_{\mathrm{engine}}}\right) \quad \textbf{(5)}$$

The CBR is distinct from the engine bypass ratio, which is the ratio of the fan to core flow rate of the engine.

The cell bypass ratio can be seen as the equivalent of the blow-away velocity parameter in the runway scenarios. Thus in a test cell, no vortices will form when the CBR_{actual} rises above a certain $CBR_{blow\text{-}away}$.

A common rule of thumb used in test cell design is that a cell must have a bypass ratio of more than 80% to avoid vortex formation. Typically, cells are designed with CBRs up to 100%, and in some cases exceeding 200%.

As mentioned in Chapter 1.2, this research is only concerned with vortex formation mechanisms, which concentrate ambient vorticity leading to single cored vortices forming in inlets in a headwind. It does not consider vortex mechanisms that do not require nonzero ambient vorticity.

It is expected that the mechanisms leading to the formation and ingestion of vortices in the test cell to be very similar to runway scenario. Hence, most of the parameters that are important in the runway scenario such as Vi, Di and W are important and are used in similar fashion in this investigation. However, the parameter H is now the distance between the engine core and the walls as opposed to the distance between the engine core and the ground.

It is also expected that a threshold value or line exists for the distance between the engine core and the cell walls, and the H/Di versus Vi/Vo plot can be used to illustrate the conditions necessary for vortex formation in the test cell.

The three conditions that Kline [58] stated for the formation of a vortex: nonzero ambient vorticity, a stagnation point on the solid surface, and an updraught from just above the stagnation point to the inlet are also expected to apply.

5.2 Investigation Methodology

Similar to the engine-over-runway scenario, investigations were performed using the commercial CFD software package Fluent from ANSYS Inc. Throughout the investigation periods, new and updated versions of Fluent were made available and were used. The investigation used Fluent 6.2.16 as well as Fluent 6.3.26. The models were meshed using the commercial meshing tool Gambit. Similar to the Fluent case, more than one version of Gambit (2.1.22, 2.2.30 and 2.3.16) was used.

Although most of the simulations and all the results published and presented in this thesis were carried out using 3D simulations, a small number of 2D simulations were carried out at the initial stages of each parameter investigation. Mesh convergence tests were carried out at critical stages of the investigations to ensure that the solution is mesh convergent.

The simulations were carried out using the incompressible flow solver. The incompressible flow solver was selected because of the reduced complexity and ease of solution convergence. A test was conducted to determine that the incompressible flow solver is adequate for the task at hand. Details of this compressible vs. incompressible solver test will be presented in the later sections.

The turbulence model used for the simulations is the SST-Kω model. The SST-Kω model was selected because it combined the best features of the K-ε scheme in free flows and the standard K-ω scheme in near wall flows, yet avoided the computational expense of the Reynolds Stress Models (RSM). The flow was anticipated to be similar in nature to the one seen in the engine-over-runway model and thus the same turbulence model was predicted to be appropriate.

The discretisation scheme used was the first order discretisation scheme. It was selected over the other schemes to avoid the computational expenses associated with the other schemes. Similar to the argument for the turbulence model, the flow was predicted to be similar in nature to the one seen in the engine-over-runway model and thus the same discretisation scheme was predicted to be appropriate.

5.2.1 Geometry, Mesh and Boundary Conditions

The models used have all the important generic features of an engine being mounted in a test cell. Details that are specific to particular engines or test cell are left out intentionally to exclude any engine or cell specific parameters that may affect the generation and ingestion of vortices. These engine or cell specific parameters, although important to the understanding of the problem, may obscure the effects of parameters that are present in all scenarios. At an immature stage of understanding, such as that when the investigation started, the effects of these universal features were considered much more important.

The engine was simulated with a simple suction inlet of negligible thickness and the structures surrounding the engine are simulated with plain no-slip walls. The engine-in-testcell model is shown in Figure 29. A low velocity region has been implemented in the cell inlet to account for the turning of the air from the vertical intake stack to the horizontal main cell area through the turning vanes. This low velocity region is hypothesized to be the reason for the occurrence of only one vortex (usually attached the ceiling in a test cell). See section 5.5 for more details.

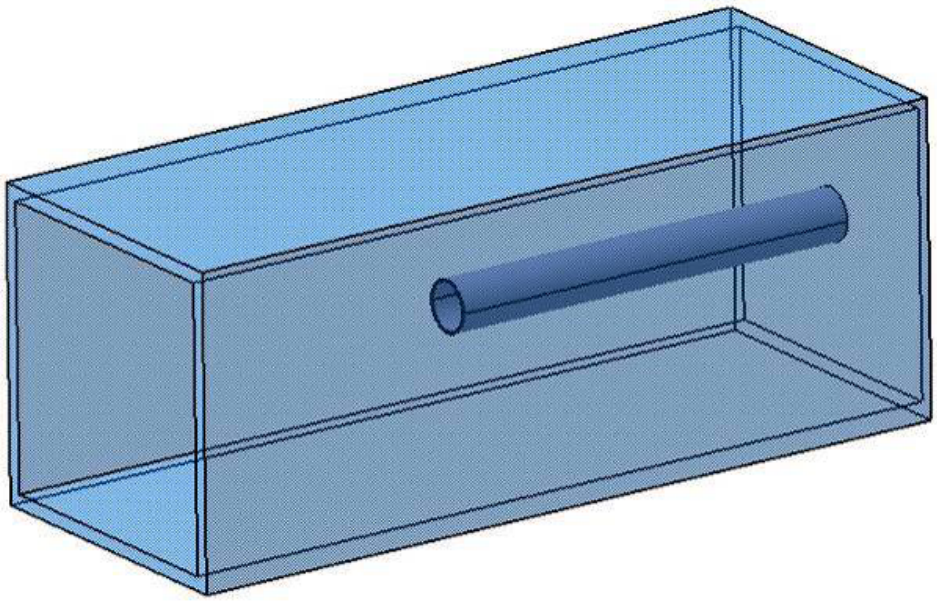

Figure 29: Engine-In-Testcell Model

The suction inlet had a diameter range of between 0.75 to 1.75m and shall be termed Di for reference purposes. The cell inlet plane and the plane downstream of the inlet

were placed at a distance of 5 x Di in the appropriate direction away from the suction inlet. The walls were placed equidistant from the suction tube as it is in JETCs.

The cell inlet is simulated using velocity inlet boundary condition. To effectively and quickly simulate specific CBRs, the engine suction inlet and plane downstream of the inlet is simulated using the outflow boundary condition. The outflow boundary condition is a pre-set boundary condition available in Fluent that governs the percentage of flow through all the outflow boundaries. If there are two or more outflow boundaries, the solver will determine the amount of total flow that exits from each of them based on the parameter "Flow Rate Weighting". The outflow boundary condition was not used for the runway simulations because it was impossible to determine the amount of flow exiting the flow domain through the freestream boundaries.

As mentioned earlier, the model was meshed using the commercial meshing tool Gambit. Tetrahedral/hybrid meshes were used throughout the flow regions and a diagram showing a typical mesh is shown in Figure 30.

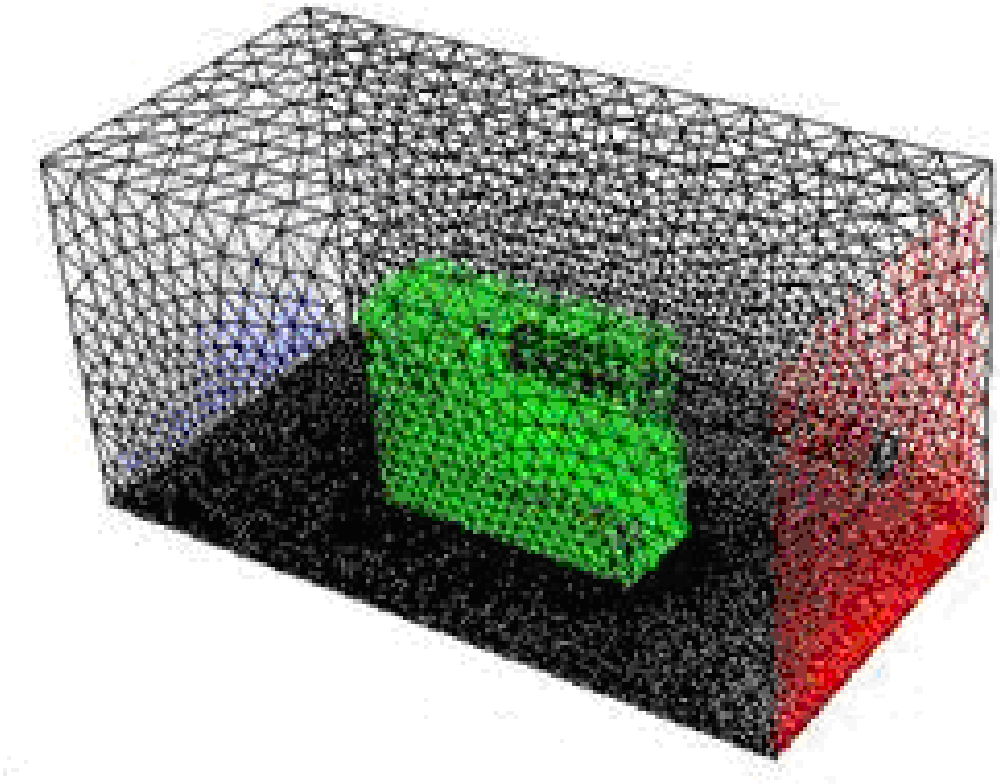

Figure 30: Typical Mesh for Engine-In-Testcell Model

The central region has a tighter mesh compared to the rest of the cell, as this was where the vortex was predicted to form. The eventual mesh of the model has between 100 000 to 200 000 cells. Similar to the Engine-On-Runway model, the appropriate Y+ value of less than 300 was maintained.

Similar to the test performed on the Engine-On-Runway model detailed in the previous chapter, a mesh convergence test was conducted before the eventual mesh was decided.

5.2.2 Compressible vs. Incompressible Solver

For the engine-over-runway scenario, only flow very close to the engine inlet had Mach number above 0.3 and hence did not require a more computationally expensive compressible solver to be utilised.

For the engine-in-testcell scenario, a compressible flow regime was predicted to have been necessary to characterise the entire flow phenomenon in all parts of the test cell but presented a problem in terms of the setting up of boundary conditions. The compressible solver made it extremely difficult (probably requiring a few iterative converged solution to be produced before the boundary condition is set correctly per solution case) to set up a linear velocity gradient at the cell inlet because velocity inlet boundary condition is not allowed in Fluent for compressible flow. Hence, a study was conducted to investigate the difference in solution output between both solvers and determine if a simpler incompressible solution was adequate. A compressible flow solution was first obtained using pressure inlet as the cell inlet boundary condition and the resultant velocity profile at the cell inlet was extracted and used as the velocity inlet boundary condition for the cell inlet in the incompressible flow solution. The results show that the position of a vortex, if produced, is very similar. With the same inlet velocity profiles and cell bypass ratios, the results show the same phenomenon (vortex or no vortex). However, a comparison of vortex threshold was not conducted because of the difficulty in controlling the resultant inlet velocity gradient in a compressible solution and the inlet velocity gradient is an important factor in determining the vortex threshold. Hence, it would be extremely difficult and

tedious to obtain enough cases with the same velocity gradient to locate the vortex formation threshold when a compressible solver is employed.

The test showed that if we can set up a compressible flow solution with a linear velocity gradient, the results would be comparable to an incompressible solution in terms of position of vortex (if formed) and the formation phenomenon although there is a slight shift in the location of the vortex (about half a vortex core diameter). What is not definite but very probable is that the threshold of vortex formation being at the same Vi/Vo value. Pressure contour plots demonstrating the location of the vortex are shown in Figure 31 below. In addition to the vortex position, these plots also show that the pressure profile of the vortex core to be similar.

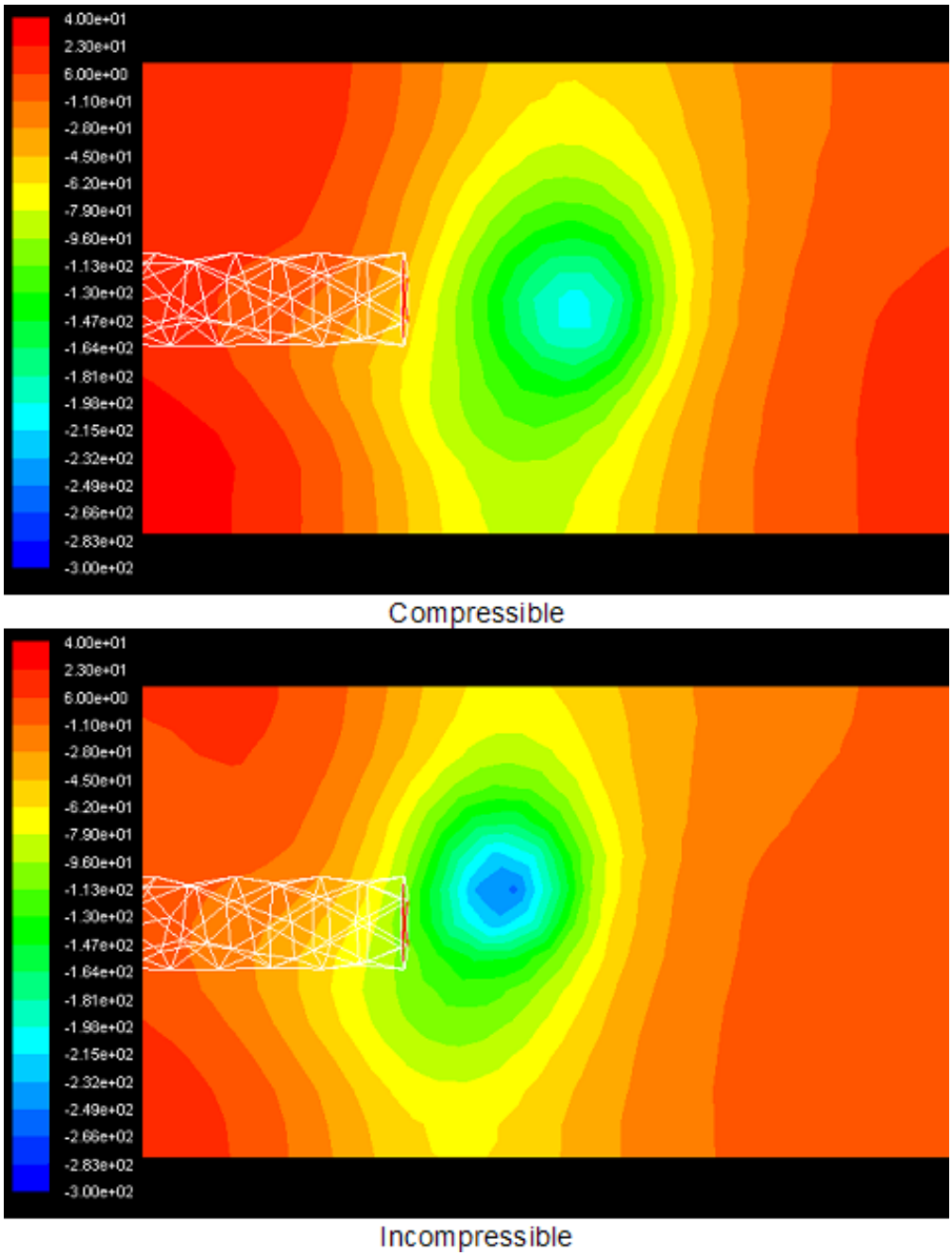

Figure 31: Pressure contours from Compressible vs. Incompressible Flow Solutions (Location of Vortex)

In the compressible calculations, the regions where the mach numbers exceed 0.1 (although the common rule of thumb for the use of compressible solvers is when the Mach number exceeds 0.3) were confined to a small region around the suction inlet. It provided good reasons to use the incompressible flow solver. This result is shown in Figure 32 below.

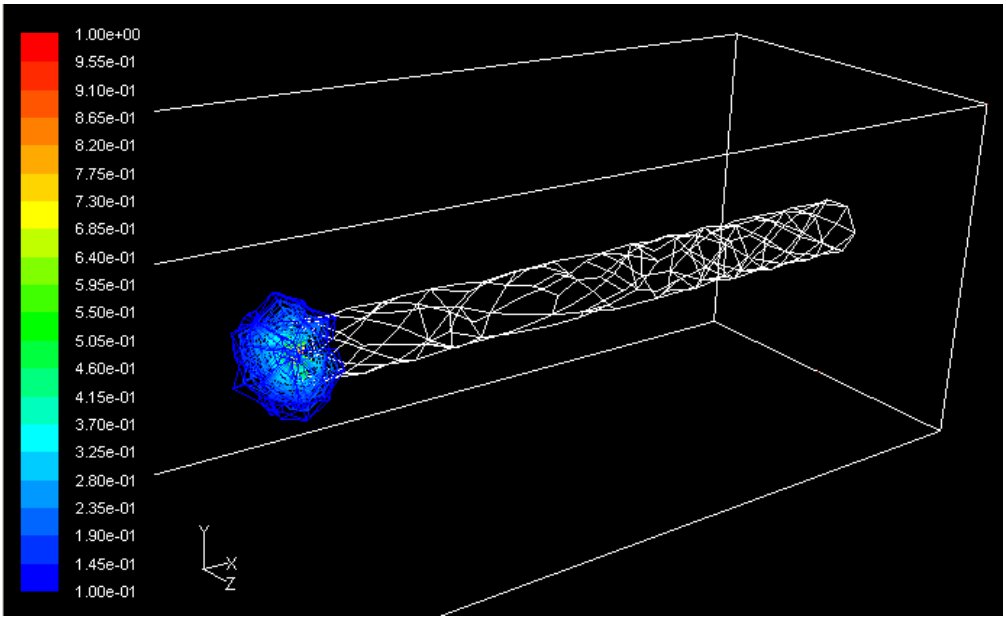

Figure 32: Contour plot of Mach number showing the regions where compressibility effects may be important in the test cell vortex simulations

5.3 Parameters Investigated

The engine-in-cell scenario shares many features with the engine-over-runway scenario thus the parameters investigated in this scenario are similar to those investigated in the engine-over-runway scenario.

As in the engine-over-runway scenario, the effects of upstream velocity gradient, suction inlet diameter and flow Reynolds Number were investigated with their description being identical with the exception of upstream velocity gradient where the reference is situated at the cell inlet plane.

Similar to the engine-over-runway scenario, the increase/decrease in suction inlet diameter occurs at a fixed H/Di ratio. This represents a scaling up of the entire cell instead of just increasing the size of the engine. This parameter is important as it provides an indication of the requirements for new test cells as engine sizes keep increasing.

The steady/unsteady nature of vortex in test cells was also investigated.

An interesting observation of actual vortices formed in test cells during operation suggests the presence of some flow phenomenon, which causes the vortex to almost always attach to the ceiling. It is interesting because the engine is usually placed equidistant from both horizontal solid surfaces (ceiling and ground) and thus the vortex should not show preference to be attached to either surface.

It is hypothesized that a low velocity region is present near the ceiling resulting in the preferential attachment of the vortex. It is certainly very reasonable for a low velocity region to be present near the ceiling of the main engine chamber in a U-shaped test cell where there is flow detachment as the flow is turned 90 degrees through the turning vanes. This was simulated by Gilmore [60] using a model of an actual test cell, and results show that a thick boundary layer and region of separation forms at the ceiling.

5.4 Flow Regimes

In the engine-over-runway simulations, there are two distinct regimes present namely vortex and no vortex. In addition, the vortex when formed is steady in nature in terms of location and vortex core characteristics. The vortex, when formed, always formed directly below the suction inlet and the size and shape remained the same and was always circular.

However in the engine-in-testcell simulations, a third regime is found to be present. This regime lies between the “circular vortex” and “no vortex” regimes and is characterised by a deformation of the vortex from the “perfect circular” shape and the vortex moving away from its “central, below suction” location. In some cases, this regime is characterised by the unsteadiness of the vortex.

It should be noted that unstable unsteady vortices are observed in real test cells. In this case, the vortex core precesses, and the vortex disappears and reforms with no clear periodicity. These real cell vortices, when formed, are likely to be between the stable vortex and no vortex regimes and very close to the threshold.

For discussion purposes, the three stages of flow regimes in the engine-in-testcell scenario shall be called “steady vortex”, “unsteady vortex” and “no vortex” respectively. These three stages are shown in Figure 33 and Figure 34.

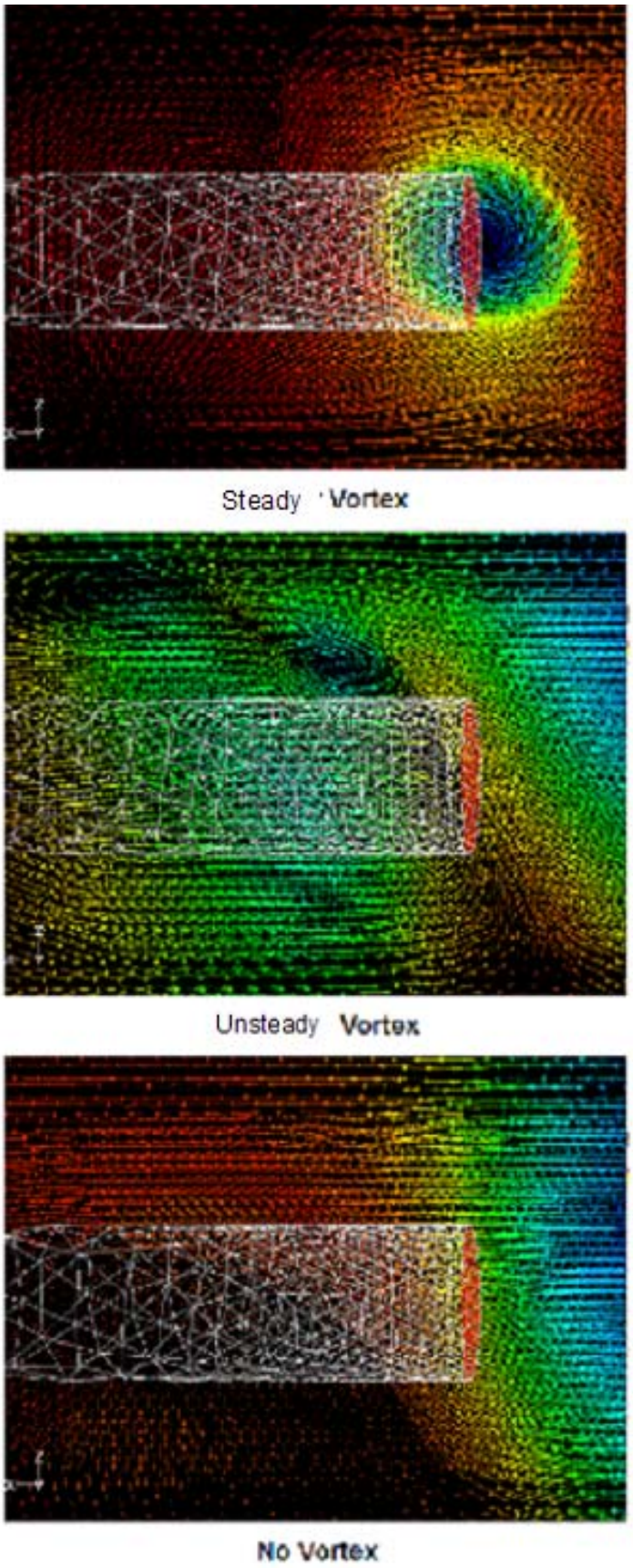

Figure 33: Vector Plots Showing Stages of Vortex

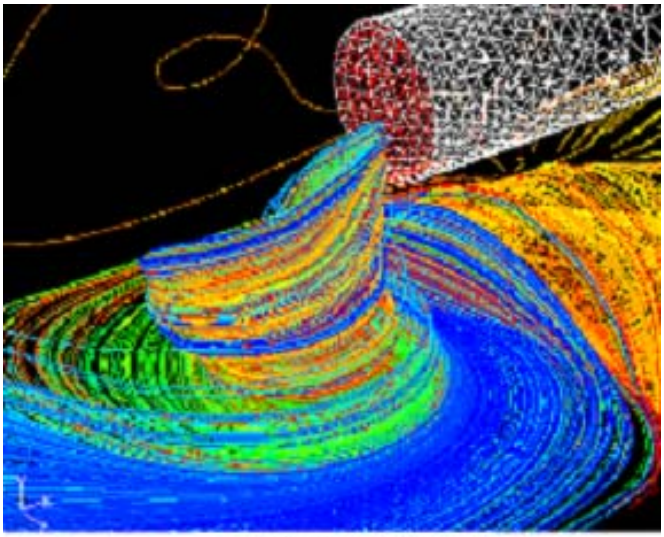

Steady Vortex

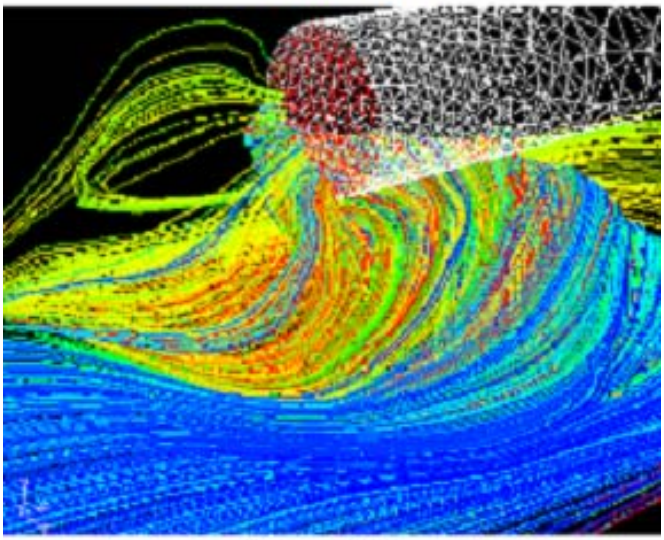

Unsteady Vortex

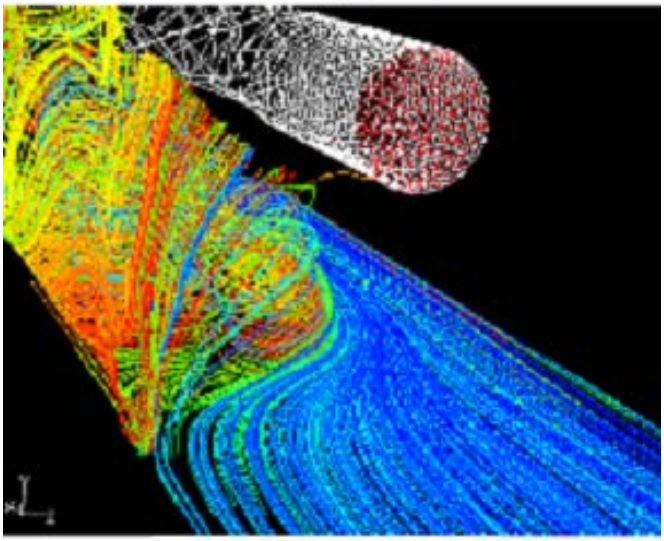

No Vortex

Figure 34: Pathlines Showing Stages of Vortex

The first stage (steady vortex stage) occurs at low cell bypass ratios. The characteristic of the vortex at this stage is very similar to the vortex stage seen in the engine-over-runway. The vortex is circular in shape and occurs directly under the suction inlet. The vortex formed at this stage is easily identifiable in velocity vectors on the ground as well as in pathlines plots.

The vortex formed at this stage is steady and the core does not move around but remains fixed in position, like those seen in the engine-over-runway scenario.

The second stage (unsteady vortex) occurs at higher cell bypass ratios than in the first stage. The vortex formed at this stage is irregular, elongated in shape and the core is located away from the bottom of the suction inlet. This is in contrast to the vortex seen in the first stage.

The third stage (no vortex) occurs at even higher cell bypass ratios. In this stage, none of the pathlines entering the suction inlet has any rotation.

One particular case of the second stage of vortex formation was solved using the unsteady solver with a time-step of 0.5s. In this simulation, the vortex was seen to be unsteady and the core moves around the floor of the cell. This unsteady nature is shown in Figure 35. The plots are generated every 2 seconds and clearly show the unsteady nature of the core.

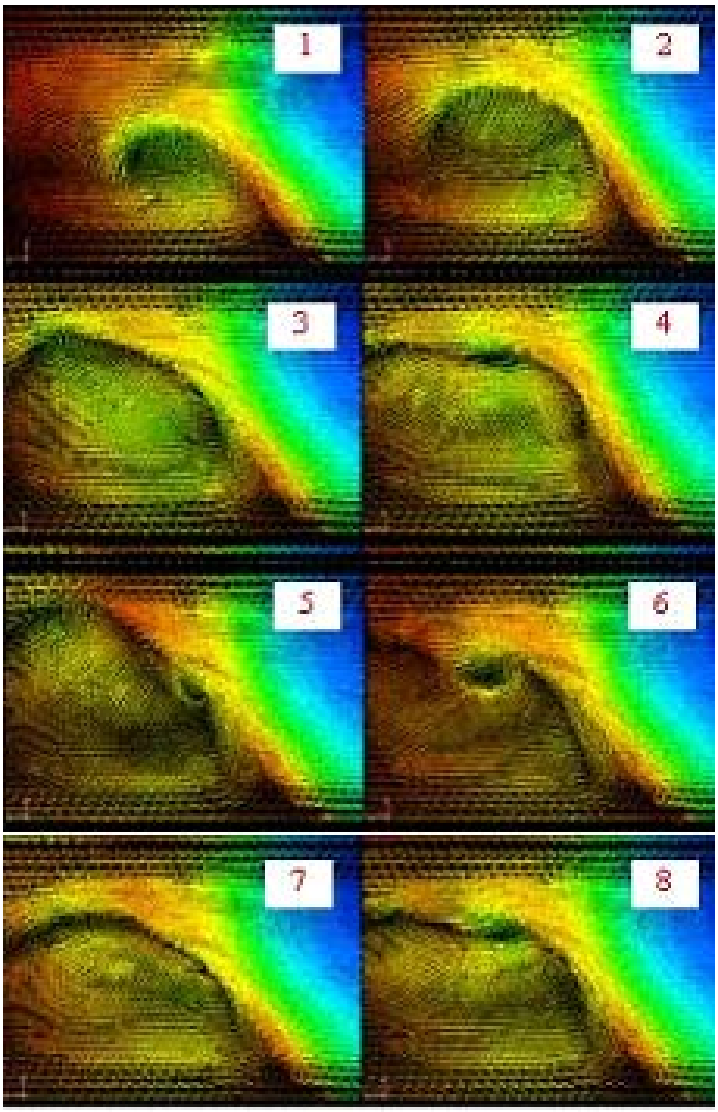

Figure 35: Unsteady Velocity Vector Plot of Unsteady Vortex near the Ground

These calculations were performed using the solver parameters detailed in chapter 5.2.

5.5 Vortex Formation in the Absence of a Low Velocity Region

In the engine-over-runway scenario, there is only one single solid surface near the suction inlet. However in the engine-in-testcell scenario there are two horizontal solid surfaces to which the vortex may be attached to namely the ground and the ceiling. In the absence of other factors, there is no perceivable reason for the vortex to be preferentially attached to either of them.

However in real test cells, only one vortex is present and is usually attached to the ceiling in a U-shaped test cell. In a U-shaped test cell, there is usually a low velocity region near the ceiling of the main test chamber because of flow is turned through 90 degrees from the inlet stack into the main chamber through the turning vanes. In such a flow scenario, a thick boundary layer typically forms from the junction and extends over the ceiling. This low velocity region is hypothesized to be one of the reasons for the preferential attachment of the vortex to the ceiling.

A simulation (W = 0.5) was conducted with no low velocity region resulting in two very similar vortices being formed from both the ceiling and the floor. Without a low velocity region, the inlet plane has a velocity profile which is essentially symmetrical about the horizontal midplane of the cell.

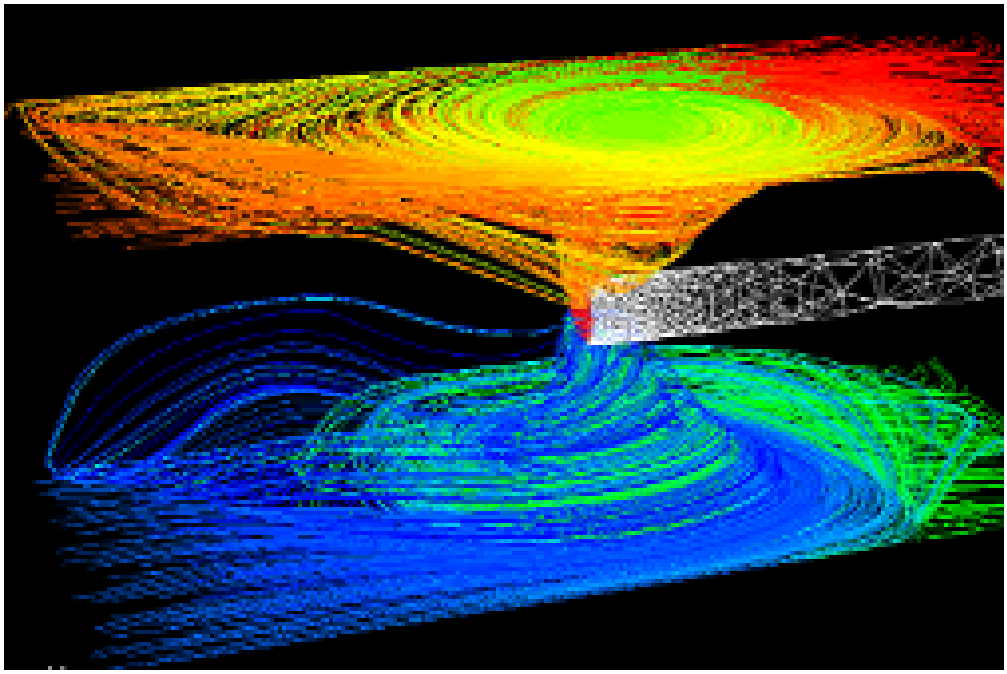

Figure 36: Two Single Core Vortex in the absence of a Low Velocity Region

Figure 36 above shows that in the absence of a low velocity region, two vortices of very similar size and location will be formed and be ingested into the suction inlet. These two vortices originate from both the ceiling as well as ground of the test cell. The colours in Figure 36 are not an indication of the value of any flow parameters but are particle identity in Fluent and are used to distinguish the pathlines.

Figure 37 below shows the pressure contours of the vortex core. They are very similar in size and in terms of the pressure gradients within the core.

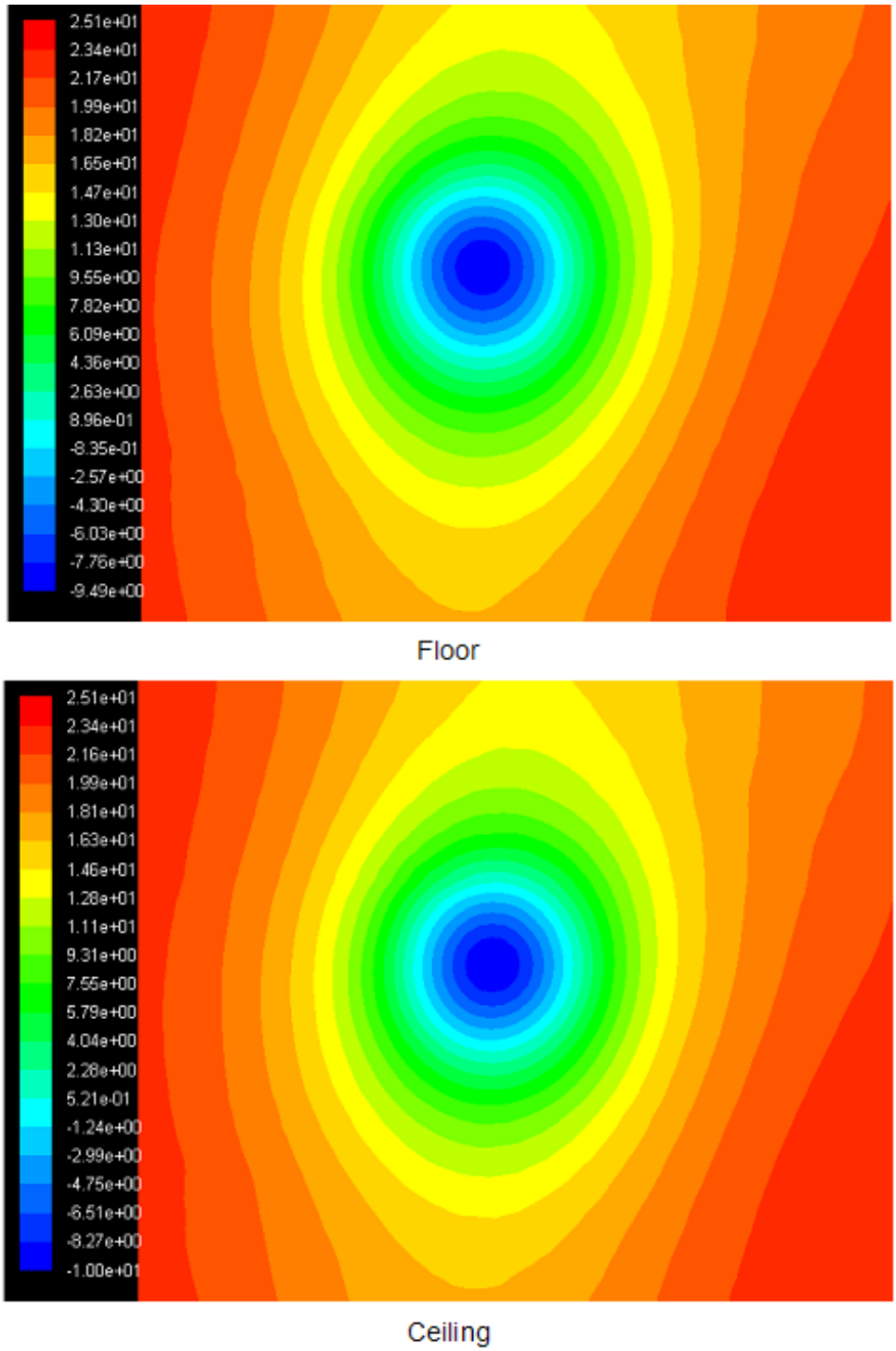

Figure 37: Contour plots showing the pressure distribution comparison within the vortex core on the when two vortices are formed in the absence of a low velocity region at the ceiling of a test cell

In all subsequent simulations that are detailed in chapters 6 - 8, a low velocity region was simulated by modifying the UDF used for the cell inlet plane.

6 Effect of Velocity Gradient

This chapter presents the effect that altering the upstream velocity gradient have on the vortex formation threshold in the test cell. It is a parametric study performed cetaris paribus.

6.1 Introduction

The vortices observed in test cells invariably have only one visible arm. We hypothesize that they are due to the concentration of ambient vorticity. Wind directions around the cell might be a cause of ambient vorticity, Appendix B presents an independent CFD simulation to investigate this. However sometimes vortices have been observed when there is no discernible wind outside.

Velocity gradient has been found to be an important parameter determining if a vortex will form and be ingested into the engine in the engine-over-runway scenario. In the engine-in-testcell scenario, the velocity gradient is taken at the inlet of the main chamber of the test cell. In U-shaped test cell, this is usually the plane at which the distortion index, an important indicator of the quality, is measured.

Velocity gradient is a direct source of vorticity. As the type of vortex concerned in this investigation is the type that concentrates ambient vorticity, velocity gradient is arguably the most important parameter in the investigation.

In the engine-over-runway scenario, it was found that the magnitude of the velocity gradient had a direct relationship with probability of vortex formation i.e. increasing the velocity gradient increases the probability of vortex formation. It is hypothesized that it will have the same effect in the engine-in-testcell scenario.

The velocity gradient is imposed using the “user-defined function” or UDF in Fluent (see Appendix C for a sample of the source code used to impose this velocity gradient). The velocity gradient imposed is a linear gradient with the lower value on the left wall of the cell, looking into the cell.

A low velocity region was generated by a stepped reduction in velocity of 1m/s from the rest of the inlet with the same vertically aligned velocity gradient, 0.5m from the ground for the H/Di value of 4.0. It was scaled proportionally lower at lower H/Di values while keeping the spatial extent of the region constant, i.e. the proportion of low velocity region to normal velocity region remains the same. The ground instead of the ceiling was selected as the surface for the attachment of the vortex because it simplifies the UDF code. This has no perceivable implication on the validity of the simulations as gravitational effects were not used.

6.2 Scope

The velocity gradient used is a constant velocity gradient and no non-linear velocity gradients were investigated.

The velocity gradients solved ranges from 0.2 to 0.5 /s.

The suction inlet diameter solved in this section of the investigation is 1 m and the range of H/Di ranges from 1.5 to 4.0.

6.3 Results

Similar to the analysis performed in the engine-over-runway simulations, formation of a vortex was determined by observation of the velocity vectors in the layer of cells closest to the walls.

In some of the results for the vortex threshold investigations, an accompanying vortex from the wall with the lower velocity was observed. The formation of this vortex is hypothesized to be a result of the vertical velocity gradient. This vertical velocity gradient is an inevitable result of the low velocity region and the use of a simple upstream velocity profile. An example of the velocity profile can be found in Appendix C. The velocity profile used in the engine-in-testcell scenario is essentially the same as the one used in the engine-over-runway scenario but with a low velocity region incorporated near one of the horizontal walls. The low velocity region causes the average velocity above and below a horizontal plane passing through the longitudinal axis of the suction inlet to be different thus resulting in a “vertical

velocity gradient". In the single simulation investigating the effect of the presence / absence of a low velocity gradient (Chapter 5.5) this wall vortex was not seen, confirming that the vortices are of the type which concentrates ambient vorticity.

The longitudinal position of the wall vortex is exactly the same as that of the floor vortex and it seems unlikely that they had an influence on each other.

The model was solved with cell bypass ratio in increasing steps of 5% until the threshold for the three stages were found. This translates into an uncertainty in Vi/Vo of not more than 2.6%.

The vortex formation threshold in terms of CBR is shown below in Figure 38 to Figure 41. It suggests that the threshold in terms of CBR does not show a clear simple relationship. However, algebraic manipulation of a linear relationship between Vi/Vo and H/Di yield a quadratic relationship between 1/(CBR+1) and 1/(H/Di). See Appendix D for details of the algebraic manipulation steps. However, they are still presented to show the level of CBR necessary for the avoidance of a vortex.

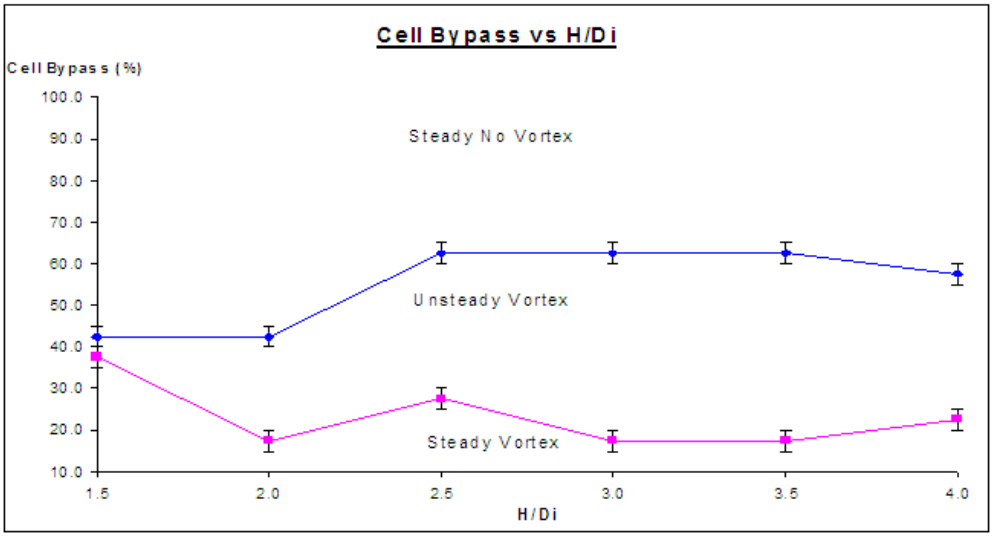

Figure 38: Vortex Formation Threshold for Upstream Velocity Gradient = 0.2 /s in terms of CBR

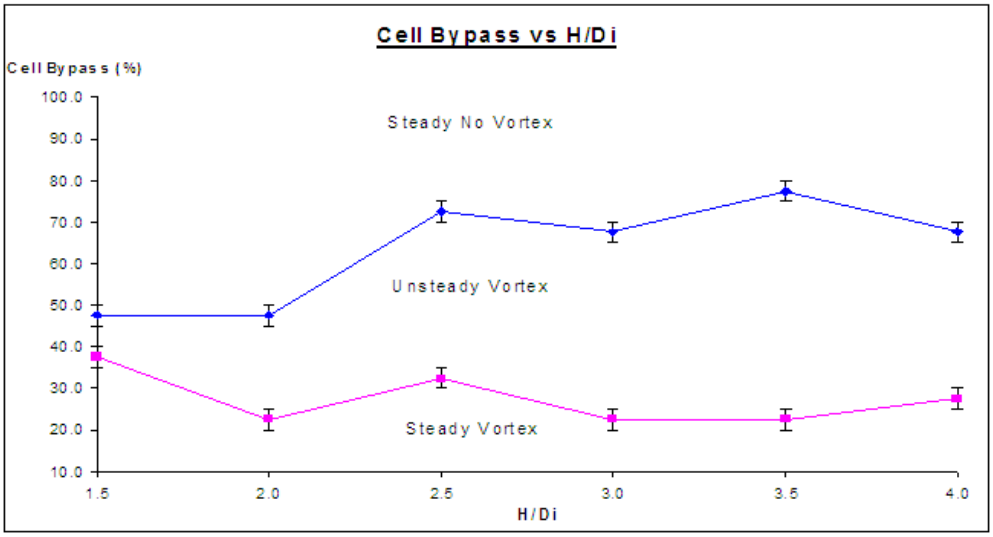

Figure 39: Vortex Formation Threshold for Upstream Velocity Gradient = 0.3 /s in terms of CBR

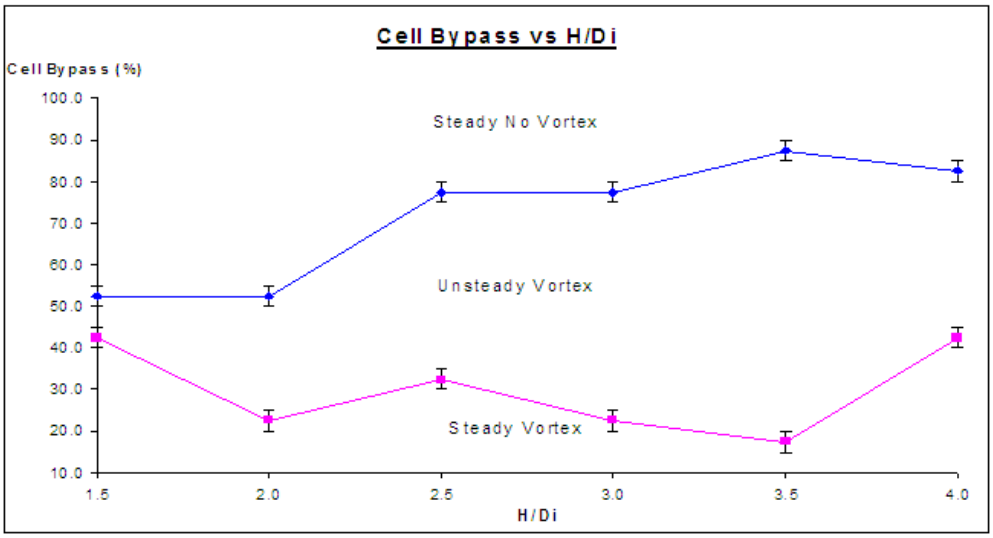

Figure 40: Vortex Formation Threshold for Upstream Velocity Gradient = 0.4 /s in terms of CBR

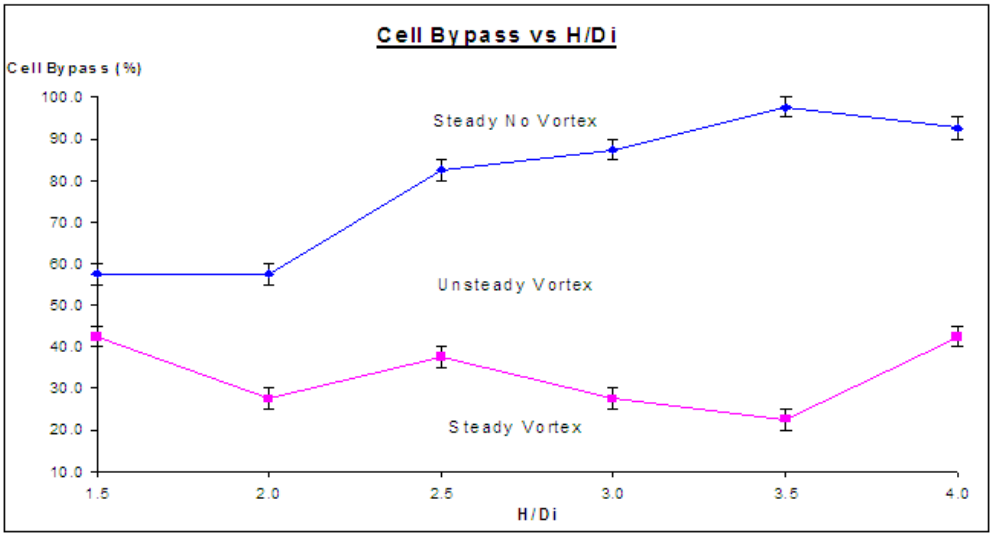

Figure 41: Vortex Formation Threshold for Upstream Velocity Gradient = 0.5 /s in terms of CBR

The same vortex formation threshold in terms of Vi/Vo is shown in Figure 42 to Figure 45 below. These clearly show that for the range of velocity gradient solved, Vi/Vo increases for increasing H/Di for both thresholds.

Figure 46 to Figure 48 combines the threshold into a single plot and clearly shows that upstream velocity gradient has an inverse effect on vortex formation threshold i.e. with an increase in the upstream velocity gradient, the vortex formation threshold moves to a lower Vi/Vo implying an increase in the probability of the vortex being formed and ingested into the engine.

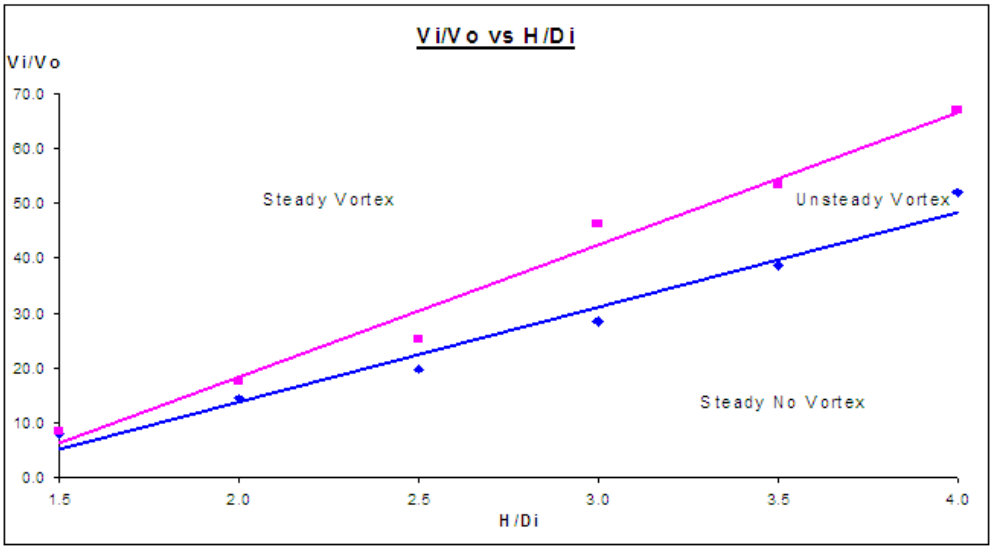

Figure 42: Vortex Formation Threshold for Upstream Velocity Gradient = 0.2 /s in terms of Vi/Vo

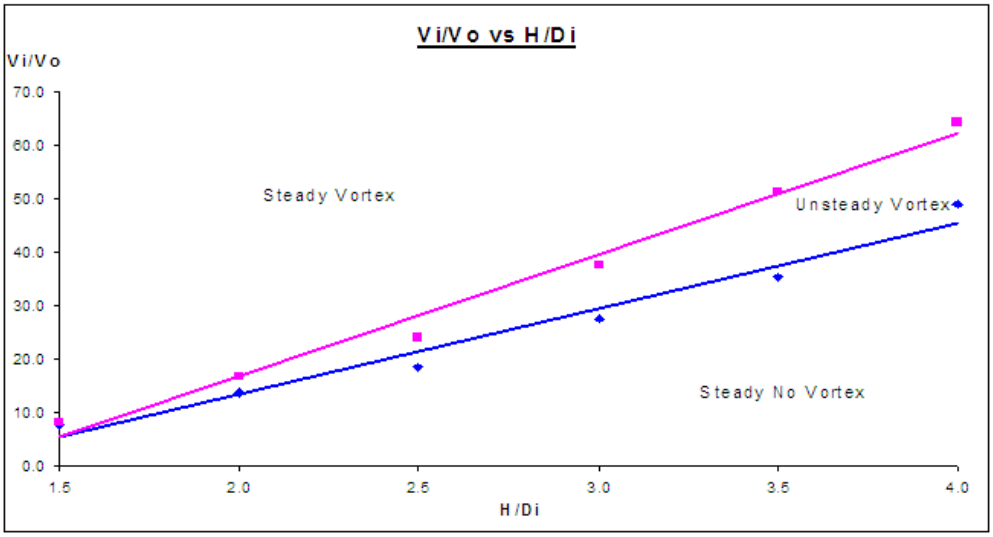

Figure 43: Vortex Formation Threshold for Upstream Velocity Gradient = 0.3 /s in terms of Vi/Vo

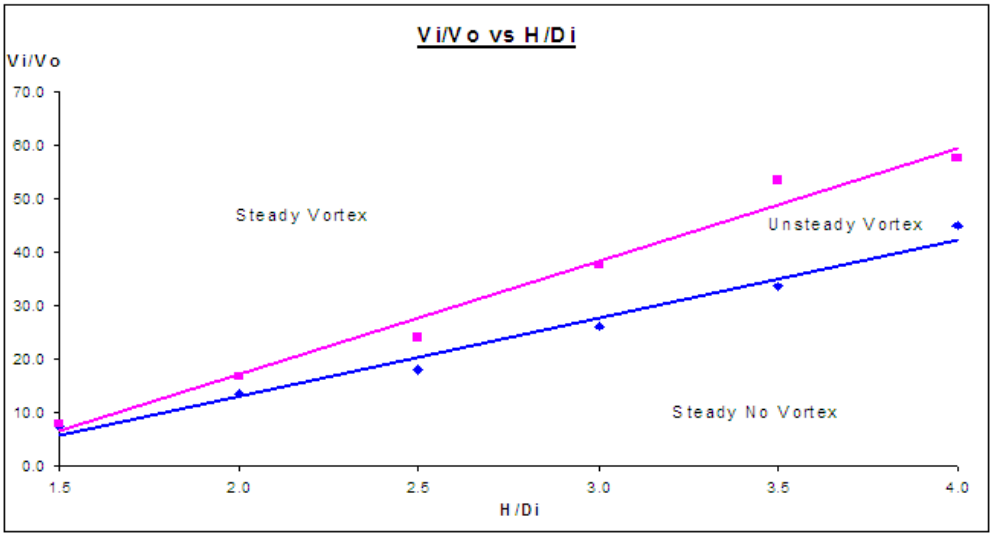

Figure 44: Vortex Formation Threshold for Upstream Velocity Gradient = 0.4 /s in terms of Vi/Vo

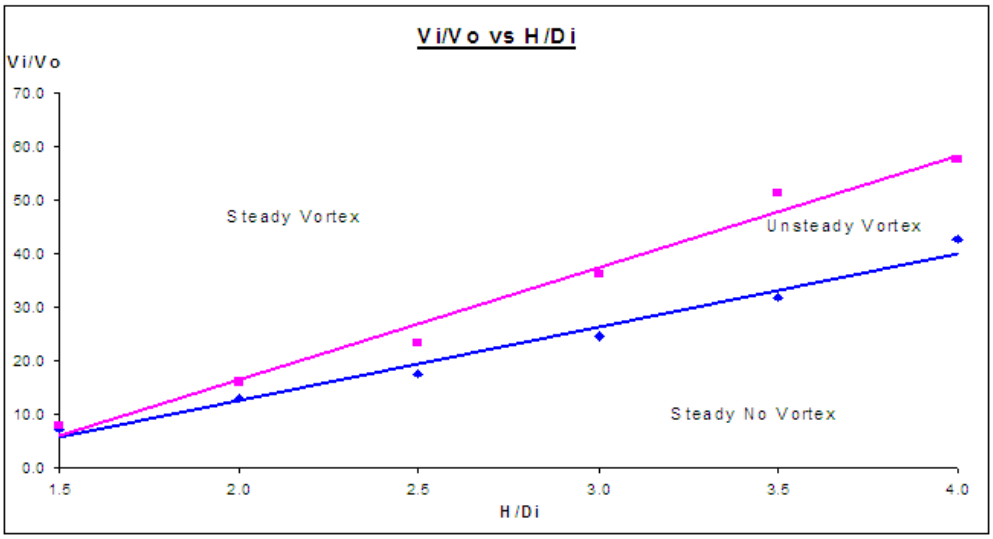

Figure 45: Vortex Formation Threshold for Upstream Velocity Gradient = 0.5 /s in terms of Vi/Vo

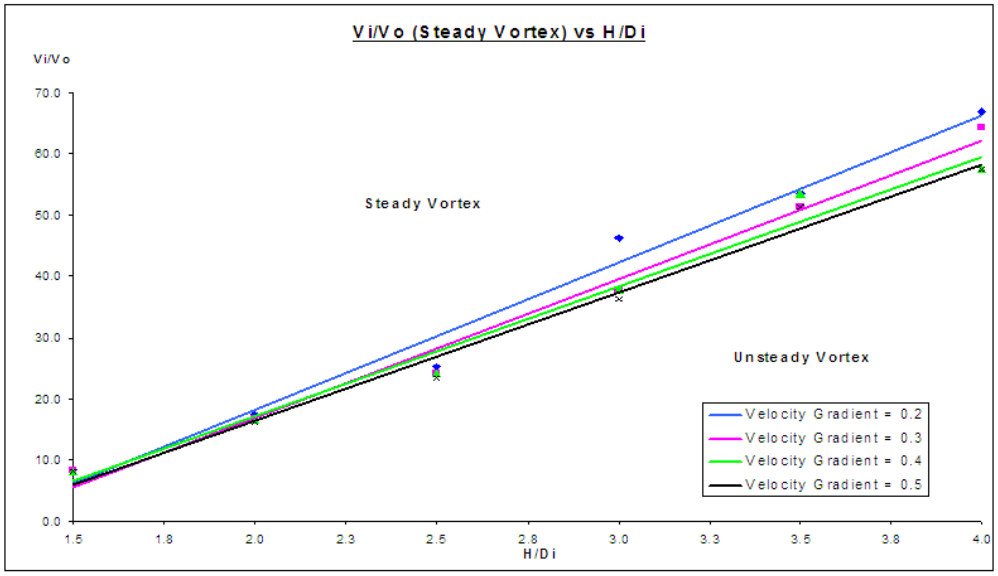

Figure 46: Vortex Formation Threshold between Steady and Unsteady Vortex

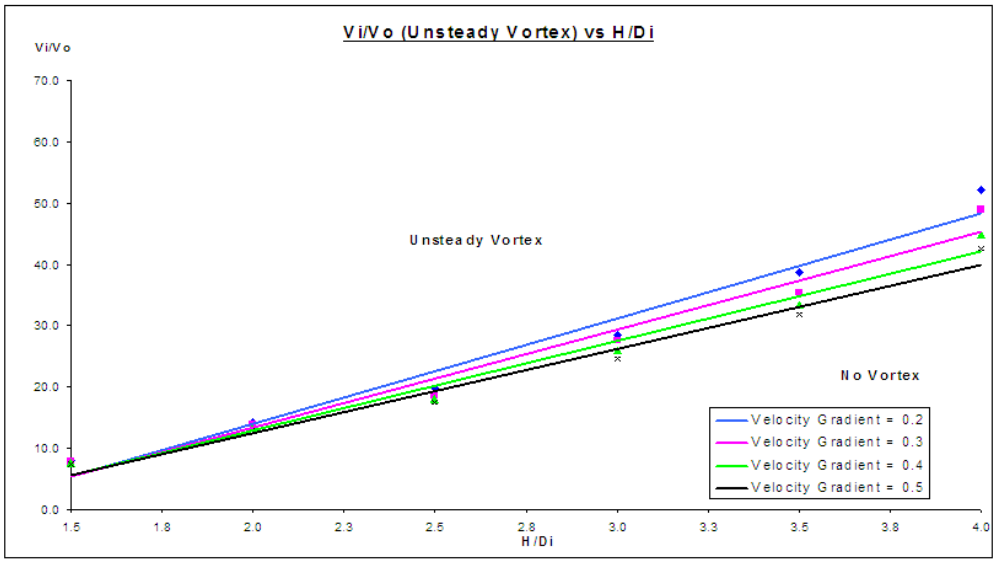

Figure 47: Vortex Formation Threshold between Unsteady and No Vortex

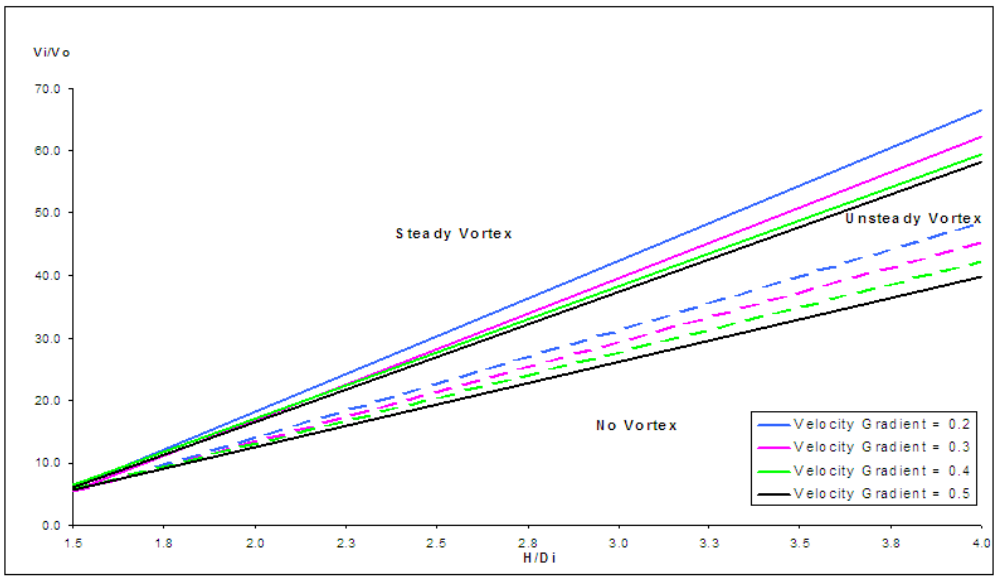

Figure 48: Vortex Formation Threshold (Combined)

Figure 49 combines the results for upstream velocity gradient = 0.2 /s for both engine-over-runway and engine-in-testcell scenarios into a single plot for comparison purposes. It shows clearly that the threshold is significantly lower in the later scenario.

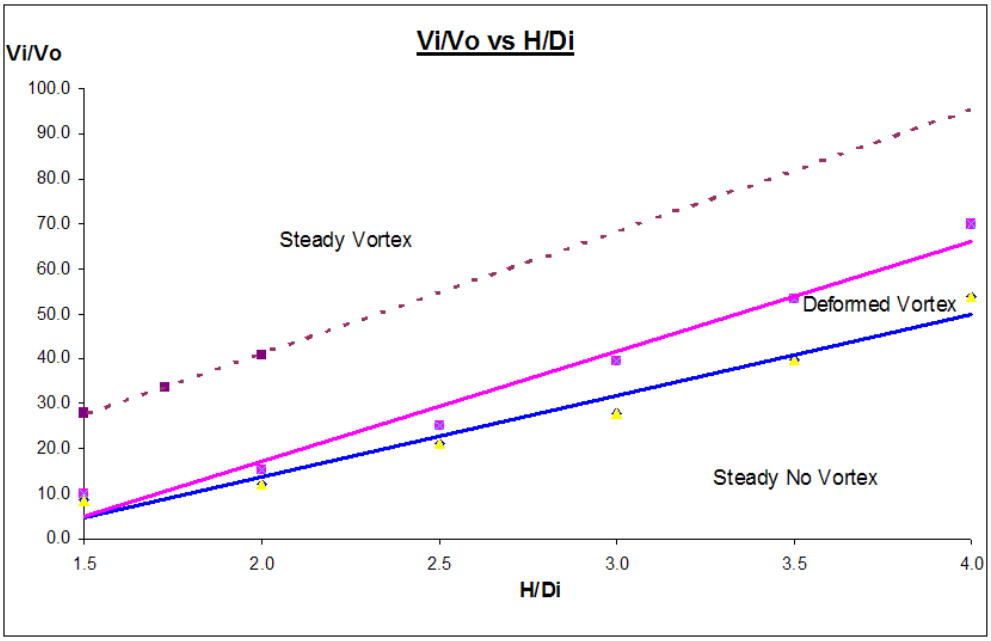

Figure 49: Comparison of Threshold between Engine-Over-Runway and Engine-In-Testcell Scenarios (The broken line is for the Runway data)

6.4 Discussion

The formation of vortices in test cells was not investigated before and the results are presented for the first time.

The results shows that the no vortex condition is guaranteed at a CBR > 90 % and even at an upstream velocity gradient of 0.5 /s. This is an excessively high distortion at the inlet flow and unlikely to occur in a practical test cell. A more realistic distortion is the 0.2 /s case. For this case, a no vortex condition requires a CBR of more than 50 – 70% (the actual value depends on the H/Di ratio). This is in agreement with the industry rule of thumb used in test cell design that a cell bypass ratio of more than 80% must be used to prevent vortex formation.

Below the no vortex region, there is a wide band of CBR at which an unsteady unstable vortex is seen, equivalent to unsteady inconsistent vortices observed in some real test cells. Test cells are designed to operate at a CBR where no vortex is formed, however a rare combination of surrounding conditions sometimes may occur to move the operational point below the threshold between the steady and unsteady vortex.

CBR is a very common term used in the test cell industry to describe the characteristics of a particular cell-engine combination and hence it was used in the results and discussion of this chapter to describe the vortex formation threshold in test cells. However for a generic study such as this one, it is perhaps more appropriate to use a generic term to describe the threshold as the CBR depends purely on the mass flow of the engine. Vi/Vo is an example of such a generic parameter and will be used solely to describe the threshold in the proceeding chapters.

A comparison between the vortex thresholds of the engine-over-runway and the engine-in-testcell scenarios shows that vortices are more likely to form in the latter i.e. the vortex forming region covers a greater range of conditions. This is probably due in some part to the constraining effect of the walls and ceiling, which was also observed during the investigation to determine the optimal ambient space in the engine-over-runway scenario. They are shown in Figure 49 above.

The threshold for vortex formation in the testcell predicted shows the following trends:

1. Vortices form when the CBR is low and are blown away and vanish as the upstream velocity increases above the "blow-away" CBR.
2. On a Vi/Vo against H/Di plot, the threshold for vortex formation shows a positive gradient i.e. as the height of the suction inlet increases, the threshold "blow-away" velocity decreases.
3. As the upstream velocity gradient increases, the range of conditions in which a vortex is formed (steady or unsteady vortex) increases, implying an increase in the probability of the vortex being formed and ingested into the cell.
4. A low velocity region near one of the horizontal surfaces is necessary to create a preference for the vortex to be formed from that surface (usually the ceiling for U-shaped test cell). Otherwise, two vortices will be formed from both surfaces.

Trends 1, 2 and 3 agrees with previous experimental data by various authors such as Nakayama and Jones [29], Liu et al. [54] and Shin et al. [55] and the engine-over-runway results presented in earlier chapters.

Point 4 is a new discovery.

More detailed analysis of the results show that the threshold points do not fit a straight line as well as in the engine-over-runway scenario. This could be due to the inappropriate use of the distance between the suction tube longitudinal axis and the floor, similar to that discussed in Chapter 4.4.

7 Effect of Reynolds Number

This chapter presents the effect that altering Reynolds numbers have on the vortex formation threshold in the test cell. It is a parametric study performed cetaris paribus.

7.1 Introduction

Reynolds number is not a parameter that was investigated intensely in the experimental setups probably because the controlling of the upstream velocity is not a trivial task. In a CFD simulation, it is a significantly easier undertaking.

Although Reynolds number is not properly investigated in any one single experiment, a collation of results from various sources shows that a relationship seems to exist between that and vortex formation threshold. Figure 19 shows such a collection from experiments resembling the engine-over-runway models.

The same relationship between Reynolds number and vortex formation threshold is expected for the engine-in-testcell scenario.

7.2 Scope

The upstream velocity profile used has a constant velocity gradient with the velocity increasing from the left to right wall equal to 0.2 /s, looking into the engine.

The Reynolds number for the simulation increased from 650 000 to 1 300 000.

The suction inlet diameter solved in this section of the investigation ranges from 1 m to 2 m and the range of H/Di from 1.5 to 4.0.

7.3 Results

Similar to all engine-in-testcell simulations, the model was solved with cell bypass ratio in increasing steps of 5% until the threshold for the three stages were found. This translates into an uncertainty in Vi/Vo of not more than 2.6%.

The vortex formation threshold for different Reynolds number (calculated using suction inlet diameter and velocity, similar to that calculated in chapter 4.4 and Table 4) shown in terms of Vi/Vo is shown from Figure 50 to Figure 60. The results for Re = 975 000 and Di = 2m are missing from the results because of a loss of data storage facility during the writing of the thesis.

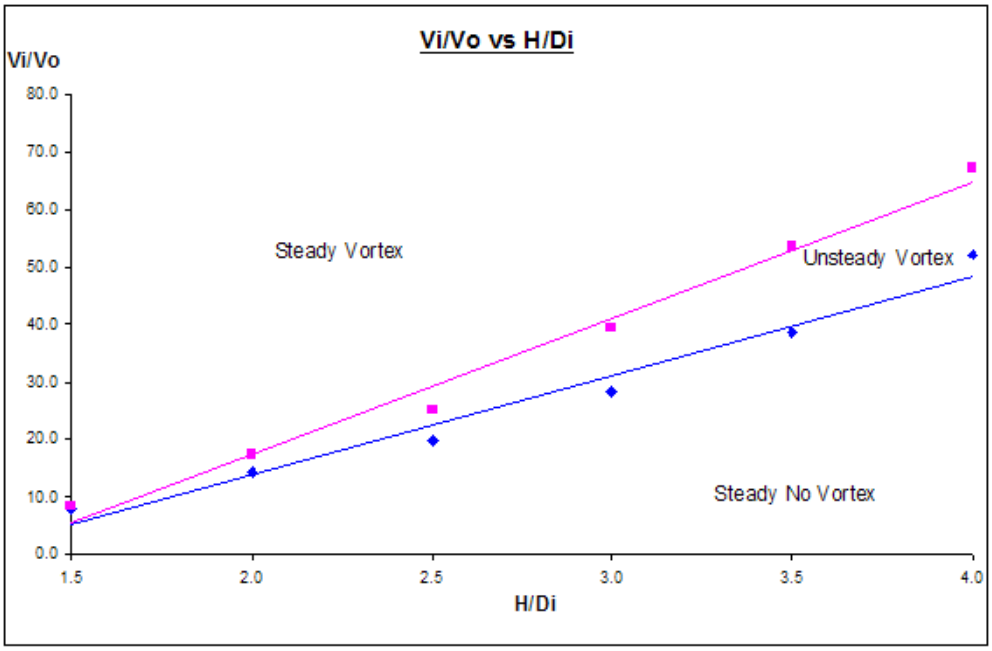

Figure 50: Vortex Formation Threshold for Re = 650 000 and Di = 1 m

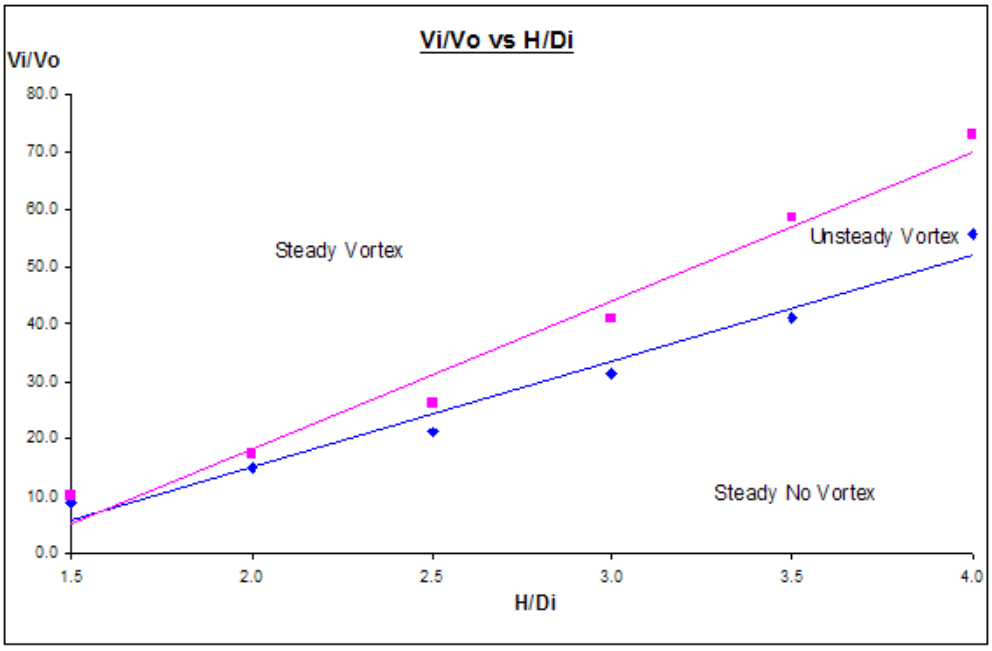

Figure 51: Vortex Formation Threshold for Re = 975 000 and Di = 1 m

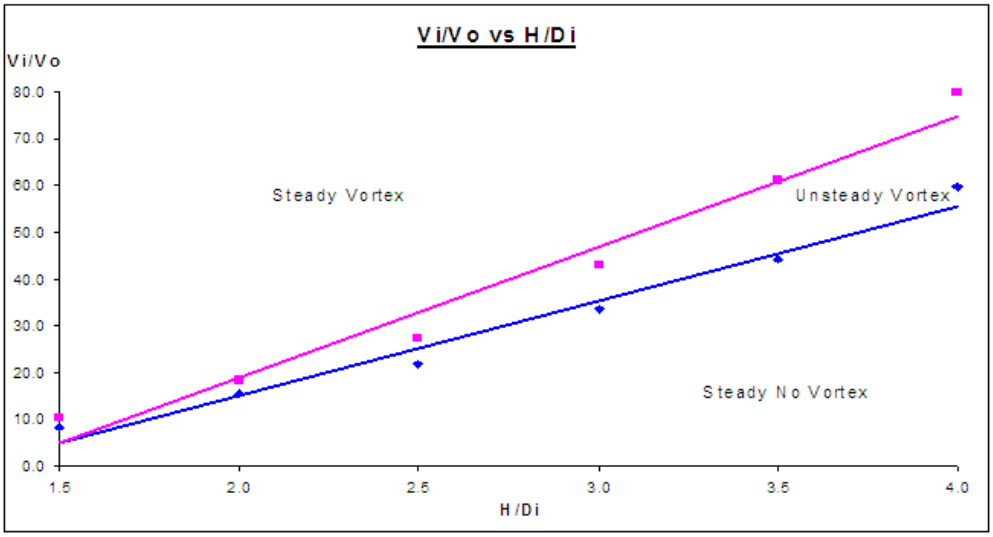

Figure 52: Vortex Formation Threshold for Re = 1 300 000 and Di = 1 m

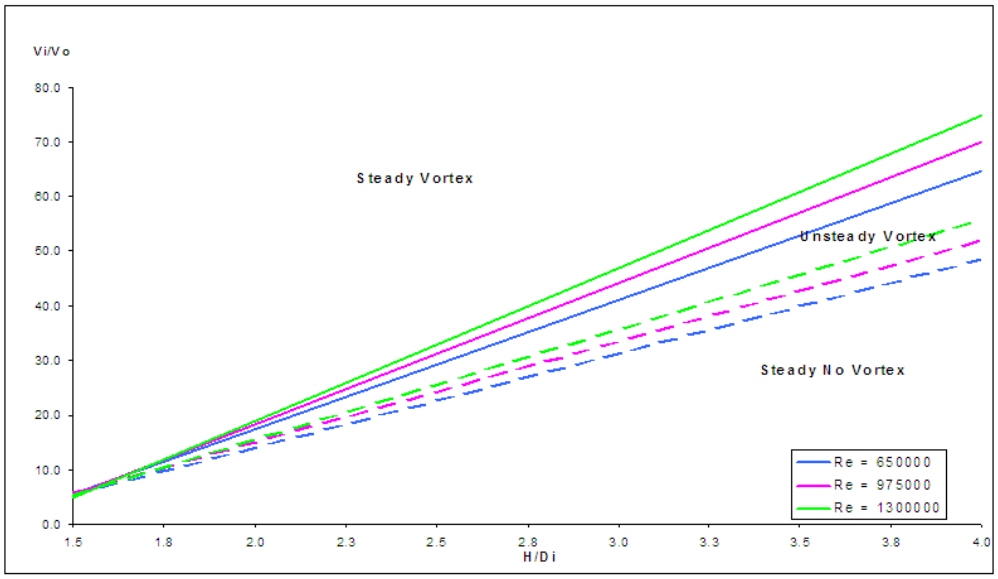

Figure 53: Combined Vortex Formation Threshold in terms of Vi/Vo for Di = 1 m at various Re

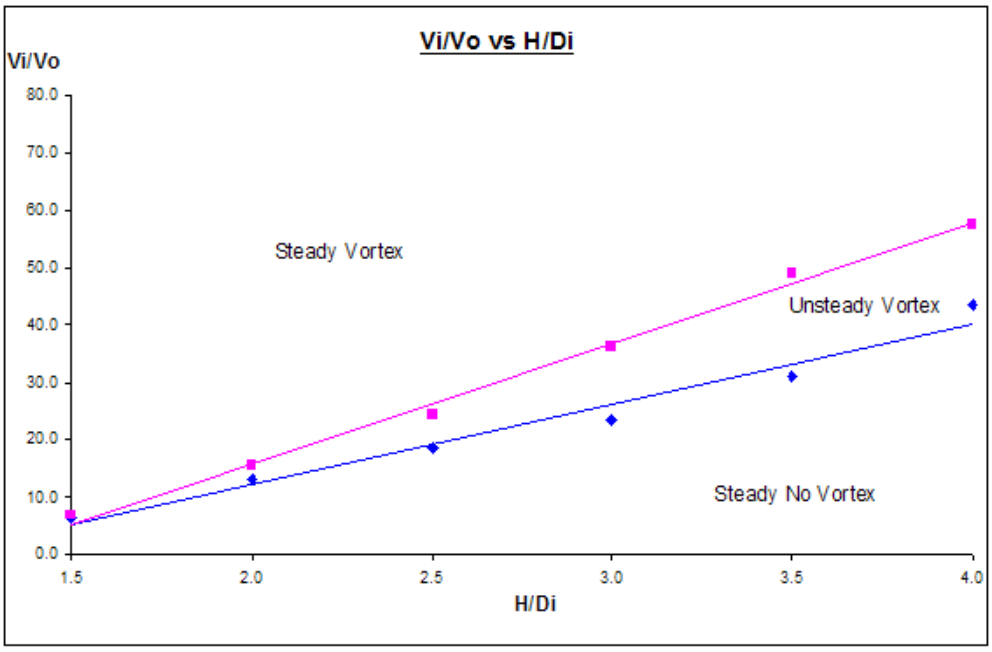

Figure 54: Vortex Formation Threshold for Re = 650 000 and Di = 1.5 m

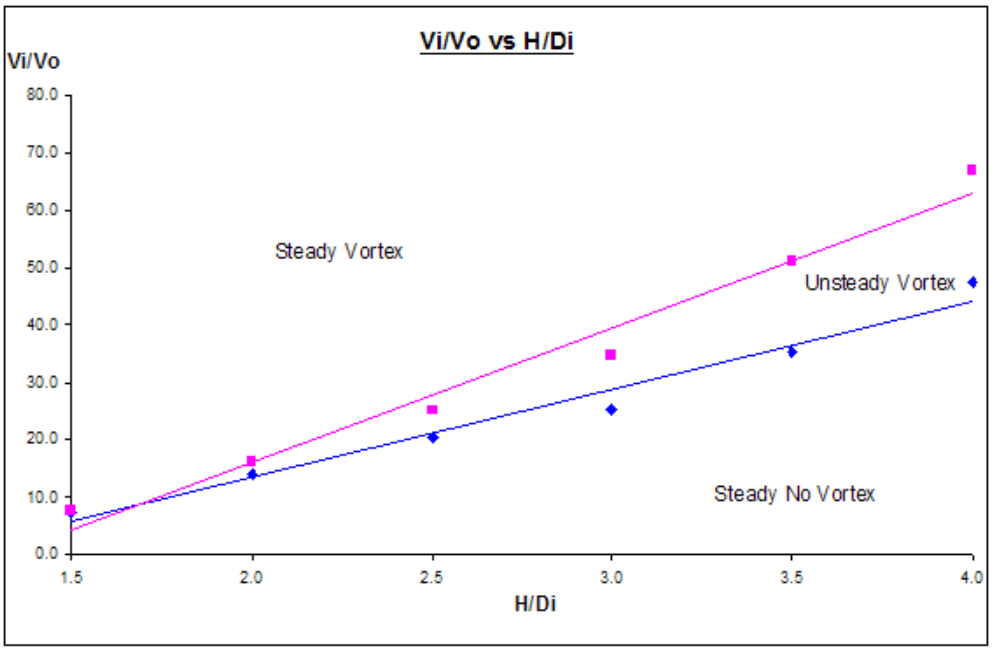

Figure 55: Vortex Formation Threshold for Re = 975 000 and Di = 1.5 m

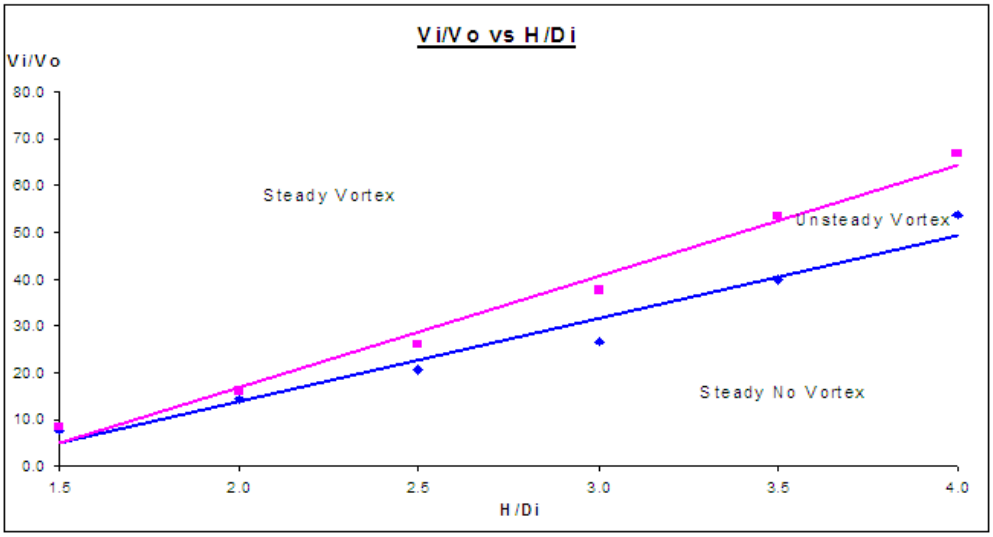

Figure 56: Vortex Formation Threshold for Re = 1 300 000 and Di = 1.5 m

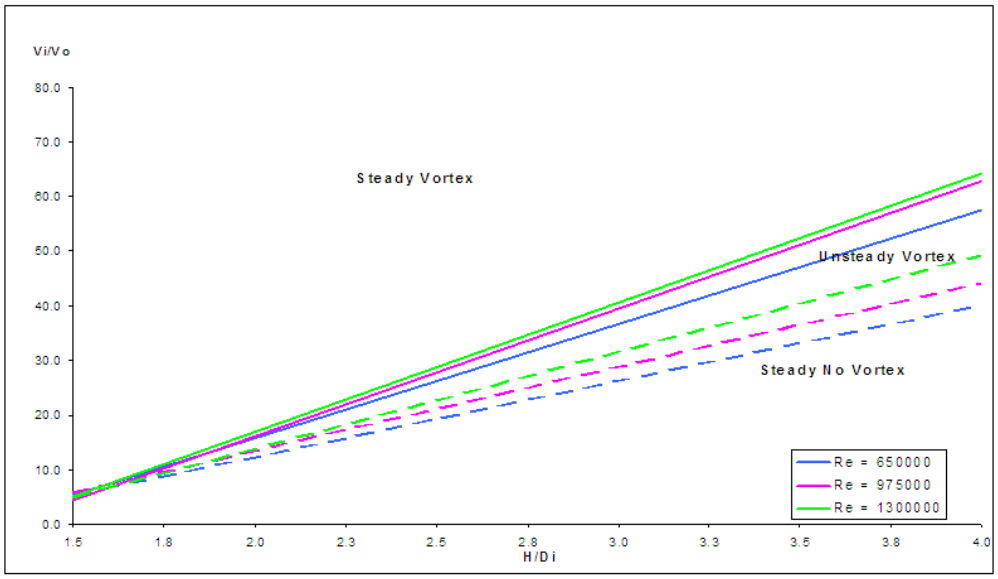

Figure 57: Combined Vortex Formation Threshold in terms of Vi/Vo for Di = 1.5 m at various Re

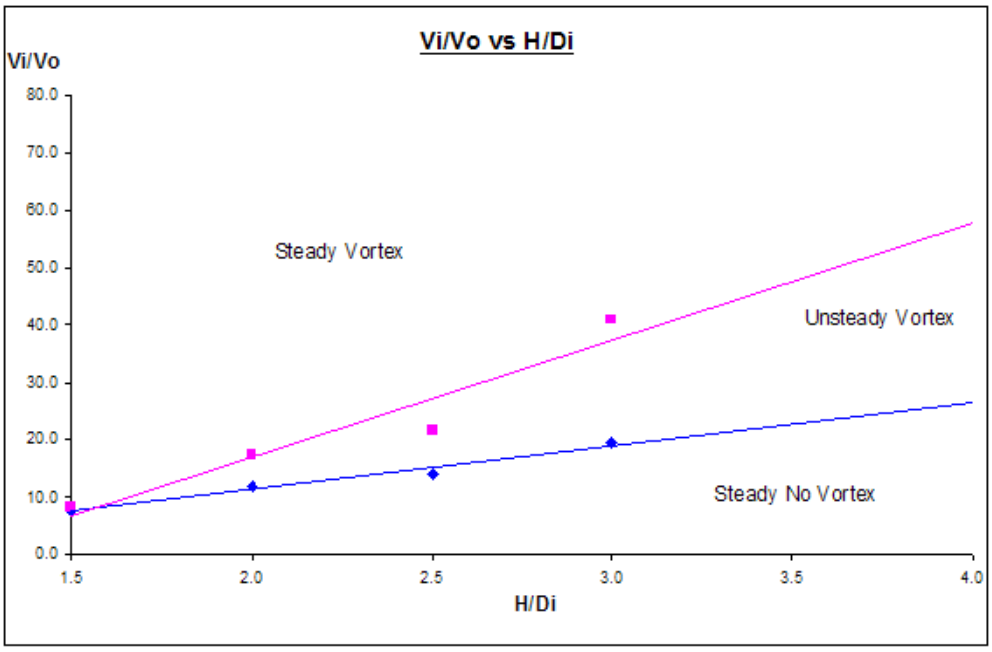

Figure 58: Vortex Formation Threshold for Re = 650 000 and Di = 2 m

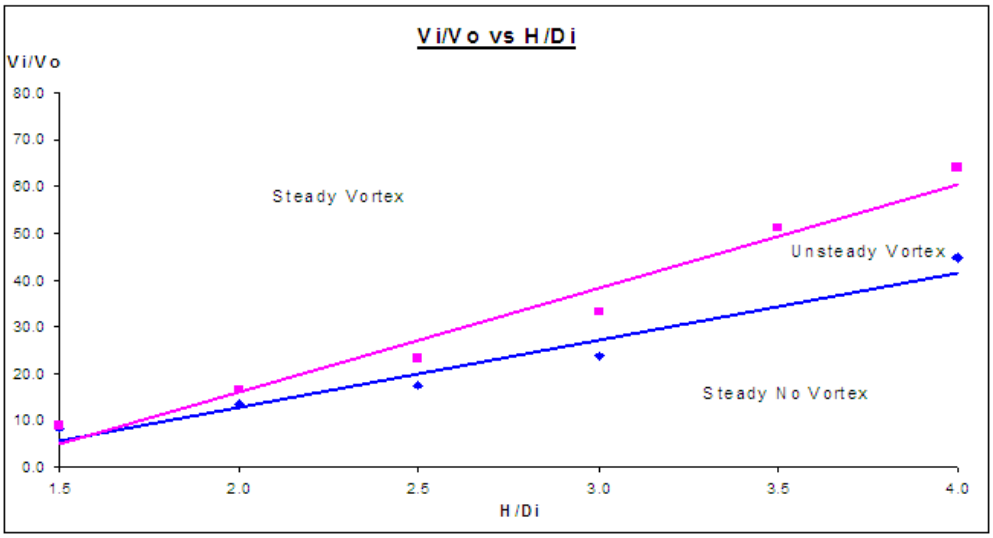

Figure 59: Vortex Formation Threshold for Re = 1 300 000 and Di = 2m

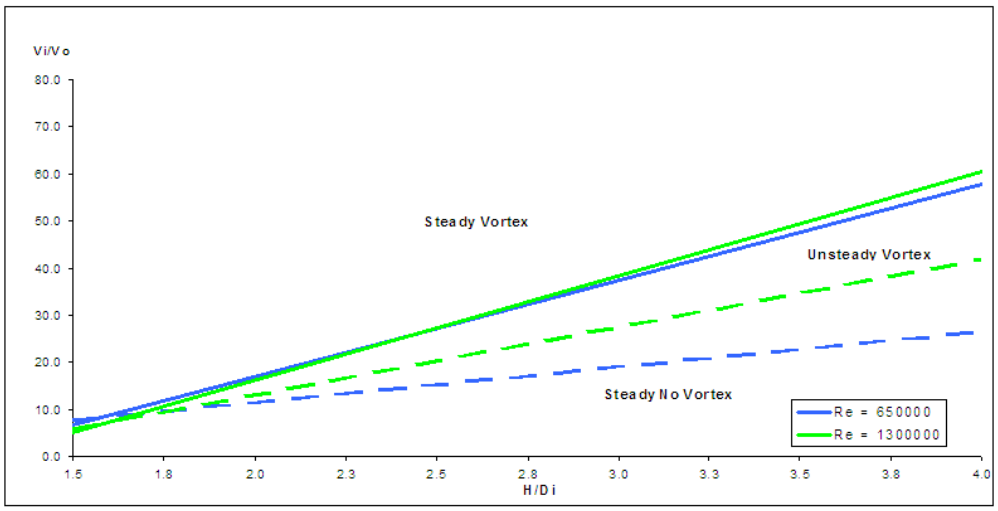

Figure 60: Combined Vortex Formation Threshold in terms of Vi/Vo for Di = 2.0 m at Various Re

7.4 Discussion

The results presented in the previous section shows the increase in Reynolds number has an inverse relationship with probability of vortex formation. From the graphs, it is clear that for a constant cell and suction inlet size, an increase in Reynolds number raises the vortex formation threshold. This decreases the probability of vortex formation.

The relationship is the same as that seen in the engine-over-runway scenario.

An increase in Reynolds number indicates an increase in the velocity of the cell bypass flow for a particular CBR. For one particular suction inlet diameter an H/Di value, there exists a $CBR_{blow\text{-}away}$. If the cell bypass flow velocity is above the blow-away velocity, any vortex will be blown downstream and will not form. Hence with an increase in Reynolds number, a lower CBR is necessary to reduce the cell bypass flow velocity below the blow-away velocity.

As mentioned previously, higher Reynolds number indicates a higher rate of turbulent mixing thus inhibiting the formation of the vortex. Additionally, a lower Reynolds number indicates that the separation of flow pathlines from the floor into the engine inlet is more likely to take place thus making it easier for the vortex to form.

8 Effect of Suction Inlet Diameter

This chapter presents the effect that altering the suction inlet diameter have on the vortex formation threshold in the test cell. It is a parametric study performed cetaris paribus.

8.1 Introduction

Suction inlet diameter is the representation of engine diameter in real test cells. It is a very important investigation parameter as it investigates the usability of existing cells for new engines, which are likely to be larger. It is also of interest to builders and designers of new test cells, as it provides information on how much larger these test cells should be in order to retain the same safety standards

Investigating the effects of a change in suction inlet diameter in experimental setups is not a trivial task due to the difficulty in isolating the effects of changes in Reynolds number and suction inlet size. As mentioned in the previous chapter, control of the upstream velocity is not a trivial task hence it is difficult to conduct an experiment to investigated the changes in size of the suction inlet whilst keeping the Reynolds number constant. No previous investigation isolating the effect of the size of the suction inlet in a test cell has been published.

In the engine-over-runway scenario, an increase in the suction inlet diameter at a constant Reynolds number lowered the threshold to a lower Vi/Vo indicating an increase in the probability of a vortex forming. In line with the similarity of trends between the two scenarios, it is expected that this parameter will also share similar trends.

8.2 Scope

The investigation of the change in suction inlet diameter uses the same simulation cases as that for the Reynolds number investigation and hence has the same scope and Reynolds number and suction inlet diameter ranges.

The upstream velocity profile used has a constant velocity gradient with the velocity increasing from the left to the right wall, looking into the engine.

The Reynolds number for the simulation increased from 650 000 to 1 300 000 and was changed independently of suction inlet diameter.

The suction inlet diameter ranges from 1 m to 2 m and the range of H/Di from 1.5 to 4.0.

8.3 Results

Similar to all engine-in-testcell simulations, the model was solved with cell bypass ratio in increasing steps of 5% until the threshold is found. This translates to an uncertainty in Vi/Vo of not more than 2.6%.

The vortex formation threshold for different suction inlet diameter at the same Reynolds numbers is shown from Figure 61 to Figure 69. These graphs are reproduced from the same set of data as Figure 50 to Figure 60 in chapter 7 but are shown separately to present the effects of the different parameters more clearly.

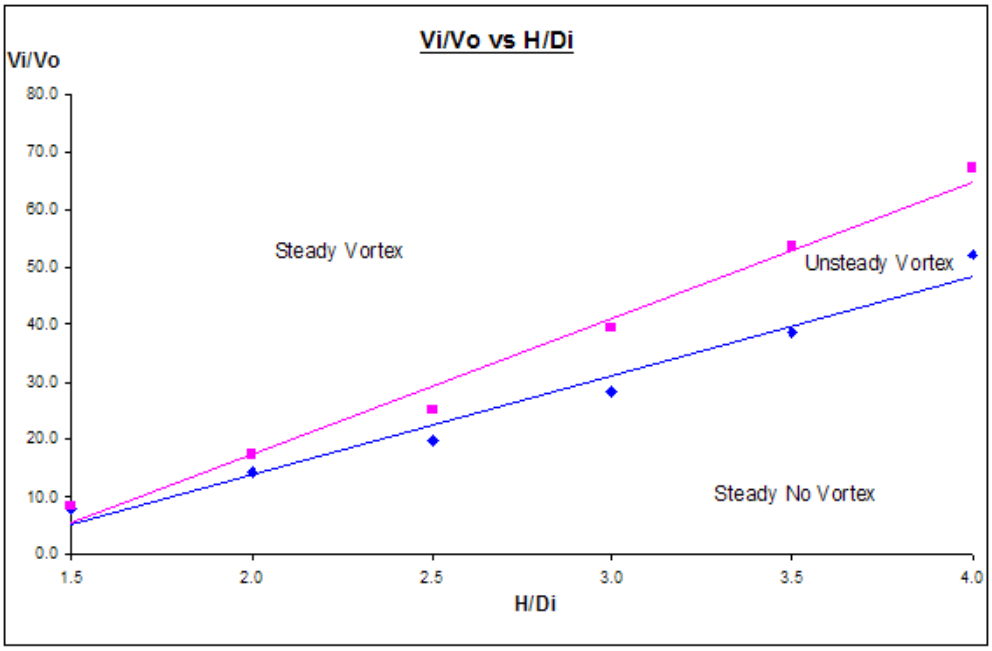

Figure 61: Vortex Formation Threshold in terms of Vi/Vo for Re = 650 000 and Di = 1m

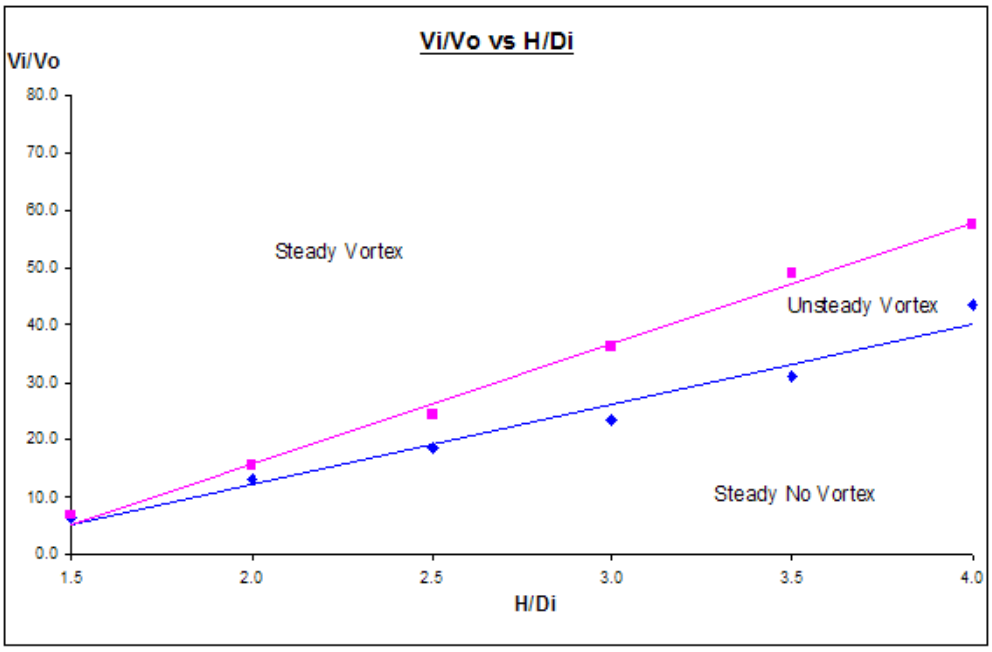

Figure 62: Vortex Formation Threshold in terms of Vi/Vo for Re = 650 000 and Di = 1.5m

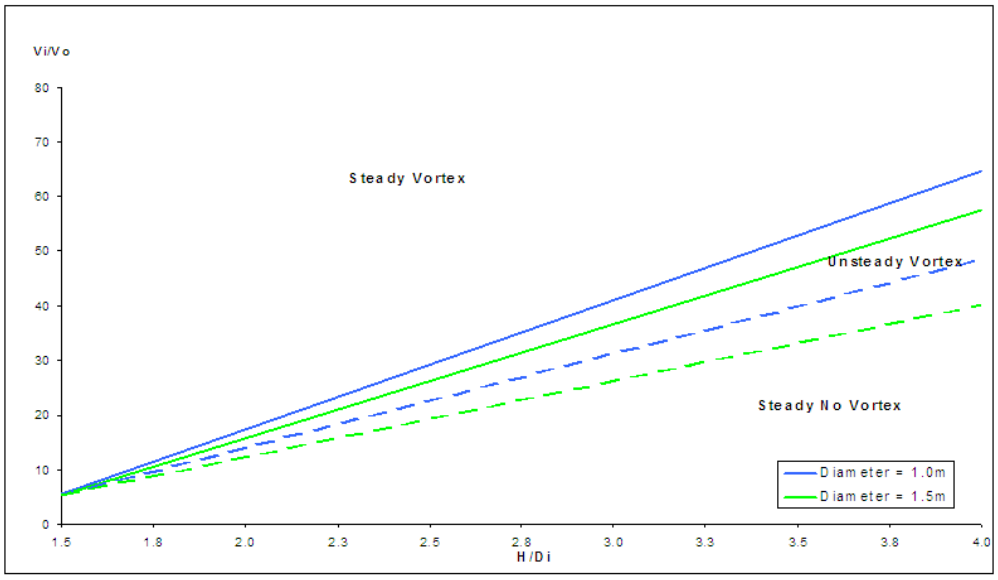

Figure 63: Vortex Formation Threshold in terms of Vi/V0 for Re = 650 000 at Different Diameters

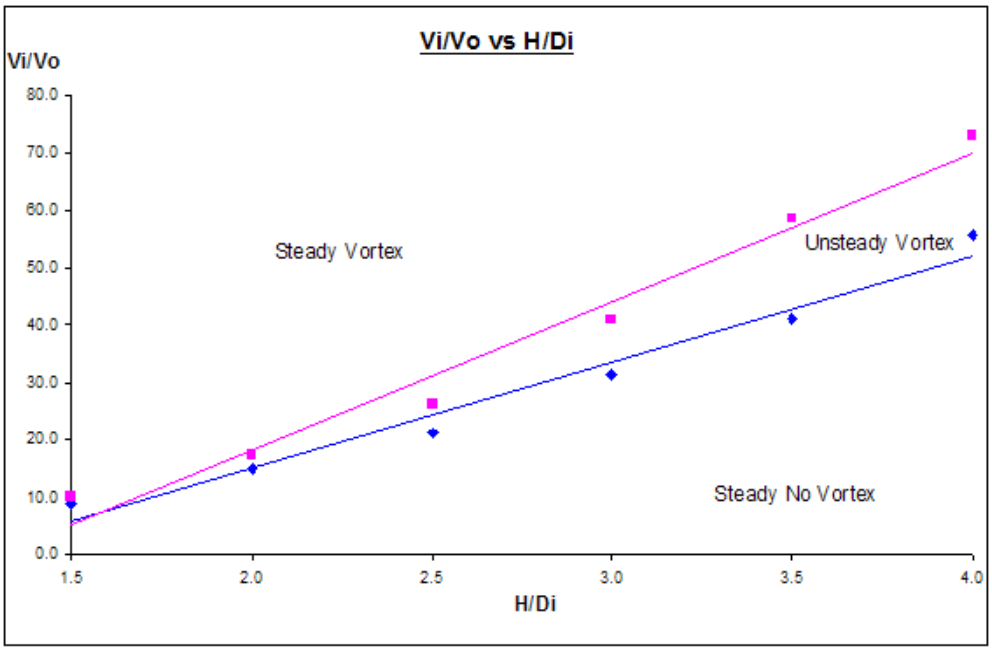

Figure 64: Vortex Formation Threshold in terms of Vi/Vo for Re = 975 000 and Di = 1m

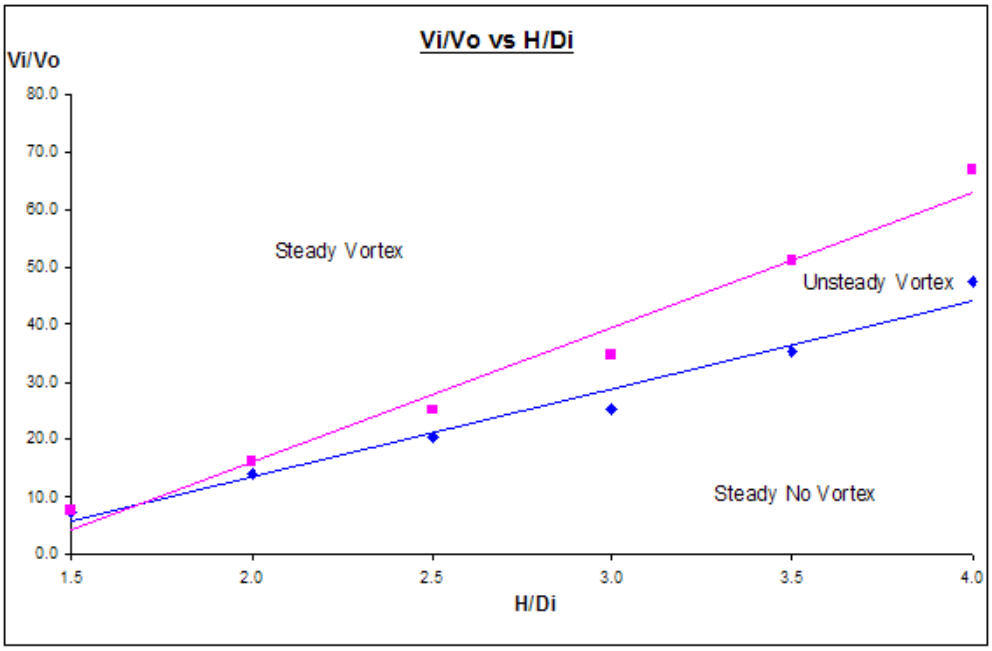

Figure 65: Vortex Formation Threshold in terms of Vi/Vo for Re = 975 000 and Di = 1.5m

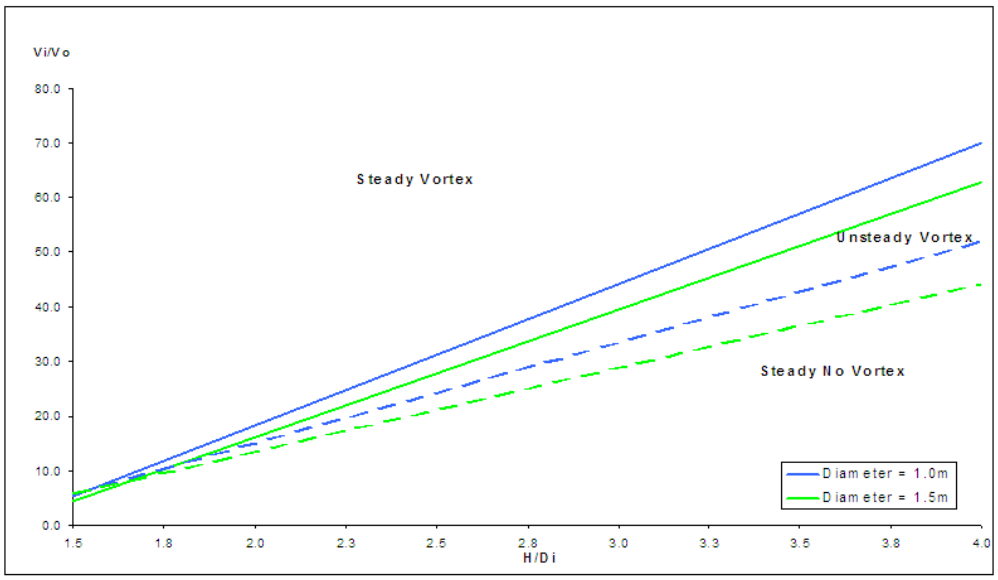

Figure 66: Combined Vortex Formation Threshold in terms of Vi/Vo for Re = 975 000 at Different Diameters

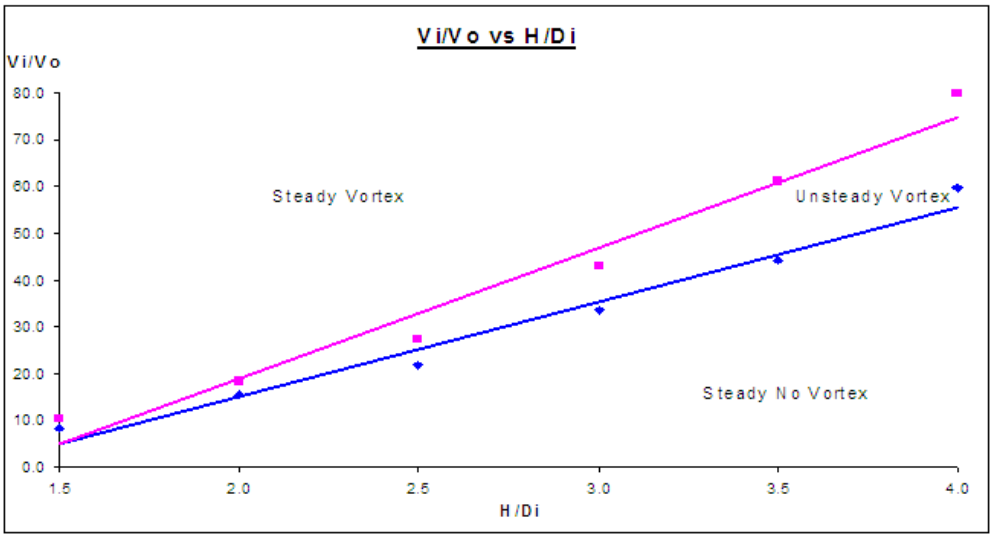

Figure 67: Vortex Formation Threshold in terms of Vi/Vo for Re = 1 300 000 and Di = 1m

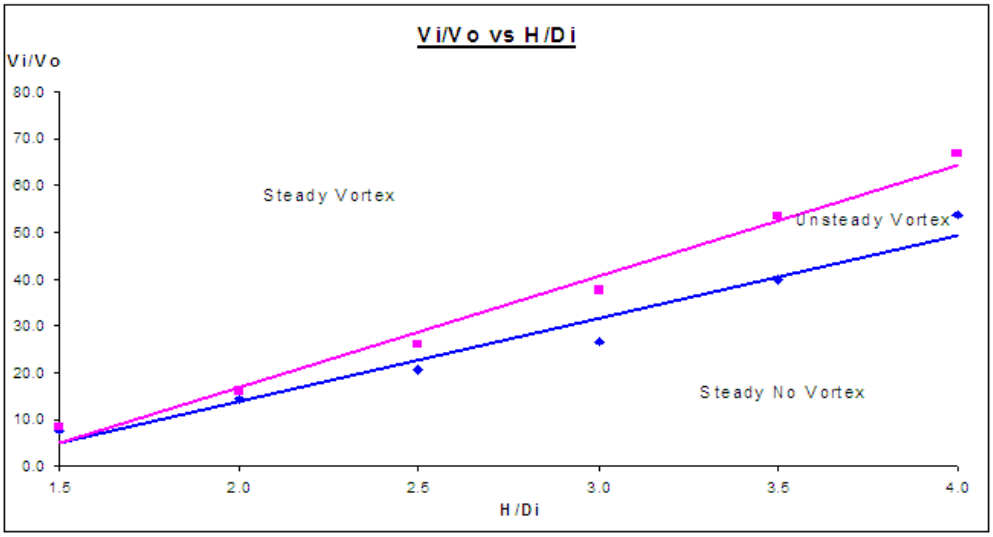

Figure 68: Vortex Formation Threshold in terms of Vi/Vo for Re = 1 300 000 and Di = 1.5m

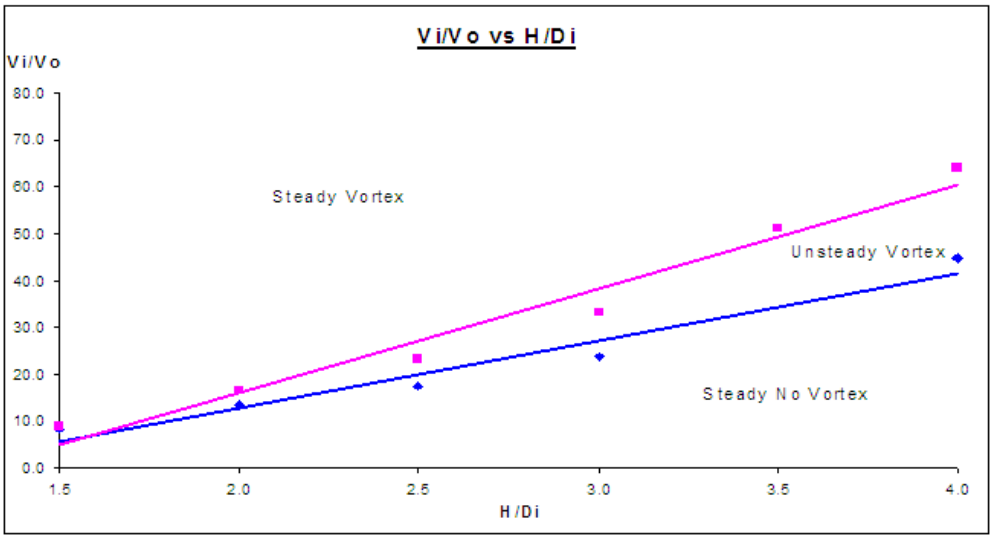

Figure 69: Vortex Formation Threshold in terms of Vi/Vo for Re = 1 300 000 and Di = 2m

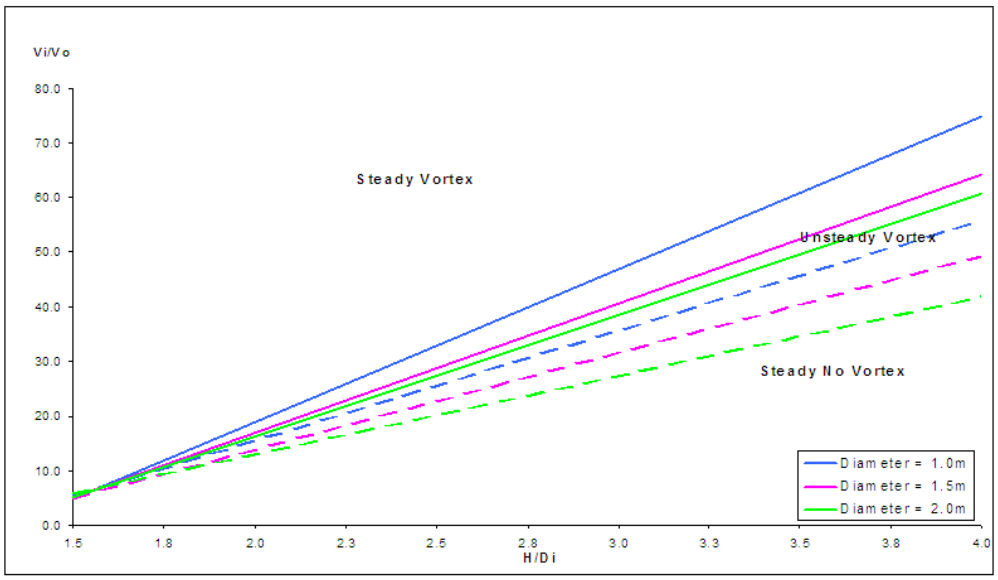

Figure 70: Combined Vortex Formation Threshold in terms of Vi/Vo for Re = 1 300 000 at Different Diameters

8.4 Discussion

The results presented in the previous section shows the increase in suction inlet diameter, whilst keeping Reynolds number constant, has a direct relationship with probability of vortex formation. From the graphs, it is clear that for a constant relative geometry and Reynolds number, a larger suction inlet diameter lowers the vortex formation threshold. This increases the probability of vortex formation by increasing the conditions favouring the formation of the vortex.

The relationship is the same as that seen in the engine-over-runway scenario. Glenny [30] also predicted a similar phenomenon.

Developments in commercial engine indicate an increasing engine core size. The results suggests that test cell sizes need to increase more than engine sizes if the same safety conditions regarding the formation of vortices are to be avoided.

Similar to the engine-over-runway scenario, the laws of dynamic scaling seemed to be violated. However the same explanation described in chapter 4.4 should also apply.

9 Concluding Statements for the Vortex Investigations

This chapter provides the conclusion of the work concerning the vortex forming and ingestion investigations. It contains only a qualitative summary of the results but not the quantitative results

Quantitative results can be found in the results sections of the preceding three chapters.

9.1 Conclusions

Prior to those detailed in this thesis, investigations on the formation threshold of single core vortices as a result of the concentration of upstream or ambient vorticity have all been conducted experimentally with the exception of the correlation by Nakayama and Jones [29]. Experimental approaches avoid the complications associated with accurate CFD calculations such as solution convergence. In any case, a complete investigation using numerical methods would ultimately need to involve some form of experimental validation.

However the use of CFD to investigate vortex formation threshold has its pros. Although the setting up of an experimental rig to simulate vortex formation is relatively simple (requiring just a suction tube and a low pressure source to simulate the engine, a solid plane to simulate the ground and some form of vortex detection techniques), the accurate control of ambient conditions may not be. It is in this that the use of CFD is more effective and flexible.

Previous experimental investigations showed that a clear threshold exists between the conditions necessary for a vortex to form and not to form. This threshold is shown as a upward sloping straight line when the ratio Vi/Vo is plotted against H/Di using linear axes.

Glenny [30] showed that upstream velocity gradient has a direct relationship with probability of vortex formation in an engine-over-runway scenario. He used Rossby number as the measure of upstream velocity gradient.

This work resulting in this thesis demonstrated the successful use of commercial CFD software package Fluent to simulate vortex formation in both the engine-over-runway as well as engine-in-testcell scenario. The CFD results of the investigation on the effects of upstream velocity gradient showed good agreement with the trend showed by Glenny [30]. The actual numerical difference between Glenny's results and the present CFD results is not analysed in depth but only qualitatively because of the lack of sufficient information regarding experimental parameters critical to the formation of a vortex. Instantaneous velocity gradient is one such information, description of the experiments casts doubt that a constant velocity gradient was maintained.

Besides demonstrating the successful use of CFD package to simulate the phenomenon in the engine-over-runway scenario, new information were also found. It was found that probability of vortex formation in the engine-over-runway scenario is directly related to suction inlet diameter and height of ground boundary layer but inversely related to Reynolds number of flow in the setup. These trends were shown to be similar in the engine-in-testcell scenario.

In the engine-in-testcell simulations, it was found that a CBR > 90% was necessary to avoid the formation of vortices in typical situations. This is in agreement with the industry rule of thumb used in test cell design that a cell bypass ratio of more than 80% must be used to prevent vortex formation.

Particular attention should be paid to the suction inlet diameter effects where the laws of dynamic scaling seemed to be violated. However Glenny [30] suggests a similar effect although he did not conduct any experimental validation on his hypothesis. Current investigation validates Glenny's hypothesized results but not his reasoning. This is a potential area for future analysis beyond this thesis.

An important new finding beyond the effects of flow parameters is the necessity of a low velocity region in the main test chamber of a U-shaped test cell. It has been shown that in the absence of such a region, two vortices will be formed from the ceiling and floor of the test cell.

10 Infrasound Problem

This chapter provides an introductory description of the infrasound problem occurring during the operation of the JETC. It provides more details, both qualitative and quantitative, from previous research and practical implementation of "solutions" then those presented in chapter 1.

The chapter ends with a section on the mode calculations based on the dimensions of the modelled cell to determine its probable resonating properties. Resonant properties are important because if the resonant frequencies do not fall in the infrasonic range then any infrasound generated will likely not be able to propagate out of the cell at objectionable levels.

10.1 Introduction

One of the tasks of the cell is to reduce noise emission during engine tests. However it is still rather noisy. An inadequately designed cell can be a very noisy building even in the far field. Far field noise can exceed 90 dBA in military cells [24,25,26].

Although, it is possible for low frequencies to be experienced at certain locations around the test cells when there are no low frequency sources, such occurrences are very rare. One such example is a test cell in Georgia where the low frequencies experienced were attributed to the "beating" of two non-infrasonic noise sources.

Howe [28] identifies two fundamentally different types of resonant oscillations within the test cell that are more common. They are the classical acoustic resonances whose frequencies and mode shapes are unrelated to the unsteady flow in the cell but depend on the geometries of the cell, and sound produced by periodic components of the flow which can arise independently of the acoustic resonances. Although the second type is typically moderate in amplitude, they become important when their frequencies match with the classical acoustic resonance frequencies.

The engine noise is probably the loudest source of noise within the test cell and is largely broadband in nature [27]. Despite this, the noise signature of the test cell may exhibit peaks at certain frequencies. This is due to a combination of factors including attenuation, eddy shedding tones and resonances. These can be classified into either source (i.e. infrasound generation) or transmission factors as shown in Table 5 below.

Table 5: Possible factors affecting infrasound emission from test cell

Sources	Transmission Mechanism
Engine exhaust noise	Reflection / Transmission at surfaces with changes in acoustic impedances
Eddy shedding tones	Cavity modes (Coincident of other driving frequencies with resonant frequency)
Helmholtz resonator	Dissipation / Attenuation / Absorption
Cavity Modes (Bulk movement of air through cell)	

Attenuation by structures is more effective at high frequencies than at low frequencies. As a result, the measured noise is usually more pronounced in the low frequency region. For the same reason, low frequency noise management is arguably more difficult than at higher frequencies. Attenuation is usually not considered a viable option for very low frequency noise management.

Flow induced low frequency noise is a commonly suspected source of infrasound. The term “suspected” is used here because the methods employed to deal with this source of infrasound have not been successful in many situations and thus may or may not be a real sources. The current body of evidence does not allow the determination of whether flow induced noise is a necessary or sufficient cause of infrasound or maybe non at all. However the success low rate of methods employed to deal these flow situations warrants deeper investigation of the matter.

Generally the methods employed to deal with flow induced infrasound involves the additional placement of an object in the path of the air flow either in the augmenter tube or at the tail-end of the exhaust stack. Objects that have been placed in the augmenter tube include but are not limited to the following:

1. Sponsons – Also referred to as core busters. They are an effective and relatively inexpensive method.
2. Augmenter Screens – An effective "core buster".
3. Koppers Harps – Consists of a series of concentric rings.
4. Rectifier Tubes

They are placed at suitable locations and works by breaking up jet flow and coherent turbulent structures formed inside the augmenter tube into smaller structures.

Objects placed at the tail-end of the exhaust stack include and are again not limited to the following:

1. Sawtooth structures – These are typically installed at the top of a vertical exhaust stack, perpendicular to the flow. They work by reduce noise by spawning random sound waves which is more likely to interfere destructively rather than constructively as would be the case for a straight edge.
2. Height of exhaust stack – Increasing exhaust stack height have been shown to be effective in reducing far-field noise [61].
3. US Patent 5837890 – Aero Systems Engineering Ltd filed a patent that supposedly reduced infrasound from a test cell by installation of a structure near the open-end of the exhaust stack. It works by "artificially" increasing the height of the exhaust stack.

Investigations on the above mentioned methods will not be conducted as there is already abundant literature on them. Instead the thesis will concentrate on new innovative strategies and includes the following:

1. The reflection of infrasound back into the cell thus reducing the noise outside of the cell.
2. Reducing the slip velocity between the engine exhaust jet and the cell bypass flow.
3. The effect(s) that the blast basket perforate and cone have on the flow profile in the blast basket and subsequent effects on acoustics.

10.2 Literature Review

This chapter will detail some of the investigations and solutions, either experimental or theoretical that have been conducted in the past. This chapter is meant as a complement to chapter 2.4.2 for readers requiring greater depth.

10.2.1 Changing of Blast Basket Termination

The blast basket is the perforated surface at the downstream end of the augmenter tube where the flow exits the augmenter into the exhaust stack. The blast basket is circled in red in Figure 71 below.

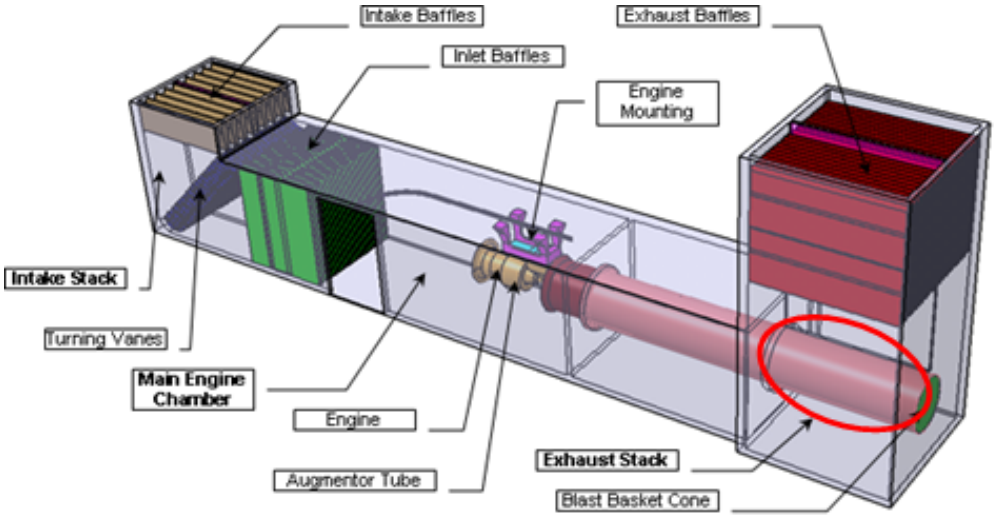

Figure 71: Blast Basket Location

The blast basket termination is termed the "Blast Basket Cone" in the Figure 71 because the termination is very often conical in shape.

Freuler and Montgomery [62] tested five different blast basket terminations in a 1:12 scaled model of a U-shaped cell similar to the modelled cell. Their investigations showed that lower amplitude of pressure fluctuations around 26.25 Hz (after conversion) were measured in the exhaust stack downstream of the blast basket, for the models with a conical termination. A concave termination produced the highest pressure fluctuation amplitude followed by the flat plate and convex dome termination, which registered the same measurements.

Although Freuler and Montgomery [62] did not provide an explanation on their observations, it provided very strong evidence on the importance of the blast basket termination to the infrasound problem.

10.2.2 Structures in the Exhaust Stack

During operation of the test cell, the large scale turbulence created by the engine is allowed to flow through the augmenter tube and exit into the exhaust stack. This large scale turbulence is converted to sound waves in the infrasound range through a resonant process similar to that of an organ pipe. Two "solutions", saw-tooth structures on top of exhaust stack and slots extending downwards from the top of the exhaust stack, have been documented to be somewhat effective in dealing with this phenomenon.

Flow restrictions have been used to reduce test cell noise by changing the characteristics of the flow. The Naval Air Engineering Centre installed a saw-tooth like structure perpendicular to the flow at the top of the exhaust stack at their T-10 test cell at NAS Lemoore as a barrier to low frequency noise [63]. Overall there was a 7 dBA reduction in noise directly behind the test cell. Jagged edges reduce noise by spawning random sound waves resulting in a higher probability of destructive rather than constructive interference [38]. Strictly speaking, the waves are not truly random but are generated with a complex phase relationship. A 1:20 scale physical model of the US Navy's T-10 test cell was used to test the effectiveness of such a saw-tooth structure. The measurements did not show the same high level of noise reduction as Lemoore and only had about 1 dB reduction [64]. This is a good example of a "solution" that is not universal and lends weight to either explanation mentioned in chapter 10.1 above.

In 1998, Long filed a US patent for an invention to deal with the infrasound problem. In it he proposes the construction of multiple slots at the top of the exhaust stack extending downwards into the exhaust stack. He claims, "If these slots or openings are large enough relative to the upper end of the exhaust stack, the stack will behave as though the height of the stack conforms to the lower end of the slot or openings". If the slot width or openings are small relative to the top end of the stack, the stack will

behave as though the stack height is the full height of the stack. At intermediate slot widths and openings, the effective stack height is diffuse and has no clear exit point. In such cases, the height or length of the stack (L) in the above equation is a variable quantity. Thus, organ pipe type resonances are less likely to occur because a clear single frequency cannot be established. Without such resonances, the noise radiation, and in particular the infrasound radiation decreases dramatically" [65]. The patent has since expired and no documentation of the effectiveness of such a structure has been found. However due to the similarity of operation between these slots and the saw-tooth structure mentioned above, its effectiveness may be due to the similar reasons.

Dickman et al. [66] showed that porous screens placed the base of the exhaust stack shows promising effects of reducing infrasound. They identified several configurations that significantly reduced the sound pressure levels (SPL) in their model between 200 and 315 Hz. The 47% porous screen placed at 45 degrees showed the greatest reduction of 23 dB.

10.2.3 Structures in Augmenter Tube

Measurements and CFD simulations have shown that low frequency aerodynamic jet noise is generated downstream of the jet nozzle (about 20 diameter downstream [67]) by vortices formed by the shearing action of the jet. Hence structures constructed and placed inside the augmenter at suitable positions should reduce low frequency noise by preventing the formation these vortices.

These structures come in different shapes and geometries but the underlying principle remains to disrupt the formation of these vortices. This section will introduce three of these structures (sponsons, wire mesh screens and the Kopper's or Cooper's harp) and discuss their usage and performance history. The origin of the name "Kopper's Harp" could not be discovered by the author and correct spelling is not clear.

Sponsons were used in the RAF hush houses located in Markham, England [68] as well as on the Concorde hush house in England. Publications detailing the performance of sponsons in these cells are very limited and no conclusive assessment can be done. Kodres [64] compared the relative effectiveness of the concorde-style

sponsons, screens placed in the jet and a cylindrical shaped screen. The concorde-style sponsons were only moderately successful and reduced far-field noise by about 2 - 3 dB.

Wire mesh screens were used on the Lewis Flight Propulsion Laboratory and reduced the SPL by up to 12 dB. The screens were effective over the entire spectrum especially at the lower frequencies [69]. Kodres [64] also showed that such screens could reduce the SPL by about 10 dB with the effective frequency range being affected by the number of screens present. The relative effectiveness increasing screens dropped drastically after the first screen. Shaping the screen into a cylindrical shape did not show any evidence to justify the increased complexity in manufacturing. The effectiveness of the screens however seem to drop for frequencies above 11 kHz.

The Kopper's harp is another device that is placed downstream of the engine nozzle inside the augmenter and has been effective in mixing the high velocity engine exhaust core flow with the fan and bypass flow. It is a series of rings that is placed in the area of the core flow within the augmenter near the entrance.

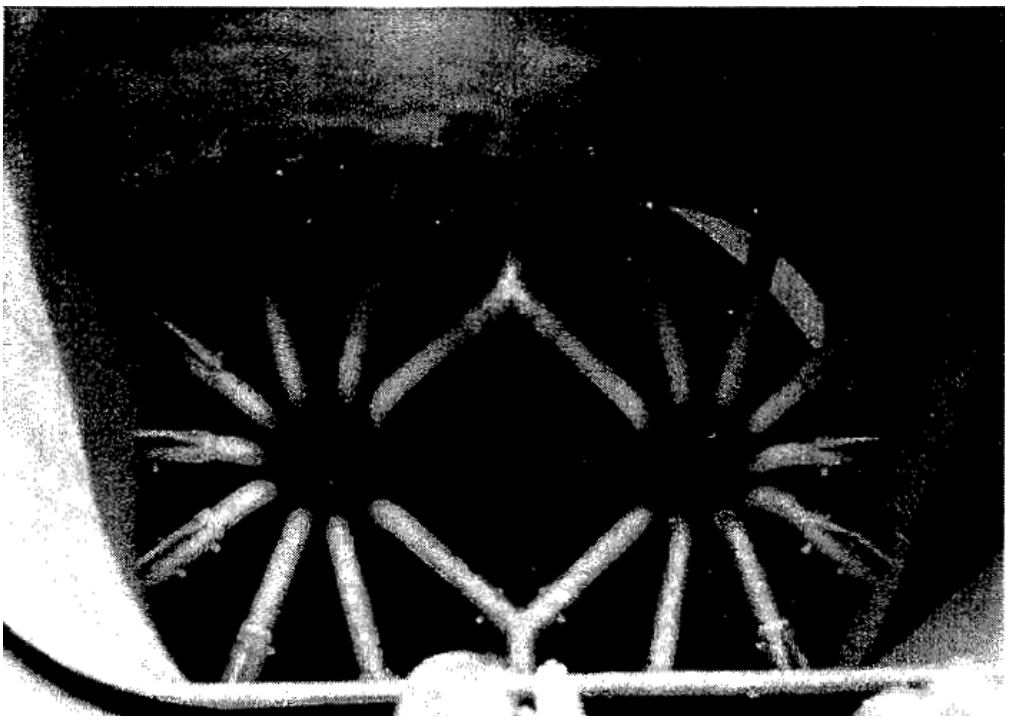

Figure 72: Sponsons installed at the entrance to the augmenter tube of a Concorde hush house [24]

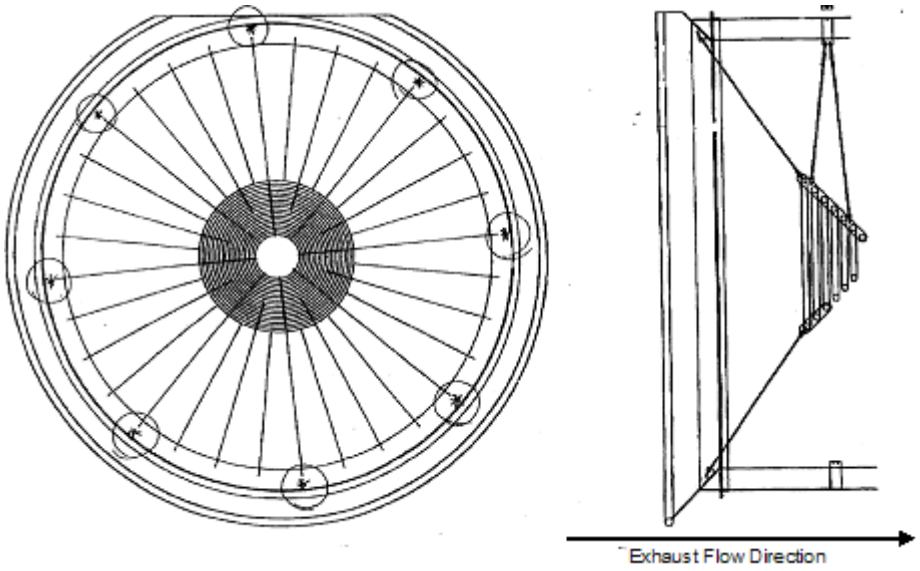

Figure 73: Rough Sketch of what a Kopper's Harp looks like when mounted inside an augmenter tube

A typical harp configuration uses a stepped change in ring diameter in the axial direction. The largest diameter ring is the first ring upstream of the flow and the smallest ring the last. This ring assembly forms a funnel shape. Harps with too few rings tend to generate some shedding noise peaks, which go away when the number of rings is increased. The axial location of the harp is particularly important to the overall effectiveness of the harp. However the main disadvantage of the harp is difficulty in keeping the harp in operation. As the harp is essentially a skeleton-like structure placed within the high speed engine exhaust core flow, structural resonances within harp can only be minimised through careful design and material selection. In fact one of the proposed modifications made to the modelled cell was the installation of the Kopper's harp but it couldn't stand up to the thrust of the engine long enough for its effectiveness to be measured.

10.2.4 Height of Exhaust Stack

Lancey and Kodres [61] showed that increasing the height of the exhaust stack had a significant effect on reducing noise emission. Fadeley [26] also reported a reduction of 10 dBA when acoustic panels were mounted on top of exhaust ramps in retrofitted test cells.

10.2.5 Fluctuating of Test Cell Flow

There has been evidence that fluctuating flow can be a potential source of low frequency noise with the frequency of fluctuation being the frequency of the noise. Frandsen and Chamberlain Architects showed that low frequency noise measured in Cell #8 at Hill AFB was a result of fluctuating flow across a diffuser placed at the aft of the augmenter between maximum air flow and a situation where there is less flow due to flow separation [70].

It has also been hypothesized that there is a similar case of fluctuating flow due to separation-reattachment of flow between adjacent panels within the inlet baffles of the modelled cell. Changes to the relative positions of the inlet baffles led to a reduction in low frequency noise emitted from the cell. However this change was made together with a series of modifications thus the actual effectiveness of this change alone is impossible to ascertain.

Fluctuation of air flow within the test cell is also the cause of low frequency noise in a USAF hush house at Langley AFB [71]. At Langley, a series of diffusers were placed in the augmenter to energise the flow near the augmenter walls. This led to a reduction of about 8 dB and 10 dB at 31 Hz and 63 Hz respectively.

10.3 Literature Review Conclusion

In conclusion, many structures and solutions have been proposed, experimented and implemented in test cells to deal with the infrasound problem. However none are widely applied and many have not been conclusive shown to be universally effective.

11 Background Information on a Problematic Cell

To facilitate the investigations, a model of an actual test cell was used whenever appropriate. Some modifications were adopted to reduce the amount of infrasound emitted from the cell. This chapter presents these modifications as well as some calculations and analysis based on them before presenting hypotheses that are investigated and presented in this thesis.

Some information will be obscured to prevention identification of the cell. This is due to non-disclosure agreements between the parties.

11.1 Test Cell Model used for Investigation

The test cell is used to test commercial large turbofan engines instead of smaller military jet engines.

The test cell is a U-shaped cell with a vertical intake and exhaust stack. There are no peculiarities in the features or structures compared to other test cells of similar applications. A picture of the test cell CAD model reconstructed from drawings is shown in Figure 74 below.

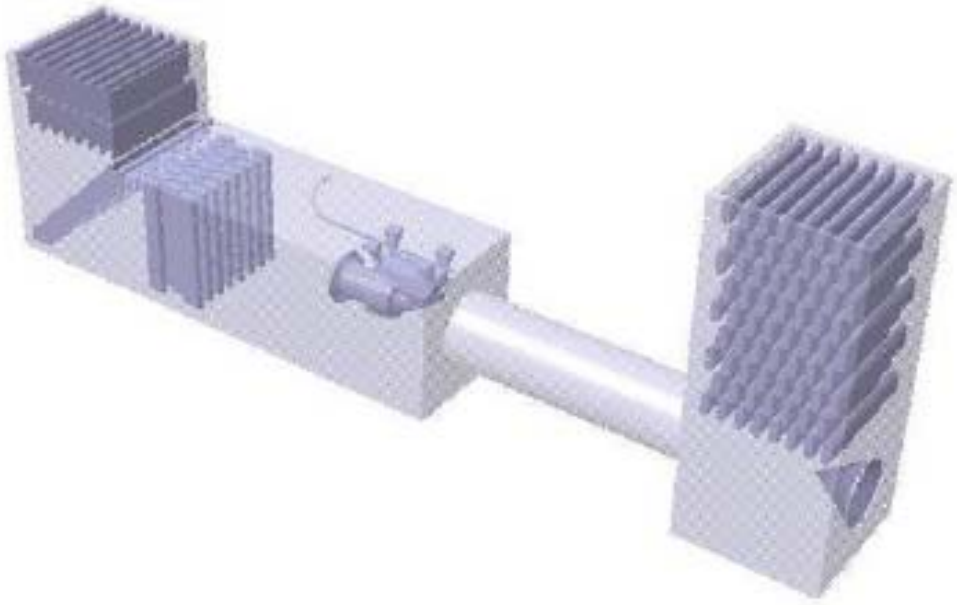

Figure 74: CAD Model of the Modelled Cell

Unfortunately, further information on the cell has to be withheld due to non-disclosure agreements with the relevant parties.

The cell initially had unacceptable levels of infrasound while testing engines at high thrust levels. Initial measurements showed that noise emissions below 63 Hz exceeded the specifications of the operator. The cell constructor made a number of modifications to cell that reduced the infrasound emission below the requirements. These modifications were made to almost all the main sections of the cell. Details of these will be presented in a later section.

First, the 'potential' for the cell to generate or accentuate any infrasound generated by other mechanisms are determined by calculating the organ-pipe or standing wave and Helmholtz resonant modes. Following that, descriptions of the modifications to the modelled cell is presented together with analysis on them.

11.2 Resonant Mode Calculation

One possibility for the generation of infrasound during the operation of a jet engine test cell is the organ-pipe resonance mode, as identified by Howe [28]. Organ-pipe or

standing wave resonance occurs when there is bulk movement of air through an elongated tube or pipe such as in woodwind musical instruments like the flute.

It is unlikely that organ-pipe resonance excited by broadband engine noise is the sole source of low frequency noise emission from the test cell. If it is, then a particular cell should exhibit low frequency noise all the time and the amplitude would always be larger at higher engine setting. However, the amplitude of low frequency emission does not seem to be simply related to engine setting which rules out organ-pipe resonance as the sole source. Although larger engines do seem to exhibit infrasound emission more frequently.

Although organ-pipe resonance is unlikely to be the sole source of low frequency emission, it is always present when there is bulk movement of air through the test cell. Hence, it is still important to calculate the organ-pipe resonance modes to determine the potential for low frequencies to be generated during an engine test in the cell.

As with the other investigations in the infrasound problem, the modelled cell will be used as an example. Organ-pipe resonances will be calculated for the intake stack, main testing chamber, augmenter tube and exhaust stack, using standing wave resonance equations as listed below [72:

$$f_{\text{organ pipe circular open}} = \frac{l}{2(L_x + 0.8d)} \quad \textbf{(6)}$$

$$f_{\text{organ pipe circular close}} = \frac{l}{4(L_x + 0.4d)} \quad \textbf{(7)}$$

$$f_{\text{organ pipe rectangular open}} = \frac{c}{2}\sqrt{\left(\frac{l}{L_x}\right)^2 + \left(\frac{m}{L_y}\right)^2 + \left(\frac{n}{L_z}\right)^2} \quad \textbf{(8)}$$

$$f_{\text{organ pipe rectangular closed}} = \frac{c}{4}\sqrt{\left(\frac{l}{L_x}\right)^2 + \left(\frac{m}{L_y}\right)^2 + \left(\frac{n}{L_z}\right)^2} \quad \textbf{(9)}$$

The possibility of one of the chambers mentioned above acting as a Helmholtz resonator is also investigated by calculating the Helmholtz resonance frequency using the equations shown below:

$$f_{\text{helmholtz}} = \frac{c}{2\pi}\sqrt{\frac{A}{Vol \bullet L}} \quad \textbf{(10)}$$

The lowest frequency that can be allowed to be propagated through the augmenter tube and the exhaust stack as plane waves is then calculated using the following formulas [73]:

$$\text{Rectagular Duct} : f_{\text{propagated}} \geq \frac{c}{2h} \quad \textbf{(11)}$$

$$\text{Circular Duct} : f_{\text{propagated}} \geq \frac{1.84c}{\pi d} \quad \textbf{(12)}$$

All higher modes, even if present, will be attenuated exponentially.

11.2.1 Cut-off Frequencies

The cut-off frequencies for higher mode acoustic waves calculated for the augmenter tube and the exhaust stack are shown in Table 6 below.

Table 6: Cut-off Frequencies

Cell Portions	Type	$F_{cut\text{-}off}$ (Hz)
Augmenter Tube	Circular	30.87
Exhaust Stack	Rectangular	11.78

11.2.2 Organ Pipe or Standing Wave Calculations

This section details the possible organ pipe frequencies that can exist in the various sections of the test cell. The calculations will determine how many modes exist between the cut-off frequencies and 60 Hz. The results are shown in Table 7 below.

Table 7: Standing Wave Calculation Results

Part of Cell	Lowest Freq (Hz) / Lowest Freq > $F_{cut\text{-}off}$	No. of Modes between $F_{cut=off}$ and 60 Hz
Intake Stack	4.23 / 30.93	779
Engine Chamber (Closed)*	2.06 / 30.94	1559
Engine Chamber (Open)*	4.13 / 31.09	222
Exhaust Stack	2.29 / 30.94	1402
Augmenter Tube (Closed)*	1.62 / 12.94	30
Augmenter Tube (Open)*	3.23 / 12.94	16

* Because of the complex termination of the engine chamber and augmenter tube, both possible terminations were calculated.

The results indicate that there exist a large number of standing wave modes below 60 Hz for different parts of the cell.

In the absence of other flow related or alternative methods, the generation of infrasound as a result of organ-pipe resonance is rather high.

11.2.3 Helmholtz Resonator

This sections details the possibility of a Helmholtz resonator existing in various sections of the test cell and the results are shown in Table 8 below.

Table 8: Helmholtz Resonator Frequencies

Cell Portions	Neck Location	$F_{helmholtz}$
Intake Stack	Thickest part of Intake Baffle	14.61
Main Engine Chamber + Augmenter	Augmenter Blast Basket Perforate	42.86
Main Engine Chamber	Augmenter Tube	1.84
Exhaust Stack	Thickest part of Exhaust Baffles	6.32

So the main engine chamber and the exhaust stack are unlikely to act as Helmholtz resonators independently. However, it is possible that together they are acting as one Helmholtz resonator with the blast basket perforate acting as the neck.

11.2.4 Conclusion

Calculations of resonant frequencies show that due to the bulk flow of air through the test cell, certain sections of the cell may exhibit either organ-pipe or Helmholtz resonance. All the major sections of the test cell (Intake Stack, Main Engine Chamber, Augmenter Tube and Exhaust Stack) have their primary frequency within the infrasonic range.

However as mentioned earlier, these two forms of resonance is unlikely to be the major or only source of infrasound emitted from the test cell.

Calculations in chapter 11.2.1 show that if a source of infrasound is present in the cell, it will be permitted to be propagated through the augmenter and exhaust stack of the cell. Some of the possible sources are the engine exhaust noise and eddy shedding tones as mentioned in chapter 1

11.3 Modifications to the Modelled Cell

As mentioned earlier, the cell operator made a number of modifications to cell, which can be categorised into 2 different phases. The descriptions of the important changes are shown below with specific information obscured:

Phase 1 Modifications

- Inlet splitters were repositioned
- Blast basket perforate open area was modified
- Blast basket cone was lengthened
- A perforated sheet located inside the augmenter tube was removed and replaced with a solid sheet
- A Kopper's harp was installed but it did not withstand the thrust of the engines and was subsequently removed, so the effect can be ignored

Phase 2 Modifications:

- Inlet baffles were changed in design to a more aerodynamic shape and construction material
- Exhaust baffles were changed in design to a more aerodynamic shape and construction material

After each phase of modifications, measurements were made at various locations outside around the exhaust and intake stack and these are compared to those measured before any modifications were made. Some measurements were also taken inside the cell. These measurements were taken at max continuous, take-off and idle engine conditions. However the measurement data cannot be provided due to the non-disclosure agreements.

Measurements of sound below 63 Hz made after the phase 1 modifications showed a reduction of 3 – 10 dB with more reduction in the lower frequencies. The reduction in noise was about the same for the intake as well as exhaust stack.

Measurements of sound below 63 Hz made after the phase 2 modifications showed a reduction of 6 – 14 dB near the exhaust stack but less than 2 dB near the intake stack.

Interestingly after the phase 1 modifications, a higher sound level was measured inside the cell compared to before the modifications. The change in sound levels exceeded 10 dB.

Other than the above-described acoustic effects, the modifications also altered some macro flow parameters through the cell. The overall mass flow rate through the cell increased from about 3080 to 3300 kg/s leading to an increase in CBR from 1.12 to 1.27 on the same engine setting.

11.3.1 Analysis of the Modifications for the Modelled Cell.

As the modifications were made together in each phase, the effect of each individual modification cannot be ascertained with a high degree of confidence but some hypotheses can be drawn from them.

Blast basket cone modifications from phase 1 modifications seemed to have reduced the low frequency noise measured. The cone modification seems to be in agreement with the findings of Freuler and Montgomery [62], although the experimental cones were not the same as the cones in the modelled cell. Progressive lengthening of the blast basket cone in test cells also seems to be the prevalent industrial design practices although the exact reasons for them are not clear.

Repositioning of splitters seemed to have the same effect as the changes to the diffusers introduced at Langley [71]. They were certainly implemented with the same effects in mind. They might have eliminated any periodic separation-reattachment of flow in parts of the cell thus eliminating a fluctuation of flow.

The perforated sheet that was originally inside the augmenter tube would have acted as a compliant or dissipative duct and its removal should reduce the attenuation of emitted noise. However, noise attenuation is less effective at low frequencies so its effect could have been insignificant.

The phase 2 modifications seem to be just a refinement of the inlet splitter effect. The changes in design to the more aerodynamic shape would further reduce the chance of

flow separation around them. The changes in construction material might have some introduced some attenuation.

One modification that seemed to be important is the blast basket perforate modification. However, no previous investigations regarding the effects have been found.

Two hypotheses were drawn regarding the blast basket perforate change. It is reasonable to infer that a change in the perforate would have an effect on the local flow characteristic. This change in local flow characteristics could have two possible effects.

First, flow separation could have existed at the perforate at certain cell flow rate. The combination of blast basket perforate and cone modifications could have altered the flow characteristics around the perforate thus eliminating any potential flow fluctuation. It could either eliminate the flow separation-reattachment or reduce the possibility of it occurring by shifting the operating flow rate or the point at which separation occurs, or both. If this causes the operating flow rate to be further away from the separation point then the possibility of flow fluctuation will be reduced.

Second, the changes to the flow characteristics around the perforate could have been modified in such a way that it alters its acoustic reflection characteristics. The measurements showed that the noise inside the cell increased after the phase 1 modifications implying either the source of noise has increased or more noise is being reflected back into the cell and less is being transmitted.

More details on these two hypotheses are presented as investigation parameters and results in later chapters.

Lastly, the change in overall mass flow through the cell as a result of the modifications suggests a reduction in the relative velocity between the high velocity exhaust jet and the lower velocity cell bypass flow. According to Lighthill [74], this relative velocity difference has a very strong influence on the noise emitted by the exhaust jet. Calculations using the formulas detailed in chapter 13 shows that the

exhaust jet noise, in the modelled cell after the modifications (both phase 1 and 2), reduced by about 2.5 dB.

The potential of reducing engine exhaust jet noise, through certain geometric modifications, as a means of reducing sound emission from the cell is presented chapter 13.

12 Fluctuating Flow Resistance in the Blast Basket

This chapter presents the investigation of the first hypothesis highlighted at the end of chapter 11.3.1.

12.1 Hypothesis

The hypothesis tested is the change in the test cell flow resistance characteristics as a result of the modifications done on the modelled cell. This hypothesis is a result of a combination of observations by Freuler [75] and R I Corporation Consultants [76]. Freuler's [75] findings suggest that blast basket termination is an important component in the remedial action for infrasound without providing analysis of the phenomena present. R I Corporation Consultants [76] further concluded that the pulsations observed was a result of a separation/reattachment cycle of flow in the diffuser thus changing the resistance (back pressure) of the augmenter flow.

Evidence suggesting pulsating flow as a result of flow resistance is an important source of infrasound comes from a particular modification performed on the modelled cell. One of the modifications is a change in the inlet baffles spacing that resulted (albeit together with the other modifications) in the reduction of infrasound emitted from the cell. Alam and Zhou [77] suggests that crossflow over parallel obstructions results in separation/reattachment of flow and its frequency is affect by the distance between the obstructions.

There is reasonable evidence to suggest that there is a change in the test cell flow resistance as a result of the modifications. One of most telling points is the difference in CBR and overall cell mass flow rate between the pre-modification and post-modification measurements (≈3100 kg/s, 112% vs. ≈3300 kg/s, 127%) at the same engine setting.

The hypothesis is that the change in the blast basket cone and perforated section led to a change in the flow resistance characteristics in a way similar to that observed by R I Corporation [76]. The similarity expected is in the observed changed in flow

resistance profile but not necessarily the mechanism. The change in flow resistance may have caused a change in the amplitude or frequency of the fluctuations.

12.2 Methodology

The methodology used in the investigation of the presence of flow fluctuations resulting from separation/reattachment cycle of flow in the diffuser is presented here. Flow resistance is the parameter of concern. If the flow resistance with respect to flow rate is not smooth and gradual, then the system will experience disturbances when there is an accidental or inevitable change in the operating flow rate.

There were two planned stages in this investigation. The first stage would attempt to mirror the investigations and validate the findings of Freuler [75] in terms of flow resistance fluctuations. In this first stage of investigation, a CFD model consisting only of the augmenter tube with a generic concave or convex blast basket termination and perforates were used. The focus of this stage of the investigation is on the change in the flow resistance as a result of the change in the termination. Other sections of the cell were excluded from the model to reduce unnecessary computational resources.

In the second stage of this investigation, the other sections would be included in the model. The focus of the second stage of investigation would be on the flow resistance profile of the entire cell. In the second stage of investigation, the change in the flow resistance characteristics of the blast basket would not be significant but its role would be to alter the flow rate to a value that is closer to or further away from the flow rate at which the disturbance occurs thus increasing or decreasing the probability of flow fluctuation.

A geometric model of the modelled cell augmenter tube was used as the geometric model with scaling performed to match the dimensions and flow approximated in Freuler's paper.

Because of time constraints, the second stage of investigation was not completed at the time of writing of this thesis to the author's regrets.

12.2.1 Model and Solver Parameters.

As mentioned above, the model for the first stage of investigation consists only of the augmenter tube starting with the augmenter entrance and ending with the blast basket perforates. The perforates were modelled as actual holes as opposed to the porous jump boundary.

Two perforate sizes, one being twice as coarse as the other, were used in the investigation. The models are shown in Figure 75 and Figure 76 with the green section denoting the perforate holes. The pictures were taken from the coarser perforate model.

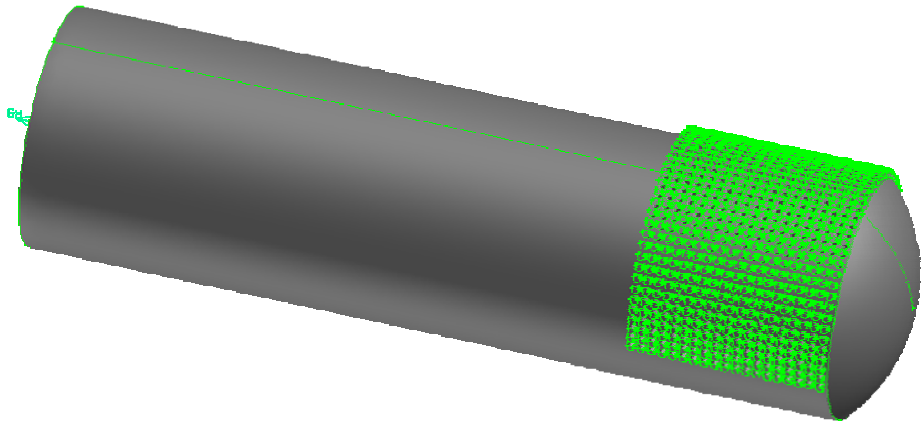

Figure 75: Model with Concave Termination

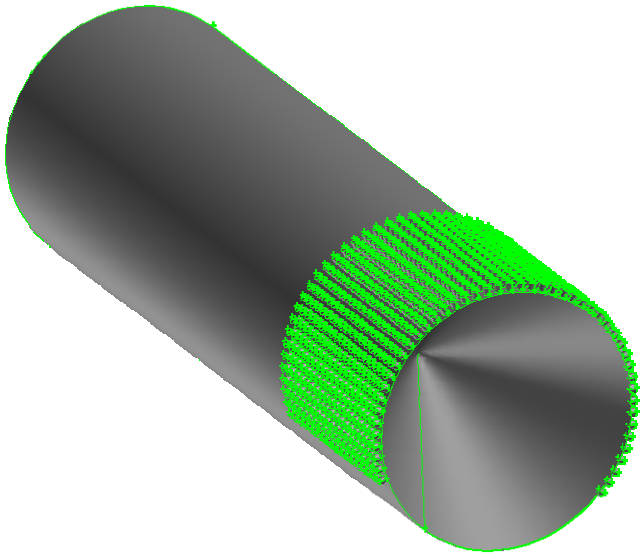

Figure 76: Model with Convex Termination

Care has been taken to make sure that the lengths of the two perforated sections and coverage are similar. In addition, the open area is kept as close to each other as possible but inevitably there is slight difference, the coarse perforate has an open area of 48.5% whereas the fine perforate is 48.9%. This may affect the flow resistance comparison between the two schemes (i.e. the fine perforate may exhibit a low overall flow resistance) but it is the flow resistance characteristics that are more important.

The model was solved at flow rates between 1500 and 2700 kg/s. This range was taken as an estimate from Freuler and Montgomery [75] data based on scaling of the augmenter dimensions and data from another cell where the flow data was available.

The solver parameters are as follows:

- Steady state solver
- Mesh size – 500 000 to 1 500 000 cells depending on the perforates
- Compressible flow solver
- SST-kω turbulence model
- Second order discretisation scheme

Entrance to the augmenter tube is modelled using a mass flow inlet and the perforate outlet using pressure outlet boundaries with uniform atmospheric pressure.

Flow rates and pressure will be extracted from the solution and be used to calculate the flow resistance.

12.3 Results

As mentioned in the earlier section, four sets of simulations were performed:

1. Concave cone, coarse perforate
2. Concave cone, fine perforate
3. Convex cone, coarse perforate
4. Convex cone, fine perforate

The flow resistance characteristics are shown in Figure 77 to Figure 80.

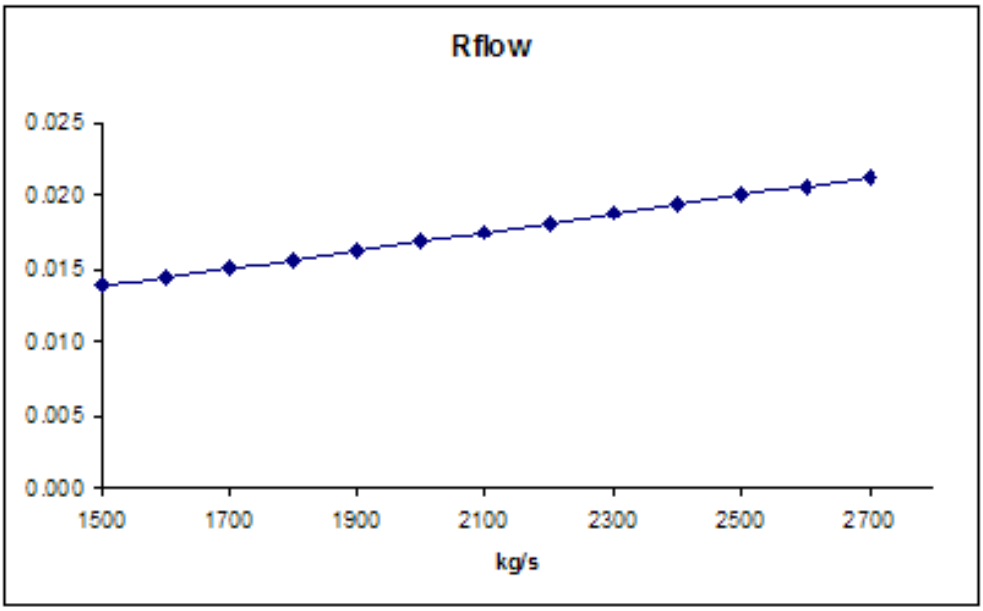

Figure 77: Flow resistance of concave cone model with coarse perforate

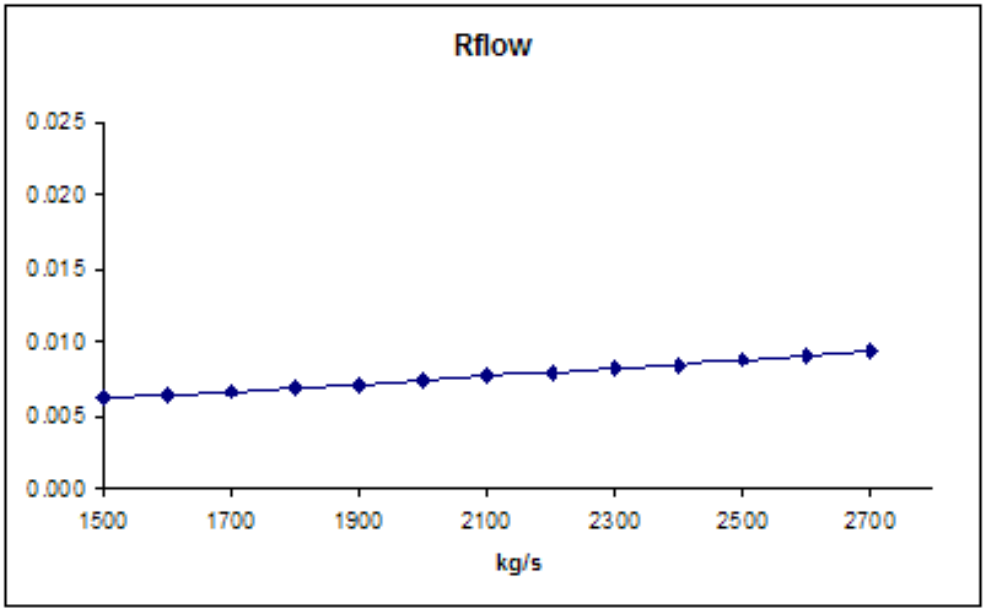

Figure 78: Flow resistance of concave cone model with fine perforate

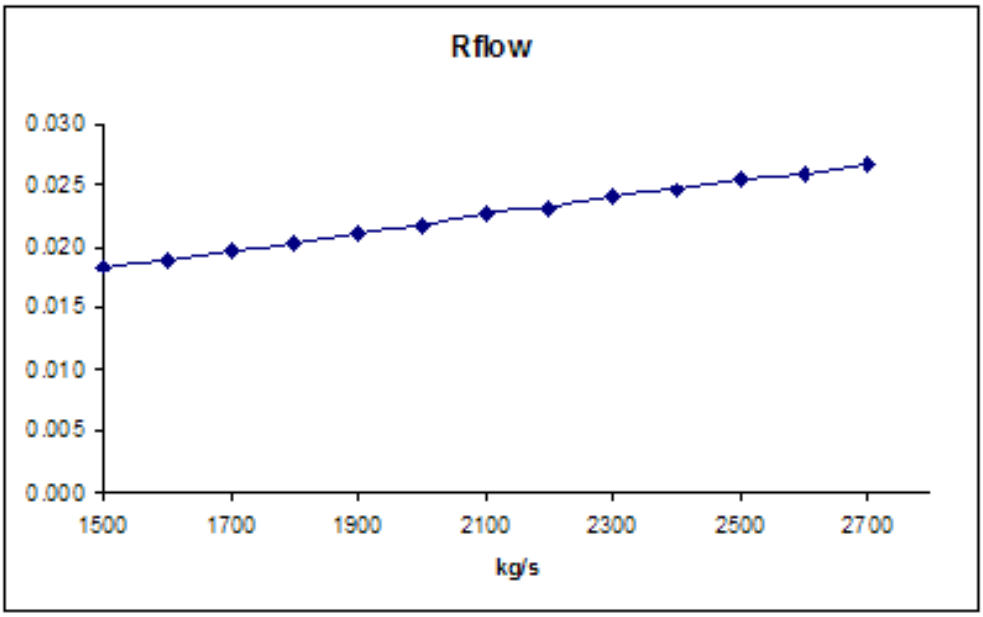

Figure 79: Flow resistance of convex cone model with coarse perforate

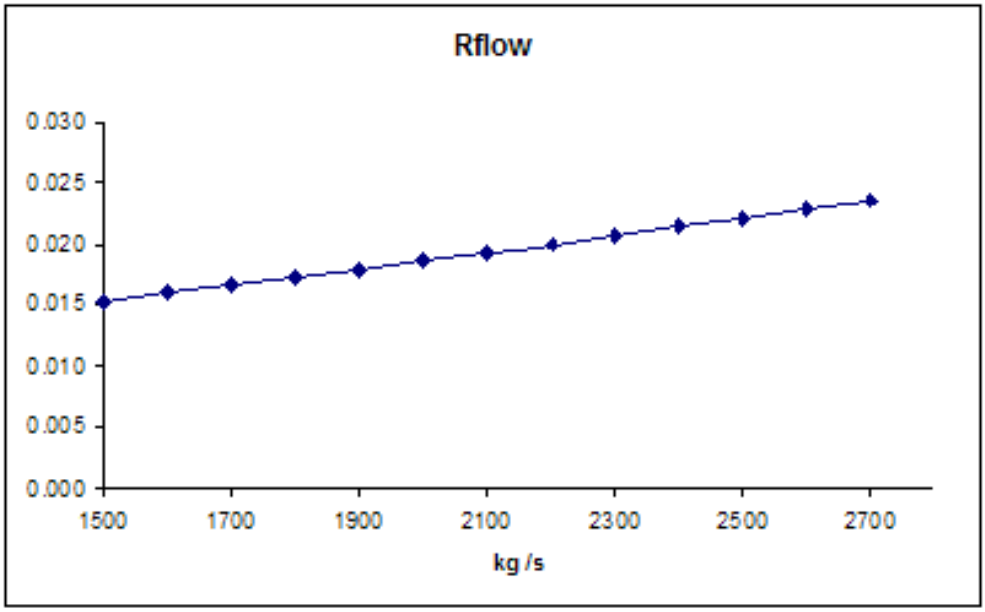

Figure 80: Flow resistance of convex cone model with fine perforate

As we can observe there are no irregularities in the flow resistance characteristics in all four solutions.

There is a possibility that the estimate of flow rates is inaccurate and more data need to be gathered or the simulation can be performed at a larger range of flow rates.

12.4 Discussion

The results do not show any fluctuation in the flow resistance for all four simulations. This suggests that there the change in blast basket termination does not have a direct influence on the level of infrasound described by Freuler and Montgomery [75]. However, the possibility remains that the "desired" flow resistance characteristics could be a cell property rather than a blast basket termination property. Fluctuating separation/re-attachment from the inlet or exhaust baffles might be a cause. This is to be the focus of the 2nd stage of the investigation. The change in blast basket termination might move the cell flow rate close to the irregularity point if it exists.

The flow in the perforates is very complex and the a LES calculation with the two separate flow at the augmenter entrance simulating the engine and cell bypass flow may be appropriate for the task. Currently a single steam of flow at the augmenter entrance is simulated under the assumption that the flow is fully mixed; this may not

be true in all test cells and may affect the fidelity of the results. However, the inconclusive results from the RANs calculation did not provide confidence to perform a much more computationally expansive LES calculation. However LES calculations would be used for the 2nd stage of the investigation if the computational requirements can be met.

13 Acoustic Reflection Coefficients

If infrasound was generated during, the operation of a test cell, and the source is unidentifiable or source reduction is not possible, then mitigation during propagation is important.

This chapter presents one such mechanism not previously investigated: the use of acoustic reflection surfaces to contain the sound within the cell and eventually be attenuated. This was hypothesized at the end of chapter 11.3.1.

It utilises a mixture of CFD and analytical calculations to examine the hypothesis based on geometric model and flow data from the modelled cell.

13.1 Hypothesis

Noise measurements taken at various positions at the modelled cell suggests that noise levels outside the cell decreased whereas the noise levels inside the cell increased after the modifications. This observation suggests that the modifications resulted in more noise being reflected back into the cell. Details of the measurements are unfortunately not available to be published for reasons of commercial confidentiality.

Detailed analysis of the modifications, suggests that the boundary which is more likely to experience a change in acoustic reflection coefficient is the blast basket perforate. The modifications to the cone as well as the perforate itself suggests that the flow field at the blast basket perforate is likely to experience the largest change. This change in flow field is likely to have affected the acoustic reflection coefficient at the blast basket perforate.

The other significant modifications to the cell are the changes to the intake baffle meshing distances, removal of a perforated surface on the wall of the augmenter, blast basket cone and perforate. The modifications to the intake baffle meshing were intended to alter the possible pressure fluctuations within the test cell. However, the geometry changes are unlikely to have significantly altered flow pattern and thus the

reflection coefficient. The perforated surface on the augmenter wall causes the augmenter wall to act as a compliant or dissipative duct and its removal should only affect the noise attenuation and not the reflection coefficient.

13.2 Methodology

The methodology used for investigating the possible increase in acoustic reflection coefficient at the blast basket perforate, as detailed in the previous section, will consists of a combination of numerical (CFD) and analytical analysis.

These consist of two different parts, namely the CFD simulation of the local flow pattern at the perforate and the calculation of attenuation and reflection coefficients at the blast basket perforate.

Results gathered from simulations performed on geometric model of the cell prior to the modifications shall be termed pre-mod and the those performed on models incorporating them shall be termed post-mod.

13.2.1 CFD Portion

A 3D geometrical model was used for the numerical analysis and consists of the augmenter tube and the exhaust stack. An illustration of the model is shown in Figure 81.

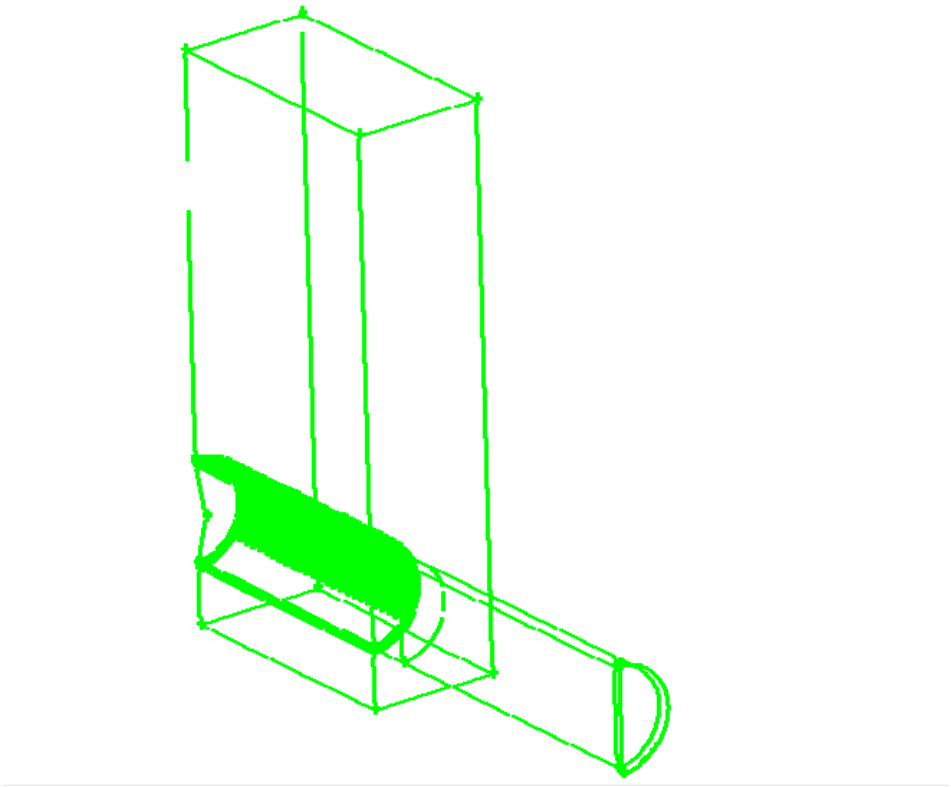

Figure 81: Acoustic Reflection Simulation Model

The modifications made to the geometry consist of two main modifications to the blast basket cone and perforate and are detailed below:

1. The cone has been lengthened from a pre-mod cone with an apex of 150° to a post-mod cone with an apex of 80°.
2. Changes have been made to the perforated surface of the blast basket. The pre-mod perforate has holes only at the top 230° of the surface whereas in the post-mod perforate, the holes have been added to the remaining 130° and blocker plates have been added to the top 230° blocking off 5 out of 7 rows of holes.

There are a number of simplifications between the actual cell sections and the model and are listed below:

1. The exhaust baffles were excluded in the model. The exhaust stack was deemed not to have a significant effect on the local flow pattern at the blast basket perforate.

2. The blast basket perforates were coarsened as a result of memory limitations. The resulting perforates were created by combining 16 actual holes into 1 larger hole at an appropriate location.
3. Only the right-half (looking into the augmenter) of the augmenter and exhaust stack is modelled and a symmetry boundary condition is used.

No convergence tests were conducted at the time of the writing of this thesis due to time and computing memory issues. Thus, only the trends exhibited by the results should be analysed and the actual numerical values should be taken with caution.

The Fluent solver parameters used are as follows:

- Mesh size ≈ 4 - 5 mil. tetrahedral cells
- Compressible flow solver
- Second order discretisation scheme
- SST-kω turbulence model

The boundary conditions used are as follows:

- Augmenter inlet – mass flow inlet
- Perforated section – actual holes were modelled so no boundary condition was needed
- Exhaust stack outlet – pressure outlet

Fluent was used to calculate the angle at which the flow exits the augmenter at each perforate. Each individual angle value at the perforate will be "combined" into an average value for the entire surface. For simplicity of expression, this value will be termed the cross-to-grazing flow ratio. This value is an integral parameter in the subsequent analytical analysis.

13.2.2 Analytical Portion

The analytical portion of the analysis consists of three main empirical formulae to calculate the acoustic impedance across the perforate [73]:

Viscous Moving Medium [73]

$$Z = \frac{V_{\text{wave propagation}}}{A_{\text{tube}}}\left(1 - k_1 + jk_1\right)$$

$$k_1 = \frac{\left(\frac{1}{r_{\text{tube}} \times V_{\text{wave propagation}}}\sqrt{\frac{\text{rpm} \times \mu}{2 \times \rho_{\text{mean}}}}\right)}{\text{wave no.}_{\text{free medium}}} + \frac{\left[\left(\frac{0.0072 + \frac{0.612}{\text{Re}^{0.35}}}{d_{\text{tube}}}\right) \times \text{Mach}_{\text{mean}}\right]}{\text{wave no.}_{\text{free medium}}} \quad \textbf{(13)}$$

Perforates in Cross Flow [73]

$$z = \frac{0.514 \times \frac{d_{\text{tube}} \times \text{Mach}_{\text{mean}}}{L_{\text{perforate}} \times \phi}}{\phi} + \frac{j0.95 \times \frac{2\pi}{\lambda}\left[\frac{\left(T_{\text{tube}} + 0.75 \times d_{\text{hole}}\right)}{\phi}\right]}{\phi} \quad \textbf{(14)}$$

Perforates in Grazing Flow [73]

$$z = \frac{7.337 \times 10^{-3}\left(1 + 72.23 \times \text{Mach}_{\text{mean}}\right)}{\phi} + \frac{j2.245 \times 10^{-5} \times \left(1 + 51 \times T_{\text{tube}}\right)\left[\frac{\left(1 + 204 \times d_{\text{hole}}\right) \times f}{\phi}\right]}{\phi} \quad \textbf{(15)}$$

As the flow at the blast basket perforate is neither purely cross nor grazing flow, a weighted average was used to calculate the impedance of the flow through the perforate.

The calculation of the reflection coefficient at an acoustic surface utilises the difference in acoustic impedances and can be calculated using the formula below [73].

$$\text{Acoustic reflection coefficient} = \frac{\frac{Z_2}{Z_1} - \sqrt{1 - \left(\frac{c_2}{c_1} - 1\right)\tan^2\alpha}}{\frac{Z_2}{Z_1} + \sqrt{1 - \left(\frac{c_2}{c_1} - 1\right)\tan^2\alpha}} \quad \textbf{(16)}$$

subscript 1 and 2 denote properties on both sides of the reflection boundary

13.3 Results

The results will be presented in two sections with the first section showing the cross flow to grazing flow ratio differences and the second section presenting the reflection coefficients.

13.3.1 Cross Flow to Grazing Flow Ratio

The post-mod model shows a slightly higher cross flow to grazing flow ratio. The post-mod model shows a 92% ratio as compared to 91% for the pre-mod model. With a higher cross flow to grazing flow ratio, a higher reflection coefficient was expected. The difference between the ratios is very low but, as mentioned in the earlier sections, the current model has not gone through the convergent tests and an error can be expected potentially yielding an even higher ratio difference.

To illustrate the point, a model utilising a polyhedral mesh generated from the post-mod model using Fluent's inbuilt function showed a cross flow to grazing flow ratio of 96%. To distinguish between the post-mod tetrahedral mesh (generated using Gambit) and post-mod polyhedral mesh, the polyhedral model will be termed post-mod-poly as opposed to post-mod-tetra.

13.3.2 Reflection Coefficient

The post-mod model showed a high cross flow to grazing flow ratio. The post-mod-poly model also showed a higher reflection coefficient compared to the pre-mod model.

Figure 82 illustrates the results. When interpreting the information, take note that the amount of reflection is determined by the absolute value of the reflection coefficient. The sign indicates the type of reflection [78].

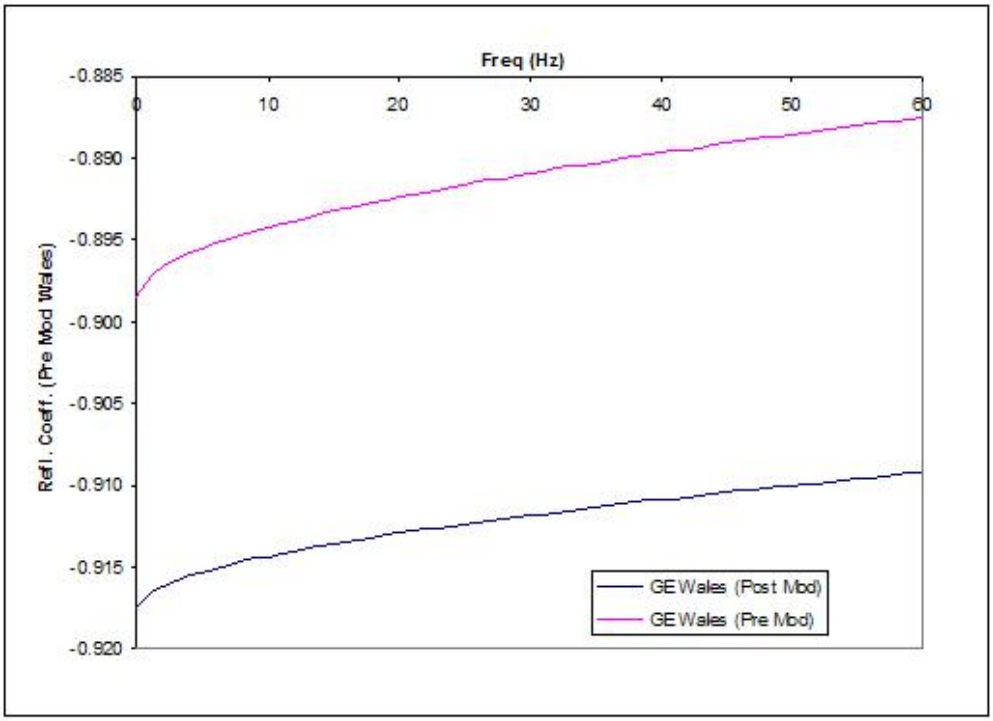

Figure 82: Reflection Coefficient between Pre-mod and Post-mod Poly Model

If a source of 140 dB is be assumed for the engine exhaust noise, then the difference in reflection coefficient between the pre-mod and post-mode cell would result in a reduction of noise emission at 10 Hz of 3 dB.

13.4 Conclusion

Calculations suggest that the reflection coefficient of the blast basket perforate was changed as a result to the modifications to the cell. The post-mod reflection coefficient was calculated to be about 2% higher than in the pre-mod scenario. This would correspond to a reduction of infrasound of about 3 dB.

The absence of convergent tests implies that complete confidence in the results gathered is not possible especially given the fact that a change in the structure of the mesh can produce a change of about 4%. Convergent tests, especially mesh convergence test, were not conducted at the time of writing of this thesis because of computing memory issues. Due to the large number of geometrically tiny perforate holes, the current model is already approaching the upper limit of the computing resources available.

However, there is strong confidence that the trends exhibited by the results are still relevant. Thus, there exists a strong possibility that practical modifications to the cell can alter the reflection coefficients at the blast basket perforate (or other parts of the cell) as it seemed to have in the modelled cell. The confidence in the trends exhibited stems from the fact that a reduction in low frequency sound measured outside the "problem" cell happens concurrently with an increase the same frequency sound inside the cell. Calculations detailed in chapter 14 indicate that the exhaust jet noise is reduced after the modifications further adding confidence to this acoustic reflection hypothesis.

In addition, Figure 82 shows that reflection of sound is more effective at lower frequencies. This makes the use of acoustic reflection surfaces to control infrasound very effective.

A simple modification which may be attractive to current test cell operators with a problematic test cell is to reduce the size of the perforated holes. Reducing the size of the perforated holes will increase the reflection coefficient. In making this modification, care must be taken to increase the number of holes so that the porosity and hence flow resistance remains constant. This is to keep the flow conditions similar and prevent the need for recalibration of the cell.

14 Engine Jet Velocity

Engine exhaust noise makes up a large proportion of the noise generated by a JETC. This chapter investigates the possibility of lowering the engine exhaust noise by simple modifications to the JETC and test configuration. The modifications investigated are the mounting position of the engine within the main chamber and the augmenter diameter.

The basic principle is that these modifications could cause a change in the CBR thus decreasing the relative velocity differences between the jet and bypass flow and hence the jet noise produced.

14.1 Hypothesis

A jet engine test cell is a structure meant for the testing of engines after overhaul. It does this in an environment that is as close as possible to the operating condition on the aircraft. However, this is not always possible and subtly each test cell is different from the others. Some of these subtle differences are due to the construction of the test cell including the main structures such as the baffles, blast basket and augmenter tube. The relative position of the engine to the augmenter entrance (engine exhaust – augmenter spacing) is also a contributing factor.

These subtle differences affect the air flow upstream of the engine intake (distortion index) as well as the engine exhaust and the cell bypass flow (efficiency of the test cell). In this section the main effects of concern is how changes in the cell bypass flow results in a change in the engine exhaust noise.

The engine exhaust is a high velocity jet and the noise generated from a flow jet is strongly correlated with the velocity difference between the jet and the surroundings governed by the following equation [79]:

$$P_{acoustic} = K\frac{\rho^2 d^2 (\Delta V)^8}{\rho_0 {c_0}^5} \quad (17)$$

subscript 0 denotes properties of surrounding medium

This equation arises from the pioneering work of Lighthill [80]

Following this trend of thought, changes in the cell bypass ratio cetaris paribus would affect the slip velocity ΔV and subsequently the engine exhaust noise and the noise emission of the test cell. As $P_{acoustic} \propto \Delta V^8$, therefore a change in ΔV can have a large change in $P_{acoustic}$. A small change in ΔV of 3 m/s would result in a change in SPL of 3 dB.

It is hypothesized that changes to the augmenter diameter as well as the distance between the engine exhaust and augmenter entrance will have a significant effect on the cell bypass ratio and hence the noise emission of the test cell.

14.2 Methodology

The methodology used to investigate this hypothesis utilises a combination of numerical CFD simulations to predict the cell bypass flow changes and analytical calculations used to calculate the acoustic power.

This investigation was performed in collaboration with a fellow University of Canterbury PhD candidate Jordan Gilmore. Gilmore performed the CFD calculations as part of his thesis work and information regarding the calculations can be found in his thesis [60]. As the author of this thesis is not involved in the CFD calculations, the model and solver information will not be presented in detailed here. However, illustrations of the engine and cell models (Figure 83 and Figure 84) basic geometries of the model will be presented here to help in appreciation of the results:

- Engine Exhaust Diameter: 2.7m (the engine model used was the R-R Trent 500)
- Engine Exhaust Flow rate: ≈ 880 kg/s
- Augmenter Diameter: 3 – 6.75m

- Cell Cross-Sectional Area: 10 x 10 m

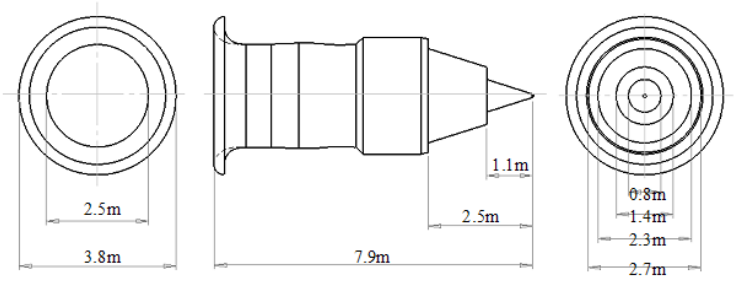

Figure 83: R-R Trent Engine Model

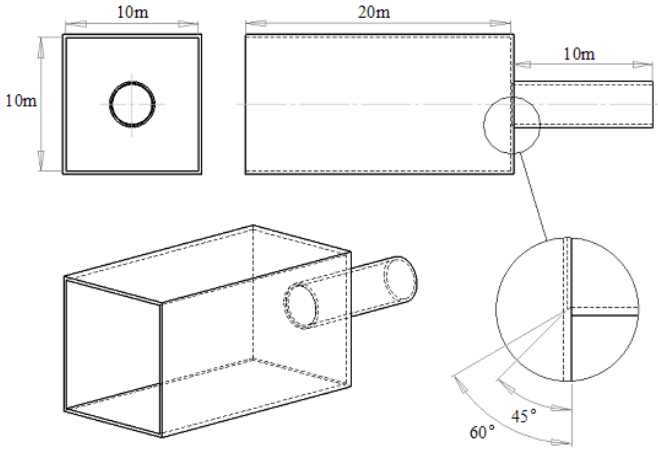

Figure 84: Test Cell Model for Jet Noise Simulations

The study of jet noise was pioneered by M. J. Lighthill [80]. He postulated that the acoustic radiation takes the characteristics of quadrupoles. He found, from the application of the laws of conservation of mass and momentum, the famous inhomogeneous wave equation for the density of the medium:

$$\frac{\partial^2 \rho}{\partial t^2} - c^2 V^2 \rho = \frac{\partial^2 T_{i,j}}{\partial x_i \partial x_j} \tag{18}$$

For a circular free jet, the acoustic power can be estimated using the following equation:

$$P_{acoustic} = K \frac{\rho_{jet}{}^2 d_{jet}{}^2 V_{jet}{}^8}{\rho_0 c_0{}^5} \tag{19}$$

subscript 0 implies properties of surround medium

As the equation implies, the acoustic power of a circular jet is strongly influenced by V, the velocity of the jet. However, the exhaust jet in the test cell is not a free jet and the enclosed environment produces a suction pump effect driving the entrained bypass flow, hence the surrounding is not stagnant. In such a situation, V should be replaced with ΔV and the equation for acoustic power modifies to the following:

$$P_{acoustic} = K\frac{\rho^2 d^2 (\Delta V)^8}{\rho_0 {c_0}^5}$$

$$= K\frac{\rho^2 d^2 (V - V_0)^8}{\rho_0 {c_0}^5}$$

$$\text{Let } V = \frac{\dot{m}}{\rho A}$$

$$P_{acoustic} = \frac{\rho^2 d^2 \left(\frac{\dot{m}}{\rho A} - \frac{\dot{m}}{\rho_0 A_0}\right)^8}{\rho_0 {c_0}^5}$$

If we take power ratio between two scenarios:

$$\frac{P_{acoustic,1}}{P_{acoustic,2}} = \frac{\frac{\rho^2 d^2 \left(\frac{\dot{m}_1}{\rho_1 A_1} - \frac{\dot{m}_{0,1}}{\rho_{0,1} A_{0,1}}\right)^8}{\rho_{0,1} {c_{0,1}}^5}}{\frac{\rho^2 d^2 \left(\frac{\dot{m}_2}{\rho_2 A_2} - \frac{\dot{m}_{0,2}}{\rho_{0,2} A_{0,2}}\right)^8}{\rho_{0,2} {c_{0,2}}^5}}$$

If we assume difference in the densities and hence speed of sound are minimal then,

$$\frac{P_{acoustic,1}}{P_{acoustic,2}} = \frac{d^2 \left(\frac{\dot{m}_1}{A_1} - \frac{\dot{m}_{0,1}}{A_{0,1}}\right)^8}{d^2 \left(\frac{\dot{m}_2}{A_2} - \frac{\dot{m}_{0,2}}{A_{0,2}}\right)^8} \quad \textbf{(20)}$$

This will be the analytical equation used to investigate the changes in acoustic power.

Two parameters will be changed and their effects analysed. They are the relative position of the engine in the main engine chamber and the diameter of the augmenter tube. The changes will be performed cetaris paribus in order to facilitate the investigation of the effects of a change in each of these parameters individually.

Five engine positions (2.750, 3.500, 4.150, **4.800**, and 5.500) and twelve augmenter diameters (3.000, 3.500, 3.750, 4.000, 4.250, 4.500, 4.750, **5.000**, 5.500, 6.000, and 6.250) were investigated, with the **bold font** indicating the baseline scenarios. The dimensions are given in m. The baseline scenario corresponds approximately to a particular test cell.

14.3 Results

The results will be presented in tabular form comparing each scenario with the baseline scenario. Three sets of results will be presented, showing the effects of engine position, augmenter size and both respectively. Each set of results will first show the acoustic power ratio then the acoustic power change in terms of dB.

The first set of results is as follows:

Table 9: Acoustic power ratio comparisons for changing engine positions

Acoustic Power Ratio (W)						
		Engine Exhaust --> Augmenter Spacing (m)				
Dia (% cell)	**Dia (m)**	**2.750**	**3.500**	**4.150**	**4.800**	**5.500**
0.300	**3.00**	0.996	0.996	0.998	1.000	1.000
0.350	**3.50**	0.998	0.999	1.000	1.000	1.001
0.375	**3.75**	0.999	1.000	1.000	1.000	1.001
0.400	**4.00**	1.000	1.001	1.001	1.000	1.000
0.425	**4.25**	1.004	1.002	1.001	1.000	0.999
0.450	**4.50**	1.007	1.005	1.003	1.000	1.000
0.475	**4.75**	1.012	1.006	1.002	1.000	0.993
0.500	**5.00**	1.027	1.016	1.018	1.000	0.992
0.550	**5.50**	1.090	1.055	1.022	1.000	0.985
0.600	**6.00**	1.151	1.066	1.000		
0.625	**6.25**	1.383	1.214	1.117	1.000	0.909

Table 10: Acoustic power change comparisons for changing engine positions

Acoustic Power Change (dB)						
		Engine Exhaust --> Augmenter Spacing (m)				
Dia (% cell)	**Dia (m)**	2.750	3.500	4.150	4.800	5.500
0.300	**3.00**	-0.016	-0.017	-0.009	0.000	0.001
0.350	**3.50**	-0.008	-0.004	-0.002	0.000	0.005
0.375	**3.75**	-0.003	-0.001	0.000	0.000	0.006
0.400	**4.00**	0.001	0.004	0.004	0.000	0.000
0.425	**4.25**	0.016	0.011	0.006	0.000	-0.004
0.450	**4.50**	0.030	0.021	0.015	0.000	0.000
0.475	**4.75**	0.053	0.028	0.007	0.000	-0.031
0.500	**5.00**	0.116	0.068	0.079	0.000	-0.034
0.550	**5.50**	0.375	0.231	0.096	0.000	-0.064
0.600	**6.00**	0.610	0.278	0.000		
0.625	**6.25**	1.409	0.843	0.482	0.000	-0.413

The second set of results:

Table 11: Acoustic power ratio comparisons for changing augmenter diameter

Acoustic Power Ratio (W)						
		Engine Exhaust --> Augmenter Spacing (m)				
Dia (% cell)	**Dia (m)**	**2.750**	**3.500**	**4.150**	**4.800**	**5.500**
0.300	**3.00**	1.436	1.451	1.450	1.480	1.492
0.350	**3.50**	1.366	1.382	1.380	1.406	1.418
0.375	**3.75**	1.321	1.337	1.334	1.358	1.371
0.400	**4.00**	1.269	1.284	1.280	1.303	1.313
0.425	**4.25**	1.212	1.224	1.219	1.240	1.248
0.450	**4.50**	1.145	1.155	1.151	1.168	1.177
0.475	**4.75**	1.075	1.080	1.072	1.090	1.091
0.500	**5.00**	1.000	1.000	1.000	1.000	1.000
0.550	**5.50**	0.841	0.823	0.796	0.793	0.787
0.600	**6.00**	0.668	0.626	0.586		
0.625	**6.25**	0.588	0.522	0.479	0.436	0.400

Table 12: Acoustic power change comparisons for changing augmenter diameter

Acoustic Power Change (dB)						
		Engine Exhaust --> Augmenter Spacing (m)				
Dia (% cell)	**Dia (m)**	**2.750**	**3.500**	**4.150**	**4.800**	**5.500**
0.300	**3.00**	1.571	1.618	1.615	1.703	1.739
0.350	**3.50**	1.355	1.406	1.398	1.479	1.518
0.375	**3.75**	1.211	1.260	1.250	1.330	1.370
0.400	**4.00**	1.035	1.085	1.074	1.149	1.184
0.425	**4.25**	0.834	0.876	0.861	0.934	0.964
0.450	**4.50**	0.588	0.626	0.610	0.674	0.708
0.475	**4.75**	0.312	0.335	0.303	0.376	0.380
0.500	**5.00**	0.000	0.000	0.000	0.000	0.000
0.550	**5.50**	-0.750	-0.847	-0.992	-1.009	-1.038
0.600	**6.00**	-1.749	-2.033	-2.322		
0.625	**6.25**	-2.310	-2.827	-3.200	-3.602	-3.980

The third set of results:

Table 13: Acoustic power ratio comparisons when changing both engine positions and augmenter diameter

Acoustic Power Ratio (W)						
		Engine Exhaust --> Augmenter Spacing (m)				
Dia (% cell)	**Dia (m)**	**2.750**	**3.500**	**4.150**	**4.800**	**5.500**
0.300	**3.00**	1.475	1.474	1.477	1.480	1.481
0.350	**3.50**	1.403	1.404	1.405	1.406	1.407
0.375	**3.75**	1.357	1.358	1.358	1.358	1.360
0.400	**4.00**	1.303	1.304	1.304	1.303	1.303
0.425	**4.25**	1.244	1.243	1.242	1.240	1.239
0.450	**4.50**	1.176	1.173	1.172	1.168	1.168
0.475	**4.75**	1.104	1.097	1.092	1.090	1.083
0.500	**5.00**	1.027	1.016	1.018	1.000	0.992
0.550	**5.50**	0.864	0.836	0.810	0.793	0.781
0.600	**6.00**	0.687	0.636	0.597		
0.625	**6.25**	0.603	0.530	0.487	0.436	0.397

Table 14: Acoustic power change comparisons when changing both engine positions and augmenter diameter

Acoustic Power Change (dB)						
		Engine Exhaust --> Augmenter Spacing (m)				
Dia (% cell)	**Dia (m)**	**2.750**	**3.500**	**4.150**	**4.800**	**5.500**
0.300	**3.00**	1.688	1.686	1.694	1.703	1.705
0.350	**3.50**	1.471	1.474	1.477	1.479	1.483
0.375	**3.75**	1.327	1.329	1.330	1.330	1.335
0.400	**4.00**	1.151	1.153	1.153	1.149	1.149
0.425	**4.25**	0.950	0.945	0.940	0.934	0.929
0.450	**4.50**	0.704	0.694	0.689	0.674	0.674
0.475	**4.75**	0.428	0.404	0.383	0.376	0.345
0.500	**5.00**	0.116	0.068	0.079	0.000	-0.034
0.550	**5.50**	-0.634	-0.778	-0.913	-1.009	-1.073
0.600	**6.00**	-1.633	-1.964	-2.243		
0.625	**6.25**	-2.193	-2.759	-3.120	-3.602	-4.015

14.4 Discussions and Conclusion

The results provided in Table 9 to Table 14 shows that controlling the CBR of a test cell have the potential to be an effective measure against test cell noise emission (both infrasonic and audible range). Two possible modifiable parameters were investigated namely the engine position and diameter of augmenter. From the results, a 1 – 3 dB reduction in engine jet noise can be expected.

For current test cell operators, a change in the engine position is a relatively easier task to perform as compared to the other modifications highlighted in this thesis including the modification of augmenter diameter discussed in this chapter.

With the augmenter diameter kept constant (results set 1); a change in the position of the engine has neglible effects in cells with smaller augmenter diameter. The effects increase in cells with larger diameter with the first significant change (situation dependent) being recorded in cells with an augmenter diameter of 6m. Another interesting observation is in the reversal of trends before and after a cell with an augmenter diameter of 4m. Cells with augmenter less than 4m in diameter shows decreasing acoustic power as the distance are reduced. This trend is clearly reversed in cells with augmenter diameter of 4.25m and above. These results are plotted in graphs and shown in Figure 85 to Figure 95 below for easier analysis. The critical augmenter diameter size is probably a property of the engine exhaust size with the trend reversal occurring at conditions where the entire exhaust stream enters the augmenter as opposed to when exhaust stream is larger than the augmenter diameter. The critical augmenter diameter is not universal but predictions can be made for other engines sizes.

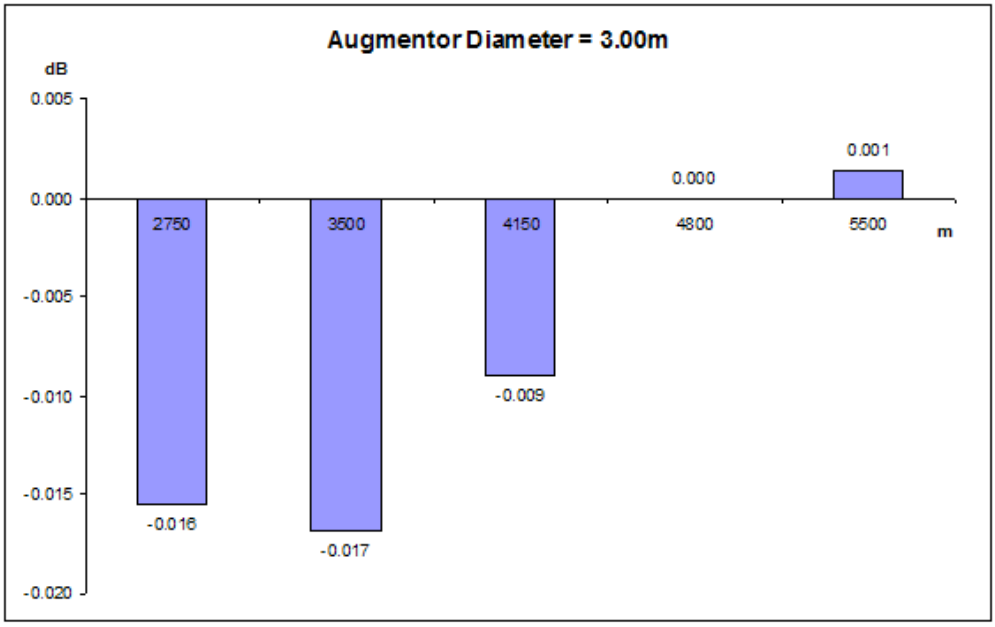

Figure 85: Comparison of engine noise reduction augmenter diameter of 3.00 m

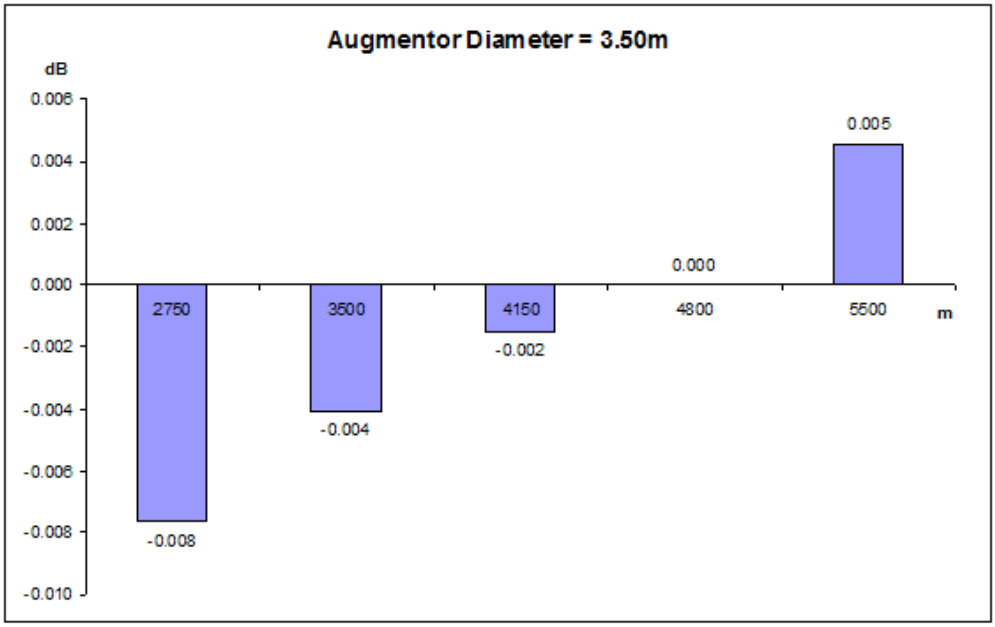

Figure 86: Comparison of engine noise reduction augmenter diameter of 3.50 m

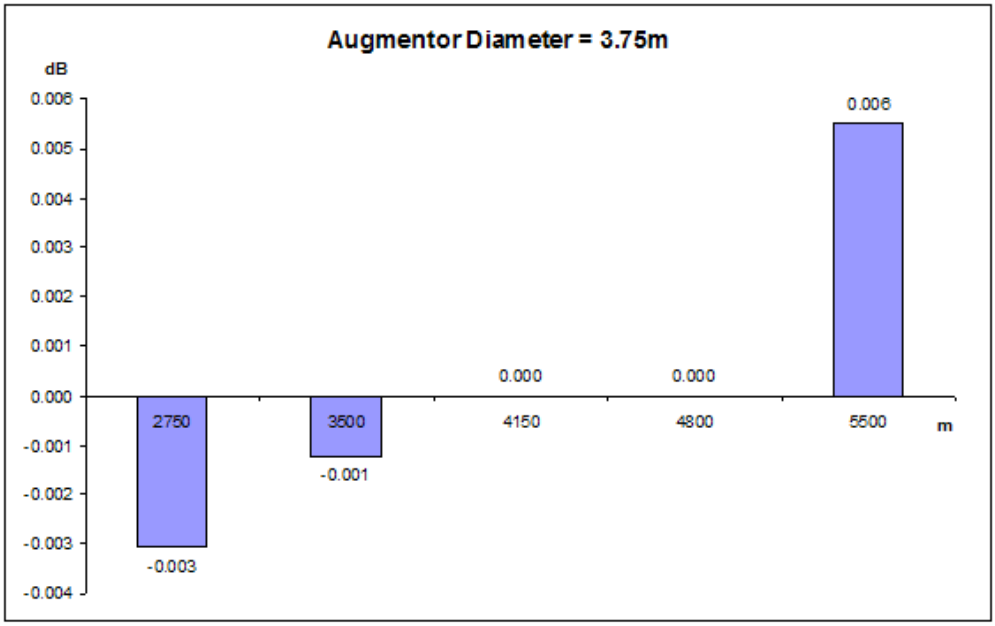

Figure 87: Comparison of engine noise reduction augmenter diameter of 3.75 m

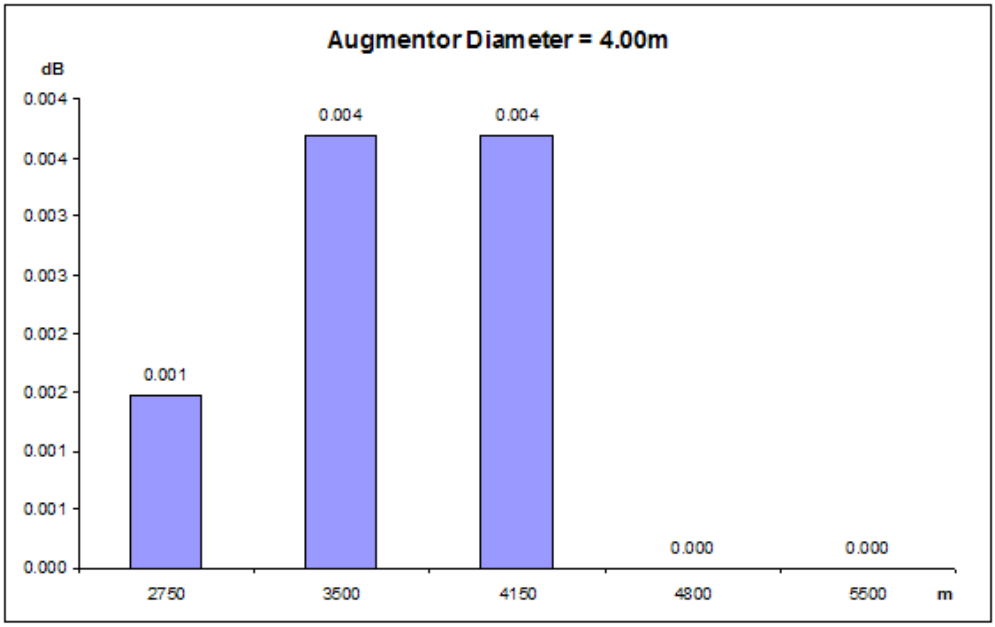

Figure 88: Comparison of engine noise reduction augmenter diameter of 4.00 m

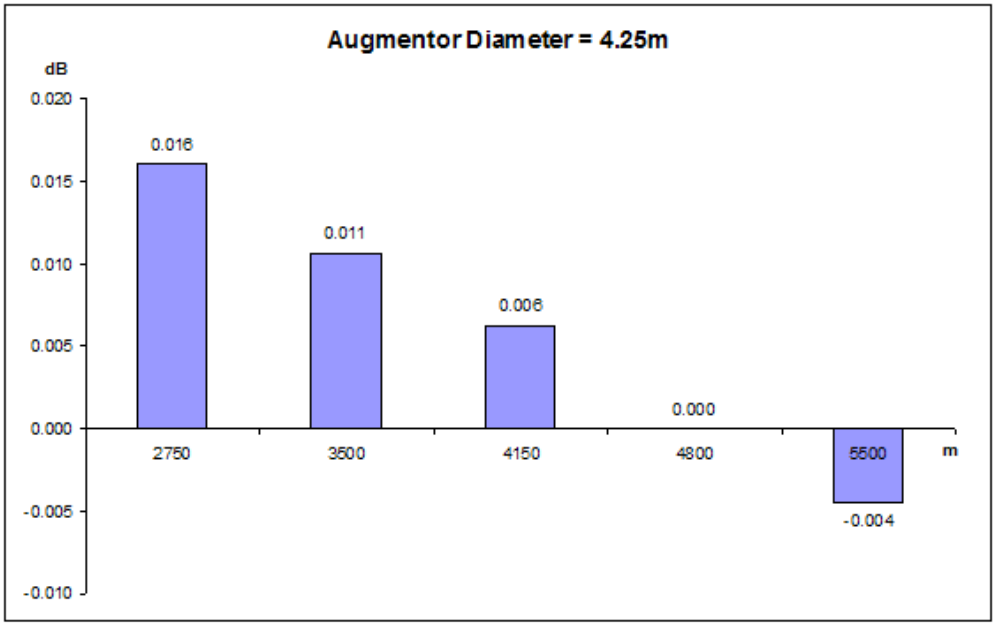

Figure 89: Comparison of engine noise reduction augmenter diameter of 4.25 m

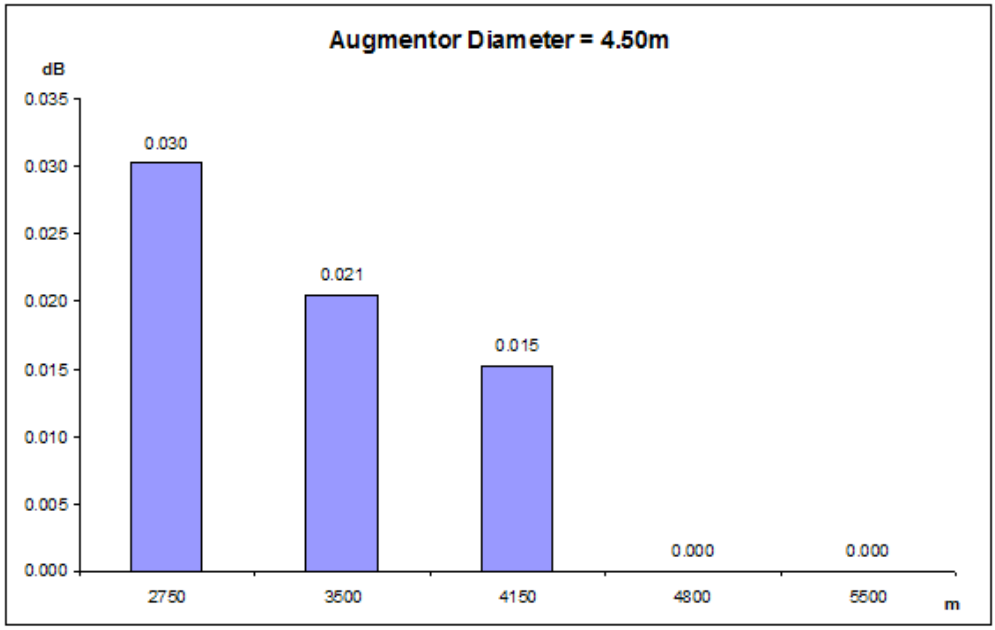

Figure 90: Comparison of engine noise reduction augmenter diameter of 4.50 m

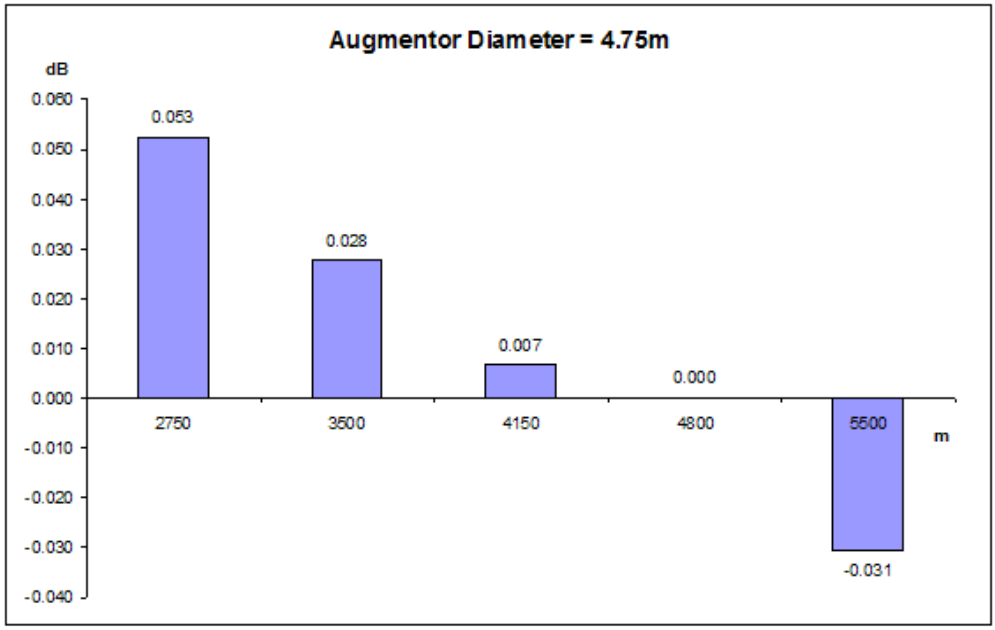

Figure 91: Comparison of engine noise reduction augmenter diameter of 4.75 m

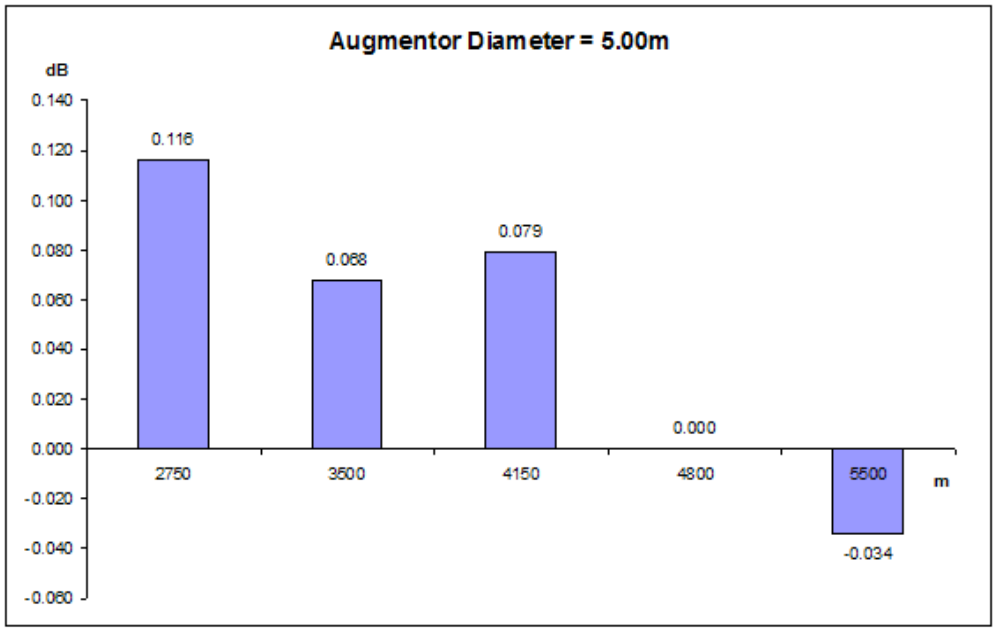

Figure 92: Comparison of engine noise reduction augmenter diameter of 5.00 m

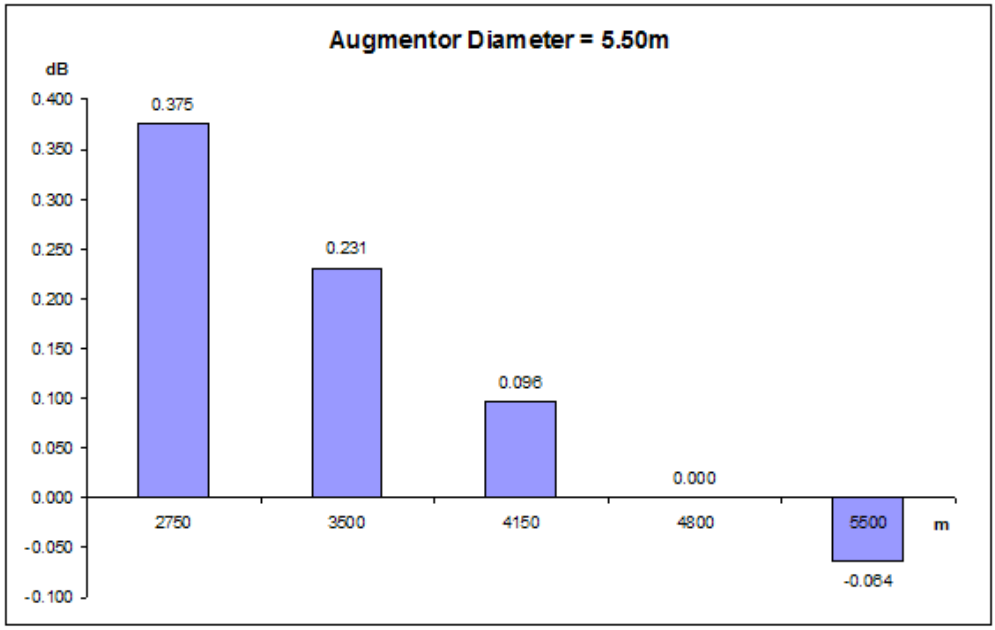

Figure 93: Comparison of engine noise reduction augmenter diameter of 5.50 m

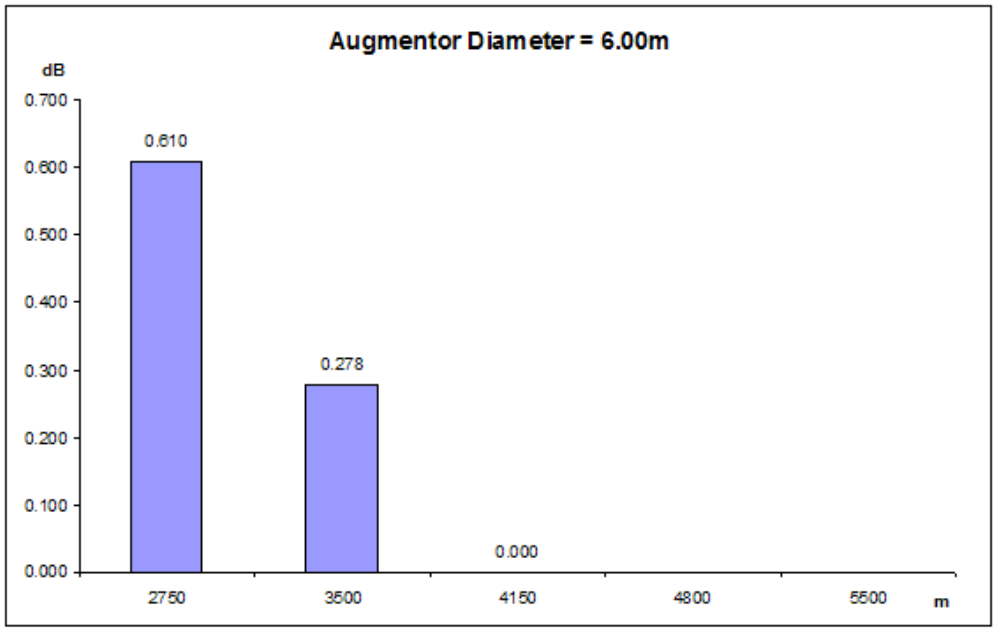

Figure 94: Comparison of engine noise reduction augmenter diameter of 6.00 m

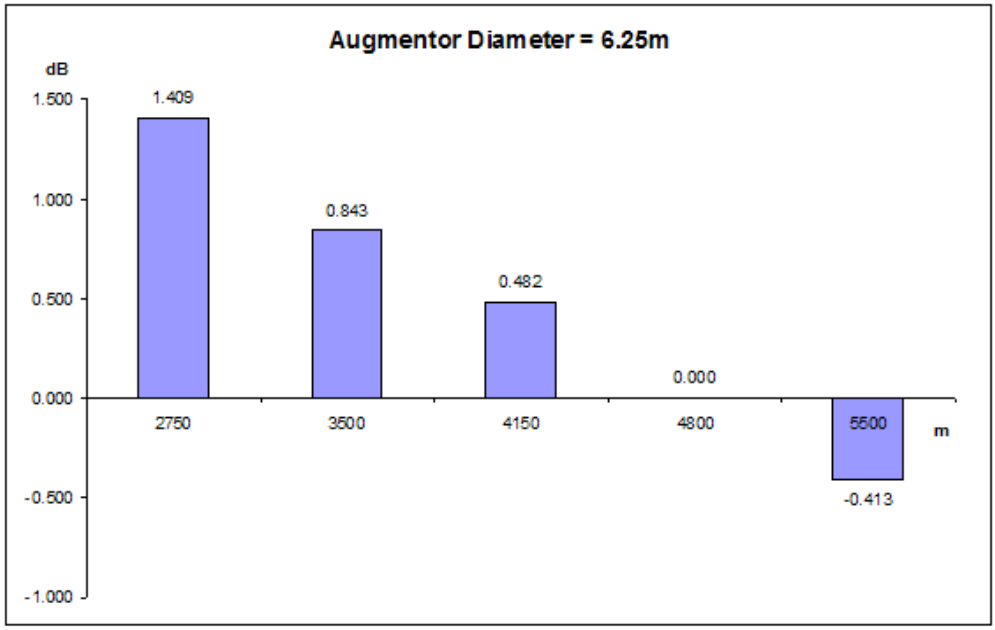

Figure 95: Comparison of engine noise reduction augmenter diameter of 6.25 m

When the relative position of the engine is kept constant, a larger augmenter diameter reduces the flow resistance thus increasing the bypass flow. This observation is consistent across the engine positions investigated and is shown in Figure 96

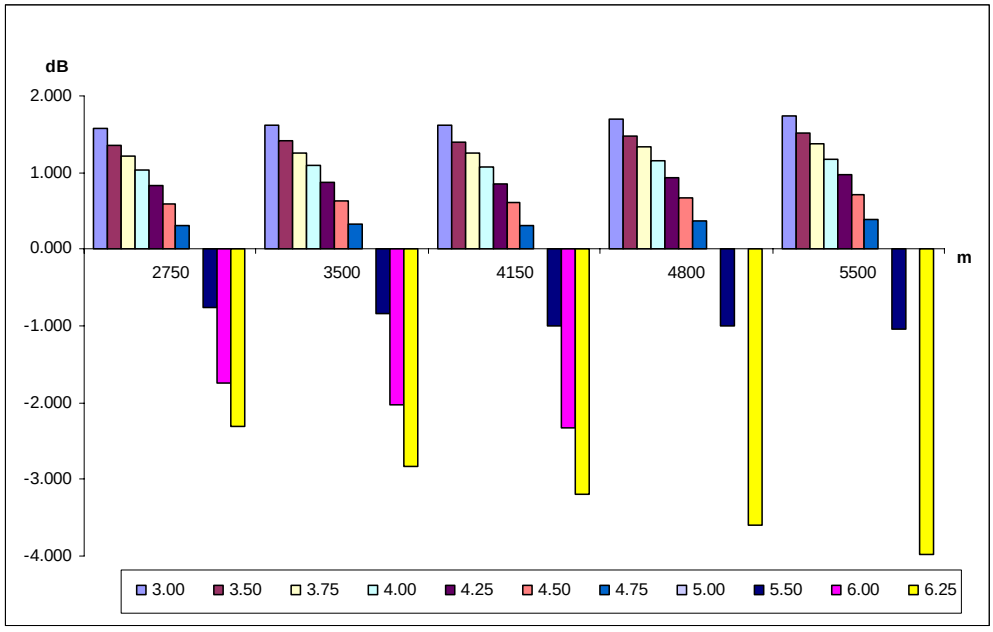

Figure 96: Comparison of engine noise reduction when engine position is kept constant

15 Summary and Concluding Remarks

This chapter provides a summary of the entire thesis and highlights the situation before and after the investigations were carried out.

15.1 Summary of Achievements

This chapter attempts to provide the reader with a macroscopic view of the achievements attained as a result of the work resulting in this thesis. Only achievements relating directly to the scope or test cell operation, design and construction will be included. Achievements relating to methodologies or use of software will not be included unless it represents a breakthrough and novel way of using the software.

This chapter will be split into two sections dealing with the two different aspects of work, namely the vortex problem and the infrasound problem. It is expected that some overlap may occur and these will be included in the next section on "Concluding Remarks".

15.1.1 Vortex Ingestion Problem

Prior to the investigations described in this thesis, knowledge about the problem of vortices forming and being ingested into an engine core during operation in the test cell was limited. The author has advanced the understanding of the phenomenon and the effects of ambient and geometric parameters have on these vortices.

Prior to the investigations, investigations relating to the topic were restricted to the take-off scenario or that of a suction inlet near a single solid surface. No investigations were carried out on models that have four or more solid surfaces surrounding a suction inlet such as that in the test cell. There has also been investigations attempting to describe the vortices, both the ones concentrating ambient vorticity or otherwise, which provide information on how and why the vortices are formed but no parametric studies on how ambient conditions promote or impede their

formation has been conducted, except for the effect of velocity gradient, especially in the test cell scenario.

Glenny [30] provided the only instance of an investigation on how ambient conditions promote or impede the formation of vortices but this was conducted for the take-off scenario. The ambient condition that he investigated was ambient vorticity in the form of the dimensionless Rossby number.

All prior investigations were conduced experimentally and no previous systematic CFD study was conducted.

The author first advanced the work of Glenny [30] by performing investigations on the effects of the presence of a ground boundary layer as well as the effects of the flow Reynolds number and size of suction inlet. Subsequently the author advanced these work by performing similar investigations on the test cell like model. A numbered summary of these work and their relationship with the probability of vortex formation, where applicable, are as follows:

Take-off Scenario

1. Effects and presence of a ground boundary layer (direct relationship)
2. Effects of the flow Reynolds number (inverse relationship)
3. Effects of the size of the suction inlet (direct relationship)

Test Cell Scenario

1. Discovery of the presence of the unsteady vortex forming regime
2. Effects of the ambient vorticity (direct relationship)
3. Effects of the flow Reynolds number (inverse relationship)
4. Effects of the size of the suction inlet (direct relationship)
5. Reasons for the preferential attachment of a vortex to the ceiling when formed

Although actual experimental validation of every investigated scenario was not carried out due to time and cost constraints, there are good evidences to suggest that the trends observed are accurate even if the actual numbers may not.

No actual test cell model was used in the investigation to prevent specific geometry related parameters from interfering and potentially obscuring and/or magnifying the effect ambient parameters.

The trends discovered in the investigation have far-reaching implications for the test cell industry in terms of future design and construction of new cells as well as the operation or modifications of current cells. Some of these are self-explanatory whilst others are not so obvious. The following sub-sections discuss the implications, which are not obvious, in detail.

15.1.1.1 Effects and Presence of a Ground Boundary Layer

The presence, and thickness, of a ground boundary layer shifts the threshold to a lower Vi/Vo thus increasing the probability of a vortex forming. This is most likely due to the lower velocity within the boundary close to the ground. Whether a vortex forms or is blown away is determined if the velocity between the solid surface and suction inlet is below the blow-away velocity of the set-up. Thus, Vo in the critical ratio Vi/Vo really should be the Vo within the boundary layer (which is lower then the ambient velocity) however; this is not always possible or convenient to measure. Hence, the general ambient velocity remains the most convenient way to measure Vo.

The results from this investigation clearly show that a thick boundary layer rapidly increases the probability of the formation of a vortex. Thus, caution should be taken in situations where an unusually thick boundary layer may be present.

15.1.1.2 Effects of Suction Inlet Size

An increase in the suction inlet size, cetaris paribus, will shift the threshold to a lower Vi/Vo thus increasing the probability of a vortex forming. This was hypothesized by Glenny [30] and replicated in current simulations and has very important implications for industrial applications. Aircraft engines have been getting bigger since the first engines appeared and would predictably continue in the same trend at least in the near future.

Results from this investigation, both the runway as well as the test cell scenario, will determine the design of new aircrafts and test cells. If the same level of safety is to be maintained a more than linear increase in the height of the engine or the size of the test cell is necessary for future larger engines. This is not due to increase in Reynolds number which has the opposite effect.

These results seemed to suggest the violation of the laws of dynamic scaling (based on Reynolds number). However Glenny [30] suggests a similar effect although he did not conduct any experimental validation on his hypothesis. Current investigation validates Glenny's hypothesis but not his reasoning. This is a potential area for future analysis beyond this thesis.

15.1.1.3 Effect of Ambient Vorticity

The vortex under investigation is the kind that concentrates ambient vorticity, hence it is obvious that the amount of ambient vorticity has a direct relationship with the probability of a vortex forming. This is also and validated by results. Steps should be taken to reduce the amount of ambient vorticity whenever possible. On the runway, ambient vorticity can be formed by crosswind or the presence of structures or objects around. Crosswind is also a potential source of vorticity in the test cell, see Appendix B.

15.1.2 Infrasound Problem

Prior to the investigations described in this thesis, knowledge about the problem of excessive infrasound being generated during the operation and testing of an engine in a test cell is limited. Previous research or investigations can be broadly characterised into two main types:

1. Detailed studies of one potential mechanism with simulations or experiments generally constrained to partial sections of test cells (e.g. augmenter tube entrance etc.) instead of the full cell. These investigations highlight the possibilities of infrasound being generated by these mechanisms but often stop short of being able to exclude the possibilities of other mechanisms.

These investigations also tended to study the mechanisms in detail and often overlooked the overall effects. In cases where the overall effects were studied and proved unaffected, little explanations were provided on the reasons for their failure.

2. Very broad general study of the test cell and identifying potential areas of problem without identifying any one particular mechanism. Freuler and Montgomery [75] performed such an investigation on a scaled model test cell. They successfully showed the relationship between the blast basket termination and the level of infrasound measured outside the cell model without much explanation on the actual mechanisms taking place. Hatlestad [81] performed another investigation of similar type when he used scale model to investigate different test cell configurations. Although Hatlestad did explain the rationale behind the two models, the study does not conclusively pinpoint any particular mechanism at work.

   Such investigations generally provide researchers with a good base to carry out future research and generate hypothesis and are particularly useful for the industry.

As a result of the division in the two research approaches, a universal set of well-understood infrasound prevention techniques is not available. There are many instances of techniques which worked perfectly in some cells but ineffective in others and it is often difficult to ascertain why they are not working.

The author set out initially to produce such a set of universal well-understood prevention techniques but was limited by time and budget amongst other factors. The author worked within the constraints to produced and test three different hypotheses with vary degrees of success:

1. No evidence to suggest that the results shown by Freuler and Montgomery [75] is a result of a change in the flow resistance characteristics leading to fluctuating flow in the cell causing the infrasound. Their results are likely due to other factors such as a change in reflection coefficient.
2. Provided evidence that a change in the reflection coefficient at the blast basket perforate is a potential mechanism to reduce infrasound propagation from the

cell. A 2% change in reflection coefficient corresponding to about 3 dB in noise emission seemed to be achieved in the modelled cell.

3. Provided evidence that a change in position of engine and size of augmenter tube is a potential mechanism to reduce engine noise, both in the infrasonic as well as audible range. A 1 – 3 dB reduction can be confidently predicted from the calculations.

The author has successfully introduced two possible methods of reducing the generation and propagation of infrasound from a test cell as well as detailed methodology to investigate and predict the reduction. These two new methods potentially target the entire sound spectrum (although different levels of effectiveness are expected at different frequencies) and are likely to be applicable to most test cells. These are revolutionary approaches not considered in the past but should be from now on for all current cell upgrades and new cell designs.

15.2 Concluding Remarks

The author has, through work presented in this thesis, advanced the level of understanding of vortex formation, due to the concentration of ambient vorticity, in the test cell. Previously unknown, though suspected, parametric relationships were discovered as a result of studies carried out to investigate their effects on the vortex formation threshold. The trends identified will help in the troubleshooting process or in future designs of a JETC.

For the infrasound work, the author set out to discover or attempted to advance the search for the “universal” solution and explanation for the generation and propagation of infrasound during the operation of test cell. This has been successful to some extent but the level of advancement is subjective.

What is certain is that the author has provided two new possible mitigation methods. These are the use of acoustic reflection surfaces to reduce noise emission from test cell and the modification of the cell bypass ratio to reduce engine exhaust noise. These two ideas have not been hypothesized nor investigated in the past.

16 Future Work

16.1 Future Work on Vortex Ingestion

Apart from more instances of experimental validation, there are some areas where the author would like to see being further investigated. These have been considered during the research period but were not carried out due to a lack of time or resources.

The most important of these are the linearization techniques for non-linear upstream or ambient velocity gradient. This is very important because a linear velocity gradient is a rare occurrence especially in the test cell scenario. Discovery of these linearization techniques increases the general applicability of research in this field thus tearing down the walls that limit their usefulness.

Two very important implications can be expected. First, it would enable easier and universal application of the data found in this thesis or in any past or future research in this field. This is extremely important in all research especially in engineering where practical application is essentially the ultimate goal of all engineers. Second, the discovery of these techniques would make it easier for future investigators in the field. In instances where simulation of actual ambient or upstream velocity profiles is difficult and time consuming but necessary, these techniques will be even more welcoming.

Critical to the discovery of these linearization techniques is a close to extensive compilation of the operational distortion indices in most of the major test cells around the world. Apart from this, CFD simulations or experimental approaches similar to that highlighted in Appendix B should be carried out to identify any potential source of ambient vorticity that are probable but not documented. In order to minimise the amount of simulations or experiments, a detailed methodology of analysing and comparing flow fields and vortices will be very useful.

Apart from the linearization techniques, additional parametric studies are always welcome.

16.2 Future Work on Infrasound Problem

The author set out to discover or attempted to advance the search for the "universal" solution and explanation for the generation and propagation of infrasound during the operation of test cell. This has been successful to a certain extent but the level of advancement, as a result of work in this thesis, is a highly subjective matter. It is still the author's desire for the discovery of this universal solution.

The first recommended future work is to complete the investigation that was not completed at the time of writing this thesis as outline in chapter 12.2. Additional modifications potentially leading to changes in reflection coefficients and engine exhaust slip velocity would be very welcomed.

The modelled cell had a calculated cut-off frequency of 30.87 and 11.78 Hz for the augmenter tube and exhaust stack respectively. Cut-off frequencies depend on the speed of sound and the geometry (see chapter 11.2.1). A potential solution to the infrasound problem could lie in raising the cut-off frequencies above the infrasonic range thus allowing only plane waves to propagate and attenuating higher order waves. This can be achieved by introducing stream-wise dividers in the appropriate cell locations to effectively reduce the relevant geometric dimensions (e.g., stream-wise dividers placed in the augmenter tube would reduce the effective diameter of the tube thus raising the cut-off frequency). Some existing cells have a divider running down from the top of the exhaust stack splitting the stack into two separate "channels".

As mentioned in earlier chapters, a universal infrasound generation and propagation mechanism is unlikely and each mechanism would require specific remedial actions. Hence any potentially "universal" solution would first require an extensive but commercially cost effective troubleshooting guide, which allows quick and accurate ways to identify the mechanisms in situ[2]. This guide should collate all or most of the currently known infrasound generation and propagation mechanisms and should contain definitive methods of identifying the presence of each of them in an industrial

[2] A latin phrase mean 'in place' or onsite

environment. Subsequently this guide can then be incorporated into a system of investigation methodologies and eventually an integrated testing software package.

Lastly a full cell acoustic model should be developed numerically. Previous investigations on the macro acoustic effects have used scaled model experiments. It is a very expensive undertaking in terms of both time and money, and a numerical model would be very welcomed. A simple analytical model is proposed in Appendix F.

References

[1] E. De Siervi, H. C. Viguier, E. M. Greitzer, and C. S. Tan, “Mechanisms of inlet vortex formation”, J. Fluids Mech., 124, pp 173 – 207, 1982.

[2] J. R. Partington, “A History of Greek Fire and Gunpowder”, 1960.

[3] Pratt and Whitney Customer Facilities Support, “Facility Planning Manual for PW4000 Engine Family”, 1994.

[4] C. A. Kodres and G. L. Murphy, “Jet Engine Test Cell Augmenter Performance”, J. of Propulsion and Power, Vol 14, No. 2, 1998.

[5] Unknown Author, “Correlation, Operation, Design, and Modification of Turbofan/Jet Engine Test Cells”, United States Department of Transportation, Federal Aviation Administration Advisory Circular, 2002.

[6] R. J. Freuler, “Recent Success in Modifying Several Existing Jet Engine Test Cells to Accommodate Large High Bypass Turbofan Engines”, AIAA 93-2542, 1993.

[7] H. Klein, “An aerodynamic screen for jet engines”, Institute of the Aeronautical Sciences, Paper 676, 1962.

[8] L. A. Robert and F. B. Garrett, “Ingestion of foreign objects into turbine engines by vortices”, NACA, TN 3330, 1955.

[9] J. L. Colehour, “A study of foreign particle ingestion for a 747 type inlet”, The Boeing Company, D6-23238, 1969

[10] J. L. Colehour and B. W. Farquhar, “Inlet vortex”, J. Aircraft, Vol 8, No. 1, pp 39 – 43, 1971.

[11] C. J. Johns, “The aircraft engine inlet vortex problem”, AIAA 2002-5894, 2002.

[12] O. Okai, M. Saito, M. Taki, A. Mochizuki, N. Nishiwaki, T. Mori and M. Fujoi, “Physiological parameters in human response to infrasound”, Proceedings of the Conference on Low Frequency Noise and Hearing, pp 121 – 129, 1980.

[13] S. Yamada, T. Kosaka, K. Bunya, and T. Amemiya, "Hearing of low frequency sound and influence on human body", Proceedings of the Conference on Low Frequency Noise and Hearing", pp 95 – 102, 1980.

[14] H. Moller and C. S. Pedersen, "Hearing at Low and Infrasonic Frequencies", Noise Health 2004, Vol. 6, pp 37 – 57, 2004.

[15] M. Garces, C. Hetzer, M. Merrifield, M. Willis and J. Aucan, "Observations of surf infrasound in Hawai'i", Geophys. Res. Lett., 30(24), 2264, 2003.

[16] G. Vassilatos, "Lost Science", Adventures Unlimited Press, Chapter 8, 2000.

[17] C. H. Chen, "Signal and Image Processing for Remote Sensing", CRC Press, 2007.

[18] C. Kenneally, "Surviving the Tsunami – What Dri Lanka's animals knew that humans didn't", Internet article address: http://www.slate.com/id/2111608, last accessed 18th Jun 2009.

[19] Unknown Author, "Can Animals Predict Disaster?", Internet address: http://www.pbs.org/wnet/nature/episodes/can-animals-predict-disaster/introduction/130/, last accessed 18th Jun 2009.

[20] V. Tandy and T. R. Lawrence, "Ghost in the Machine", Journal of the Society of Psychical Research, Vol. 62, No. 851, 1998.

[21] V. Tandy, "Something in the Cellar", Journal of Society of Psychical Research, Vol. 64, No. 860, 2000.

[22] A. Danielsson and U. Landstroem, "Blood pressure changes in man during infrasonic exposure", Acta Medica Scandinavica 217 (5), pp 531 – 535, 1985.

[23] U. Landstroem, R. Lundstroem and M. Bystroem, "Exposure to infrasound – perception and changes in wakefulness", J. of Low Frequency Noise and Vibration 2, pp. 1 – 11, 1983.

[24] C. A. Kodres, "Jet Engine Test Cell Noise Reduction", Naval Facilities Engineering Command Technical Review TR-2118-ENV, 2000.

[25] D. R. Schmidt, “Noise Levels of the NAS Cubi Point, T. P., TIO Test Cell During J52, J52/P408, F404, TF30/P414, and TF41 Engine Runups”, Naval Ocean Systems Center Technical Note 1501, 1987.

[26] C. Fadeley, “TECHEVAL of the ALF32T-10 Turbofan/Jet Engine Test Facility”, Naval Air Test Center Technical Report SY50-90-042, 1991

[27] D. L. Huff, “Noise Reduction Technologies for Turbofan Engines”, NASA TM 2007-214495, 2007.

[28] M. S. Howe, “Self-Excited Oscillations in Jet Engine Test Cells”, Journal of Fluids and Structures, Vol 1, pp 128 – 148, 1987.

[29] A. Nakayama and J. R. Jones, “Vortex formation in inlet flow near a wall”, 34th Aerospace Sciences Meeting and Exhibit, AIAA 96-0803, 1996.

[30] D. E. Glenny and N. G. T. E. Pyestock, “Ingestion of debris into intakes by vortex action”, Aeronautical Research Council CP no. 1114, 1970.

[31] S. O. Ridder and I. Samuelsson, “An experimental study of strength and existence domain of ground-to-air inlet ortices by ground board static pressure measurements”, Stockholm Royal Institute of Technology, KTH AERO TN 62, 1982.

[32] W. F. Wiles, British Patent 898 417, Rolls Royce Ltd, 1962.

[33] P. E. Rubbert et al., “A general method for determining the aerodynamics characteristics of fan-in wing configurations”, The Boeing Company, D-6-13476-1, 1967.

[34] Clark et al., “Gas Turbine Engine Test Cell”, US Patent 5293775.

[35] R. A. Dickman, H. W. Hehlnann, W. Hoelmert and R. J. Freuler, “A solution for aero-acoustic induced vibrations originating in a turbofan engine test cell”, AIAA 84-0594, 1984.

[36] G. Porges, “Applied Acoustics”, Peninsula Press, CA, 1987.

[37] R. E. Glass, “Acoustic Performance of Air-Cooled Jet Engine Test Facilities”, Naval Ocean Systems Center Technical Report 1142, 1986.

[38] R. E. Klingner, “Effective Noise Barrier Solutions for TxDOT”, Centre for Transportation Research Report CTR 0-1471-1, University of Texas, 1996.

[39] J. M. de Bedout, “Adaptive-Passive Noise Control with _Self-Tuning Helmholtz Resonators”, MSc Thesis, Purdue University, 1996.

[40] P. Lueg, “Process of Silencing Sound Oscillations”, United States Patent 2 043 416, 1936.

[41] L. J. Fogel, “Method of Improving Intelligence under Random Noise Interference”, United States Patent 2866848, 1958

[42] L. J. Fogel, “System for Improving Intelligibility”, United States Patent 2920138, 1960.

[43] L. J. Fogel, “Apparatus for Improving Intelligence under High Ambient Noise Levels”, United States Patent 2966549, 1960

[44] R. A. Graves Jr., “Computational Fluiddynamics – The Coming Revolution”, Astronautics and Aeronautics, Vol. 25, pp 20 – 29, 1982.

[45] J. D. Anderson, “Basic Philosophy of CFD”, Computational Fluid Dynamics: An Introduction, Springer-Verlag, pp 6, 1992.

[46] Z. Kopal, “Tables of Supersonic Flow around Cones”, Department of Electrical Engineering, Centre of Analysis, M.I.T., Cambridge, 1947.

[47] J. Boussinesq, “Théorie de I’Ecoulement Tourbillant”, Mem. Présentés par Divers Savants Acad. Sci. Inst. Fr., Vol. 23, pp 46 – 50, 1877

[48] Unknown Author, “FLUENT 6.2 Documentation”, Fluent Inc.

[49] T. Jiyuan, H. Y. Guan and C. Liu, “Computational Fluid Dynamics: A Practical Approach”, Butterworth-Heinemann, USA, 2008.

[50] A. Karlsson and L. Fuchs, “Time evolution of the vortex between an air inlet and the ground”, AIAA paper 2000-0990 (2000)

[51] A. Secareanu, D. Morioanu, A. Karlsson and L. Fuchs, “Experimental and numerical study of ground vortex interaction in an air-intake”, AIAA paper 2005-1206 (2005)

[52] A. Gullia, P. Laskaridis, K. W. Ramsden and P. Pilidis, "A preliminary investigation of thrust measurement correction in an enclosed engine test facility", AIAA paper 2005-1128 (2005)

[53] D. L. Motycka, W. A. Walter and G. L. Muller, "An analytical and experimental study of inlet ground vortices", AIAA paper 73-1313 (1973)

[54] W. Liu, E. M. Greitzer, C. S. Tan, "Surface static pressure in an inlet vortex flow field", ASME Journal of engineering for gas turbines and power, 107, pp. 387-393 (1985)

[55] H. W. Shin, W. K. Cheng, E. M. Greitzer, C. S. Tan, C. L. Shippee, "Circulation measurements and vortical structure in an inlet-vortex flow field", J. Fluid Mech. 162 pp. 463-487 (1986)

[56] D. L. Motycka et al., Pratt and Whitney Aircraft TDM 2414 (not available at the time of writing) (1975)

[57] W. C. Ruehr, "General Electric Technical Information Series Report", R75AEG384 (1975)

[58] H. Kline, "Small scale tests on jet engine pebble aspiration tests", Douglas Aircraft Company, Report SM-14885 (1953)

[59] G. Mallinson, Private Communication (2009)

[60] J. D. Gilmore, "Computational Fluid Dynamics Analysis of Jet Engine Test Facilities", PHD Thesis, University of Canterbury, submitted 2009.

[61] T. W. Lancey and C. A. Kodres, "TCNOISE: A Computer Program to Calculate Noise Levels and Directivity from a Jet Engine Test Cell", Naval Facilities Engineering Services Center Technical Report TR-2085-ENV, 1997.

[62] R. J. Freuler and K. A. Montgomery, "Reducing Large Pressure Fluctuations in an Engine Test Cell by modifying the Exhaust Blast Basket", CEAS/AIAA 95-128, 1995

[63] D. Corce, “Feasibility Study for Utilizing Sawtooth Noise Reduction Device wit Type T-10 Turbofan/Jet Engine Test Cells”, Naval Air Engineering Centre Design Data Report, 1990.

[64] C. A. Kodres, “Jet Engine Test Cell Noise Reduction”, Naval Facilties Engineering Command Technical Report TR-2118ENV, 2000.

[65] D. F. Long, “Jet Engine Test Cell Structure”, US Patent 5837890.

[66] R. A. Dickman, H. W. Hehlnann, W. Hoelmert and R. J. Freuler, “A solution for aero-acoustic induced vibrations originating in a turbofan engine test cell”, AIAA 84-0594, 1984.

[67] G. Porges, “Applied Acoustics”, Peninsula Press, Los Altos, CA, 1987.

[68] R. E. Glass, “Acoustic Performance of Air-Cooled Jet Engine Test Facilities”, Naval Ocean System Centre Technical Report 1142, 1986.

[69] E. E. Callaghan and W. D. Coles, “Investigation o Jet-Engine Noise Reduction By Screens Located Transversely Across the Jet” National Advisory Committee for Aeronautics Technical Note 3452, 1955.

[70] Frandsen and Chamberlain Architects, “Study of Pulsations, Cell #8, Bldg 268 Hill AFB, UT”, Report No. RIC 1239A-4, 1984.

[71] Unknown Author, “Addition of Low-Frequency Noise Suppressor in USAF Hush-House Improves Airbase Community Relations”, Industrial Acoustics Company Bulletin 2.1210.0

[72] D. E. Hall, “Basic Acoustics”, John Wiley & Sons Inc., 1987.

[73] M. L. Munjal, “Acoustics of Ducts and Mufflers”, Wiley-Interscience Publication, 1987.

[74] M. J. Lighthill, “"Sound Generated Aero- dynamically", The Rakerian Lecture, The Royal Society, London, 1961.

[75] Freuler R. J. and Montgomery K. A., “Reducing Large Pressure Fluctuations in an Engine Test Cell by modifying the Exhaust Blast Basket”, CEAS/AIAA 95-128, 1995.

[76] R I Corporation Consultants and Frandsen and Chamberlin Architects, "Study of Pulsations Cell #8, Bldg 268 Hill AFB UT", Report No. RIC-1239A-4, 1984.

[77] Md. Mahbub Alam and Zhou Y., "Dependence of strouhal number, drag and lift on the ratio of cylinder diameters in a two-tandem cylinder wake", 16th Australasian Fluid Mechanics Conference, 2007.

[78] F. Teglas, "Sound Reflection", Internet article, address:

http://interactivesonicspaces.interfaculty.nl/ferenc_teglas/reflection.htm, last date accessed: 30th March 2009

[79] R. A. Dickman et al., "A solution for aero-acoustic induced vibrations originating in a turbofan engine test cell", AIAA84-0594, 1984.

[80] M. J. Lighthill, ""Sound Generated Aero- dynamically", The Rakerian Lecture, The Royal Society, London, 1961.

[81] K. W. Hatlestad, "Scale model testing of infrasound produced by various jet engine test cell configurations", AIAA 2006-2540, 2006

Appendix A Velocity Gradient for Glenny's Data

Values extracted from Glenny's result

Table 15: Values from Glenny's Result

Ro	D(""/m)		V
8	12	0.30	45.72
18	12	0.30	45.72
25	12	0.30	45.72
25	6	0.15	45.72
12	12	0.30	45.72
17	12	0.30	45.72
17	6	0.15	45.72

Table 16: Calculation of Velocity Gradient from Rossby Number (Glenny's Data)

Ro	D(""/m)		V	$W_{apparent}$
8	12	0.30	45.72	18.75
18	12	0.30	45.72	8.33
25	12	0.30	45.72	6.00
25	6	0.15	45.72	12.00
12	12	0.30	45.72	12.50
17	12	0.30	45.72	8.82
17	6	0.15	45.72	17.65

Calculation of velocity gradient (W) directly from Rossby number

assuming V_i is 150 ft/s but it was mentioned that the maximum velocity used is 350 ft/s which doesn't alter the result much in fact it increases the $W_{apparent}$ and hence the W_{actual} shown in later calculations

However, according to Glenny's diagram (Fig. 5, pp. 33 of his paper) it suggests (but not confirmed) that $W_{apparent}$ is measured or calculated in line with the longitudinal axis of the fan (which was mentioned as 55 degrees). If we use simple geometry on the experimental positions of Glenny, given in Figure 97 below, with the yellow and blue triangle representing the apparent and actual velocity gradients respectively.

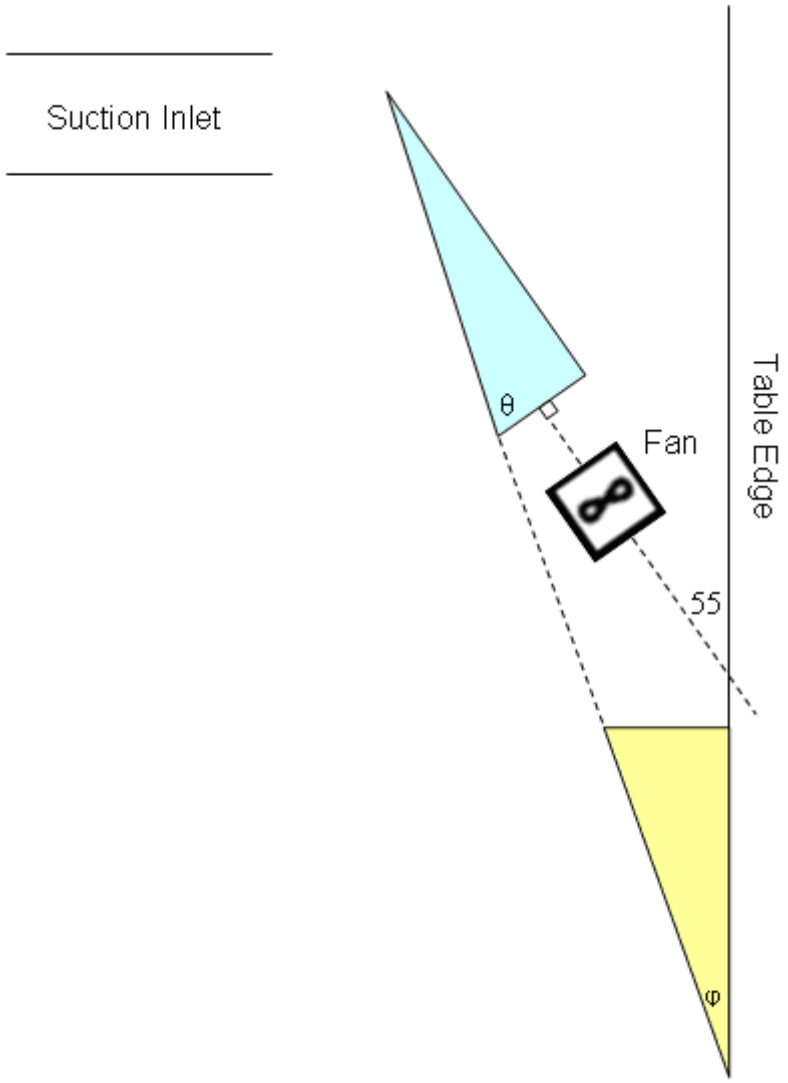

Figure 97: Glenny's Experimental Positions (not drawn to scale)

The velocity gradient we should be comparing is tan(φ) instead of tan(θ). Thus the actual W should be corrected from $W_{apparent}$ using the following formula:

$$W_{actual} = \tan\left(\tan^{-1}\left(W_{apparent}\right) - 35^{\circ}\right) \quad \textbf{(21)}$$

Table 17: Calculation of actual Velocity Gradient (Glenny's Experiment)

Ro	D(""/m)		V	$W_{apparent}$	W_{actual}
8	12	0.30	45.72	18.75	1.28
18	12	0.30	45.72	8.33	1.12
25	12	0.30	45.72	6.00	1.02
25	6	0.15	45.72	12.00	1.20
12	12	0.30	45.72	12.50	1.21
17	12	0.30	45.72	8.82	1.13
17	6	0.15	45.72	17.65	1.27

The correction of the velocity gradient may not be necessary as the velocity gradient in the cross-flow direction could be important to the formation of vortices as shown by Shin et al. [1].

References

[1] H. W. Shin, W. K. Cheng, E. M. Greitzer, C. S. Tan, C. L. Shippee, "Circulation measurements and vortical structure in an inlet-vortex flow field", J. Fluid Mech. 162 pp. 463-487 (1986)

Appendix B Effect of Crosswind over a U-Shaped JETC

The work detailed in this appendix was conducted by an undergraduate Final Year Project student with limited input from the author. It has been included in this thesis because it is closely related to the vortex work and the results have been published in a conference proceedings and journal paper together with some of the results from this thesis.

A CFD simulation was conducted using Fluent to investigate how the direction of the wind blowing around the intake stack of a U-shaped test cell affects the upstream velocity gradient. A CFD model was created of a vertical intake stack, turning vanes and the front portions of the main engine chamber. The CFD model and mesh is shown in Figure 98 and Figure 99 respectively.

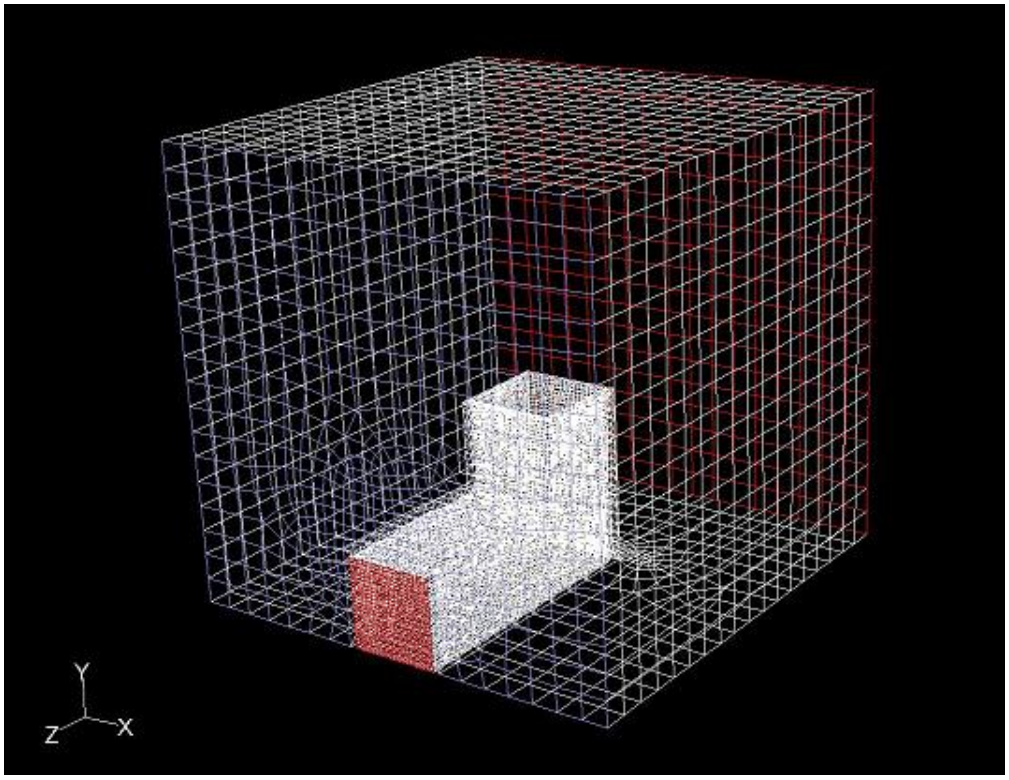

Figure 98: CFD model used for the cross-wind simulations

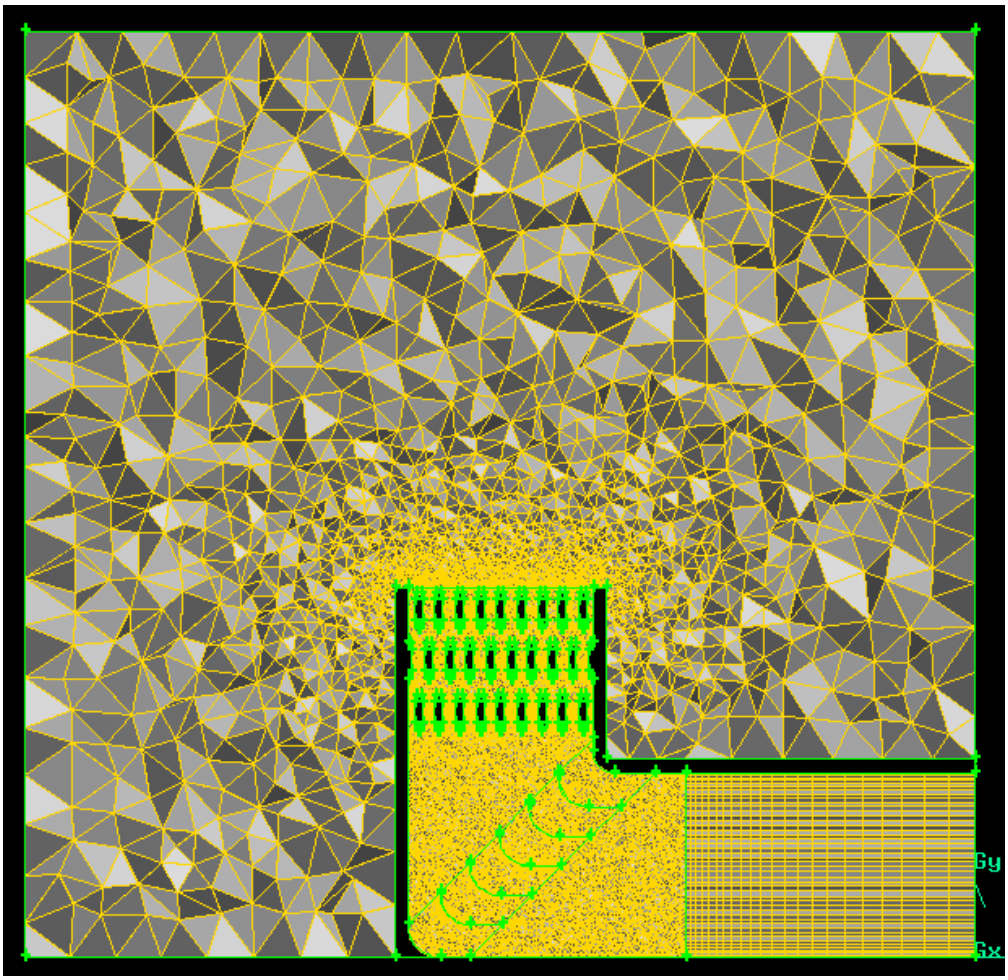

Figure 99: Mesh used for the cross-wind simulations

Six different scenarios, including five wind directions and one no wind condition, were solved and are as listed:

1. No Wind
2. +Z
3. -Z
4. -X
5. +Z-X
6. -Z-X

The wind profile was of the power law type $\left(U = U_{ref}\left(\frac{z}{z_{ref}}\right)^{a} \right)$ as described in CFD simulations of the wind Environment around an Airport Terminal Building [1] and is

applied to the appropriate boundaries in the model. This profile was validated with experimental data at an airport of comparable layout. The profile was implemented using a UDF in Fluent; which was applied to the upwind velocity inlet boundary. In the case of diagonal winds, the UDF was rewritten using Pythagoras's theorem and applied to the two upwind boundaries. The profile has a reference velocity of 10 ms^{-1} at a reference height of 14m (the height of the test cell inlet).

Contour plot of velocity at a plane in the X-Y direction for each of the wind cases is shown in Figure 100 below.

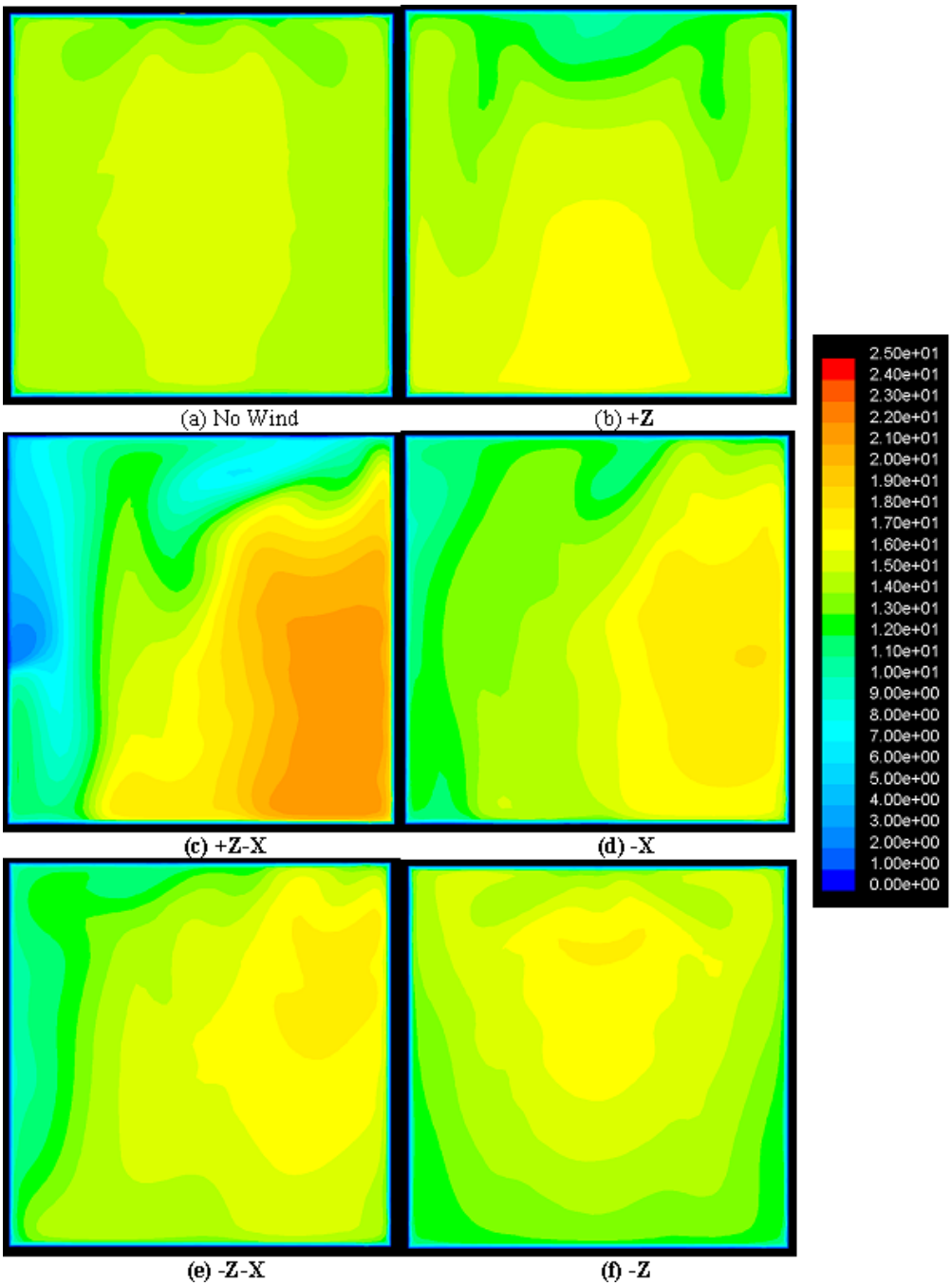

Figure 100: X-Y plane velocity contour plot

References

[1] Neofytout P., Venestsanos A. G. et al., “CFD Simulations of the Wind Environment around an Airport Terminal Building” QNET CFD Newsletter, July 2003

Appendix C UDF Source Code for Vortex Simulations

The following are examples of the codes used to generate the upstream/ambient velocity gradient in the vortex simulations.

The first set is for generating a velocity gradient without a boundary layer and the second has an additional equation simulating a boundary layer with a pre-determined thickness.

```
#include "udf.h"

DEFINE_PROFILE(Scenario1 /*profile name*/, thread, index)
{
 double x[ND_ND];
 double Y;
 double Uref = 1.0;                    /*Denote starting value of vel.*/
 double Yref = -13.75;                 /*Denote the position of the vel. profile*/
 double Gradient = 0.2;                /*Denote the vel. gradient desired*/
 face_t f;

 begin_f_loop(f, thread)
   {
    F_CENTROID(x,f,thread);            /*Direction of the gradient*/
          Y = x[2]; /*x[0] denotes x-direction, x[1] denotes y-direction, x[2] denotes z-direction*/

    F_PROFILE(f, thread, index) = ((Y-Yref)*Gradient)+Uref;
   }
 end_f_loop(f, thread)
}
```

```
#include "udf.h"

DEFINE_PROFILE(Scenario1 /*profile name */, thread, index)
{
 double x[ND_ND];
 double Y;
 double Z;
 double z_grad=0.2;
 double BL_thickness=5;
 double n=0.143;
 double Uref=5.3;
 double Zref = -13.75;
 face_t f;

 begin_f_loop(f, thread)
   {
    F_CENTROID(x,f,thread);
          Y = x[1];
          Z = x[2];
```

```
    if (Y<BL_thickness)                /*Boundary layer profile*/
          F_PROFILE(f, thread, index) = (pow((Y/BL_thickness),n))*(((Z-Zref)*z_grad)+Uref);
           else
    F_PROFILE(f, thread, index) = ((Z-Zref)*z_grad)+Uref;
   }
 end_f_loop(f, thread)
}
```

Appendix D Arnault's Experiment Procedures

The test rig used in this study (Figure 101 and Figure 102) consists of a suction inlet of diameter D_i = 14mm mounted above a ground plane extending approximately 400mm upstream of the inlet, 250mm downstream and 4mm thick suspended 20mm above the wind tunnel floor to control boundary layer growth. A screw jack allows the height of the inlet centreline (H) to be varied from 26 to 60mm above the ground plane. H was measured with an electronic vernier gauge to ±2%.

The inlet was connected to a centrifugal fan. A static tapping behind the inlet allowed a measurement of the inlet throat velocity. The tapping was calibrated against a pitot-static tube in a length of 100mm diameter pipe between the inlet and the fan. The uncertainty in V_i was +2,-1m/s with 80% of this uncertainty being systematic, due to the calibration against a previously calibrated Pitot tube, and 20% being random.

The wind tunnel speed (V_0) was measured with a static tapping in the contraction preceding the test section. The measurement of V_0 had an uncertainty of ±10% at the lowest speeds to ±5%, approximately half being systematic and half random. The air temperature in the tunnel was monitored with a thermocouple.

This gives uncertainty ranges of ±2.2% on H/D_i, dominated by random errors, and ±14% on V_i/V_o, consisting of 5% random errors and 9% systematic errors. The whole ±14% V_i/V_o error bar is plotted on the V_i/V_o increasing data in Figure 103 and ±5% (random uncertainty only) on the V_i/V_o decreasing points.

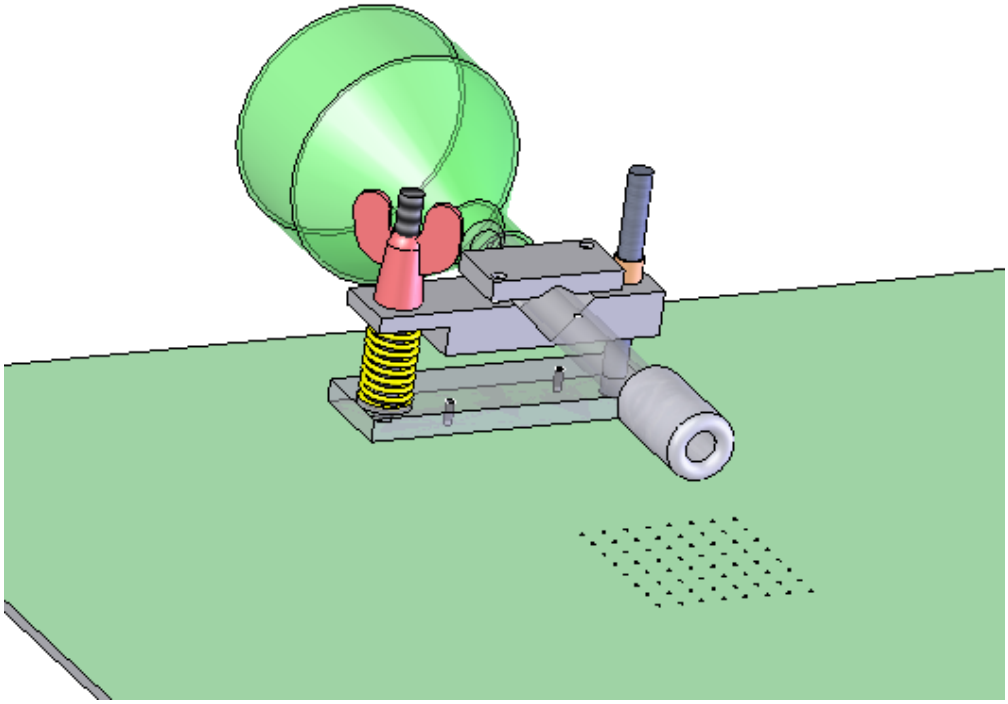

Figure 101: Arnault's Experimental Setup (CAD)

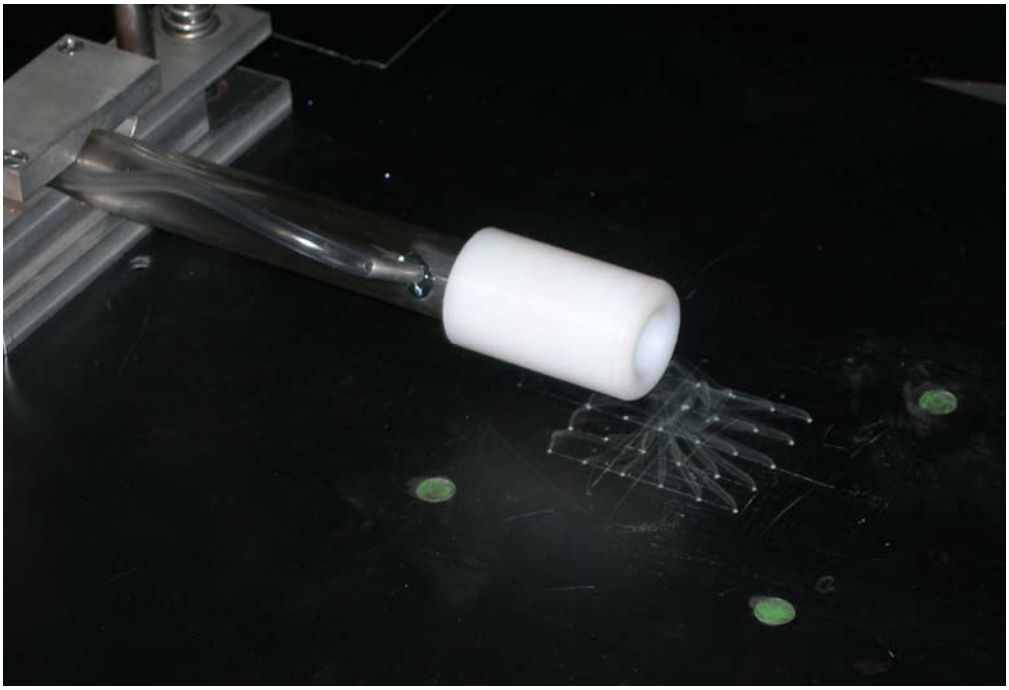

Figure 102: Arnault's Experimental Setup (Actual)

The ground plane was pierced with a 5x5 grid of 1mm diameter holes communicating with a plenum fed by a smoke generator. In this way 25 threads of smoke emerged, initially perpendicular to the ground plane, so that the flow just upstream of the inlet could be visualised.

Initial tests with a smoke wand laid on the ground plane showed that the momentum of the smoke flow was sufficient to trigger a vortex and determine its direction of rotation. Looking downstream, if the smoke wand was on the left hand side of the inlet, it generated a clockwise torque on the flow and triggered a clockwise vortex. An anticlockwise vortex could be created with the smoke wand on the right hand side of the inlet. By contrast, the vertical holes in the ground plane contributed no z-axis vorticity to the flow and did not prejudice the formation and/or direction of the vortex beyond that natural to a flow without artificial sources of angular momentum. In addition, the momentum of the smoke flow was greatly reduced by the pressure losses in the system, and was being spread out over a wide area symmetrical about the inlet centreline.

The flow pattern was imaged with a light sheet from a 40mW green diode laser with a cylindrical lens illuminating a plane parallel to the ground, between the ground and the inlet. A video camera mounted above the rig captured images of the illuminated smoke trails. Inspection of this video revealed the presence or absence of the vortex.

The height was set to a given value, with wind tunnel closed and the fan speed varied with a Variac.

Each test was repeated three times and the results averaged. The standard deviation of the V_i threshold in the three tests at each V_0 was 1-5% of the mean, less than the experimental uncertainty in V_i/V_o.

The threshold values of V_i were averaged over all three tests at each V_o. The standard deviation of this average over all three V_0 was 3-8%, comparable to the random component of the experimental uncertainty in V_i/V_o.

In all observations the vortex had a single core. Double core vortices were never observed. In 65% of instantaneous observations in the present study the vortex had a clockwise rotation, in the remainder an anticlockwise rotation. The direction of rotation fluctuated with a period of typically 2 or 3 seconds between changes in direction.

Results

Table 18 gives the test results. The points are also plotted in Figure 103.

Table 18: Arnault's Result

V_o (ms^{-1})	3.11		2.54		1.80	
Re_o	2886		2357		1666	
	↑ V_i	↓ V_i	↑ V_i	↓ V_i	↑ V_i	↓ V_i
H/D_i	V_i/V_o	V_i/V_o	V_i/V_o	V_i/V_o	V_i/V_o	V_i/V_o
1.9	12.1	11.4	10.7	10.4	11.3	9.7
2	13.7	13.0	12.4	12.1	13.0	11.3
2.1	14.9	13.9	14.0	13.6	14.5	13.0
2.2	16.6	15.7	15.6	14.7	16.4	14.4
2.3	18.0	17.3	17.4	16.6	17.1	15.0

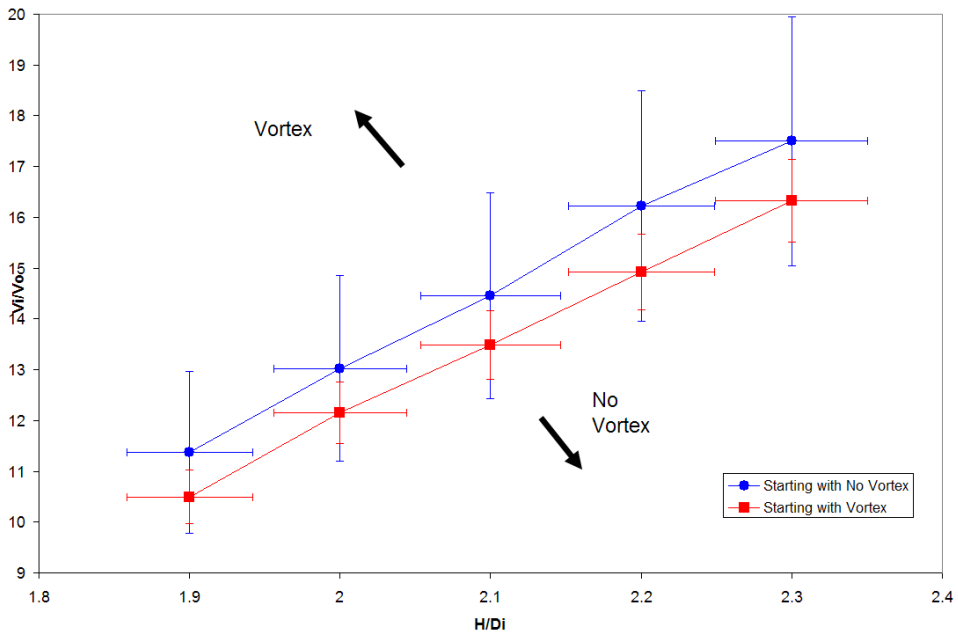

Figure 103: Arnault's Vortex Threshold

Appendix E Derivation of CBR – H/Di Relationship

If $\frac{V_i}{V_0}$ vs. $\frac{H}{D_i}$ is a linear relationship,

$$\Longrightarrow \qquad \frac{V_i}{V_0} = m\left(\frac{H}{D_i}\right) + C$$

And

$$\begin{aligned} CBR &= \frac{\dot{m}_{cell} - \dot{m}_{engine}}{\dot{m}_{engine}} \\ &= \frac{Q_0 - Q_i}{Q_i} \\ &= \frac{Q_0}{Q_i} - 1 \end{aligned}$$

Assume $\rho_0 \approx \rho_i$

$$\begin{aligned} CBR &= \frac{V_0 A_0}{V_i A_i} - 1 \\ &= \frac{V_0}{V_i}\left(\frac{A_0}{A_i}\right) - 1 \\ \therefore \frac{V_0}{V_i} &= \frac{(CBR+1)}{A_0 / A_i} \\ \frac{V_i}{V_0} &= \frac{A_0}{(CBR+1)A_i} \end{aligned}$$

$$\begin{aligned} m\left(\frac{H}{D}\right) + c &= \frac{A_0}{(CBR+1)A_i} \\ \frac{A_0}{A_i} &= (CBR+1)\left[m\left(\frac{H}{D}\right) + c\right] \\ \frac{4H^2}{\pi D^2 / 4} &= (CBR+1)\left[m\left(\frac{H}{D}\right) + c\right] \end{aligned}$$

$$\frac{16H^2}{\pi D^2} = (CBR+1)\left[m\left(\frac{H}{D}\right)+c\right]$$

$$\frac{16}{\pi}\left(\frac{H}{D}\right)\left(\frac{H}{D}\right) = (CBR+1)\left[m\left(\frac{H}{D}\right)+c\right]$$

$$\frac{16}{\pi}\left(\frac{H}{D}\right) = (CBR+1)\left[m+c\left(\frac{D}{H}\right)\right]$$

$$1 = (CBR+1)\left[\frac{m}{16/\pi}\left(\frac{H}{D}\right)^{-1}+\frac{c}{16/\pi}\left(\frac{H}{D}\right)^{-2}\right]$$

$$\frac{1}{CBR+1} = k_1\left(\frac{1}{H/D}\right)+k_2\left(\frac{1}{H/D}\right)^2$$

For the test cell industry or any parties where CBR is a more readily available flow parameter compared to $\frac{Vi}{Vo}$, the above relationship might be very useful.

Appendix F Analysis of JETC Noise Propagation

This appendix presents some formulae, which may be used to perform an analytical calculation of the noise emission from a JETC by calculating sound paths from the source. If more accurate numerical simulations or scaled experimental models can be afforded, it should take a higher priority. However if these are not possible or a quick estimation is required, then these analytical calculations could be used. Some of the applicability of the formulae or relationships is implied from the similar geometric profiles.

As with most complex analytical calculations, it consists of a number of separate formulae for the different parts of the cell. The engine exhaust noise is assumed to be loudest source of noise in the JETC. The parts that are covered in this section are as follows:

1. Engine exhaust noise
2. Propagation from source to inner side of wall
3. Propagation from inner side of wall to outside
4. Parallel baffles
5. Turning vanes
6. Reflection at blast basket perforate
7. Double Walls

The actual derivation of the formulae will not be presented as they can be found in the relevant reference source.

Matlab, Simulink or other analytical tool could be used to combine the individual sections together into a complete model.

F.1 Engine Exhaust Noise

The engine exhaust noise should usually be measured data. In the absence of such data, some kind of estimation techniques may be appropriately used.

F.2 Propagation from engine to inner side of wall

$$\mathrm{SPL(dB)} = \mathrm{SWL_{source}} + 10\log\left(\frac{Q_\theta}{4\pi r^2} + \frac{4}{R_c}\right)\ [1] \quad \textbf{(22)}$$

Alternatively, if an open planned layout is assumed:

$$\mathrm{SPL(dB)} = \mathrm{SWL} - 20\log r - 11\ \ [1]\ \text{For}\ r < 2\mathrm{m} \quad \textbf{(23)}$$

For distance between 2 and 6 m, there is a 3 dB loss for every doubling of distance. For distances greater than 6 m, there is a 6 dB loss for every doubling of distance.

F.3 Propagation from inner wall to the outside

Woods Practical Guide to Noise Control [2] provides an engineering estimate for the transmission of sound from the inside of an enclosure to the outside at a distance (r) away.

$$\mathrm{SPL_{outside}} = \mathrm{SPL_{inside}} - 10\log\frac{1}{\tau_{av}} + 10\log S_{wall} - 20\log r - 14 \quad \textbf{(24)}$$

F.4 Parallel Baffles

Parallel baffles such as those found at the top of the intake and exhaust stack can be estimated from the parallel-baffle duct relationship provided by Munjal [3]. The general solution is a complicated complex equation but he provides the normalized attenuation vs. frequency curves for parallel-baffle duct and one of them is reproduced in Figure 104.

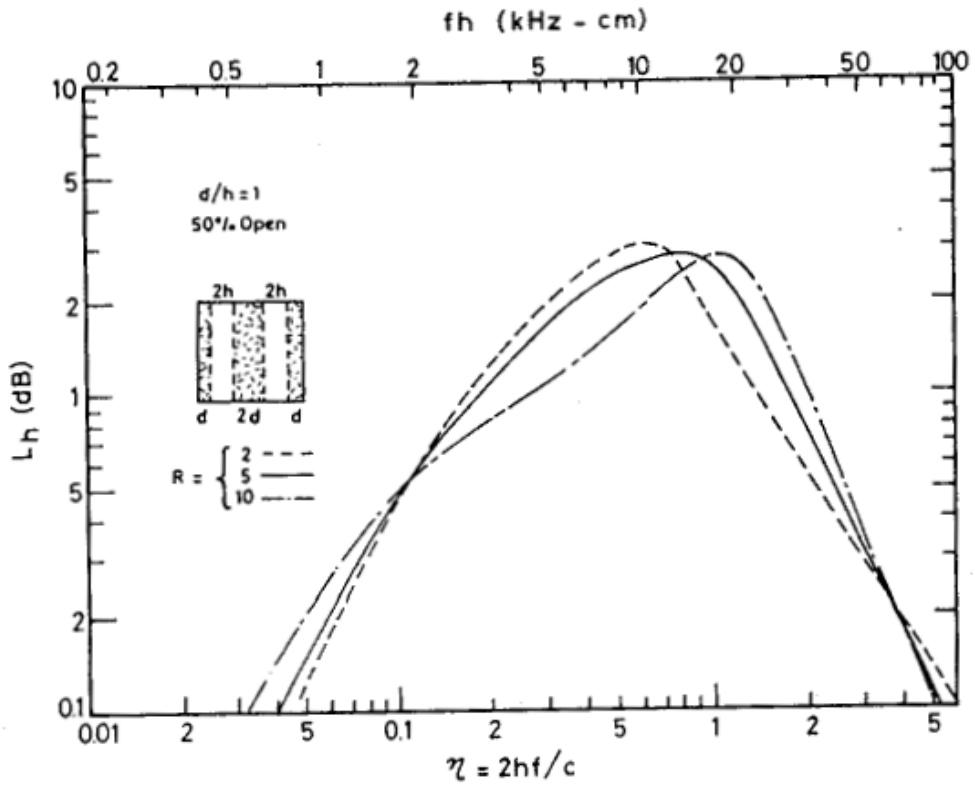

Figure 104: Normalized attenuation vs. frequency curves for parallel-baffle ducts with 50% open area illustrating the effect of baffle flow resistance R (Adapted from [4])

At low frequencies, the attenuation due to the parallel baffles is very low.

F.5 Turning Vanes

The closest estimate for turning vanes would be lined beds in ventilation ducts. Typical values of insertion loss of a 90° lined bend varies linearly from about 1 dB at 63 Hz to about 10 dB at 4 kHz and remains about the same in the next higher octave band [5]

F.6 Reflection Coefficient at Perforated Surface

See chapter 13 for details.

F.7 Double Walls

Most test cells have got double wall constructions typically with an air gap sandwiched by two concrete walls. Double or even triple walls are lighter and more cost effective than a single wall when a high transmission loss is required.

Bies and Hansen [6] provides good explanation on how to calculate the transmission loss of a double wall using the equations developed by Sharp [7]:

$$\begin{aligned} TL &= TL_{1+2} && (f \le f_0) \\ TL &= TL_1 + TL_2 + 20\log_{10} fd - 29 && (f_0 < f < f_l) \\ TL &= TL_1 + TL_2 + 6 && (f \ge f_l) \end{aligned} \qquad \textbf{(25)}$$

Where:

f_l = limiting frequency $= \dfrac{c}{2\pi d} \approx \dfrac{55}{d}$

It also provides details on the construction of a design chart for estimating the transmission loss of a double panel wall based on Sharpe's analysis [8] and is reproduced in Figure 105 below.

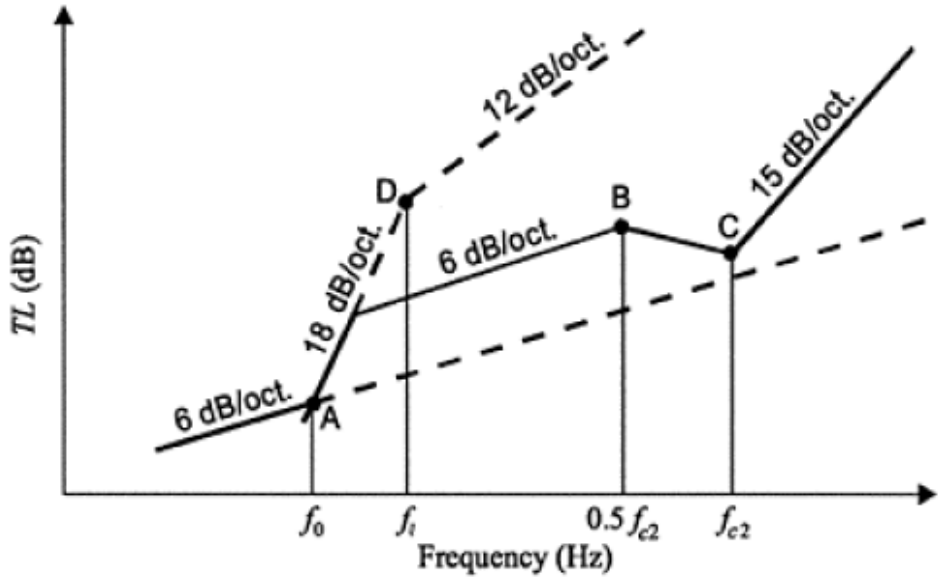

Figure 105: Design chart for estimating transmission loss of a double panel wall (reproduced from [6])

Where f_{c1} and f_{c2} are the critical frequencies of the sandwiching panels.

References

[1] Sharland I., "Woods Practical Guide to Noise Control", Woods Acoustics, pp 62 – 71, 1972

[2] Sharland I., "Wood's Practical Guide to Noise Control", Woods Acoustics, pp75 – 76, 1972

[3] Munjal M. L., "Acoustics of Ducts and Mufflers", John Wiley and Sons, pp 244 – 247, 1987

[4] Munjal M. L., "Acoustics of Ducts and Mufflers", John Wiley and Sons, pp 247, 1987

[5] J. D. Irwin and E. R. Graf, "Industrial Noise and Vibration Control", Prentice-Hall, Englewood Cliffs, NJ, 1979

[6] D. A. Bies and C. H. Hansen, "Engineering Noise Control – Theory and Practice", Spon Press, 1988

[7] B. H. Sharp, "Prediction Methods for the Sound Transmission of Building Elements", Noise Control Engineering, 11, 5533, 1978.

[8] B. H. Sharp, "A Study of Techniques to Increase the Sound Installation of Building Elements", Wylie Laboratoris Report WR 73-S, prepared for Department of Housing and Urban Development, Washington DC, under contract H-1095, 1973.